



**HAL**  
open science

**Characterization of the infiltration in the cave of Villars  
(Dordogne) by geophysical and isotopic methods :  
Importance for paleo-climatic studies based on  
speleothems as well as for the conservation of heritage  
sites**

Jian Zhang

► **To cite this version:**

Jian Zhang. Characterization of the infiltration in the cave of Villars (Dordogne) by geophysical and isotopic methods : Importance for paleo-climatic studies based on speleothems as well as for the conservation of heritage sites. Environmental Engineering. Université de Bordeaux, 2023. English. NNT : 2023BORD0167 . tel-04210988

**HAL Id: tel-04210988**

**<https://theses.hal.science/tel-04210988v1>**

Submitted on 19 Sep 2023

**HAL** is a multi-disciplinary open access archive for the deposit and dissemination of scientific research documents, whether they are published or not. The documents may come from teaching and research institutions in France or abroad, or from public or private research centers.

L'archive ouverte pluridisciplinaire **HAL**, est destinée au dépôt et à la diffusion de documents scientifiques de niveau recherche, publiés ou non, émanant des établissements d'enseignement et de recherche français ou étrangers, des laboratoires publics ou privés.

**DOCTEUR DE**  
**L'UNIVERSITÉ DE BORDEAUX**

ÉCOLE DOCTORALE DE Sciences et environnements

SPÉCIALITÉ : Géologie sédimentaire, paléocéanographie, climatologie

**Caractérisation de l'infiltration dans la grotte de Villars  
(Dordogne) par des méthodes géophysiques et isotopiques:  
Importance pour les études paléo-climatiques basées sur les  
spléleothonèmes ainsi que pour la conservation des sites  
patrimoniaux**

Par **Jian ZHANG**

Sous la direction de: Dominique GENTY

(Co-directrice: Colette SIRIEIX)

Soutenue le 26/Juin/2023

Membres du jury :

M. LARTIGES Bruno	Professeur, Université de Toulouse III Paul Sabatier	Rapporteur/Président
M. CHALIKAKIS Konstantinos	Maître de Conférences, HDR, Avignon Université	Rapporteur
M. BRUXELLES Laurent	Directeur de Recherche, CNRS, Université de Toulouse - Jean Jaurès	Examineur
M. BOURGES François	Docteur, Ingénieur, Géologie Environnement Conseil	Examineur
M. GENTY Dominique	Directeur de Recherche, CNRS, Université de Bordeaux	Directeur de thèse
Mme. SIRIEIX Colette	Professeur, Université de Bordeaux	Co-directeur de thèse



## Résumé

La géométrie du milieu environnant les grottes et les zones d'infiltration d'eau ainsi que les processus d'infiltration des précipitations dans les zones karstiques sont complexes et encore mal comprises. Ces connaissances sont pourtant cruciales pour l'interprétation des reconstructions climatiques basées sur les spéléothèmes, pour l'étude des recharges en eau des zones karstiques et pour la conservation du patrimoine des grottes préhistoriques. Afin d'approfondir nos connaissances sur ce sujet, nous avons choisi une grotte peu profonde typique (la grotte de Villars, dans le sud-ouest de la France) qui a été monitorée pendant des décennies et où de nombreuses études ont déjà été faites sur l'environnement actuel et sur les spéléothèmes.

La première question sur laquelle nous avons travaillé concerne le signal d'entrée des précipitations au-dessus de la grotte de Villars. Quelle est la source des précipitations au-dessus de la grotte, et comment varie-t-elle ? Pour cela, nous avons utilisé un modèle de rétro-trajectoires atmosphériques (HYSPLIT) pour mieux comprendre les sources isotopiques de l'oxygène des précipitations ( $\delta^{18}\text{O}$ ) et de l'eau d'infiltration. Les résultats ont révélé une saisonnalité bien marquée des sources pluviales (ici exprimées en pourcentage des sources d'humidité initiales (PSHI)) liées à la distance entre la grotte de Villars et les régions sources d'humidité, ainsi que des tendances à long terme.

La deuxième question concerne la caractérisation de l'infiltration et de son évolution temporelle à partir de la composition isotopique de la pluie jusqu'à l'eau qui alimente les stalagmites. Nous avons utilisé à la fois un ensemble de données isotopiques à très long terme (>20 ans) combiné à un modèle conceptuel (KarstFor) qui mélange les flux d'eau et les isotopes pour mieux comprendre le processus d'infiltration karstique. Les résultats ont montré que les variations modélisées de la quantité d'eau de stockage et du débit d'infiltration coïncident avec les taux d'écoulement par égouttement observés sous les stalactites à deux niveaux différents de la grotte. Le fait que le modèle simule de manière frappante la différence isotopique faible, mais constante, entre les galeries supérieures et inférieures de la grotte de Villars, non seulement renforce le modèle lui-même, mais révèle également l'impact des voies d'infiltration multiples et de la dynamique du réservoir karstique sur le  $\delta^{18}\text{O}$  de l'eau d'égouttement.

La troisième question portait sur la géométrie de la zone d'infiltration : réservoirs d'eau et voies d'écoulement préférentielles. Pour cela, nous avons appliqué la méthode de tomographie de la résistivité électrique en 2D (TRE) au-dessus de la grotte de Villars à un intervalle d'un à deux mois pendant trois ans (février 2020 à janvier 2023). À l'aide d'une approche statistique multidimensionnelle (classification hiérarchique ascendante, CHA), les images de TRE ont mis en évidence une saisonnalité marquée des variations de la résistivité dans différentes zones d'infiltration. Ceci nous a permis de visualiser des zones karstiques spécifiques caractérisées par leur résistivité et leurs variabilités de résistivité, conduisant à l'identification de galeries de grottes, de réservoirs de stockage d'eau, de fronts d'infiltration, de couches de sol et de chemins d'écoulement préférentiels potentiels jusqu'à 30 m de profondeur.

En combinant la tomographie électrique, l'hydrologie et les méthodes isotopiques, nous avons considérablement amélioré notre compréhension des écoulements et de la variabilité de l'écoulement de l'eau au-dessus de la grotte de Villars, ainsi que des processus de mélange dans les réservoirs qui alimentent les stalactites. Ces connaissances sont de première importance pour la préservation de l'environnement des grottes et pour la recherche paléoclimatique basée sur l'étude des spéléothèmes.

**Mots clés :** Précipitation; Rapports isotopiques; Modèle HYSPLIT; Sources d'humidité ; réservoirs karstiques ; Infiltration ; Zones non saturées ; TRE ; Géophysique ; Taux d'égouttement ; Grotte de Villars ; spéléothèmes ; Sud-ouest de la France



# **Title: Characterization of the infiltration in the cave of Villars (Dordogne) by geophysical and isotopic methods: Importance for paleo-climatic studies based on speleothems as well as for the conservation of heritage sites**

## **Abstract**

The geometry of caves and infiltration zones as well as the rainfall infiltration processes in karst areas are complex and still not completely understood. This knowledge is, however, crucial for the interpretation of speleothem-based climatic reconstructions, water sustainability, and heritage conservation. In order to deepen our knowledge on this topic, we choose a typical shallow cave (Villars Cave, SW-France) that has been monitored for decades and where numerous studies have been already made on both present-day environment and speleothem studies.

The first question that we worked on was about the rainfall “input” signal above the Villars Cave. What is the source of the rainfall above the cave, and how does it vary? For that, we used a backtracking (HYSPLIT) model to better understand the rainfall original oxygen isotopic sources ( $\delta^{18}\text{O}$ ) of the seepage water. Results revealed a well-marked seasonality of the rainfall sources and long-term trends, depending on the distance between Villars Cave and moisture source regions, expressed in the percentage of initial moisture sources (PIMS).

The second question concerns the characterization of the infiltration and its time evolution using isotopic composition from the rainfall to the stalactite dripping water that feeds stalagmites. We used both a very long monitoring (>20 years) isotopic data set (of rainfall and dripping rates at a different level in this cave) combined with a conceptual model (KarstFor) that mixes water flows and isotopes to better understand the process of karst infiltration. Results showed that the modeled output variations in the quantity of storage water and infiltration flow coincide with the observed dripping discharge rates made under stalactites at two different gallery levels in the cave. The fact that the model strikingly simulates the small, but constant, isotopic difference between the upper and the lower galleries of Villars Cave, not only reinforces the model itself but also reveals the impact of multiple infiltration routes and karst reservoir dynamics on the drip-water  $\delta^{18}\text{O}$ .

The third question focused on the geometry of the infiltration zone: water reservoirs and preferential flow routes. For that, we applied a 2D ERT (Electrical resistivity tomography) method above the Villars Cave at a one-two monthly interval during three years (February 2020 and January 2023). With the help of a multidimensional statistical approach (Hierarchical agglomerative clustering, HAC), ERT monitoring images revealed the seasonal variation of resistivity in different ERT regions. This allowed us to visualize specific karst zones characterized by their resistivity and their variability in resistivity, leading to the identification of cave galleries, water storage reservoirs, wetting fronts, soil layers and potential preferential flow paths as deep as 30 m.

By combining ERT, hydrology and isotopic methods, we have significantly improved our understanding of the source and variability of the water flow above Villars Cave, as well as the mixing processes in the reservoirs that feed the stalactites. This knowledge is invaluable for the preservation of the cave environment and for speleothem-based paleoclimatic research.

**Keywords:** Rainfall; Isotope ratios; HYSPLIT model; Moisture Sources; Karst reservoirs; Infiltration; Unsaturated zones; ERT; Geophysics; Drip rate; Villars Cave; Speleothems; Southwest France



## Scientific productions and submissions

### Peer-reviewed journal articles arising directly from this thesis:

1. **Jian Zhang, Dominique Genty, Colette Sirieix**, Simon Michel, Bénédicte Minster, Edouard Régnier, Quantitative assessments of moisture sources and temperature governing rainfall  $\delta^{18}\text{O}$  from 20 years' monitoring records in SW-France: Importance for isotopic-based climate reconstructions, *Journal of Hydrology*. 2020. <https://doi.org/10.1016/j.jhydrol.2020.125327>.
2. **Jian Zhang, Dominique Genty, Colette Sirieix**, Cécile Verdet, Sylvain Mateo, Ludovic Devaux, Giovanni Sgubin, Stéphane Bujan, Bénédicte Minster, Edouard Régnier, Ting-Yong Li, François Bourges, Ming-Qiang Liang, Chaojun Chen. Data-model comparisons of isotopic and hydrological variability of the karst vadose zone above Villars Cave, SW-France: implications for speleothem paleoclimate records. *Chemical geology* (Revised)
3. **Jian Zhang, Colette Sirieix, Dominique Genty**, Cécile Verdet, Fabien Salmon, Shan Xu, Sylvain Mateo, Marie Larcanché, Stéphane Bujan, Ludovic Devaux. Imaging hydrological dynamics in karst unsaturated zones by time-lapse electrical resistivity tomography. *Science of the Total Environment* (Under review)

### Peer-reviewed journal articles published and submitted during doctoral candidature but not directly related to the thesis:

4. **Jian Zhang**, Ming-Qiang Liang, Ting-Yong Li, Chao-Jun Chen, Jun-Yun Li. Asian-Australian monsoon evolution over the last millennium linked to ENSO in composite stalagmite  $\delta^{18}\text{O}$  records. *Quaternary Science Reviews*. 2022. <https://doi.org/10.1016/j.quascirev.2022.107420>
5. **Jian Zhang, Dominique Genty**, François Bourges, Simon Michel, Bénédicte Minster, Edouard Régnier, Ludovic Devaux, Zhen Su, Terhi K. Laurila., Origin of the rainfall and cave drip-water  $\delta^{18}\text{O}$  variations in the Chauvet–Orgnac Mediterranean sites (SE-France) based on 20 years-long monitoring records. *Science of the Total Environment* (Will be submitted)





# Contents

<b>Résumé</b> .....	<b>III</b>
<b>Abstract</b> .....	<b>V</b>
<b>Scientific productions and submissions</b> .....	<b>VII</b>
<b>Contents</b> .....	<b>IX</b>
<b>List of Figures</b> .....	<b>XII</b>
<b>List of Tables</b> .....	<b>XVIII</b>
<b>General Introduction</b> .....	<b>1</b>
<b>Chapter 1- Rainfall sources and infiltration process in karst terrains in state of the art</b> .....	<b>4</b>
1.1 Rainfall stable isotopes in the hydrological cycle.....	7
1.1.1 Rainfall isotopic effect.....	8
1.1.2 Rayleigh distillation process.....	12
1.2. Stable isotopes and hydrology in cave drip-water.....	13
1.3. Electrical resistivity tomography.....	17
1.4. Importance for isotopic-based speleothem reconstructions.....	19
<b>Chapter 2-Study area</b> .....	<b>21</b>
2.1 Geological setting.....	21
2.2 Climatic environment around the Villars Cave.....	27
2.3 Vegetation and soil.....	30
<b>Chapter 3- Methods</b> .....	<b>32</b>
3.1 Rainfall stable isotopes.....	32
3.1.1 Stable isotopic composition of rainwater and dripping water.....	32
3.1.2 Meteorological data.....	33
3.1.3 HYSPLIT model for tracking moisture source.....	33
3.1.4 Statistical methods and packages.....	37
3.2 Drip water Stable isotope.....	37
3.2.1 Meteorological data.....	37
3.2.2 Drip discharge rate.....	38
3.2.3 Modeling infiltration process and lag time calculation.....	39
3.3 ERT measurements.....	45
3.3.1 Basic principle.....	45
3.3.2 Factors affecting resistivity.....	46
3.3.3 ERT inversions.....	48
3.3.4 Temperature correction.....	48
3.3.5 Hierarchical Agglomerative Clustering (HAC).....	51
3.4 Determination of depth and location of dripping stations by magnetic field angle (MFA) method.....	52
3.5 Complementarity off the different methods.....	55

<b>Chapter 4 - Origins of precipitation isotopic signature in Villars</b> .....	<b>57</b>
Introduction .....	58
Abstract.....	60
4.1 Results .....	61
4.1.1 Relationship between $\delta^{18}\text{O}_p$ and local/regional climate parameters .....	61
4.1.2 Relationship between $\delta^{18}\text{O}_p$ and initial moisture source on a monthly timescale .....	69
4.1.3 Relationship between $\delta^{18}\text{O}_p$ , d-excess and initial moisture source/local climate parameters on the annual and inter-annual timescale .....	75
4.2. Discussion.....	82
4.2.1 Causes of the variations of precipitation isotope ( $\delta^{18}\text{O}_p$ , $\delta\text{D}_p$ ) in SW-France .....	82
4.2.2 Variations of d-excess on the annual timescale .....	85
4.2.3 Links between NAO and $\delta^{18}\text{O}_p$ in SW-France .....	86
4.2.4 Quantifying the relationship between PIMS/temperature and $\delta^{18}\text{O}_p$ in SW-France .....	87
4.3 Conclusions .....	89
<b>Chapter 5 - Hydrological characterizations of the karst unsaturated zone by using a reservoir-flow model – Simulations of present day and future infiltration characterizations</b> .....	<b>91</b>
Introduction .....	92
Abstract.....	93
5.1 Results .....	94
5.1.1 Rainfall and drip water $\delta^{18}\text{O}$ time series .....	94
5.1.2 Rainfall amount, evapotranspiration, and drip rate relationships .....	98
5.1.3 ERT gives a realistic image of the reservoirs .....	104
5.1.4 Simulations of flowing rate of dripping water .....	105
5.1.5 Simulations of isotopes in dripping water .....	111
5.2 Discussion.....	114
5.2.1. Linking observed drip stations to ERT image and KarstFor model.....	114
5.2.2. Present and future long-term changes of Villars Cave drip water $\delta^{18}\text{O}$ .	116
5.2.3 Infiltration “time delay” versus isotopic mixing process.....	120
5.2.4. Implications for speleothem records .....	121
5.3 Conclusions .....	124
<b>Chapter 6 - Using Time-lapse electrical resistivity tomography to visualize the karst unsaturated zone</b> .....	<b>126</b>
Introduction .....	127
<b>Chapter 6-Part I ERT measurement with a 1m spacing</b> .....	<b>129</b>
Abstract.....	129
6.1 Results .....	130
6.1.1 ERT measurements.....	130
6.1.2 HAC method applied to ERT image classifications.....	135
6.1.3 Rainfall amount, evapotranspiration, and drip rate .....	139

6.2 Discussion.....	145
6.2.1 Recognition of soil layers and cave zones from ERT images .....	145
6.2.2 Clustering resistivity variabilities with local water-excess .....	148
6.2.3 Schematic diagram of the unsaturated karst zone around Villars Cave .	157
6.3 Conclusions .....	160
<b>Chapter 6-Part II ERT measurement with a 1.5m spacing.....</b>	<b>163</b>
6.4 ERT measurement-1.5m spacing results.....	163
6.5 HAC in ERT images-1.5 m spacing .....	166
6.6 Comparisons of variabilities in resistivity in ERT-1.5m and ERT-1m spacing	170
6.6.1 Mutually-validated HAC clusters in ERT-1.5m and ERT-1m spacing .....	170
6.6.2 Unvalidated HAC clusters: Cluster 3-1m and Cluster 6-1.5m.....	175
6.7 Summary.....	176
<b>General conclusion .....</b>	<b>178</b>
<b>Acknowledgments .....</b>	<b>181</b>
<b>Appendix Figures .....</b>	<b>182</b>
<b>Appendix Data .....</b>	<b>187</b>
<b>List of abbreviations .....</b>	<b>206</b>
<b>Bibliography.....</b>	<b>207</b>

# List of Figures

## Chapter 1

Figure 1. 1 A schematic illustration of karst hydrogeology and cave system processes, modified by Fairchild and Baker (2012) according to Villars Cave, depicts various dripping points marked A, B, and C. These dripping points are influenced by different infiltration paths and reservoirs, leading to changes in drip rate and isotopic compositions.....	4
Figure 1. 2 The Karstolution model is represented by a conceptual figure consisting of various reservoirs shown as boxes. Blue lines indicate water levels, while grey arrows represent fracture flow and the red arrow represents diffuse flow..	7
Figure 1. 3 Diagram illustrating the primary processes related to $\delta^{18}\text{O}$ variations for speleothem palaeoclimatology (Lachniet, 2009).....	8
Figure 1. 4 A gridded $\delta^{18}\text{O}$ map of the ocean, based on data from LeGrande and Schmidt (2006). .....	10
Figure 1. 5 Based on data from the GNIP stations, the global land distribution of annual mean rainfall $\delta^{18}\text{O}$ shows significant spatial variation, as reported by Bowen and Wilkinson (2002).....	10

## Chapter 2

Figure 2. 1 Villars Cave map. (A) Locations of Villars Cave. (B) A 3D cave structural diagram and the distribution of surveillance sites (red circles) of Villas Cave (Vil-#3, Vil-#1A and 1B, Vil-#10A and Vil-#10B). The reader is referred to (Genty, 2008; Genty et al., 2014a) for detailed site descriptions and maps. (C) Profile of ERT and the location of Villars Cave (Red line for ERT-1m spacing, and red and blue lines for ERT-1.5 m spacing) (Cassou and Verdet, 2021). .....	22
Figure 2. 2 Geological maps of area around the Villars Cave. (C): Cretaceous (Green color); (J): Jurassic (Brown-Yellow colors) where Villars Cave developed (red dot) in Bajocian and Bathonian limestone; from BRGM, Service Géologique National, Orléans, France; Thiviers Map XIX-33 1/50000 (From L. Bruxelles).....	23
Figure 2. 3 Distribution of rivers and towns around Villars Cave. The map is from Géoportail ( <a href="https://www.geoportail.gouv.fr/carte">https://www.geoportail.gouv.fr/carte</a> ).....	24
Figure 2. 4 Photos of monitoring stations inside Villars Cave (from D. Genty) .....	25
Figure 2. 5 A structural diagram and the distribution of surveillance sites of Villas Cave (Vil-#1A&1B, Vil-#10A&10B, and Vil-3#). The red square shows the Profile of ERT. The drip points Vil-#1B and Vil-#3 are about 5 m apart, located on the lower level of the cave. The drip points Vil-#10A located on the upper level of the cave. This section clearly shows that Station Vil-#1B and Vil-#3 are at the same altitude as the Trincou stream (from Daniel Chailloux, 2022). .....	26
Figure 2. 6 (A) Comparison of local precipitation and (B) potential evapotranspiration above Villars Cave (data from Meteo France). .....	27

Figure 2. 7 Location of the two monitoring stations. (A) Location of the study area, including Villars (a, blue point) and Le Mas (b, red point) in SW-France.....	29
Figure 2. 8 The photo of soil depth and soil type of ERT profile at 9.5 m, 24 m, 38 m, 56 m, and 60.5 m.....	31

### Chapter 3

Figure 3. 1 Conceptual model of karst hydrology in individual karst water reservoirs..	42
Figure 3. 2 Principles of ERT. C1 and C2 are the current electrodes and P1, P2 are the potential electrodes. ....	45
Figure 3. 3. ERT investigation cross section.....	46
Figure 3. 4 Electrical conductivity and resistivity of common rocks based on Palacky, 1988. ....	47
Figure 3. 5 Temperature time series in the air outside the cave, soil, rock, and inside the cave from 2/7/2020 to 27/01/2023. $T_{ref}$ is the reference temperature of 12.55°C, which is the annual average temperature recorded inside the cave (upper level) during the entire monitoring year.....	50
Figure 3. 6 The transmission beacon transmits at 3496 Hz.....	53
Figure 3. 7 Schematic diagram of depth calculation principle from Daniel Chailloux.....	54
Figure 3. 8 A summary figure that illustrates what has been gleaned from this combination of ERT, long-term monitoring, and modeling to underscore the benefit of this approach.....	56

### Chapter 4

Figure 4. 1 Time series of monthly rainfall $\delta^{18}O_p$ at Villars (A) and Le Mas (B) stations. (C) Local meteoric water line (LMWL) for Le Mas (red), and Villars (blue) based on the linear regression. The Global Meteoric Water Line (GMWL) in green (Craig, 1961) is plotted for comparison. ....	62
Figure 4. 2 (A) Correlation between $\delta^{18}O_p$ and local monthly temperature for the 1997-2016 period. (B) Correlation between $\delta^{18}O_p$ and local monthly precipitation for the 1997-2016 period. ....	64
Figure 4. 3 Seasonal correlation maps between $\delta^{18}O_p$ from Le Mas (top panel) and Villars (bottom panel) and temperatures over Europe during the period of 1997-2016 (Some disconnected data is not considered). ....	65
Figure 4. 4 Seasonal correlation maps between $\delta^{18}O_p$ from Le Mas (top panel) and Villars (bottom panel) and precipitation over Europe during the period of 1997–2016 (Some disconnected data is not considered).....	66
Figure 4. 5 Seasonal correlation maps between $\delta^{18}O_p$ from Le Mas (top panel) and Villars (bottom panel) stations and SST in North Atlantic during the 1997–2016 period (Some disconnected data is not considered).....	68
Figure 4. 6 Correlation between $\delta^{18}O_p$ and NAO index at Le Mas and Villars .....	69

Figure 4. 7 Back trajectories for contrasted seasons, winter (December (A), January (B), February (C)) and summer (June (D), July (E), August (F)).....	72
Figure 4. 8 Back trajectories for March (A), April (B), May (C), September (D), October (E) and November (F).....	73
Figure 4. 9 Correlation between annual mean precipitation $\delta^{18}\text{O}$ ( $\delta^{18}\text{O}_{\text{ap}}$ ) and local annual mean temperature and precipitation at Le Mas and Villars. ....	76
Figure 4. 10 Back trajectories for initial moisture sources for the 1997–2016 period. The star indicates the location of Villars, and the detailed data of moisture source were listed in Appendix Table 2.....	79
Figure 4. 11 Comparisons of $\delta^{18}\text{O}_{\text{ap}}$ and the percentage of initial moisture sources (PIMS) and local annual mean temperature and precipitation at Le Mas and Villars on the inter-annual timescale.....	80
Figure 4. 12 Comparisons of the d-excess with the percentage of initial moisture sources (PIMS) and the local annual mean temperature at Le Mas and Villars on the inter-annual timescale. (A) the inter-annual variation of the d-excess at Villars, (B) the inter-annual variation of the d-excess at Le Mas, (C) the inter-annual variation of DA, (D) the inter-annual variation of NAGR. (E) the inter-annual variation of local annual mean temperature in Villars. The fitting dashed lines .....	81

## Chapter 5

Figure 5. 1 The combined time series of meteoric conditions and isotope hydrology of waters in Villars Cave. (A) Comparison with rainfall and drip water $\delta^{18}\text{O}$ values of sites (Vil#1A, Vil#1B, Vil#10A and Vil#10B) in Villars Cave. (B) A separate zoom figure was created to display the $\delta^{18}\text{O}$ values for Vil-#10A. (C) A separate zoom figure was created to display the $\delta^{18}\text{O}$ values for Vil-#1A, Vil-#1B, and Vil-#10B in Villars Cave. (D) The monthly average air temperature outside of Villars Cave. (E) Water excess outside Villars Cave. The pink shading represents the winter months. ....	95
Figure 5. 2 Local meteoric water line (LMWL) (red solid line) based on the $\delta^{18}\text{O}$ and $\delta\text{D}$ values of rainfall outside of Villars Cave. (A) The $\delta^{18}\text{O}$ and $\delta\text{D}$ values for drip waters (Vil-#10A) in Villars Cave are distributed around the LMWL. (B) The $\delta^{18}\text{O}$ and $\delta\text{D}$ values for drip waters (Vil-#1B, Vil-#10A and Vil-#10B) in Villars Cave with a depressed amplitude as compared to that of precipitation. The Global Meteoric Water Line (GMWL) in black (Craig, 1961) is plotted for comparison. ....	97
Figure 5. 3 Comparison of the variability of daily rainfall amount, R-ETP and drip-water rates during 2013-2019. A smoothed (10 points) average to R-ETP in blue line was applied, making it easier to identify daily variabilities.....	99
Figure 5. 4 The delay time between drip-water rates and water excess after the threshold the percolation threshold (R-EPT>0) during 2014-2018 using Pearson's linear correlation coefficient in the MATLAB coherence package. (A-E) Vil-#1A &Water-excess, (F-J) Vil-#1B &Water-excess, (L-M) Vil-#10B &Water-excess.....	100
Figure 5. 5 Comparison of the variability of daily rainfall amount, R-ETP and drip-water rates during 2014-2016. Red arrows indicate the delay days between Vil-#10A and water excess.....	103

Figure 5. 6 Comparison of the variability of daily rainfall amount, R-ETP and drip-water rates during 2017-2019. Red arrows indicate the delay days between Vil-#10A and water excess..... 104

Figure 5. 7 The resistivity model of 07/January 2021 with an electrode spacing of 1 m. The inversion was performed based on the concatenation of the data of all the two arrays (Gradient Array and Pole-Dipole Array), using Res2Dinv software to process data. The ERT image is well coupled with the simulation results of the isotope model. The dashed circles are the possible locations of the monitoring points. .... 105

Figure 5.8 Model hydrological output for 2006-2019. (A) Comparison of local precipitation and ETP in Villars Cave. (B) Water excess (Precipitation minus potential evapotranspiration (P-ETP)>0). (C) The modeled discharge (F1, F4, F7) in the unsaturated zone of Villars Cave. (D) The modeled discharge (F5) in the unsaturated zone of Villars Cave. (E) The modeled discharge (F3, F6) in the unsaturated zone of Villars Cave. Hydrological output is implemented as a python module. Examples are provided for using it from <https://github.com/agriff86/karstolution>..... 107

Figure 5. 9 Correlation and comparison between the simulated flux and the observed drip rate during 2013-2019. (A) Vil-#10A& F4 flow, (B) Vil-#1B & F5 flow, (C) Vil-#10B& F7 flow. Correlation is calculated on a monthly scale. .... 108

Figure 5. 10 The variability of modeled fluxes in the soil store, Epikarst store, and Karst store 2 and 1 with the same vertical axis. .... 109

Figure 5. 11 The variability of modeled fluxes in the soil store (A), Epikarst store (B), and Karst store 2 (C) and 1 (D). .... 110

Figure 5.12 Optimization and the sensitivity test using different parameters in path processes (F) and overflow (Epicap and Ovicap) based on KarstFor model for Villars Cave. (A) Comparisons of modeled epikarst  $\delta^{18}\text{O}$  and observed Vil-#10A (upper gallery) in Villars Cave based on adjusting in F1 and overflow (Epicap) in Epikarst. (B) Comparisons of modeled Karst store 2  $\delta^{18}\text{O}$  and observed Vil-#10B (upper gallery) by adjusting in F4 and overflow (Ovicap) in karst store 2 in Villars Cave. (C) Comparisons of modeled Karst store 1  $\delta^{18}\text{O}$  and observed Vil-#1A and #1B by adjusting in F5 and overflow (Ovicap) in karst store 2 in Villars Cave (lower gallery). There is a temperature difference of 1 °C between different galleries with the upper gallery of 12.5°C and the lower gallery of 11.5°C; therefore, we set different evaporation ( $k_{d18O\_epi}$ ) parameters in upper galleries (Vil-#1B) in a high value: 0.06‰ and in a lower value: 0.04‰ in low galleries (Vil-#1A and #1B). We did not consider the influence of humidity as it remained above 90% saturation throughout. .... 113

Figure 5.13 Optimization and the sensitivity test using different  $k_{d18O\_epi}$  parameters in path processes (F1=0.1) and overflow (Epicap=160) based on KarstFor model for Villars Cave. .... 114

Figure 5. 14 (A) Modeled  $\delta^{18}\text{O}$  in the Karst store 1 & 2 and observed Vil-#10B (Upper gallery) and Vil-#1A/#1B (lower gallery) in Villars Cave. (B) Inside cave temperature (Vil-#1B and Vil-#10B), (C) Mean annual outside water excess calculated on a monthly scale. (D) Mean annual outside ETP calculated on a monthly scale. The red-fitted linear regression indicates its inter-annual change trend. .... 116



Figure 5. 15. (A) Modeled and predicted  $\delta^{18}\text{O}$  in the Karst store 1 & 2 and Epikarst in Villars Cave from 2016 to 2100. (B) Outside cave temperature a monthly (left axis) and annual (right axis) from 2016 to 2100, (C) Mean outside rainfall amount calculated on an annual scale from 2016 to 2100. (D) Mean outside ETP calculated on a monthly (left axis) and annual (right axis) scale from 2016 to 2100. (E) Mean outside water-excess (Rainfall-ETP>0) calculated on a monthly (left axis) and annual (right axis) from 2016 to 2100. The fitted linear regression indicates its inter-annual change trend. To input rainfall oxygen isotopes in the KarstFor model, we used the equation  $\delta^{18}\text{O}=0.15T-7.93$  (Zhang et al., 2020) to simulate the rainfall oxygen isotopes in the next 100 years in Villars Cave, and temperature data is based on monthly outside cave temperature. We set the proportion of karst evaporation water ( $k_{\text{eevap}} = 0.016$ ) to predict reservoir  $\delta^{18}\text{O}$  according to the ERT trend in next 100 year. .... 119

## Chapter 6

Figure 6. 1 The specific electrical resistivity distribution of line 71 m above Villars Cave from Feb/2020 to Jan/2023. The inversion was performed based on the concatenation of the data of the two arrays (Gradient Array and Pole-Dipole Array), using Res2Dinv software to process data. .... 132

Figure 6. 2 Relative frequency and cumulative frequency of the concatenation of two arrays (Gradient Array and Pole-Dipole Array) for the whole data set. .... 133

Figure 6. 3 The resistivity model of 07/January 2021 with an electrode spacing of 1 m above the Villars Cave. .... 134

Figure 6. 4 Results of the Hierarchical Agglomerative Classing (HAC) for all monitoring periods for the profile (71m) above Villars Cave. (A) Dendrogram create three and eight clusters. (B) Distribution of blocks taking into account their clusters. .... 137

Figure 6.5 Comparison of the variability of daily R-ETP (rainfall minus evapotranspiration) and drip-water rates (Vil-#3, Vil-#1B, Vil-#10A) during September/2019- September/2022. .... 141

Figure 6. 6 Using Pearson's linear correlation coefficient in the MATLAB coherence package, the delay time between drip-water rates and water excess (R-EPT>0) during 2020-2022. (A, D) Vil-#10A & Water-excess, (B, E) Vil-#1B & Water-excess, (C, F) Vil-#3 & Water-excess. The delay days (X is the highest value) have been exhibited in the diagram too. We performed a five-day smoothing on water excess and drip-water rates to remove small peak effects. .... 142

Figure 6. 7 The soil depth and soil type of the ERT profile at 9.5m, 24m, 38m, 56m, 60.5m. .... 145

Figure 6. 8 (A) Cluster 2 is divided into clusters 2.1 and 2.2, (B) Comparison between median resistivity variations for clusters 2.1 and 2.2 and water excess. .... 146

Figure 6. 9 Evolution of the median resistivity of clusters 1-8 with local water excess. The individual blocks from the synthetic model were associated with a similar resistivity seasonal variability gathered into 6 clusters (1-6). However, Clusters 7 and 8 only exhibit high resistivity without obvious seasonal variability. The arrows indicate the resistivity in cluster 6 decreased in the dry/summer periods. .... 149

Figure 6. 10 Comparison between median resistivity of clusters 2-5 and water-excess (R-ETP >0) (A) Evolution of the median resistivity of clusters 2&4 with local water excess (B) Evolution of the median resistivity of clusters 3&5 with local water excess. A similar resistivity seasonal variability gathered into 4 clusters (2-5) with no or few days delays with a local water excess. ....	151
Figure 6. 11. Relative frequency and cumulative frequency for the month data set. ....	152
Figure 6. 12 Comparison between median resistivity (clusters 1 and 6) and water-excess (R-ETP >0) (A) Evolutions of the median resistivity of cluster 1. (B) Evolutions of the median resistivity of cluster 6.....	154
Figure 6. 13 Schematic geo-electrical model of the ERT survey line in ERT-1m spacing. The wiggle arrows represent preferential flow, straight arrows represent vertical infiltrations in karst fracture.....	159
Figure 6. 14 Electrical resistivity 106.5 m profile above the Villars Cave from July/2021 to January/2023. The inversion was performed based on the concatenation of the data of the two arrays (Gradient Array and Pole-Dipole Array), using Res2Dinv software to process data. ....	163
Figure 6. 15 (A) The resistivity model of 27th/January 2022 with an electrode spacing of 1 m above Villars Cave. (B) The resistivity model of 27th/January 2022 with an electrode spacing of 1.5 m above Villars Cave.....	165
Figure 6. 16 Relative frequency and cumulative frequency of the concatenation of two arrays (Gradient Array and Pole-Dipole Array) for the whole data set in 1.5 spacing. ....	166
Figure 6. 17 Results of the Hierarchical Agglomerative Classing (HAC) for all monitoring periods for the ERT-1.5m profile (106.5m) above Villars Cave. (A) Dendrogram creates four and eight clusters. (B) Distribution of blocks taking into account their clusters.....	167
Figure 6. 18 Dendrogram creates eight clusters in 1 m and 1.5m spacing.....	170
Figure 6. 19 Comparison between median resistivity and water-excess (R-ETP >0) (A) Cluster 3-1.5m and cluster 4-1m. (B) Cluster 2-1.5m and cluster 2-1m.....	172
Figure 6. 20 Comparison between median resistivity and water-excess (R-ETP >0) (A) Cluster 5-1m and cluster 1-1.5 m (B) Cluster 6-1m, cluster 6-1.5m, and cluster 7-1.5 m. ....	173
Figure 6. 21 Comparison between median resistivity and water-excess (R-ETP >0) (A) Cluster 5-1.5m and cluster 1-1m; (B) Cluster 4&8-1.5m and cluster 7&8-1m.....	174

## List of Tables

Table 3.1. Compilation of selected model parameter values and notes about its implementation and configuration. All parameter names are from conceptual Figure 3.2. ....	43
Table 3.2 Calculate the depth in Station #10A and Station #1B .....	54
Table 4.1. Parameters of the fitting for LMWL, OLSR and PWLSR methods for Le Mas and Villars, SW-France and then for all stations (The method refer to Hughes and Crawford, 2012).....	64
Table 4.2 Variation of monthly PIMS for Le-Mas and Villars for all months of the year for 1997-2016 period. ....	71
Table 4.3 Linear correlations between monthly $\delta^{18}\text{O}_p$ with monthly PIMS and temperature. ....	74
Table 4.4 Variation of annual PIMS for Le-Mas and Villars stations based on the integration of annual trajectories.....	74
Table 5. 1 Parameters of the fitting for LMWL, OLSR, and PWLSR methods for Villars, SW-France (The method refers to Hughes and Crawford, 2012) .....	96
Table 5. 2. Average and ranges for the $\delta^{18}\text{O}/\delta\text{D}$ values for rainfall and drip water (Vil-#10A, Vil-#10B, Vil-#1A, Vil-#1B) in Villars Cave.....	101
Table 5. 3 The delay time between drip-water rates and water excess during 2013-2019. ....	102
Table 5. 4 The observed mean $\delta^{18}\text{O}_d$ and mean drip rates in the different monitoring sites .....	112
Table 6. 1 Statistical parameter: for the resistivity of each cluster in ERT-1m spacing (Median and Standard Deviation (SD), Average value).....	138
Table 6. 2 Calculate the monthly average drip rate and Water-excess (Total monthly amount). ....	139
Table 6.3 Statistical parameters for the resistivity of each cluster (Median and Standard Deviation (SD), Average value) in ERT-1.5m spacing. ....	169
Appendix Table. 1 Average values for $\delta^{18}\text{O}_p$ , $\delta\text{D}_p$ and their standard deviation (SD) for different months at Le Mas and Villars stations from 1997 to 2016 A.D. ....	187
Appendix Table. 2 Average values for $\delta^{18}\text{O}_p$ , $\delta\text{D}_p$ and their SD for 1997-2016 at Le Mas and Villars stations.....	187
Appendix Table. 3 The equations of multiple linear regression between $\delta^{18}\text{O}_p$ and different sources/local temperature (T) by adding different variables step by step at Le Mas and Villars stations.....	189
Appendix Table. 4 Number of remaining electrodes after removing points of filtering and rejecting gapfiller in the measurements of all sequences (1m).....	190
Appendix Table. 5 Number of remaining electrodes after removing points of filtering and rejecting gapfiller in the measurements of all sequences (1.5 m).....	192

Appendix Data 1. The original data for $\delta^{18}\text{O}_p$ , $\delta\text{D}_p$ and local precipitation/ temperature for the period 1997-2016 at Le Mas and Villars stations.....	193
Appendix Data 2. The original data for $\delta^{18}\text{O}_p$ of drip water for the period 1997-2019 at Villars Cave. ....	201

## General Introduction

Karst hydrology is critical to the understanding of the sustainability of groundwater resources in the context of global warming and population growth ([Goldscheider et al. 2012](#); [Ford and Williams, 2013](#); [Hartmann et al. 2012](#); [2013](#); [2015](#); [Hartmann and Baker, 2017](#)). However, the detailed processes in karst infiltration zones located above shallow caves (also called unsaturated zones) are still poorly understood, although these studies are important for assessing karst water resources and hydrological dynamics.

Villars Cave is a decorated cave that has been monitored since 1996 (over 20 years) to understand karst recharge zones by isotopic and hydrological variability analysis. ([Genty et al., 2014a](#); [Baker et al., 2019](#)). The former work suggested that (1) the rainfall that effectively infiltrates (water excess > 0) occurs during a longer period than expected (i.e., most of the year) and (2) For the average age of Villars drip water determined, the first study used a simple isotopic mixing model using rainfall quantity and rainfall  $\delta^{18}\text{O}$  for input ([Genty et al., 2014a](#)). Later, [Jean-Baptiste et al., 2019](#) used tritium measurements (tritium excess was produced by atmospheric bomb tests) in the dripping water combined with the water  $\delta^{18}\text{O}$  values to produce a more precise value. This determined transit time is  $7.0\pm 0.5$  years for the upper gallery and  $11.1\pm 0.5$  years for the lower gallery and the estimated uncertainty for age determination is  $\pm 0.5$  years. (3) Previous studies have also observed a long-term increase in drip water  $\delta^{18}\text{O}$ , but it is unclear why this occurs ([Genty et al., 2014a](#)).

Although prior works in Villars Cave have provided insight into infiltration seasonality, key questions remain about reservoir dynamics and geometry. Utilizing 2D time-lapse electrical resistivity tomography (TL-ERT), a non-destructive and minimally invasive, allows measuring resistivity against air/soil/rock-filled volumes to

describe the cave reservoir dynamics and geometry (Xu et al., 2015; Leopold et al., 2021). ERT, in combination with Hierarchical agglomerative clustering (HAC) (Xu et al., 2015), is utilized to identify different zones, including top-soil, high-resistivity cave zones, low-resistivity reservoirs, and recharge-active supplying zones. This approach provides a comprehensive understanding of the subsurface structures and their characteristics, enabling researchers to study the seasonal changes in these zones.

(1) The relationships and mechanisms are unclear between the initial source and rainfall  $\delta^{18}\text{O}_p$  with various controlling factors (temperature, rainfall, and water source) on monthly and interannual timescales.

(2) In a cave where the rainfall seasonality is strictly limited, how does the recharge water occur, and how do these fluxes control the change of drip rate?

(3) How to model the stable isotope and the infiltration drip flows to rainfall from the different reservoirs identified in the ERT profile using KarstFor (karst hydrological model) model?

(5) How are distributed these reservoirs in the unsaturated zone above Villars Cave? What is their geometry?

To address these questions, I structured my PhD thesis into six chapters as outlined below:

**Chapter 1** reviews the literature on the rainfall/drip water isotope, hydrological models and ERT;

**Chapter 2** gives introduction to the study area, including hydrology, climate, vegetation, and cave monitoring sites in Villars Cave;

**Chapter 3** outlines the methodology employed in the study, including isotopic measurement techniques for drip water and precipitation, cave dripping hydrology, the principles of electrical resistivity tomography (ERT), temperature correction and

Hierarchical Agglomerative Clustering (HAC) method, as well as the magnetic field angle (MFA).

**Chapter 4** determines the origin of precipitation isotopic signature in Villars. The HYSPLIT model is used to identify the variation of the initial moisture sources and its relation to the stable isotopic composition of the rainfall in the Villars Cave and Le-Mas (SW-France);

**Chapter 5** presents the results of using the KarstFor model to reasonably replicate observed drip water  $\delta^{18}\text{O}$  and hydrological variabilities, with the rainfall  $\delta^{18}\text{O}$  ( $\delta^{18}\text{O}_r$ ) and outside temperature increase identified as driving the long-term trend;

**Chapter 6** employs ERT measurements to determine the number, position, depth, and size of reservoirs and their seasonal changes in resistivity, which can be related to changes in cave dripping rate and water-excess data.

## Chapter 1- Rainfall sources and infiltration process in karst terrains in state of the art

The karst system is characterized by a complex network of underground channels, caves, and sinkholes, which serve as a primary source of drinking water and as a home to many species of plants and animals (Ford and Williams, 2013). This carbonate bedrock controls the hydrology and ecological climate of Karst landscape, which interacts with the flow of fresh water, soil formations, and most terrestrial life on the earth (Hartmann and Baker, 2017). However, the fragility of this system also makes it vulnerable to human activities, such as groundwater pumping, and pollution, leading to its degradation (Kiraly, 2003).

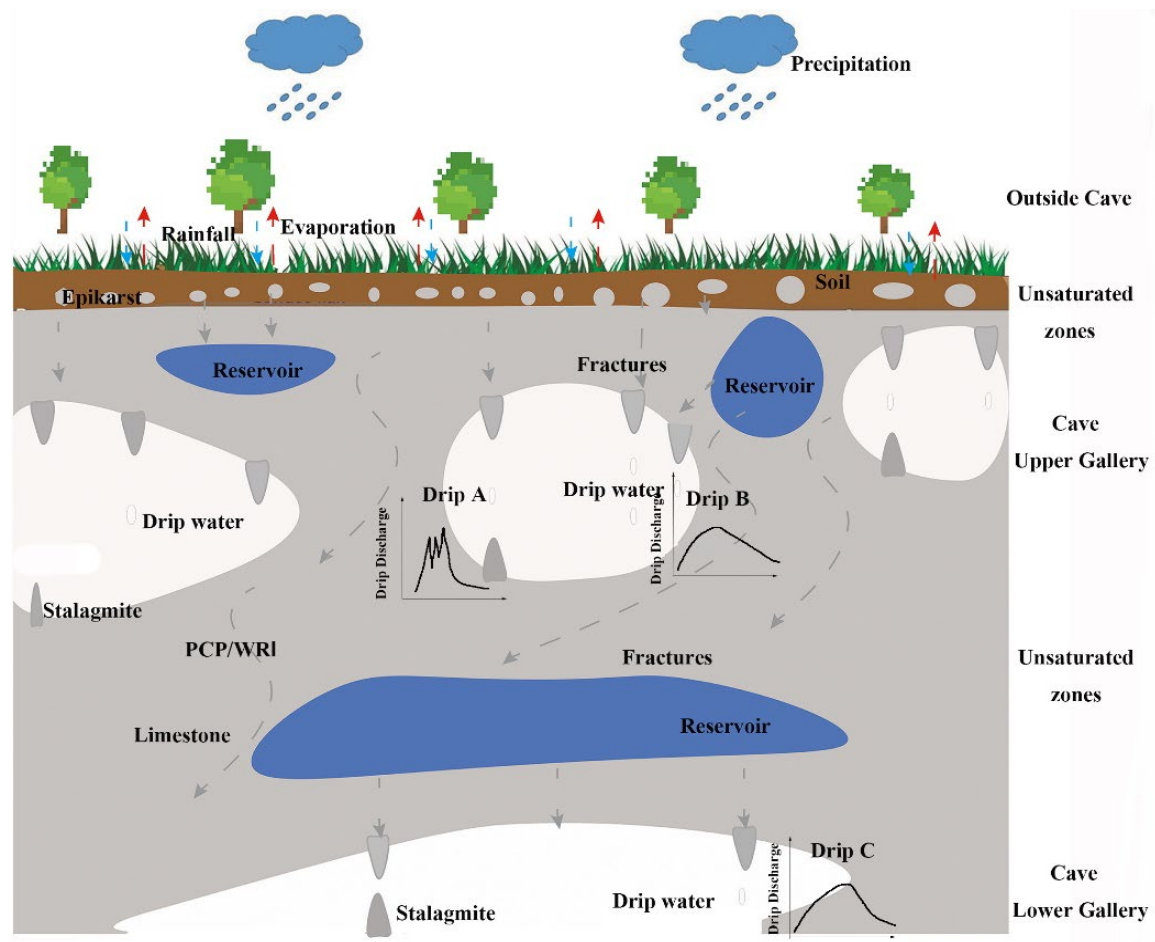


Figure 1. 1 A schematic illustration of karst hydrogeology and cave system processes, modified by Fairchild and Baker (2012) according to Villars Cave, depicts various



*dripping points marked A, B, and C. These dripping points are influenced by different infiltration paths and reservoirs, leading to changes in drip rate and isotopic compositions.*

Karst water slow infiltration and subsequent calcium carbonate precipitation by  $H_2CO_3$  solution led to karst formations, whose main karst can contain several types of pores, such as compact to porous rock, joints, fractures, and fluid conduits (Ford and William, 2007). Karst Critical Zone (KCZ), including karst surface and unsaturated zones, groundwater is one of the most crucial water resources worldwide, providing drinking water for approximately a quarter of the world's population (Ford and Williams, 2007). Therefore, improving our understanding of the complex hydrogeology of karst aquifers is extremely important to protect this drinking water resource (White, 2002). However, the typical feature of karst aquifers, like "black boxes", is that they are transmitted through a permeability network of fractures and pipelines with the uncertainty of the geometry, resulting in some challenges in observing the aquifer characterization (Vacher and Mylroie, 2002; Massei et al., 2007; Hartmann et al., 2012; 2013; 2015; Opsahl et al., 2017; Hartmann and Baker, 2017).

Karst landforms are characterized by well-developed caves, deficient drainage, and non-Drainage groundwater flowing through aquifers (White, 2002). Groundwater runoff and groundwater flow through carbonate pores (micropores), fractures, and solubilization tubes (macropores) can transport water through the epikarst (or subcutaneous zones) (Figure 1.1). The infiltration water penetrates the soil area and permeable surface karst and finally reaches the caves. These vadose waters may participate in depositing calcite in the unsaturated zone (Figure 1.1). Due to the process of karst formation, the typical feature of karst aquifers is that they are stored in aquifer matrix rocks with different porosities and transmitted through a high-permeability network of fractures and pipelines (Vacher and Mylroie, 2002). In addition, the karst aquifer has a highly dynamic regulation, and its water level and water

geochemistry proxy respond to precipitation, pumping, and drought on different time scales (Martin et al., 2016).

Currently, modeling karst hydrology takes into account a wide range of processes (Hartmann et al., 2012). It can be found that most of these methods are attributed to the group of lumped parameter or distributed methods (or something in between), referring to the spatial discretization in the model (Troch et al., 2003; Anagnostou et al., 2015). Distributed models discretize the karst system into rectangular or triangular grid cells, and then calculate the groundwater level and flow for each cell (Hartmann et al., 2014). Meanwhile, the lumped approach considers the entire karst system through a set of reservoirs, each representing a subsystem (such as epikarst, fracture matrix, or pipeline) (Aquilina et al., 2006). Thus, lumped models provide important information on karst systems and storage behavior (Hartmann et al., 2014).

When it comes to studying groundwater recharges (Ireson and Butler, 2013) and cave fluid dynamics (Markowska et al., 2015), more focus is given to the processes in the unsaturated zone. This is because the unsaturated zone plays a crucial role in the hydrology of karst systems (Figure 1.2). The soil is the first reservoir for precipitation and its storage capacity is dependent on physical properties such as soil depth, clay content, and organic matter (Figure 1.2). The amount of water that can be stored in the soil at any given time is determined by its storage capacity and the soil moisture content, which is influenced by local hydrological conditions (Hartmann and Baker, 2017). However, due to the subsurface heterogeneity of karst systems, soil thickness and hydraulic conductivity can vary greatly, leading to variations in soil storage capacity and the interplay between diffusion and preferential flow processes (Hartmann and Baker, 2017).

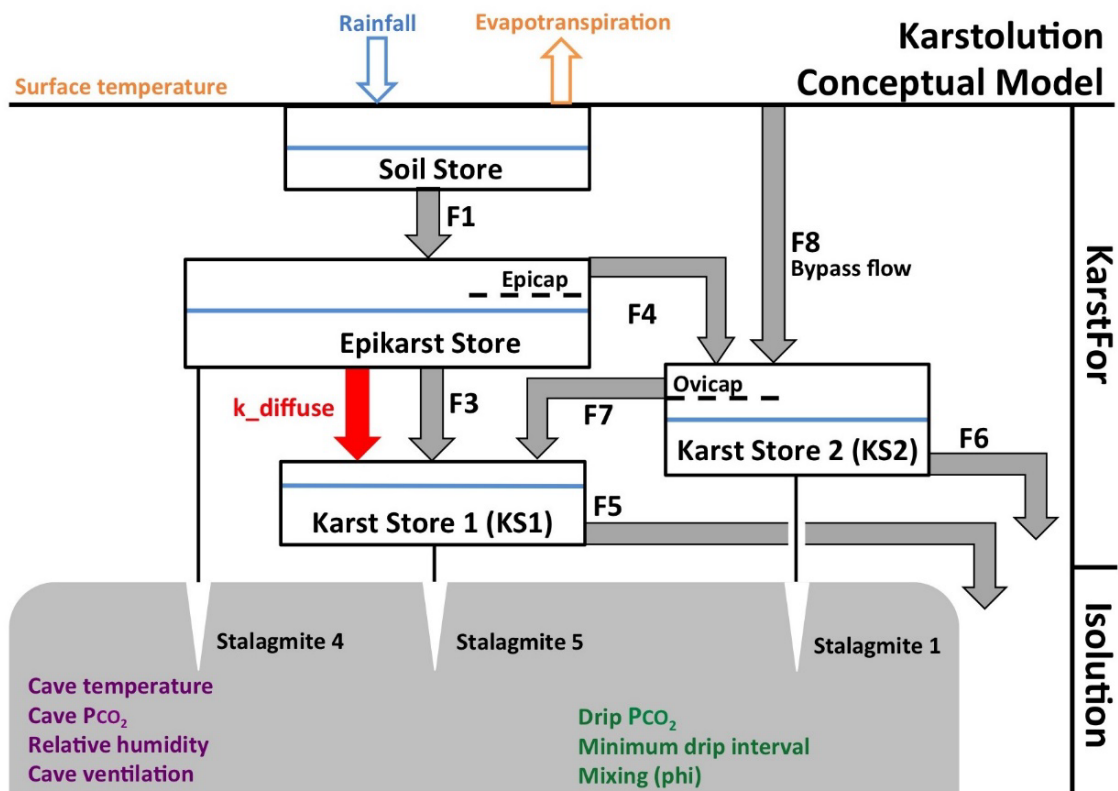


Figure 1. 2 The Karstolution model is represented by a conceptual figure consisting of various reservoirs shown as boxes. Blue lines indicate water levels, while grey arrows represent fracture flow and the red arrow represents diffuse flow. The model is designed to simulate karst aquifers and their response to external forces. The KarstFor model, described in Baker et al. (2013), and the ISOLUTION model, described in Deininger et al. (2012), form the basis of this model. The Karstolution model incorporates modifications and additions to the original models to enhance their coupling and provide more accurate simulations. The model considers various cave parameters, such as temperature and drip rate, as described by ISOLUTION, to generate stalagmite outputs.

## 1.1 Rainfall stable isotopes in the hydrological cycle

Stable isotopes of atmospheric precipitation, such as  $\delta^{18}O$  and  $\delta D$ , play a crucial role in comprehending regional atmospheric patterns and local hydrological cycles (Dansgaard, 1964; Alley and Cuffey, 2001; Sharp, 2007; Gat, 2010; Genty et al., 2014a). Rainfall  $\delta^{18}O$  and  $\delta D$  is influenced by local climate and moisture sources (Aggarwal et al., 2004). This information can be recorded in stalagmites as climate

proxies, but it is important to understand how fractionation processes alter isotopic ratios during transportation in the hydrological cycle. The dominant controls are based on variations in temperature and relative humidity, which influence the  $\delta^{18}\text{O}$  values through various processes and phase changes in the ocean, atmosphere, hydrosphere, soil and epikarst zones, and ultimately in speleothem  $\text{CaCO}_3$  (Figure 1.3). By analyzing oxygen and hydrogen isotope ratios in various compartments, it is possible to understand these transport processes and the impact of climate on precipitation  $\delta^{18}\text{O}$  changes on seasonal and interannual timescales (Figure 1.3).

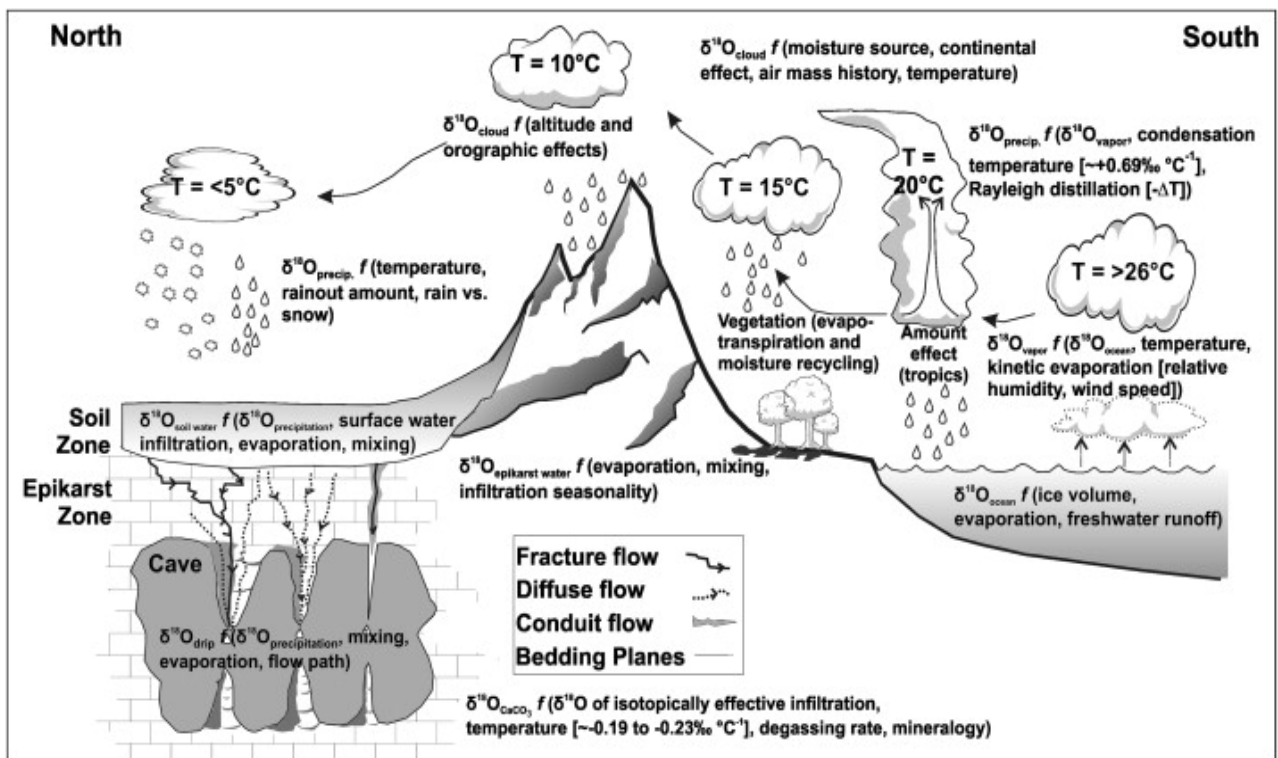


Figure 1. 3 Diagram illustrating the primary processes related to  $\delta^{18}\text{O}$  variations for speleothem palaeoclimatology (Lachniet, 2009).

### 1.1.1 Rainfall isotopic effect

To understand precipitation stable isotopic compositions on temporal and spatial variations, the isotopic composition of precipitation has been monitored globally (Figures 1.4 and 1.5). The most influential effort is from the Global Network of

Precipitation Isotopes (GNIP), organized in a monthly monitoring since 1960 by the International Atomic Energy Agency (IAEA) and the World Meteorological Organization (WMO) (Figures 1.4 and 1.5). Through global observations, some leading isotopic effects have been identified (Dansgaard, 1964; Rozanski et al., 1993; Araguás-Araguás et al., 2000; Allen et al., 2018; Figures 1.4 and 1.5). The most fundamental isotope effects are the “temperature effect” and the “amount effect”. The average monthly local temperatures, generally measured 2 m above ground level, are statistically correlated with the monthly  $\delta^{18}\text{O}_p$  and  $\delta\text{D}_p$  on middle and high-latitude monitoring stations, called the “temperature effect” (Dansgaard, 1964; IAEA working group, 2000). However, the relationship on the inter-annual timescale remains unclear. The negative isotope with the increased precipitations occurs in many tropical islands and monsoon climates is the so-called “amount effect”, which describes a negative correlation between surface precipitation and the heavy isotope content of the rain (Dansgaard, 1964; Rozanski et al., 1993; Lee and Fung, 2008). However, local precipitation amounts and monthly isotope ratios do not exhibit significant correlations in continental Europe (Dansgaard, 1964). These established relationships between changes in precipitation isotopes and changes in climatic conditions (especially temperature) have been used to interpret paleoclimate proxies such as ice cores (Johnsen et al., 1989). The mechanism between the temperature/precipitation and isotope ratios in rainfall is considerably complex, including these processes like Rayleigh fractionation, diffusive exchange of isotopes between raindrops and vapour, as well as re-evaporation of falling rain (Fricke and O’Neil, 1999; Araguás-Araguás et al., 2000, 2005; Risi et al., 2008; Lachniet, 2009; Field et al., 2010). Therefore, the  $\delta^{18}\text{O}$  in many natural archives have been used to reconstruct the paleoenvironment in

the publications of past few years (Pettit et al., 1999; Wang et al., 2001; Hu et al., 2008b; Zhang et al., 2008; McDermott et al., 2011).

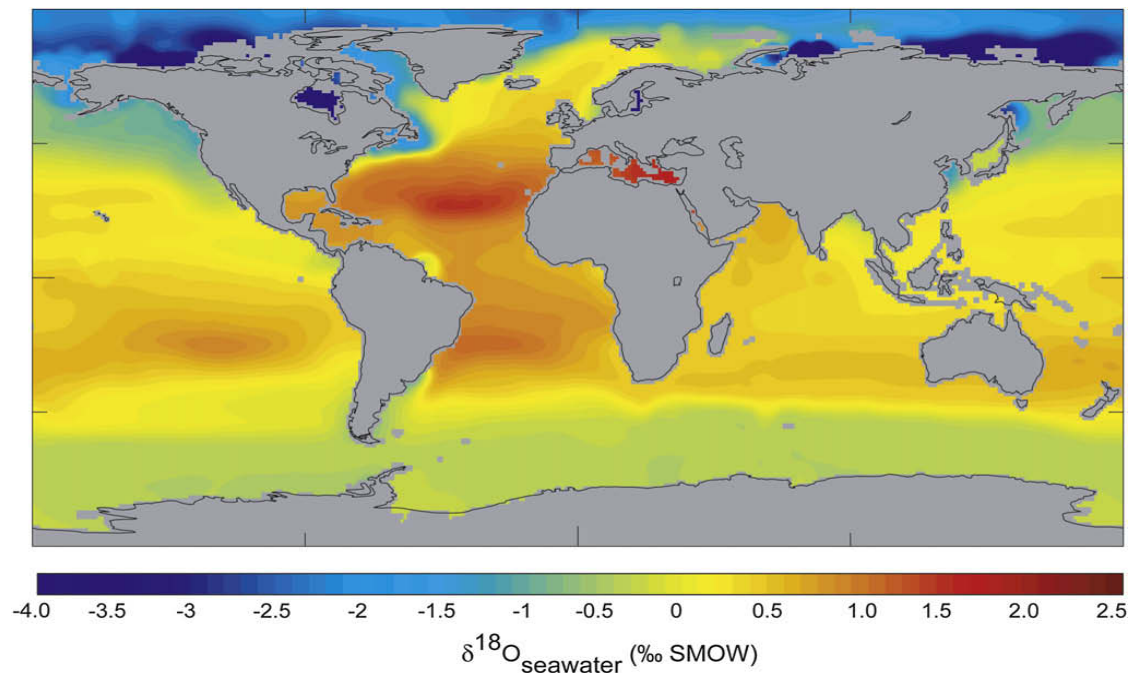


Figure 1. 4 A gridded  $\delta^{18}\text{O}$  map of the ocean, based on data from [LeGrande and Schmidt \(2006\)](#).

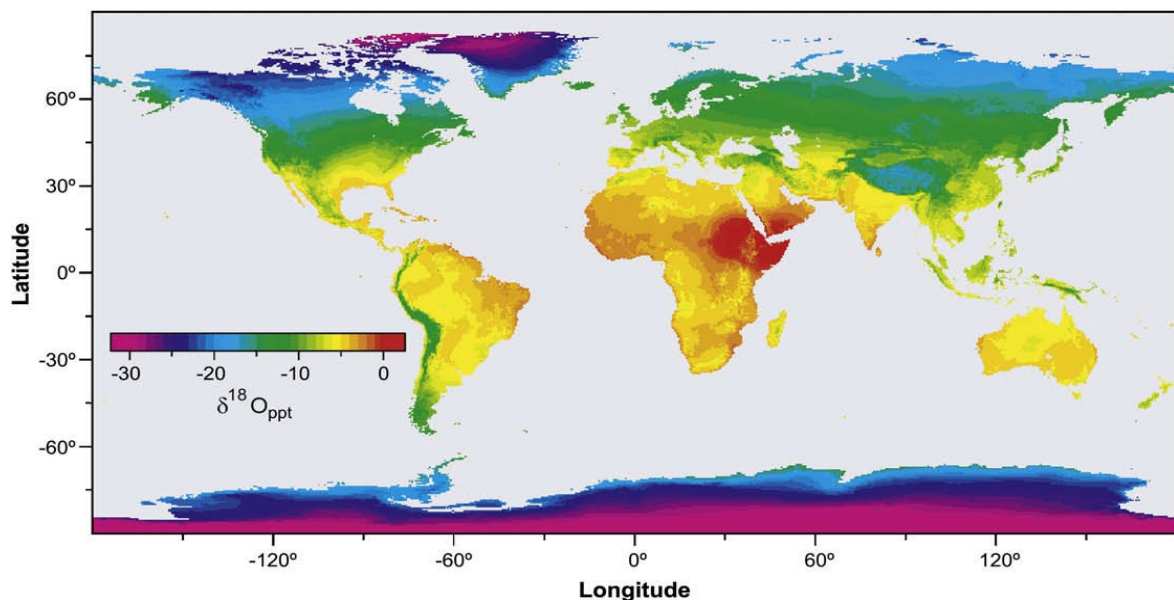


Figure 1. 5 Based on data from the GNIP stations, the global land distribution of annual mean rainfall  $\delta^{18}\text{O}$  shows significant spatial variation, as reported by [Bowen and Wilkinson \(2002\)](#).

However, other effects on isotopes have been linked to the latitude, continentality, altitude, and seasonality. Additionally, some researchers have revealed that inter-

annual atmospheric variability, such as North Atlantic Oscillation (NAO), also controls the rainfall isotopic value (Baldini et al., 2008; Fischer and Matthey, 2012). Thus, the investigation and qualification of the various factors governing the stable rainfall isotopes are of great importance to the paleoclimate community (Krklec and Domínguez-Villar., 2014; Krklec et al., 2018).

Some previous studies have proposed that the moisture source was an important controlling factor for  $\delta^{18}\text{O}_p$  and  $\delta\text{D}_p$  (Cruz et al., 1992; Cole et al., 1999; Friedman et al., 2002; Lachniet, 2009). Moisture source location is generally estimated by the calculation of the deuterium excess (d-excess), which is significantly different between the Atlantic Ocean and the Mediterranean Sea (Dansgaard, 1964; Craig and Gordon, 1965; Vimeux et al., 1999; Uemura et al., 2012). Moreover, d-excess reflects near-surface relative humidity (RH) variation during evaporation and moisture source temperature variations (Pfahel and Sodemann, 2014). However, using this method makes it extremely difficult to quantify the pathway of water vapour transportation, limiting the understanding of the change of moisture source for  $\delta^{18}\text{O}_p$  and  $\delta\text{D}_p$ , particularly for spatial and temporal evapotranspiration (ET) contributions.

The history of air masses has been calculated by studying regional/general circulation using Lagrangian models to overcome this issue. However, apparent discrepancies between observed isotopes and the variation of modeled air masses were questioned, which may be due to the insufficient accuracy of the models (Hoffmann et al., 1998; Sturm, 2005; Schmidt et al., 2007; Sodemann et al., 2008; Pfahl and Wernli, 2008; Langebroek et al., 2011). Therefore, this raised question of how to accurately quantify the variability of initial moisture sources, which are important for explaining the climatic significance of  $\delta^{18}\text{O}_p$  and  $\delta\text{D}_p$  (Aggarwal et al., 2004; Dayem et al., 2010).

The Hybrid Single-Particle Lagrangian Integrated Trajectory (HYSPLIT) model (Draxler and Hess, 1998), an advanced system calculating air parcel trajectories, has been dramatically promoted (Stein et al., 2015). This atmospheric calculation model based on the Eulerian and hybrid Lagrangian approaches can accurately reflect the variation of moisture source (Stein et al., 2015). Among them, the Lagrangian method uses a moving framework as a reference for the calculations of diffusion and advection when the trajectories or air parcels move from the initial source region. The Eulerian methodology uses a restricted three-dimensional grid cell to compute air concentrations (Stein et al., 2015). Additionally, HYSPLIT software has been successfully applied in several studies, including tracking atmospheric circulation change (Sjostrom and Welker, 2009; Breitenbach et al., 2010; Abouelmagd et al., 2012; Dumitru et al., 2017; Sánchez - Murillo et al., 2020), predicting the direction of pollutant diffusion (Chen et al., 2012) and monitoring wildfire smoke (Rolph et al. 2009).

### **1.1.2 Rayleigh distillation process**

The gradual condensation of water vapor on a global scale can be represented as a continuous Rayleigh distillation process. In this process, as air masses cool, condensate forms in liquid-vapor equilibrium and is immediately removed from the remaining vapor in the transport process (Gat, 1996). The Rayleigh model, introduced by Dansgaard (1964), was used to evaluate the impact of temperature, latitude, and vapor mass.

Isotopic mass is typically measured as the ratio (R) of rare heavy isotopes to abundant light isotopes. The stable isotopic composition of water is expressed relative to the International Atomic Energy Agency (IAEA) Vienna Standard Mean Ocean Water (V-SMOW) standard. For the two main rare isotopes, D/H and  $^{18}\text{O}/^{16}\text{O}$ , the V-



SMOW values are  $155.95 \times 10^{-6}$  and  $2005.2 \times 10^{-6}$ , respectively (Araguás-Araguás et al., 2000; Sharp, 2007).

The oxygen isotope composition of a water sample ( $R_{\text{sample}}$ ) can be expressed using the  $\delta$  notation, in units of permil (‰), as:

$$\delta^{18}\text{O} = \frac{R_{\text{sample}} - R_{\text{V-SMOW}}}{R_{\text{V-SMOW}}} \times 1000$$

$\delta\text{D}$  and  $\delta^{18}\text{O}$  in meteoric waters typically vary linearly and can be related through the equation  $\delta\text{D} = 8 \cdot \delta^{18}\text{O} + 10$  (Craig, 1961). The d-excess equation:  $\text{d-excess} = \delta\text{D} - 8 \cdot \delta^{18}\text{O}$ , which results from different evaporation rates for the different isotopologues of water (Dansgaard, 1964), is globally averaged at 10‰ in meteoric water (Craig, 1961). Deviations from the slope of 8 in the  $\delta\text{D}$ - $\delta^{18}\text{O}$  relationship can provide important information about non-equilibrium processes involved in evapotranspiration, moisture transport, and precipitation.

## 1.2. Stable isotopes and hydrology in cave drip-water

The process of rainfall infiltration in karst zones is challenging to describe and model, even though this knowledge is of first importance for freshwater quality preservation and cave heritage protection (Ford and Williams, 1989; Hartmann et al., 2012; Hartmann and Baker, 2017; Bourges et al., 2014; 2020). Cave monitoring studies have been conducted to better understand the relationship between rainfall and seepage water in the epikarst zone in several cave sites (Villars Cave in SW-France, Chauvet Cave in SE-France, Obir Caves in Austria, St. Michaels Cave in Gibraltar and others) in the world (Spötl et al., 2005; Pape et al., 2010; Matthey et al., 2010; Genty et al., 2014a; Rau et al., 2015; Duan et al., 2016; Baker et al., 2019; 2020).

It is recognized that the infiltration duration and its routing, controlled by the reservoirs and infiltration types, influence cave drip water oxygen isotopes ( $\delta^{18}\text{O}_d$ ). The infiltration time in the seepage zone has been estimated by different methods: 1) the lag time of  $\delta^{18}\text{O}_d$ , relative to local rainfall and sudden rainfall events (Ayalon et al., 1998; Long and Putnam, 2004; Cruz et al., 2005; Cobb et al., 2007; Matthey et al., 2008); 2) hydro-chemical variations in karst waters (Even et al., 1986); 3) fluorescence of drip waters (Baker et al., 1999) and 4) Tritium dating methods (Kaufman et al., 2003; Kluge et al., 2010; Jean-Baptiste et al., 2019). It is worth pointing out, that more recently, Ellis et al. (2020) used a mixing model to make  $\delta^{18}\text{O}_d$  variations closely match rainfall  $\delta^{18}\text{O}$  ( $\delta^{18}\text{O}_r$ ) variations to calculate the residence time in epikarst, which ranges from 3 to 18 months in Gunung Mulu National Park, Northern Borneo. Consequently, inside-cave answers to outside climate changes may vary depending on the geometry and the dynamics of reservoirs above the cave.

Generally, due to mixing in the soil zone and epikarst,  $\delta^{18}\text{O}_d$  variability is damped compared to  $\delta^{18}\text{O}_r$ , and it is usually considered to be close to the annual weighted average  $\delta^{18}\text{O}_r$  (Yonge et al., 1985; Tooth and Fairchild, 2003; McDermott, 2004; Li et al., 2011; Riechelmann et al., 2011; Zhang and Li, 2019). In some cases, where there is less storage and faster infiltration, the seasonality was observed in the drip water  $\delta^{18}\text{O}$  in the Mawmluh Cave, India (Breitenbach et al., 2015) and the Black Chasm Cavern, California (Oster et al., 2012). But recently, it has been suggested that the  $\delta^{18}\text{O}_d$  may be considered an averaged value of weighted  $\delta^{18}\text{O}_r$  for a much more extended period up to several years (Genty et al., 2014a; Jean-Baptiste et al., 2019). Indeed, rainfall infiltration in karst terrain is heterogeneous and combines slow infiltration and fast one that may be a mixture of “old and new” waters in the reservoirs, resulting in different responses of the  $\delta^{18}\text{O}_d$ . The latter may represent various outside-

cave climate dynamics: 1) the seasonality (Oster et al., 2012); 2) atmospheric circulation patterns, such as El Niño-Southern Oscillation (ENSO) (Tadros et al., 2016; Chen and Li, 2018; Zhang and Li, 2019; Ellis et al., 2020); 3) heavy rain events in the wet season (Pape et al., 2010), 4) a degree of enrichment of drip evaporations between replenishment events in arid regions (Cuthbert et al., 2014).

Modelling the variation of drip rates can be a powerful method to understand karst hydrology further because the output of the integrated hydrology-isotopic model indicates the changes in water flow patterns and hydrological variability in the unsaturated zone (Fairchild & Baker, 2012). However, the “Mixing effect” (Mixing of the new and old recharge water in the unsaturated zone) and the “temperature effect” makes it difficult to discern the detail of the physical processes that control the recharge (Dansgaard, 1964; Genty et al., 2014a). For example, an increase in the atmospheric temperature will provoke an increase in the rainfall  $\delta^{18}\text{O}$ , but if the temperature increases in the cave will cause a decrease in the calcite  $\delta^{18}\text{O}$ . If there is a mixing, the rainfall  $\delta^{18}\text{O}$  variations will be homogenized, and only calcite precipitation temperature will control the speleothem  $\delta^{18}\text{O}$  with the fractionation if it is out of equilibrium (Lachniet, 2009; Rau et al., 2019). The monitoring of hydrological variability based on the drip rate of automated loggers is not only easily applicable to karst zone where drip loggers can be installed to obtain continuous hydrological data in karst fracture zones but also can be used to compare recharge events in drip water and abrupt rainfall outside caves (Baker et al., 2020). Modeled infiltration through the reservoir in karst terrain is not a new topic. For example, Cuthbert et al. (2014) previously applied a single-reservoir (soil moisture balance – karst) model to the drip recharge, and this method was then used to compare modeled and measured  $\delta^{18}\text{O}$  for two modern speleothems (Markowska et al., 2020). Meanwhile, Dee et al. (2015) proposed a simple convolution

of the  $\delta^{18}\text{O}_r$  time series to simulate  $\delta^{18}\text{O}_d$  using drip water transit time distributions (pulse response function) in their PRoxY System Model (PRYSM). Additionally, based on a lumped parameter approach to model the complexities of karst hydrogeology, the KarstFor model was also developed by [Bradley et al. \(2010\)](#) and enhanced with multiple adaptations in different climate systems, such as monsoon, temperate and Mediterranean climates ([Baker et al., 2013](#); [Treble et al., 2013](#); [2019](#); [Figures 1.2 and 1.6](#)). The initial schematic illustration of the KarstFor model consisted of climatic inputs and a monthly time-step for reservoirs, representing the soil, epikarst and vadose zone (Karst Store 1 and 2).

In view of this, [Healy \(2010\)](#) reported for the first time the use of the high frequency and continuous discharge time series of drip water infiltrating into caves as a physical method for quantifying rainfall thresholds in the karst unsaturated zone. Generally, in the time frame of several months to several years, the fluctuations of drip flow are usually driven by seasonal changes in rainfall availability ([Hu et al., 2008a](#)), water excess ([Genty and Deflandre, 1998](#)), and long-term circulation patterns forcing, the North Atlantic Oscillation (NAO) or El Niño-Southern Oscillation (ENSO) ([Proctor et al., 2000](#); [McDonald, 2004](#)). However, on a daily to the weekly time scale, the drip rate may respond to a single rainfall event ([Baldini et al., 2012](#)) and inside-cave air pressure ([Genty and Deflandre, 1998](#); [Tremaine and Froelich, 2013](#)). Moreover, flow rates also influence speleothem climate proxies, such as the  $\delta^{18}\text{O}$  and trace elements, through the dilution and mixing of percolation waters before reaching the cave ([Figure 1.2](#)). Therefore, it is necessary to conduct monitoring on long durations to compare hydrological climate parameters with isotopic geochemistry's proxies in the karst area, so that the paleoclimate proxy records from related speleothems can be appropriately explained.

### 1.3. Electrical resistivity tomography

The electrical resistivity tomography (ERT) technique is widely used in Geophysics for shallow subsurface investigations related to hydrogeology, engineering, or agriculture. In the past, the technique relied on 1D imaging and was popularly used from the 1920s to the 1980s. However, when it comes to resolving complex subsurface geology, the accuracy of the 1D imaging method was limited (Burger et al., 2006). Fortunately, the development of multi-electrode arrays, automated acquisition systems, and new inversion algorithms has significantly improved the ERT technique's capability to resolve complex subsurface geology over the last three decades (Loke et al., 2014). The ERT technique has also seen recent advancements, including the use of 3D surveys, which provide better subsurface resolution in complex geological areas. Additionally, a four-dimensional (4D) survey and 4D inversion technique have been proposed to monitor and derive more details in such areas (Loke, 2004; Kim et al., 2009; Chambers et al., 2014; Loke et al., 2013; 2015).

The application of 2D TL-ERT (time-lapse electrical resistivity tomography) has the major advantage of being non-destructive and minimum-invasive to measure the electrical resistivity targeting the air/soil/rock-filled volume and water-filled voids in the highly heterogeneous aquifers to analyze changes in groundwater characteristics (Samouëlian et al., 2005; Vanderborght et al., 2005; Al Hagrey, 2007; Brunet et al., 2010; Binley et al., 2015; Watlet et al., 2018). The advantage of the ERT approach is that it can effectively track changes in the electrical properties of the subsurface, reflecting changes in moisture contents, groundwater contents, water storage zones, and geochemical properties (Brunet et al., 2010). For example, Al Hagrey et al. (1999) used a combination of techniques, including ERT methods and tracer tests, to characterize the preferential flow paths and estimate their impact on the contaminant

transport. Changes in resistivity over time can be used to infer the variability of flow paths and the mixing of stored water (Pakzad et al., 2008). Likewise, previous studies have tracked irrigation-induced groundwater migration by analyzing and monitoring the spatial variability of the soil moisture content using ERT measurements in the subsurface zone (Barker and Moore, 1998; Michot et al., 2003). Moreover, the ERT has been applied to delineate soil horizons and subsurface lithology from changes in resistivity values, providing a useful method for root surveys to describe the shape and behavior in subsurface soils, resulting in an important reference for agricultural production activity (Zenone et al., 2008). In summary, ERT monitoring is a very efficient method, especially in some hydro-geophysics studies (Coscia et al., 2012; Kuras et al., 2009; Revil et al., 2012; Uhlemann et al., 2016; 2017) as well as in geotechnical Engineering monitoring of landslide regions (Genelle et al., 2012), groundwater contaminated sites (LaBrecque et al., 1996; Caterina et al., 2017).

More specifically for karst landforms, researchers have used TL-ERT to identify subsurface features, sinkholes, caves, and reservoir dynamics (Gautam et al., 2000; Zhou et al., 2002; Valois et al., 2010, Robert et al., 2011; Chalikakis et al., 2011 ; Carrière et al., 2013; Sirieix et al., 2014; Xu et al., 2017; Verdet et al., 2020; Leopold et al., 2021). For example, TL-ERT measurements have been used to visualize changes in the resistivity of karst-unsaturated conduits to assess the mixing of matrix water and surface water in the upper Floridan karst aquifer, USA (Meyerhof et al., 2012). In addition, TL-ERT and magnetic resonance sounding (MRS) were used to determine the role of porous matrices in regulating water infiltration of apparent karst structures in southern France (Carrière et al., 2016). Regarding the link between resistivity changes and flow rate variations, Xu et al. (2017) revealed a close link between some cluster zones and measured underground flows in Lascaux Cave, SW-

France. More recently, [Watlet et al. \(2018\)](#) used long-term permanent electrical resistivity tomography (ERT) monitoring to investigate the complex karst vadose zone in Belgium. This study found evidence of seasonal recharge processes with different dynamics, resulting in the clustering of different zones with a contrasting evolution during the different hydrological cycles. Taken together, these studies have demonstrated the applicability interest of the ERT method to karst hydrological research.

#### **1.4. Importance for isotopic-based speleothem reconstructions**

Karst water supersaturated with calcium carbonate is responsible for the formation of cave deposits such as stalactites and stalagmites ([Holland et al., 1964](#); [Hendy et al., 1971](#); [Bar-Matthews et al., 1996](#); [Baker et al., 2010](#); [Genty et al., 2003, 2006; 2008](#); [Stoll et al., 2015](#); [Wong and Breecker, 2015](#); [Zhang et al., 2022](#)). When reconstructing past climates using isotopic proxies from natural archives, such as the  $\delta^{18}\text{O}$  of speleothems, it is crucial to understand the original isotopic composition of the precipitation and of the dripping water. The  $\delta^{18}\text{O}$  of the precipitation do not change significantly during the infiltration, but further fractionation occurs during the calcite precipitation. These fractionation processes can be influenced by environmental parameters, such as temperature and out of equilibrium fractionation due to fast degassing.

The physical fractionation processes that impact the changes in  $\delta^{18}\text{O}$  (oxygen isotope composition) throughout the global hydrological cycle are influenced by atmospheric circulation mechanisms that have similarities to those in the past, and are involved in similar moisture transport patterns as seen in the present day. Studies have been done to understand karst hydrology, cave environment, and in-cave speleothem

oxygen isotopic composition as a function of numerous processes (Fairchild et al., 2006; Hartmann and Baker, 2016). A final temperature-dependent fractionation occurs during the incorporation of the water into the speleothem calcite (Kim and O'Neil, 1997).



## Chapter 2-Study area

### 2.1 Geological setting

The Villars Cave is situated in southwestern France in the northern Dordogne department. It is located at a latitude of  $45.44^{\circ}\text{N}$  and a longitude of  $0.78^{\circ}\text{E}$ , with a cave entrance altitude of 173 m (NGF) (Figure 2.1A). The map of the entire cave, which consists of more than 10 km of galleries, was made by the speleo club of Périgueux. More recently, a more precise topographical map was made by J.P. Cassou with the help of C. Verdet in 2021 (Figures 2.1C).

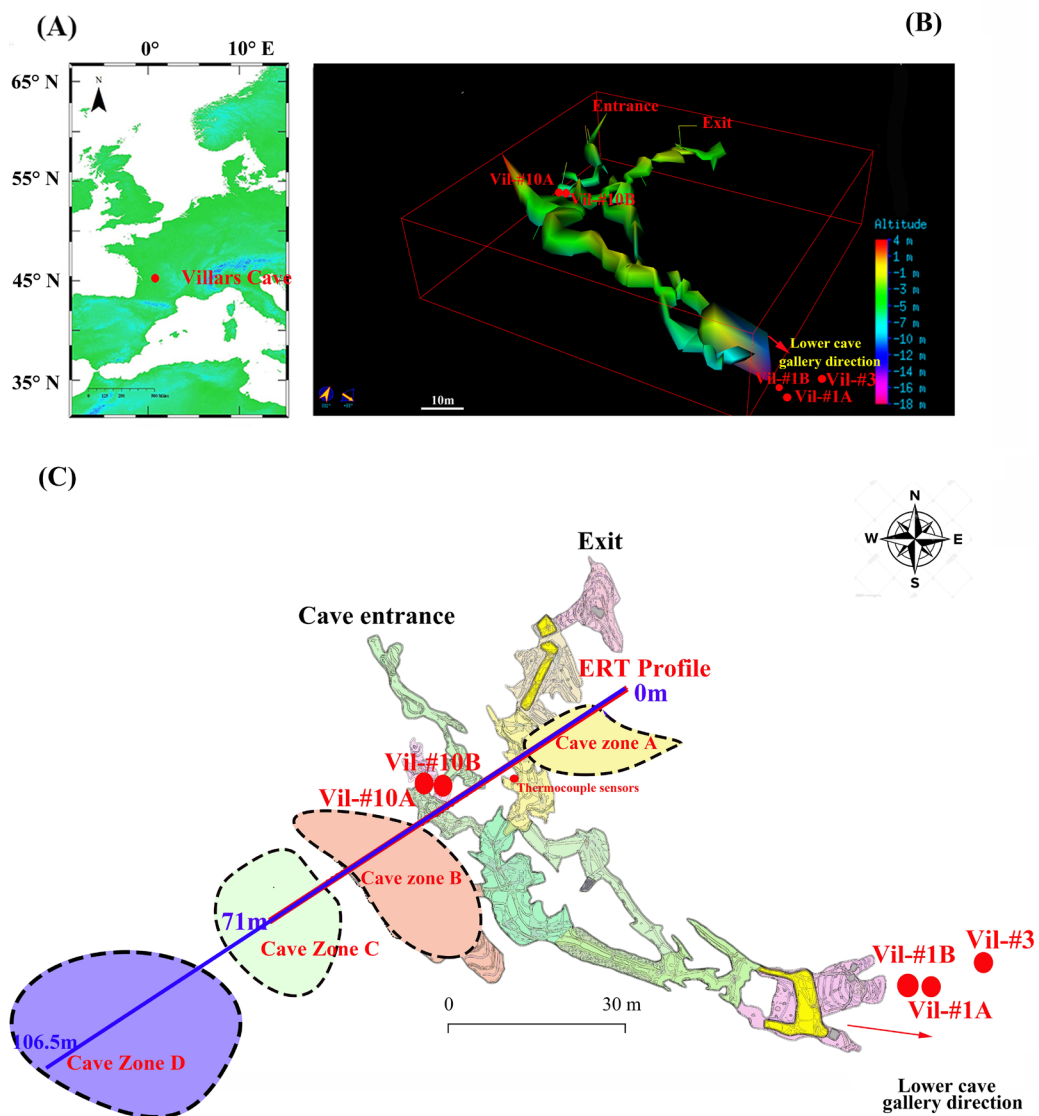
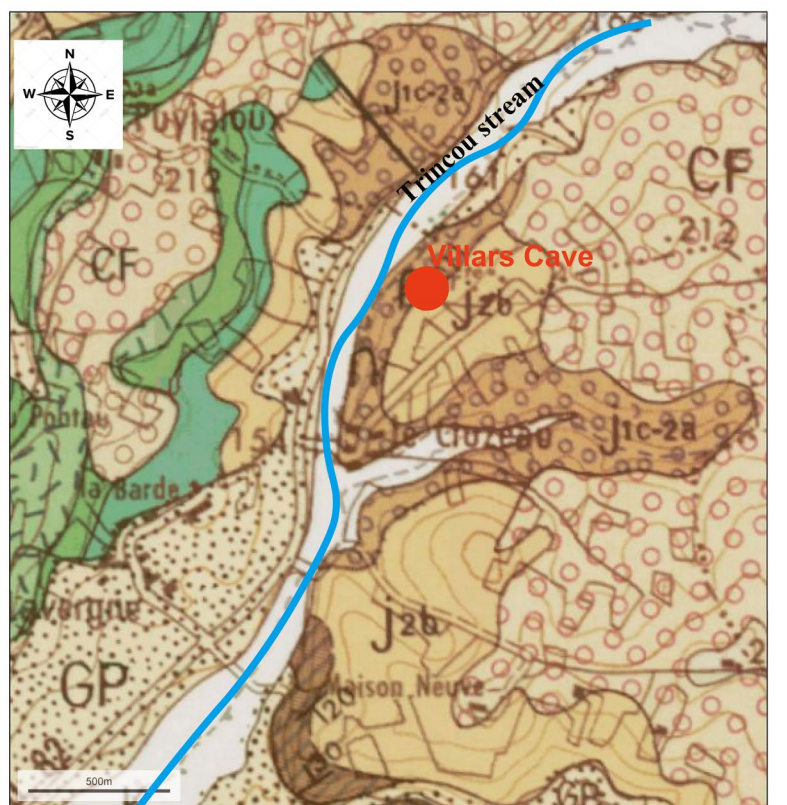




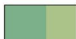


Figure 2. 1 Villars Cave map. (A) Locations of Villars Cave. (B) A 3D cave structural diagram and the distribution of surveillance sites (red circles) of Villas Cave (Vil-#3, Vil-#1A and 1B, Vil-#10A and Vil-#10B). The reader is referred to (Genty, 2008; Genty et al., 2014a) for detailed site descriptions and maps. (C) Profile of ERT and the location of Villars Cave (Red line for ERT-71m with 1m spacing, and red and blue lines for ERT-106.5 m with 1.5 m spacing) (Cassou and Verdet, 2021). The dotted circles labeled as Zone A, Zone B, Zone C, and Zone D correspond to the ERT image identifying cave galleries. The different colors in Panel C indicate the cave galleries.

The exact age of the Villars Cave formation is yet to be determined with certainty, but it is thought to have formed early, potentially during the Tertiary or early Quaternary period, which is consistent with other caves in the Dordogne region. The cave is mainly developed in a Middle Jurassic Oolitic limestone formation (Bajocian) with some upper parts of crystalline limestone of the Bathonian (Figure 2.2, Genty, 2008).



#### Legend

		
j2b: Jurassic-middle Bathonian	j1c-2a: Jurassic-middle upper Bajocian and Bathonian	GP: Sandstone
		
CF: Colluvions or siderolithique Quaternary or late tertiary deposits	Green color: Cretaceous	

*Figure 2. 2 Geological maps of area around the Villars Cave. (C): Cretaceous (Green color); (J): Jurassic (Brown-Yellow colors) where Villars Cave developed (red dot) in Bajocian and Bathonian limestone; from BRGM, Service Géologique National, Orléans, France; Thiviers Map XIX-33 1/50000 (From L. Bruxelles).*

Most of the rivers flowing out of this ancient impervious massif flow northward through underground galleries. A small trincou stream that flows near Villars Cave (near "Le Cluzeau") (Figure 2.3). Fluorescent water staining confirmed that these streams resurfaced in the Dronne River (La Dronne) in Chazelle, a small village 5 km southeast of Villars Cave (Figure 2.3). An essential feature of the local hydrology is that the water flow does not go in the direction of the dry valley, but through fractures (Genty, 2008).

Aside from its geological significance, the main interest in Villars Cave has been its prehistoric paintings. Remains of paintings were found in the cave, some made directly on the rock surface or previous calcite layers. These paintings, such as the "Cheval Bleu" (blue horse) and other horses in the "Rotonde des Chevaux," are of great cultural and historical value and have been dated around 20 ka (Genty, 2008, Genty et al., 2014a).

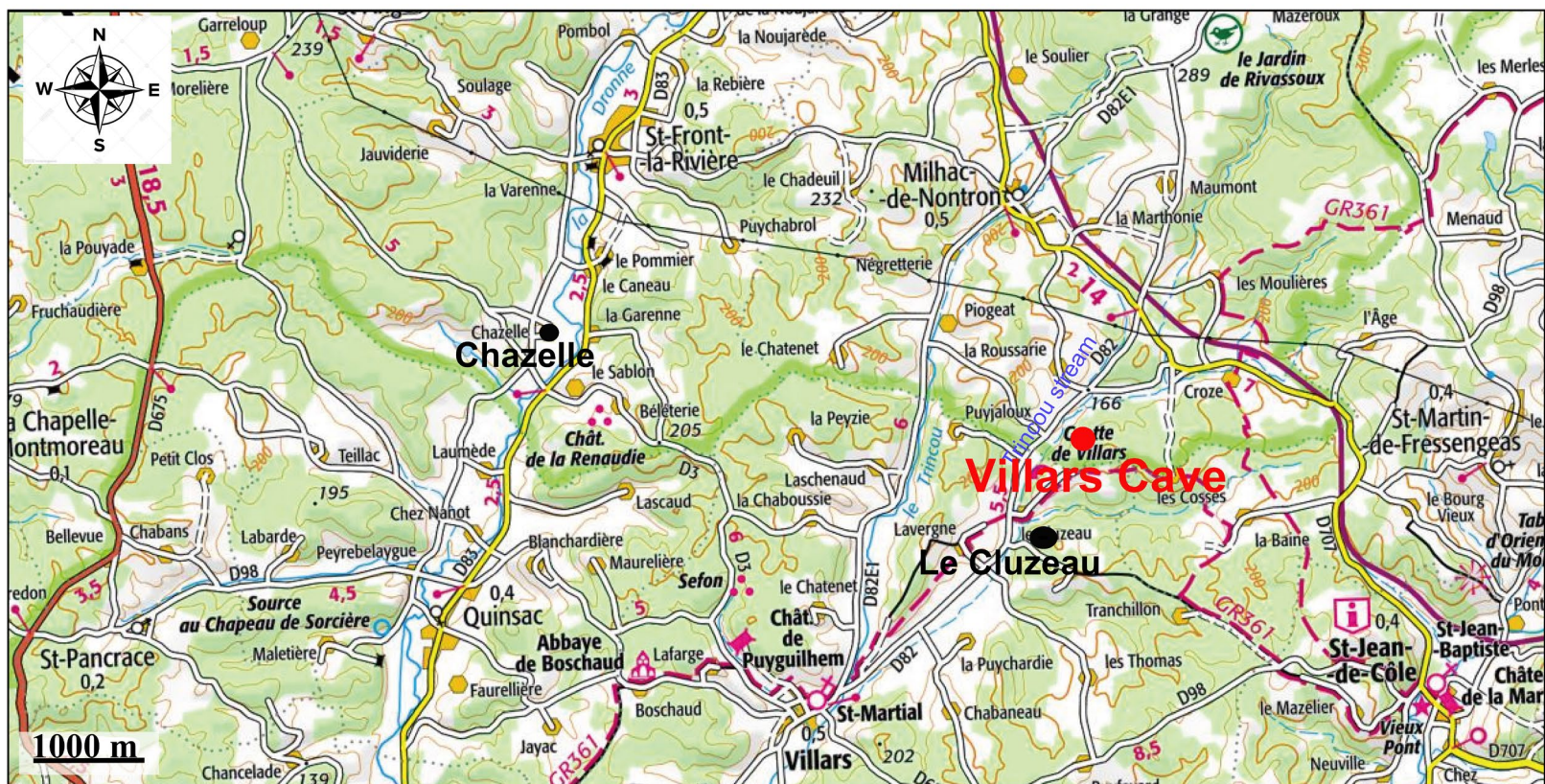


Figure 2. 3 Distribution of rivers and towns around Villars Cave. The map is from Géoportail (<https://www.geoportail.gouv.fr/carte>)

Five dripping stations have been used to monitor stable isotopes and drip rates: Vil-#10A and Vil-#10B in the upper gallery (14m deep) and Vil-#1A, Vil-#1B , and Vil-#3 in the lower gallery (36 m deep) (Figure 2.4; Figure 2.5). Although Villars Cave does not have huge shafts, we can distinguish two different levels of galleries: the upper galleries at about 10-20 m deep below surface and the lower galleries at about 30-40 m deep below surface (Figure 2.5). The lowest gallery is occupied by clay deposits that make up the ancient riverbed of Trincou, which stopped flowing into the cave some three decades ago when drainage works were carried out in the fields area of the cave (Genty, 2008).

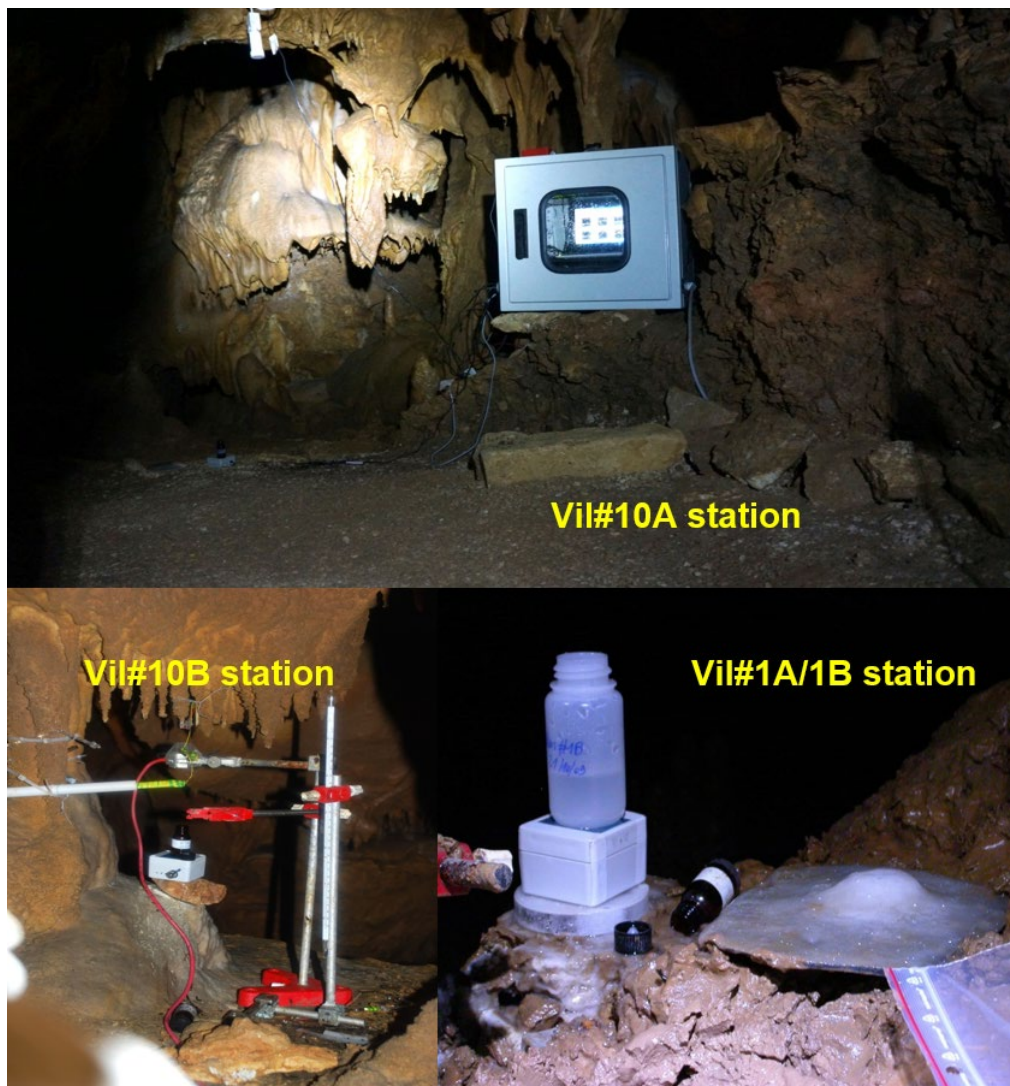
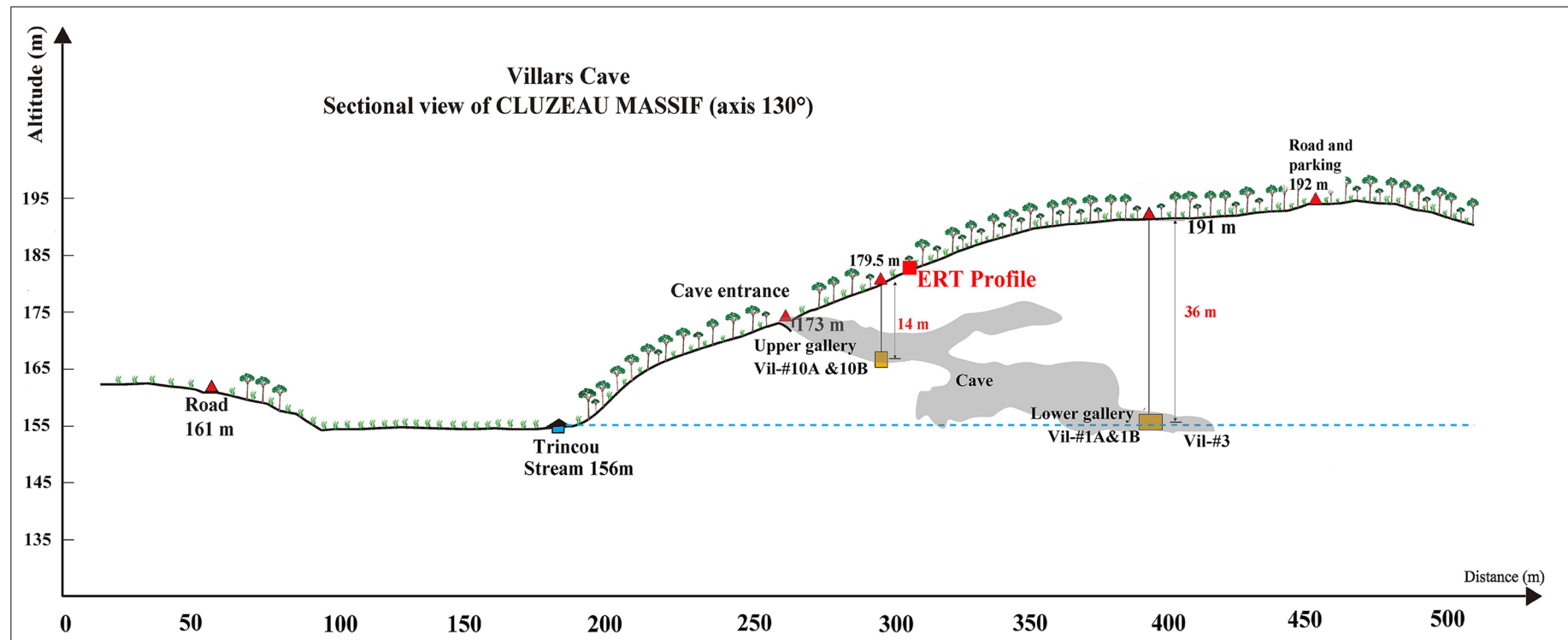


Figure 2. 4 Photos of monitoring stations inside Villars Cave (from D. Genty)



Daniel Chailloux - 2022

Figure 2. 5 A structural diagram and the distribution of surveillance sites of Villas Cave (Vil-#1A&1B, Vil-#10A&10B, and Vil-#3). The red square shows the Profile of ERT. The drip points Vil-#1B and Vil-#3 are about 5 m apart, located on the lower level of the cave. The drip points Vil-#10A located on the upper level of the cave. This section clearly shows that Station Vil-#1B and Vil-#3 are at the same altitude as the Trincou stream (from Daniel Chailloux, 2022).

## 2.2 Climatic environment around the Villars Cave

The Villars Cave, SW-France, belongs to the maritime climate region with mild winters and warm summers (Figure 2.6). During the monitoring period (1997–2019 A.D.) the total annual precipitation (P) above the Villars Cave was 1014 mm (Standard Deviation: SD=197 mm) and the mean yearly temperature was 12 °C (Genty, 2008; Genty et al., 2014a). There is a seasonal variability in the outside temperatures contrary to the local precipitations, which are more or less spread all over the years (Genty et al. 2014a).

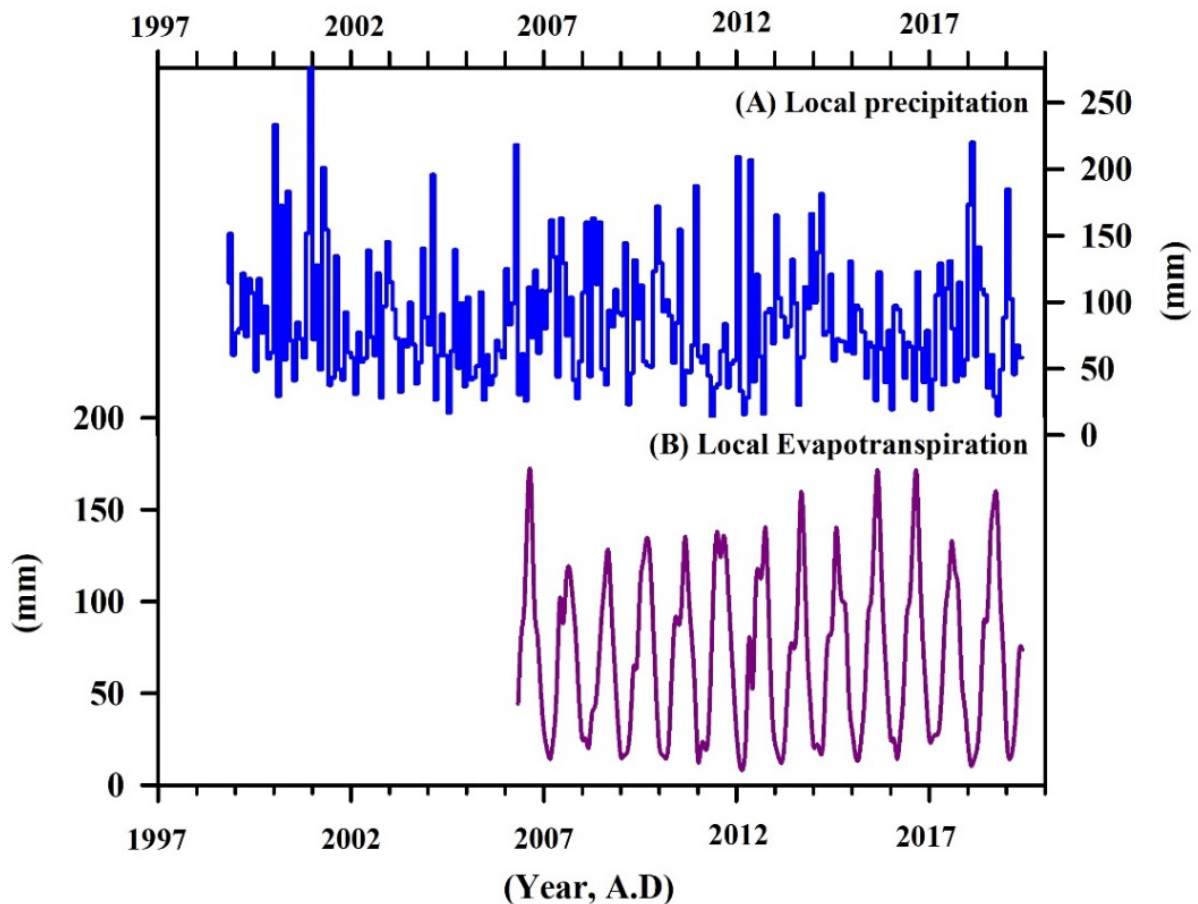


Figure 2. 6 (A) Comparison of local precipitation and (B) Potential evapotranspiration above Villars Cave (data from Météo France).

Large-scale circulation patterns, such as the North Atlantic Oscillation (NAO), the Arctic Oscillation (AO), and the Atlantic Multidecadal Oscillation (AMO) influence the climatic variation in the region of Villars Cave (Cassou et al., 2004; O'Reilly et al., 2016; Zhang et al., 2020). The most critical circulation pattern is the winter North Atlantic Oscillation (NAO), which is a driver for streamflow in North and West European, and also leads to variability of moisture sources (Zhang et al., 2020). These characteristics result in a winter climate that is mostly characterized by disturbances originating over the Atlantic Ocean and moving eastwards to reach the western European coasts, in addition to storms coming from the Scandinavian and Siberian regions (Lionello et al., 2006).

In order to better quantify spatial distributions of initial moisture sources, the research region was divided into six sections (Figure 2.7; Appendix Table 1), namely Proximal Atlantic and West Europe (PAWE), Distal Atlantic (DA), North Atlantic (NA), North America and Greenland (NAGR), Mediterranean (ME), Northern European and Northern Atlantic (NENA) (referred and modified from Krklec and Domínguez-Villar, 2014). These different regions have been defined on the basis of European geographical limitations (e.g., ocean-continent borders and ocean boundary) and distribution patterns of the initial seawater isotopic composition as well as the concentrated locations of moisture sources (Figure 2.7; Lachniet, 2009, Krklec and Domínguez-Villar, 2014).



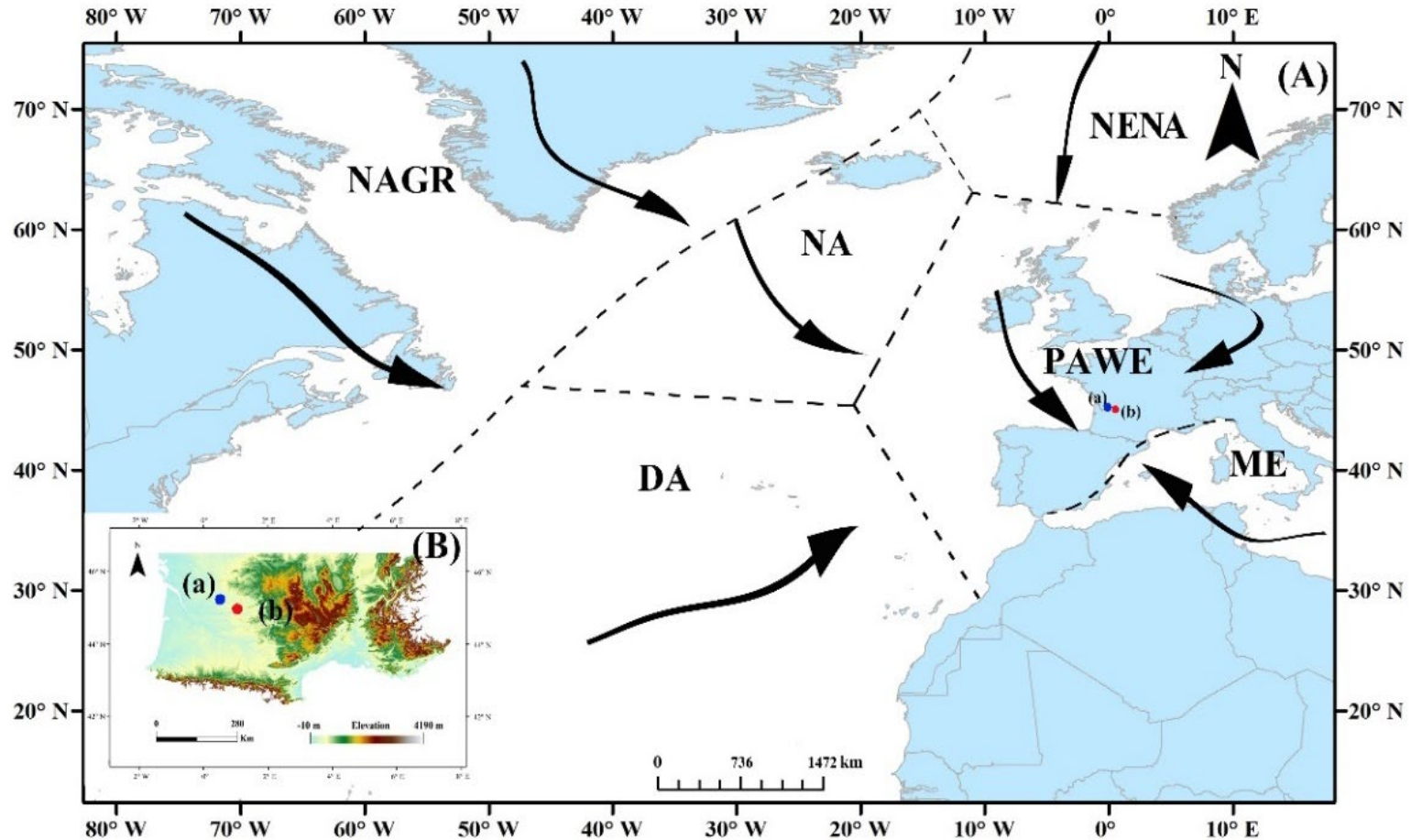


Figure 2. 7 Location of the two monitoring stations. (A) Location of the study area, including Villars (a, blue point) and Le Mas (b, red point) in SW-France. The range of initial  $\delta^{18}\text{O}_{\text{sw}}$  value is from 0 to 1.5 ‰ in PAWE (see Appendix Table 1 for region names), 0.5 to 2.0 ‰ in DA, 0 to 0.5 ‰ in NA, -4.0 to 0 ‰ in NAGR, 1.5 to 2.5 ‰ in ME, and 0 to 1.0 ‰ in NENA (referred and modified from Lachniet, 2009; Krklec and Domínguez-Villar, 2014). (B) Geomorphologic map and site distribution for the surrounding of the Villars and Le Mas stations. The arrows indicate the direction of the initial moisture source.

## 2.3 Vegetation and soil

Moss vegetation samples collected in the forest revealed a high proportion of tree pollen (77%) and a variety of taxa representing the local vegetation (34 species), according to studies by [Genty \(2008\)](#) and [Genty et al. \(2014\)](#). The most common species found in the moss samples were *Carpinus* (39%), followed by *Pinus* (16%), *Corylus* (6.1%), *Quercus* bark (4.1%), ferns (less than 1%), *Poaceae* (10.2%), and saprophytic fungal fragments. Micro-fragments consisting of organic matter particles larger than 5 µm and unknown plant tissue less than 100 µm in length were also found, as well as small opaque particles less than 20 microns in length composed of micro-charcoal and/or inert organic substances. These findings provide valuable insight into the local vegetation and environmental conditions in and around the Villars Cave area ([Genty, 2008 and Genty et al., 2014a](#)).

The vegetation surrounding the Villars Cave primarily consists of oak trees, hornbeams, hazelnut trees, and moss. The soil thickness is ranging from 0-20 cm to 40 cm ([Figure 2.8](#)). In fact, tree roots can be seen near the painted portion of the cave, about 14 meters below the surface ([Genty, 2008 and Genty et al., 2014a](#)). Most of the cave galleries are located under the forest, except for the east and most of the southern portions, which are now situated under meadows near the owner's farm ([Genty, 2008 and Genty et al., 2014a](#)).

(A) 9.5m, Soil depth=0.4 m (B) 24 & 38 m, Soil depth =0.2m (C) 56 m, Soil depth=0.4 m (D) 60.5 m, Soil depth=0.3 m

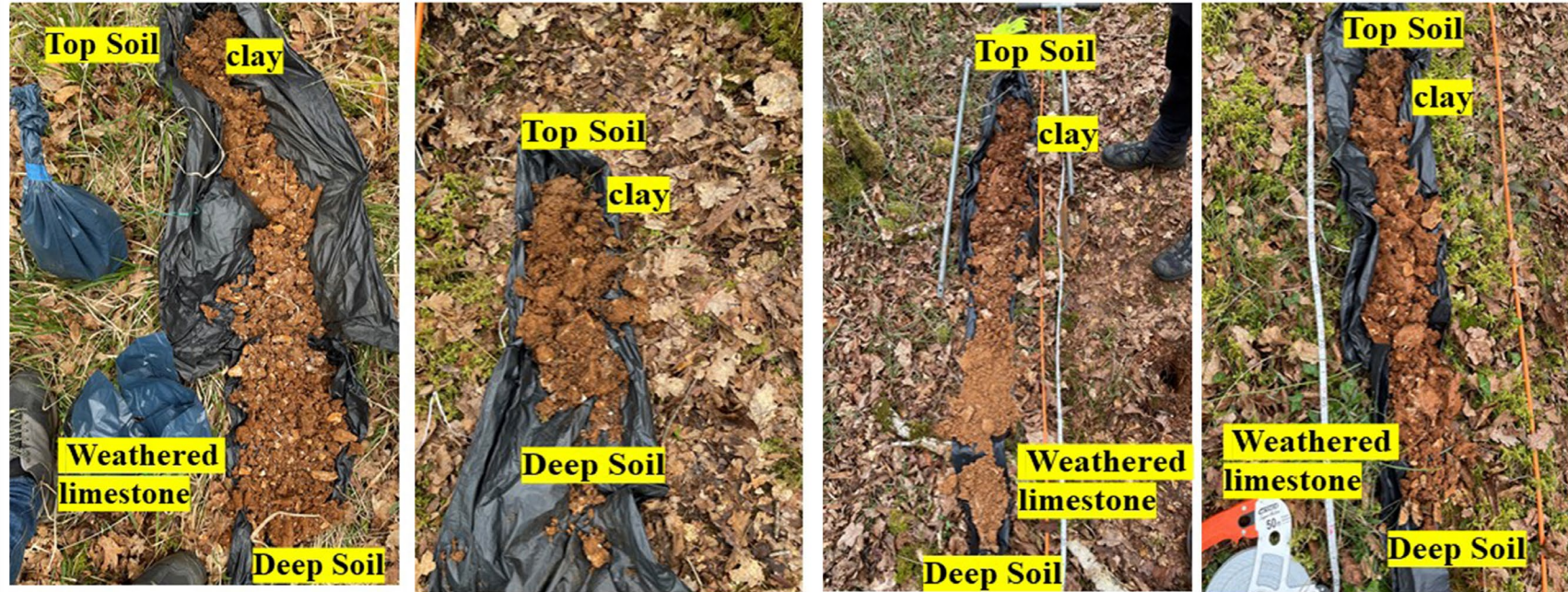


Figure 2. 8 The photo of soil depth and soil type of ERT profile at 9.5 m, 24 m, 38 m, 56 m, and 60.5 m.

## Chapter 3- Methods

### 3.1 Rainfall stable isotopes

#### 3.1.1 Stable isotopic composition of rainwater and dripping water

The stable isotopic samples were collected in the Le Mas and Villars stations at an approximately monthly scale during the period from 1997 to 2019. Rainfall sampling protocol follows the recommended principles from the Global Network of Isotope in Precipitation (GNIP) from the International Atomic Energy Agency (IAEA) ([www-naweb.iaea.org/napc/ih/documents/userupdate/sampling.pdf](http://www-naweb.iaea.org/napc/ih/documents/userupdate/sampling.pdf)). The rainwater is collected in a 5 L tank with a funnel. Before the tank is buried in the soil, each sample has added a few ml of liquid paraffin to prevent any evaporation. Water is collected into a 15 ml glass bottle which is closed by a specific cork with a conical funnel making sure waterproofness.

Rainfall and drip water were collected for  $\delta^{18}\text{O}$ - $\delta\text{D}$  isotopes measurements in the monitoring period from 1997 to 2019 (Genty et al., 2014; Zhang et al., 2020). The  $\delta^{18}\text{O}$  time series from 2006 to 2019 provides the most continuous data, with sampling intervals occurring on average every 1-2 months. There were intermittent gaps in the data collection between 2003 and 2006. However, before 2003, the sampling intervals were conducted approximately every 1 to 2 months. Samples dedicated to oxygen isotope ratios were sent to the LSCE lab (Laboratoire de Sciences du Climat et de l'Environnement, Gif-sur-Yvette, France) and analyzed according to two methods. Firstly, rainfall and drip water  $\delta\text{D}$  and  $\delta^{18}\text{O}$  were also measured using a PICARRO laser spectrometer analyzer, with the same standards, leading to an accuracy of 0.5 ‰ for  $\delta\text{D}$  and  $\delta^{18}\text{O}$  values. Secondly, however, it is commonly known that using a

PICARRO laser spectrometer analyzer for  $\delta^{18}\text{O}$  measurements may result in less accurate results. To address this issue, we utilized a MAT 252 mass spectrometer to measure  $\delta^{18}\text{O}$  by equilibration with  $\text{CO}_2$ . We compared the results with the PICARRO and ultimately decided to retain the measurements obtained from the MAT 252 mass spectrometer. The measurements have a 2-sigma error of  $\pm 0.05\text{‰}$  and were calibrated to the V-SMOW international standard.

### 3.1.2 Meteorological data

European precipitation data was downloaded from the Global Precipitation Climatology Project (GPCP) Version 2.3 combining observations and satellite precipitation data with  $2.5^\circ \times 2.5^\circ$  global grids (Website: <https://www.esrl.noaa.gov/psd/data/gridded/data.gpcp.html>). The air temperature data were obtained from the Jones CRU Air Temperature Anomalies Version 4 with  $5^\circ \times 5^\circ$  global grids. The sea surface temperature (SST) data were obtained from Kaplan Extended SST Version 2 with  $5^\circ \times 5^\circ$  global grids ([https://psl.noaa.gov/data/gridded/data.kaplan\\_sst.html](https://psl.noaa.gov/data/gridded/data.kaplan_sst.html)). The NAO index was downloaded from the following official websites: <https://www.ncdc.noaa.gov/teleconnections/nao/data.csv>. We also have: 1) a local meteorological station; 2) the data from Saint Martin de Freyssengeas from Meteo France.

### 3.1.3 HYSPLIT model for tracking moisture source

To diagnose the moisture transportation pathways and better understand the  $\delta^{18}\text{O}_p$  variability in SW-France, we employed the method of back trajectories of air parcels from the NCEP reanalysis data (Website:

<ftp://arlftp.arlhq.noaa.gov/pub/archives/reanalysis>). The HYSPLIT model was downloaded from the NOAA Air Resources Laboratory (Website: <http://ready.arl.noaa.gov/HYSPLIT.php>) (Draxler and Rolph, 2010). In order to analyze the temporal variability of moisture sources, we have divided a year into four seasons: spring (March–May), summer (June–August), autumn (September–November), and winter (December–February of the following year).

Previous studies have revealed that trajectories with the average residence time of water vapor in the atmosphere are 120 hours (5 days) (Numaguti, 1999; Krklec and Domínguez-Villar, 2014). Therefore, the variation of moisture sources was identified in the Villars station (we assumed a common source for Le Mas station being very close to Villars) during the previous 120 h (5 days) (Krklec and Domínguez-Villar, 2014; Krklec et al., 2018). The water vapor transportation usually occurs mainly at 1500m–3000m (above ground level: a.g.l) in the mid-low troposphere, however, the peak value of water vapor transportation in the plain is at an altitude of about 1500 m (~ 850 hPa) (Tang et al., 2015; Cai et al., 2017). Moreover, the back trajectories from different elevations showed similar paths and regulations (Krklec and Domínguez-Villar, 2014; Krklec et al., 2018), therefore we consider the only altitude of 1500 m (a.g.l) as the initial vertical height for the water vapor transportation.

The integrated system was operated for computing the daily trajectory at the time of 00:00, 06:00, 12:00 and 18:00, and the output of trajectories are made every 6 hours. The cluster analysis tool was applied for integrating all trajectories, which were grouped according to the horizontal moving speed and direction in the HYSPLIT model (Tang et al., 2015). Finally, HYSPLIT4 software is used for superposition analysis and designed to get the diagram to determine the variation of the initial moisture source.

Many upgrades that reflect the most recent advances in the computation of dispersion and transport have been incorporated into HYSPLIT. The calculation of the new position at a time step ( $t + \Delta t$ ) due to the mean advection by the wind determines the trajectory that a particle or puff will follow. In other words, the change in the position vector  $P$  means with time:

$$P_{\text{mean}}(t + \Delta t) = P_{\text{mean}}(t) + \frac{1}{2} [V(P_{\text{mean}}, t) + V(\{P_{\text{mean}}(t) + [V(P_{\text{mean}}, t)\Delta t]\}, t + \Delta t)]\Delta t$$

Equation (1)

Calculated from the average of the three-dimensional velocity vector  $V$  of the initial position and the initial guess ([Draxler and Hess 1998](#)). Equation (1) is the basis for the trajectory calculation in HYSPLIT. Only the advective component is considered when running the trajectory. Only the turbulent dispersion component is needed to describe the atmospheric transport and mixing processes of 3D particles and puffs. The dispersion equations are formulated in terms of turbulent velocity components. In the 3D particle implementation of the model in Equation (2), the dispersion process is represented by adding a turbulent component to the average velocity obtained from meteorological data ([Fay et al., 1995](#)): i.e.,

$$\begin{aligned} X_{\text{final}}(t + \Delta t) &= X_{\text{mean}}(t + \Delta t) + U'(t + \Delta t)\Delta t \\ Z_{\text{final}}(t + \Delta t) &= Z_{\text{mean}}(t + \Delta t) + W'(t + \Delta t)\Delta t \end{aligned}$$

Equation (2)

where  $U'$  and  $W'$  correspond to the turbulent velocity components,  $X_{\text{mean}}$  and  $Z_{\text{mean}}$  are the mean components of particle positions, and  $X_{\text{final}}$  and  $Z_{\text{final}}$  are the final positions in the horizontal and vertical, respectively. The turbulence component is always added after the advection computation.

Here are some advantages of using the HYSPLIT model for moisture source tracking. The HYSPLIT model utilizes a Lagrangian approach, which tracks the movement of individual air parcels over time. This allows for a detailed analysis of the transport pathways and sources of moisture. The HYSPLIT model incorporates various input data, including meteorological data, emission sources, and land surface information. This enables comprehensive analysis and simulation of the atmospheric processes that influence moisture transport. The HYSPLIT model provides the capability to examine the vertical profile of air mass transport. This is particularly useful for understanding the influence of different atmospheric layers on moisture transport and source attribution. The HYSPLIT model can simulate both backward and forward trajectories, allowing for the identification of moisture sources in the past or potential future destinations. This helps in understanding the historical origins and potential impacts of moisture on a given region. The HYSPLIT model allows for sensitivity analysis by modifying input parameters such as release heights, particle numbers, or meteorological conditions. This helps in assessing the relative importance of different factors in moisture transport and source attribution. The HYSPLIT model offers graphical tools for visualizing trajectory paths and moisture sources. These visualizations aid in interpreting the results and effectively communicating the findings to researchers and stakeholders. Overall, the HYSPLIT model provides a robust framework for tracking moisture sources by considering the complex interplay of atmospheric processes, offering valuable insights into the origin and transport of moisture in different regions.



### 3.1.4 Statistical methods and packages

The correlation between regional parameters and  $\delta^{18}\text{O}_p$  variability in SW-France was calculated using the programming language R (<https://rstudio.com/products/rstudio/download/>). The degrees of freedom corrections were calculated by time-series autocorrelations (McCarthy et al., 2015):

$$\text{Neff} = N \cdot ((1 - ax \cdot ay) / (1 + ax \cdot ay)) \quad \text{Equation (3)}$$

where Neff is the degrees of freedom, N is the number of observations and ax, ay are the regional parameters and  $\delta^{18}\text{O}_p$  variability values, respectively.

The links between PIMS/temperature and  $\delta^{18}\text{O}_p$  were established using multiple linear regression analysis methods by Statistical Package for the Social Sciences (SPSS) software:

$$y_i = \beta_0 + \beta_1 x_{i1} + \beta_2 x_{i2} + \dots + \beta_p x_{ip} + \epsilon \quad \text{Equation (4)}$$

where, for i denotes n factors;  $y_i$  denotes dependent variable;  $x_i$  denotes explanatory variables;  $\beta_0$  denotes y-intercept;  $\beta_p$  denotes slope coefficients for each explanatory variable;  $\epsilon$  denotes residuals.

## 3.2 Drip water Stable isotope

### 3.2.1 Meteorological data

For the historical period, we collected external air temperature and precipitation from 1997 to 2019 provided by a meteorological station located just above the cave. The ETP (Potential Evapotranspiration) and water excess (Rainfall-Evapotranspiration > 0 also called efficient rainfall) have been calculated using meteorological measurements provided by the nearby Meteo-France station (Saint-Martin de Freissengeas, 4.8 km East) during the period 2006-2019. The ETP

calculation relies on the Penman-Monteith method (Allen et al., 1998), accounting for the minimum and maximum temperature, the average wind speed at 10 m (or 2m), the average vapor pressure, the exposure time, and the global radiation.

For the future period, we have used simulated monthly data for Temperature ( $^{\circ}\text{C}$ ), precipitation (mm/month), and potential evapotranspiration (ETP) (converted from  $\text{kg m}^{-2}\text{s}^{-1}$  to mm/month) for the grid point including Villars Cave (lat=45.44; lon=0.78) from January 2016 until December 2100. These data were generated by the CNRM-CM5 model (Voldoire et al., 2013), which participated in the CMIP5 project (Taylor et al., 2012). We used simulations prefiguring a stabilization of radiative earth budget imbalance at  $8.5 \text{ W m}^{-2}$  in 2100, i.e., the RCP8.5 emission scenario (Meinshausen et al., 2011), which have been then dynamically downscaled within the CORDEX project (Jacob et al., 2014). More specifically, we used the CNRM-CM5 simulations under the RCP8.5 scenario downscaled at the European scale with the SMHI-RCA4 regional model (Samuelsson et al., 2011), over the EUR-11 domain, which consists of a grid spacing of  $0.11^{\circ}$  (12.5 km). Finally, these data have been adjusted based on EURO4M MESAN observational data (Barring et al., 2014), for the period between 1989-2005. In this context, we used de-biased data provided by “the Climate Data Factory” (<https://theclimatedatafactory.com/>), whose procedure relies on the Cumulative Distribution Function transform (CDF-t) method (Michelangeli et al., 2009; Vrac et al., 2016), which is based on the quantile mapping (QM) method (Vrac et al., 2012).

### 3.2.2 Drip discharge rate

Drip water monitoring sites were set in Villars Cave at different levels in order to detect potential differences in the recharge of the karst aquifer (Figure 2.7; Genty, 2008; Genty et al., 2014a). Vil-#10A and Vil-#10B is about 4 m apart, located on the

upper level of the cave, and drip site Vil-#1B is located deeper in the lower level (there is no drip counter at Vil-#1A station which is 0.5 m aside, but only  $\delta^{18}\text{O}_d$  measurements). Drip discharges, presented in this work, were recorded between October 2013 and April 2019 A. D. This period coincides with a continuous measurement period with no stop due to technical problems. Drip loggers (STALAGMATE) recorded the frequency of dripping rate from falling onto the surface of the sealed box containing an acoustic sensor at 10 min intervals during the period of 10/2013-11/2017 and at 15 min intervals during the 11/2017-10/2022 period.

### 3.2.3 Modeling infiltration process and lag time calculation

The modelling study conducted by [Genty et al. \(2014\)](#) and [Dee et al. \(2015\)](#) focused on modeling stable isotopes and hydrology in cave drip-water. They employed a running mean approach to analyze the data. Another study by [Moerman et al. \(2014\)](#) incorporated the concept of lagged storage time, considering the delayed response in the karst system. [Harman \(2015\)](#) accounted for epikarst in their study but did not take into account the number of reservoirs present. In contrast, [Treble et al. \(2019\)](#) and this study considered multiple reservoirs, including soil, epikarst, and unsaturated zone reservoirs.

Our model provided a more comprehensive understanding of the hydrological processes. Drip water hydrological flux and  $\delta^{18}\text{O}$  were modeled using a version of a karst hydrology model (KarstFor) first developed by [Bradley et al., 2010](#). This model has been applied to multiple climatic regions so that we can determine the theoretical range of drip  $\delta^{18}\text{O}$  in some locations: northern temperate (Tartair Cave, Scotland), monsoonal (Ethiopia), and Mediterranean (St. Michaels Cave, Gibraltar, South Spain Peninsula), and sub-humid to semi-arid (central Texas caves, United States of America)

(Bradley et al., 2010; Baker et al., 2013; Treble et al., 2013; 2019; Hu et al., 2021).

Here, our final configuration parameter settings are based on Bradley et al., 2010, and we have adjusted some parameters based on the temperate oceanic climate in the context of Villars Cave. It ensures that the model can still adapt in all drips under various configurations (Table 3.1). Four storage reservoirs were set in the conceptual model: Soil store, Epikarst store, Karst store 1, and Karst store 2 (Figure 3.1) based on ERT image-identified reservoirs. All the main hydrological parameters of each reservoir are summarized in Table 3.1. KarstFor model is based on a local physical understanding of each parameter and then adjusting the parameters one by one. For example, as shown above, we set the different drainage fluxes (F1, F4, F5) and overflow (Ovicap and Epicap) of the karst reservoirs to control the variance of  $\delta^{18}\text{O}$  in Epikarst and Karst store 1 and 2. The term “Ovicap” is used to refer to the setting parameter that represents the overflow capacity threshold of the karst store. On the other hand, “Epicap” pertains to the setting parameter that represents the overflow capacity threshold of the epikarst (Treble et al., 2013). The high/low proportion of karst water available for evapotranspiration (k\_eevap) corrects the mean value of drip  $\delta^{18}\text{O}$  (Bradley et al., 2010; Treble et al., 2013; 2019; Hu et al., 2021).

The previous simulation model of the infiltration was a simple 1-D model of the downward water percolation without considering the complex fact that there may be multiple reservoirs in the unsaturated zone (Jean-Baptiste et al, 2019). However, our new modeling uses several reservoirs representing the soil, epikarst, and unsaturated zone, along with monthly climate as inputs, to simulate drip water oxygen isotopes (Almalki and Nadarajah, 2004; Treble et al., 2019). KarstFor simulations include oxygen isotope fractionation during evaporation, mixing water in matrix flow with conduit flow in the reservoir, and overflow. The model simulates rainfall through the

soil reservoir, epikarst reservoir, and two underlying reservoirs before surface rainfall reaches the top of the cave. Therefore, the new model has multiple additional parameters and reservoirs, improving the results compared to the previous models evaluated in this study.

In the model, the variable infiltration routing of percolating waters is conceived between two sub-surface water stores (Soil Store and Epikarst Store, Figure 2) and two lower-level karst water reservoirs (Karst store 1 and 2). Each of them potentially represents the source of drip-water in the cave (Bradley et al., 2010; Treble et al., 2013; 2019). The flow route or hydrology dynamic of the conceptual model is as follows:

- (1) In Soil Store, the soil thickness is ranging from 20 cm to 40 cm based on field observation, and we set an initial storage volume of only 50 mm (Table 3.1, while it can go up to 150 mm for more developed soil (Treble et al., 2013)). The local precipitation amount is considered an input parameter into the “Soil Store” receiving precipitation directly. Outputs are evapotranspiration and drainage to Epikarst (F1).
- (2) In the Epikarst, the hydrological flux receives drainage from Soil Store (F1), and outflows to Karst store 2 (F4) or Karst store 1 (F3) according to the proportional drainage function:  $\text{Epikarst} \times (\text{Epikarst}/\text{Epikarst capacity}) \times 0.25$ , i.e., flow is 25% of volume when Epikarst is at capacity.
- (3) In Karst store 2, the hydrological flux receives drainage from Soil Store and Epikarst, “Karst Store 2” receives F4 from “Epikarst” and F8 from a “bypass” (refer to Table 3.1) when the drainage is over its capacity.
- (4) Karst Store 1 receives hydrological fluxes provided by Epikarst (F3) and Karst Store 2 (F6 and F7).

The  $\delta^{18}\text{O}$  values in each store are updated with the time step based on the water balance calculations and isotopic evaporation coefficient in terms of rainfall,

evapotranspiration, drainage, and overflow. Three outputs, representing multiple karst configurations, are modeled similarly to Bradley et al., 2010. The karst component of the model follows the KarstFor version presented in Bradley et al., 2010, with water levels in the reservoirs (Soil Store, Epikarst Store, Karst Store 1, and Karst Store 2) given by an initial storage value (mm), and then recalculated (starting from the top store) at a monthly time step via:

$$\Delta V = (\Sigma In - \Sigma Out) \Delta t \quad \text{Equation (5)}$$

Where  $\Delta V$  = net change in monthly storage volume (mm), In = input flow, out = output flow (mm/month),  $\Delta t$  = 1 month. Besides the model analysis, we also studied the time lags between drip rate and water-excess at the different drip sites. For that, we made a cross-correlation analysis between two-time series types.

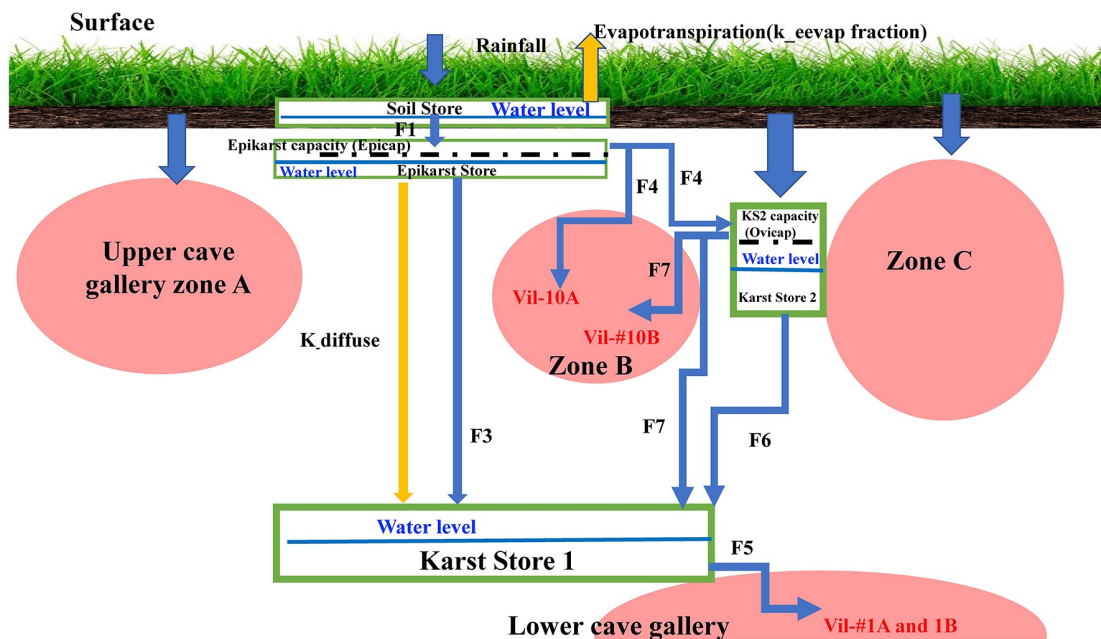


Figure 3. 1 Conceptual model of karst hydrology in individual karst water reservoirs. The boxes represent different reservoirs, blue lines represent water levels, blue arrows represent fracture flow, and the red arrow represents diffuse flow (Baker et al., 2013, Bradley et al., 2010; Treble et al., 2013; 2019). A brief overview of the overall model is given in the main text, and the details of the KarstFor model are given in (Baker et al., 2013, Bradley et al., 2010; Treble et al., 2013; 2019), also see Table 3.1 for a summary of model inputs and parameters.

**Table 3. 1. Compilation of selected model parameter values and notes about its implementation and configuration. All parameter names are from conceptual Figure 3.1. Based on the final configuration of Treble et al. (2013) and update here:**

Parameter	Description	Final configuration*
Soil store (mm)	Set to a small configuration, no soil evaporation. To determine the storage volume, the available water storage capacity was also taken into account. Soil thickness range from approximately 20 to 40 cm. According to the soil handbook, the clay component of the soil has a water storage capacity of about 21% of its volume (Soil guidelines, 2005). From these values, a selection of 50 mm was made as the initial soil storage volume.	Init: 50 Max: 150
Epikarst (mm)	Set to a small configuration, no epikarst evaporation	Init: 100 Max: 180 Epicap: 50/100/160
KS1 (mm)	The main karst storage that receives flux from epikarsts by $k_{diffuse}$ and/or F3; may also receive the overflow from KS2.	Init: 200 Max: 200
KS2 (mm)	Secondary karst storage, filled through F4, through F6 or allows modeling the switchable overflow of KS1 via F7. The amount of overflow is proportional to the ratio of $KS2 / KS1$ .	Init: 200 Max: 200 Ovicap: 50/100/180
F1 (mm/month)	Determines steady state values in soil store.	0.1/0.5/0.95
F3 (mm/month)	The flux represents the fracture flow from Epikarst to KS1. The setting is based on field observation, and the flow is zero diffusion flow.	0.0008
F4 (mm/month)	Flux from Epikarst to KS2 is activated when threshold 'Epicap' is reached.	0.1/0.5/0.6/0.9
F5 (mm/month)	Drainage flux of KS1.	0.01/0.1/0.2/0.5

F7 (mm/month)	Overflow from KS2 back into KS1 once 'ovicap' is exceeded.	0.4
F6 (mm/month)	Drainage flux of KS2.	0.001
F8 (mm/month)	Bypass from the surface to KS2. Used to test the configuration used by Treble et al. (2013), rainfall events > 7mm/month give priority to charging KS2, but it is set to zero in the final configuration.	0.0001
k_diffuse (mm/month)	The flux is to simulate the diffusion flow through the pdf function.	0.001
k_eevap	Fraction of water remaining in epikarst reservoir available to evaporate	0.016
k_d18O_soil	Isotopic evaporation coefficient for soil reservoir	0.06 ‰ month <sup>-1</sup> mm <sup>-1</sup>
k_d18O_epi	Isotope evaporation coefficient of epikarst reservoir	0.01/0.04/0.06/0.1 ‰ month <sup>-1</sup> mm <sup>-1</sup>

To determine the lag time between drip rate and water excess at different drip sites, we employed the Pearson correlation coefficient, which is commonly used to assess the strength of a linear relationship between two variables (x and y). By calculating the maximum correlation coefficient (r) for specific days, we were able to identify the time lag in days between the drip rate and water excess. We utilized the following equation:

$$r = \frac{\sum_i (x_i - \bar{x})(y_i - \bar{y})}{\sqrt{\sum_i (x_i - \bar{x})^2} \sqrt{\sum_i (y_i - \bar{y})^2}} \quad \text{Equation (6)}$$

In the equation, r represents the Pearson correlation coefficient, x represents water excess, y represents drip rate, and the number of lag days corresponds to the days with the highest correlation coefficient.



### 3.3 ERT measurements

#### 3.3.1 Basic principle

The electrical resistance  $R$  is defined based on Ohm's law (Equation 7):

$$R=U/I \quad \text{Equation (7)}$$

Where  $U$  is the voltage (V),  $R$  is the resistance ( $\Omega$ ), and  $I$  is the current (A).

Electrical resistivity tomography (ERT) measurements consist of injecting a known electrical current into the medium using two so-called current or injection electrodes (C1 and C2 in Figure 3.2), and measuring by two other electrodes, called potential electrodes (P1 and P2 in Figure 3.2).

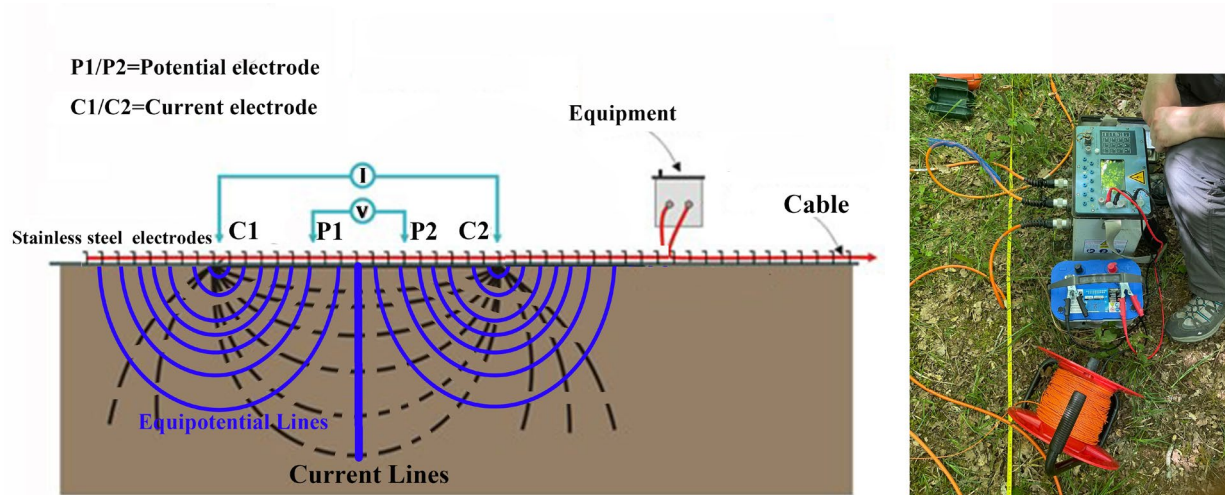


Figure 3. 2 Principles of ERT. C1 and C2 are the current electrodes and P1, P2 are the potential electrodes.

Wherever these measurements are made over a real heterogeneous earth, as distinguished from the fictitious homogeneous half-space, the  $\rho$  is replaced by  $\rho_a$  for the apparent resistivity. The apparent electrical resistivity  $\rho_a$  can be calculated as follows:

$$\rho_a = k * \frac{\Delta V_{P_1 P_2}}{I_{C_1 C_2}} \quad \text{Equation (8)}$$

with  $k$  the geometric factor (depending on the device's geometry),  $\Delta V_{P1P2}$  is the potential difference between the measuring electrodes, and  $I_{C1C2}$  is the intensity of the injected current.

Several electrodes (multiples of 16 or 24, depending on the device) are implanted in line in ERT (Figure 3.3). Several measuring devices represent various electrode arrays: Wenner, Schlumberger, dipole-dipole, pole-dipole, pole-pole, gradient, etc. In conclusion, the choice of electrode array should be considered to ensure that the electrical resistivity measurements accurately represent the subsurface resistivity structure.

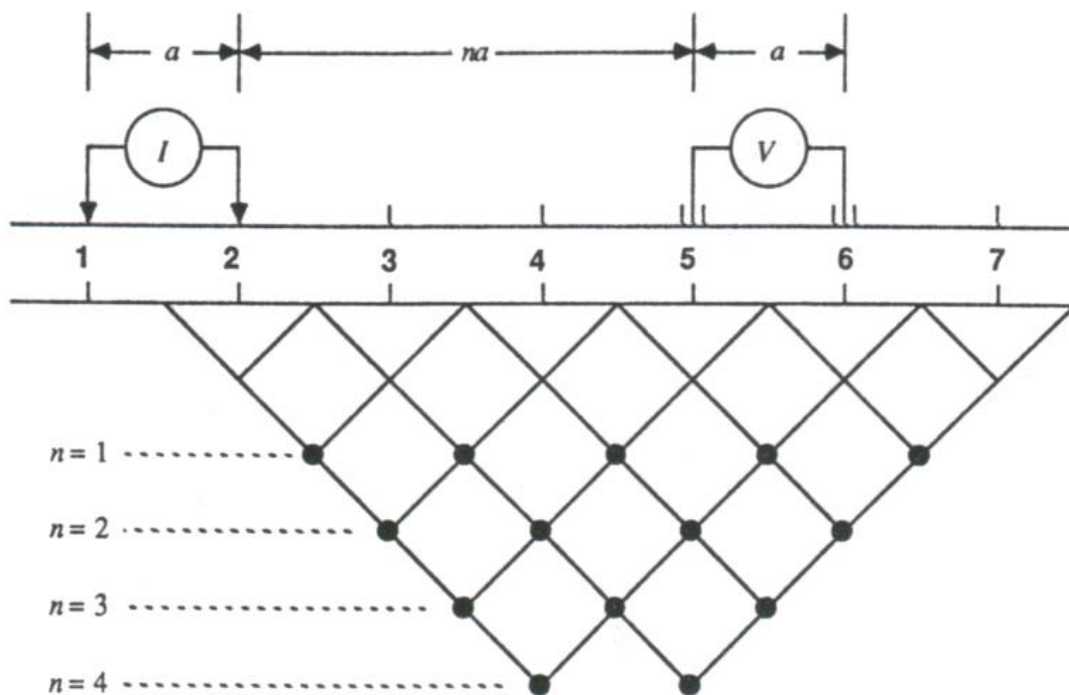


Figure 3. 3. ERT investigation cross section. The example of the dipole-dipole device. Each “ $n$ ” represents the pseudo depth level as a function of electrode spacing. “ $a$ ” corresponds to the inter-electrode distance. We obtain for each point an apparent resistivity ( $\rho_a$ ) for the whole forming the pseudo-section (Loke, 2004).

### 3.3.2 Factors affecting resistivity

Subsurface resistivity depends on the texture and structural characteristics and is sensitive to water content (Keller and Frischknecht, 1966; Daniels and Alberty, 1966;

Telford et al., 1990). Several parameters influence the variation in resistivity: saturation, porosity, particle size, and mineralogy, voids as pore size distribution and connectivity, fluid content on the pores, and their resistivity properties and temperature. For common rock types shown in Figure 3.4:

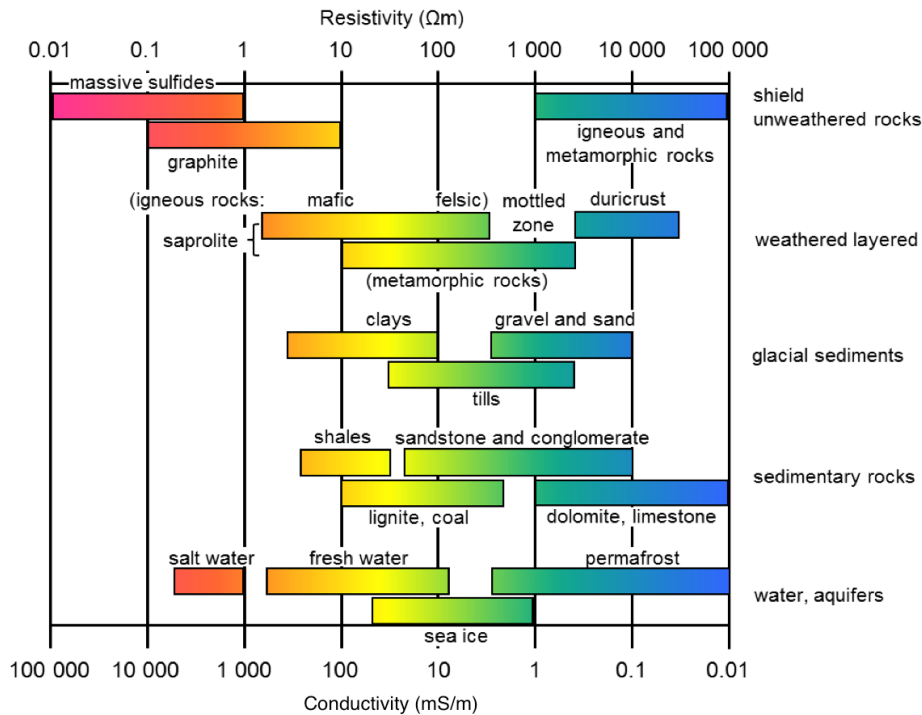


Figure 3. 4 Electrical conductivity and resistivity of common rocks based on Palacky, 1988.

In the case of materials whose solid matrix is insulating, the resistivity is conventionally expressed according to Archie's law (1942) defined by Equation (9):

$$\rho = \rho_w * \varphi^{-m} * S_w^{-n} \quad \text{Equation (9)}$$

$\rho$  is the resistivity of the rock,  $\rho_w$  is the resistivity of the fluid,  $\varphi$  is porosity,  $S_w$  is the degree of saturation,  $m$  is the cementation factor ( $m < 4$ ) and  $n$  is the saturation factor ( $1.5 < n < 3$ , Montaron, 2009).

### 3.3.3 ERT inversions

ERT survey line was established to characterize both temporal and spatial variation in the unsaturated zone above and near the Villars cave. We present the ERT monitoring from February 2020 A.D. to January 2023 A.D., representing 17 datasets acquired approximately at 1–2-month intervals ([Appendix Tables 4 and 5](#)). After several tests on-site in February 2020, we have decided to perform the electrical resistivity measurements with the SYSCAL Pro resistivity using a Pole-Dipole (forward and reverse, injection pulse duration:500ms) and a gradient array (injection pulse duration:250 ms) of 72 stainless steel electrodes with a 1m and 1.5m spacing.

An inversion resistivity model was calculated using the Res2Dinv® software, using the L1 norm on the data and a model associated with the refinement of the mesh model ([Loke, 2004](#)) to account for large resistivity contrasts. We performed seven iterations on each survey data, after which the absolute error stabilized. After seven iterations, the inversion model misfit ranged between 0.83% and 1.7% for all 17 inversion models in ERT-1m spacing and 2.5% to 7.9% for 8 inversion models in ERT-1.5m spacing.

### 3.3.4 Temperature correction

The electrical resistivity measurement depends on the rock temperature, which varies with time. Therefore, we have corrected the ERT measurements for temperature ([Hayley et al., 2007](#); [Genelle et al., 2012](#); [Hermans et al., 2014](#)). This correction requires the knowledge of the temperature in the rock mass at any given time ([Lacanette et al., 2007](#); [Salmon et al., 2023](#)). The heat equation governing thermal diffusion must be reconsidered in terms of temperature. However, this equation

requires the thermal diffusivity of the rock, which is unknown. Therefore, we adjust the thermal diffusivity for the calculated temperature to match in situ measurements (Salmon et al., 2023). To do this, we placed three thermocouple sensors at 0.1 m, 0.5 m, and 1 m below the surface above the cave, close to the ERT profile location (about 3 m, Figure 2.1C), and also measured the temperature of the air outside and inside the caves.

Based on this estimated diffusivity, we solve the heat equation in the rock mass, which gives the temperature at each point of the massif according to the time series. We then perform the temperature correction on the inverted resistivity. We use a ratio model (equation (10)), which is commonly used to correct resistivity data with the corresponding reference temperature (Ma et al., 2011; Xu et al., 2015; 2017; Figure 3.5).

$$\rho_c = \rho_i \times [1 + \delta \times (T_c - T_{ref})] \quad \text{Equation (10)}$$

Where  $\rho_c$  stands for resistivity after temperature correction;  $\rho_i$  is interpreted as resistivity after inversion;  $T_c$  represents temperature during the ERT survey.  $\delta$  is the temperature slope compensation value, which is set to 0.025 by most geophysicists (Keller and Frischknecht, 1966; Besson et al., 2008). In addition,  $T_{ref}$  is the reference temperature of 12.55°C, which is the average annual temperature recorded in the cave during the entire monitoring year (Figure 3.5).

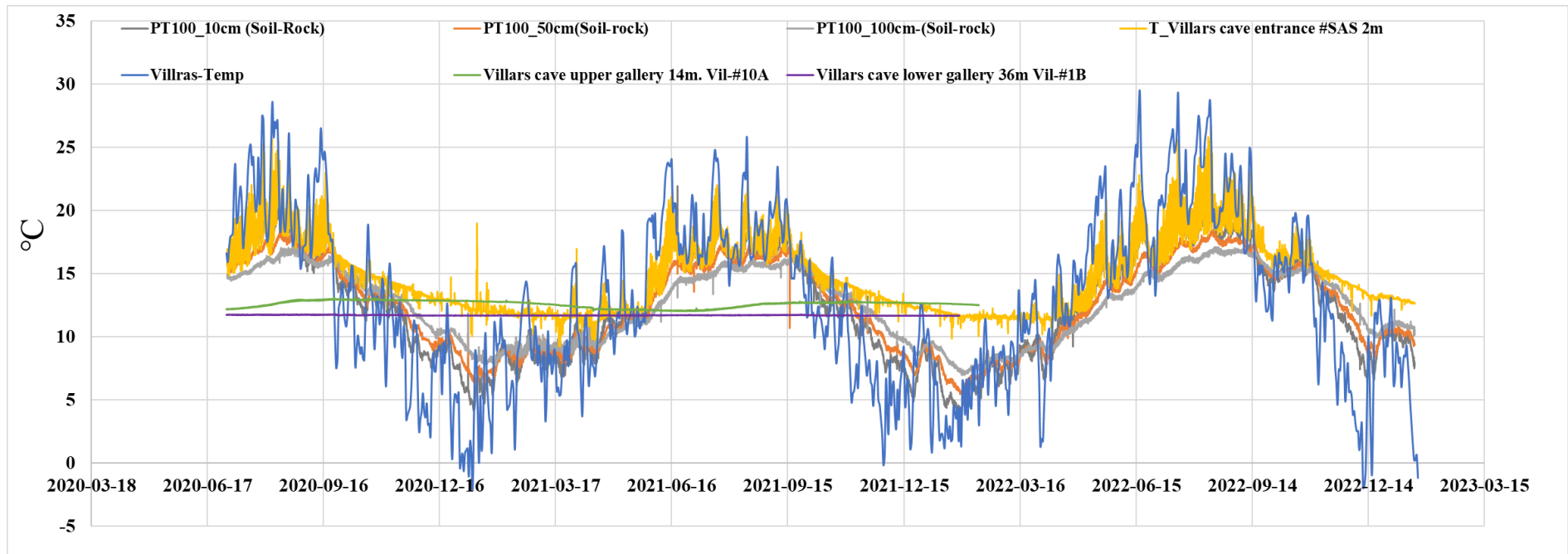


Figure 3. 5 Temperature time series in the air outside the cave, soil, rock, and inside the cave from 2/7/2020 to 27/01/2023.  $T_{ref}$  is the reference temperature of 12.55°C, which is the annual average temperature recorded inside the cave (upper level) during the entire monitoring year.

### 3.3.5 Hierarchical Agglomerative Clustering (HAC)

In addition, in order to characterize the differences in resistivity between seasons, we need to interpret the variability observed in the different zones of ERT images. Therefore, a classical unsupervised classification method, Hierarchical Agglomerative Clustering (HAC), was applied with a bottom-up algorithm (Saporta, 1990), which can produce an ordering of blocks that provides a single image in which different zones are distinguished by their seasonality. HAC has been applied in several cases to identify geological heterogeneity in different contexts. For example, Genelle et al. (2012) used HAC to identify the zones of heterogeneity in a landfill cover. The method was also applied to a cave study, the prehistoric Lascaux Cave in SW- France, which allowed us to recognize the reliability of the method (Xu et al., 2015; 2017). Later, Lharti et al. (2023) compared the HAC and K-means methods in Lascaux Cave, highlighting that the HAC method was particularly effective in identifying areas already known to be waterlogged or clayey (Lharti et al., 2023).

The HAC classification was finalized using 16 ERT images captured between February 2020 and September 2022. However, a new experiment was conducted in January 2023 and the resulting data was incorporated into the original HAC classification. Each resistivity model contains 2252 blocks of resistivity distributed over 21 layers. Then, these original resistivity values are taken logarithmically and standardized as following equation (Xu et al., 2015; 2017; Equation 11):

$$\rho_{DCRi} = \frac{\log_{10}(\rho_i) - \mu \log_{10}(\rho_i)}{\sigma \log_{10}(\rho_i)} \quad \text{Equation (11)}$$

$\rho_{DCRi}$  is the reduced centered resistivity, and  $\mu \log_{10}(\rho_i)$  the average of the log10 of the original resistivity, and  $\sigma \log_{10}(\rho_i)$  is the standard deviation of the log10 of the

original resistivity.

To perform HAC, the resistivity data assigned to blocks are arranged in a matrix with the number of rows equal to the number of blocks and the number of columns equal to the number of surveys. The results are generally summarized in a dendrogram, where the number of clusters to retain the  $\rho_{DCRi}$  resistivity measurements can be selected. We choose the Euclidean distance and the Ward linkage criterion for the HAC analysis methods, which allow clusters to be formed such that the sum of squares of pooling within clusters is minimized.

### **3.4 Determination of depth and location of dripping stations by magnetic field angle (MFA) method**

A magnetic field is generated by passing current through one coil, which in turn induces a current in a second coil held at a distance (Figure 3.6). The extremely small current induced in the second coil is then amplified by a receiver and used to create sound in a set of headphones. This technique, known as cave radiolocation, can be used to determine the surface location and depth of a cave passage with a reasonable degree of accuracy, depending on the depth of the passage.

Under ideal conditions with a leveled antenna and an experienced operator, an x-y accuracy at the ground level of 1 meter for a 50-meter depth (2%) and a depth accuracy of approximately 5% can be achieved. However, errors in measurement increase with the angle of tilt of the antenna. For instance, a 5-degree tilt of the antenna can induce additional errors of 3%.





*Figure 3. 6 The transmission beacon transmits at 3496 Hz. The coil (red solenoid) produces the magnetic field generated by the oscillator (center). The power supply is a 4-cell 5Ah Ph. D.C. LiPo battery. The receiving equipment, including the receiver, the antenna, the high impedance headphones, the Palm which runs the Radioloc 3D application, and the DistoX for measuring the field angle Ph. D.C from Daniel Chailloux.*

To determine the depth of the dripping stations, we utilized the magnetic field angle method as shown in [Figure 3.7](#). Moving away from Ground Zero (GZ) along a previously set up line with the receiver loop held horizontally, we obtained a null signal at a point where the magnetic field is parallel to the ground surface. The receiver loop was equipped with a clinometer or spirit level to ensure it was held horizontally. The depth was then calculated using Equation 13 ([Figure 3.7](#)), as proposed by [Gibson \(1996\)](#) and [Chailloux \(2021\)](#):

$$\text{Depth (D)} = \frac{L1}{\sqrt{2}} \quad \text{Equation (12)}$$

L1: the distance between GZ and the point of  $\alpha_1$

At any other null angle,  $\alpha_2$  on the profile view, the depth may be calculated from the general equation ([Equation 13; Figure 3.7](#)):

$$\text{Depth (D)} = \frac{2 L2}{\sqrt{(9 \text{tg}^2 \alpha_2 + 8) - 3 \text{tg} \alpha_2}} \quad \text{Equation (13)}$$

Note: L2 is the distance between GZ and the point of  $\alpha_2$ , and Alpha angle ( $\alpha$ ) is

referenced to the horizontal surface of the ground.  $\alpha = 0^\circ$  when the loop antenna is flat on the ground.  $\alpha = 90^\circ$  when the loop antenna is vertical.

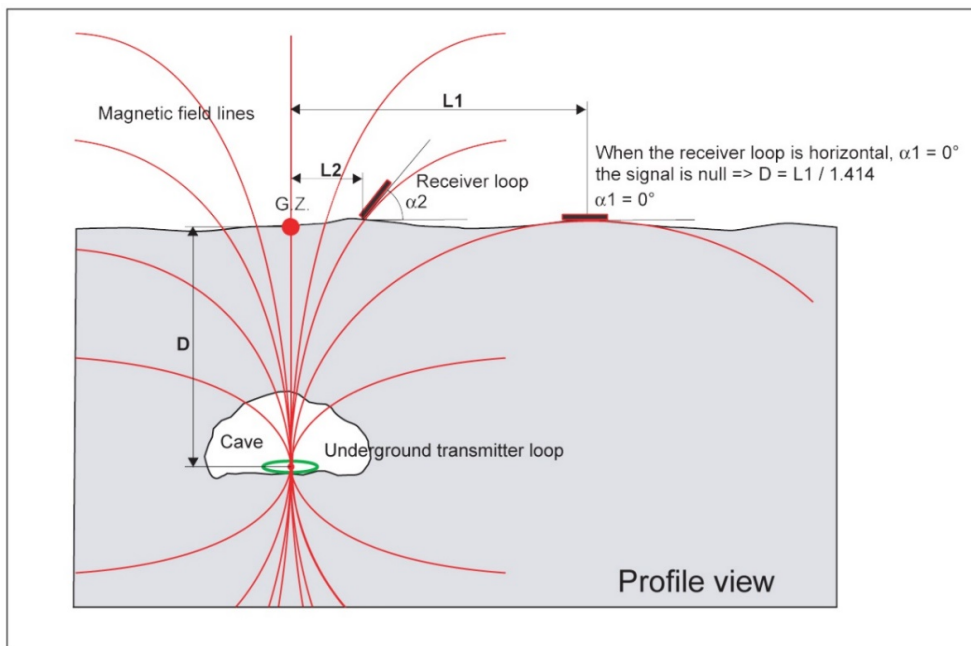


Figure 3. 7 Schematic diagram of depth calculation principle from Daniel Chailloux.

We calculated the depth of the Vil-#10A station (upper cave gallery), which is 14 m below the surface. The depth of the Vil-#1B & Vil-#3 stations (lower cave gallery), which are located at a depth of 36 m below the surface (Figures 2.5& 3.7 & Table 3.2). The position of Vil-#10A is 4.3 m away from the slope of ERT. However, the position of Vil-#1B and Vil-#3 is about 100 m from the profile of ERT (Figures 2.1C& 2.5).

Table 3. 2 Calculate the depth in station Vil-#10A and station Vil-#1B

Station Vil-#10A			Station Vil- #1B		
Distance (L)	Angle Alpha ( $\alpha$ )	Depth	Distance (L)	Angle Alpha ( $\alpha$ )	Depth
4 m	66.8°	14.55 m	10 m	66.4°	35.73 m
5 m	60.9°	14.35 m	15 m	56.4°	36.91 m
7 m	50.9°	14.60 m	20m	47.7°	36.29 m
9 m	39.5°	14.02 m			
Depth: 14.38 m $\pm$ 0.23 m (2%)			Depth: 36.31 m $\pm$ 0.48 m (1%)		

### 3.5 Complementarity of the different methods

By testing and validating ERT/hydrology/isotope methods in a specific site (Villars Cave) developed in a karst area (Villars Cave), we can deepen our understanding of this particular site and its hydrological behavior, which may be similar to other caves in the region. This can help to improve our understanding of the hydrogeological and hydrological processes in the karst environment and improve our ability to manage and protect these sensitive karst environments.

(1) All the methods are summarized as the following (Figure 3.8):

i) local meteorological data are used to calculate the water excess (efficient rainfall) which is significant for the interpretation of cave drip rate variations and their isotopic compositions;

ii) stable isotopes from rainfall and cave dripping stations are used with the dripping rates and rainfall quantity to model the infiltration;

iii) ERT images are used for the determination of the reservoirs (number, position, depth, size) and for their changes in their water saturation that can be put in relation to the drip rate changes and the water- excess data.

(2) Links in different methods-ERT/Hydrology/Isotope:

i) by comparing the seasonal signal variation of ERT with rainfall data (input) and dripping rate data (output), we can estimate the inertia of the reservoirs and understand how drip rates respond to rainfall changes.

ii) by analyzing isotopic variations between rainfall and dripping stations and develop models to simulate infiltration using both isotopic and flow rate signals. To do this, we use the KarstFor isotopic model to simulate its variabilities.

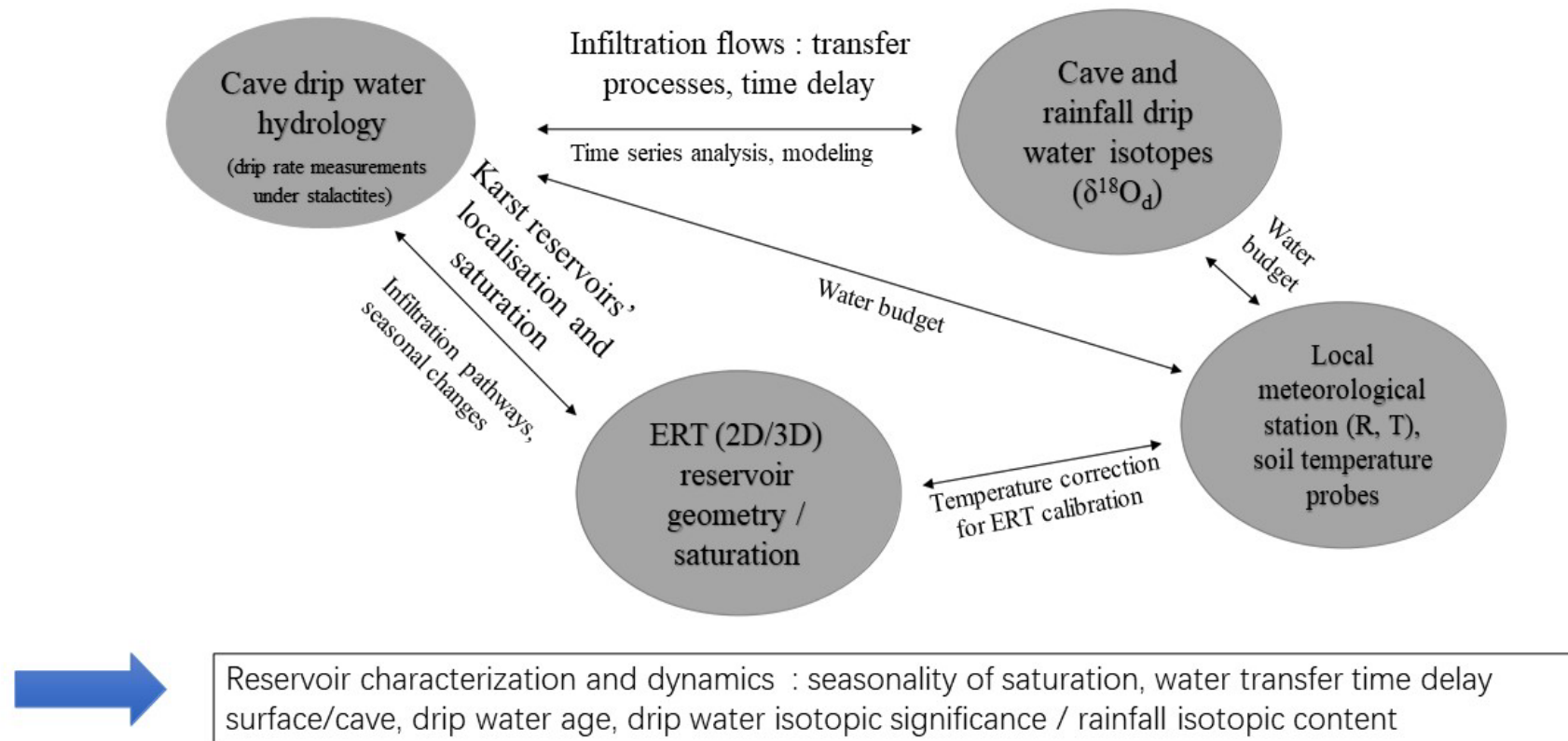


Figure 3. 8 A summary figure that illustrates what has been gleaned from this combination of ERT, long-term monitoring, and modeling to underscore the benefit of this approach.

# **Chapter 4 - Origins of precipitation isotopic signature in Villars**

---

## Introduction

Because rainfall oxygen isotopes are the main source of speleothem oxygen isotopes, understanding their origin is of first importance. Our study, in this section, aims to combine rainfall  $\delta^{18}\text{O}_p$  data with information on moisture sources and regional/local climatic parameters to investigate variations in initial moisture sources.

In Southwest France (SW-France), there are very few published data concerning stable isotopes of precipitation, especially for long time-series (i.e., >20 years). Here we use two important rainfall stations, Le Mas and Villars sites both located in the Dordogne area separated by about 30km, that have been monitored since 1996 ([Genty et al., 2014a](#)). The isotopic composition of the rainfall collected in these stations have been extensively used for the understanding of speleothem deposits from the Villars Cave ([Genty et al., 2001](#); [Genty et al., 2006](#); [Genty et al., 2014a](#); [Genty, 2008](#)). But it appears that this area is a key place for studying the moisture pathway from the North Atlantic and the Mediterranean across the European continent ([Duffourg and Ducrocq, 2011](#)), and our long-term observations for rainfall  $\delta^{18}\text{O}$  as input as well as its environment parameters allow us to confidential understand the local hydrological cycle and climate change.

However, there are still questions about the stable isotopic compositions of rainfall in SW-France, as for example: (1) there are still unclear relationships and mechanisms between initial moisture sources and local rainfall  $\delta^{18}\text{O}_p$  on the monthly and inter-annual timescales. (2) there are still unquantified links between  $\delta^{18}\text{O}_p$  and various controlling factors like temperature, rainfall and moisture source.

In the article presented below, we combined rainfall  $\delta^{18}\text{O}_p$  with data of moisture sources and regional/local climatic parameters. In this way, we aim to determine the

variation of initial moisture sources and their relation to stable isotopic compositions of rainfall in Southwest France using the Hybrid Single-Particle Lagrangian Integrated Trajectory (HYSPLIT) model.

**Article 1:** Zhang, J., Genty, D., Sirieix, C., Michel, S., Minster, B., & Régnier, E. (2020). **Quantitative assessments of moisture sources and temperature governing rainfall  $\delta^{18}\text{O}$  from 20 years' monitoring records in SW-France: Importance for isotopic-based climate reconstructions.** *Journal of Hydrology*, 591, 125327.4.4

## Abstract

In the mid-high latitude region, variations of stable isotopic compositions of atmospheric precipitation ( $\delta^{18}\text{O}_p$  and  $\delta\text{D}_p$ ) were commonly regarded as reflecting the “temperature effect”. However, some studies have indicated that changes in moisture sources are important controlling factors for  $\delta^{18}\text{O}_p$ . To clarify whether there are connections between  $\delta^{18}\text{O}_p$  and variations of moisture sources in Southwest France (SW-France), whose implications for speleothem  $\delta^{18}\text{O}$  are of great importance, we have used among the longest isotopic time-series from SW-France (Le Mas and Villars stations) and a 5 days’ reconstruction of air mass history during the 1997–2016 A.D period based on the HYSPLIT tracking model. We found the percentage of initial moisture sources (PIMS) as important factors controlling the oxygen isotope composition of precipitation in SW-France, whether monthly or inter-annual timescale was considered. Additionally, we observed that the  $\delta^{18}\text{O}_p$  preserved the signal of local temperature, supporting the “temperature effect”, while no evidence for its “amount effect” has been observed. These quantified links between PIMS/local-temperature and  $\delta^{18}\text{O}_p$  appear useful references to understand the link between stable oxygen isotopes and climate parameters. Our long-term monitoring of  $\delta^{18}\text{O}_p$ , d-excess, and moisture sources reveals decadal trends, highlighting a tight coupling in hydrologic systems and relatively fast changes on rainfall sources controlled by atmospheric circulations in SW-France.



## 4.1 Results

### 4.1.1 Relationship between $\delta^{18}\text{O}_p$ and local/regional climate parameters

The correlation of the  $\delta^{18}\text{O}_p$  between Villars and Le Mas stations is 0.72 ( $p < 0.01$ ) (Figures 4.1A&4.1B), suggesting that both were controlled by the same air masse and climate. Local meteoric water line (LMWL) in the two monitoring sites is defined by:  $\delta\text{D}_p = 6.91 \cdot \delta^{18}\text{O}_p + 3.02$  ( $p < 0.01$ ) for Le Mas and  $\delta\text{D}_p = 7.08 \cdot \delta^{18}\text{O}_p + 5.03$  ( $p < 0.01$ ) for Villars (Figure 4.1C). In order to verify the reliability of LMWL equation, we also used other different methods, including ordinary least squares regression (OLSR) and precipitation weighted least squares regression (PWLSR) (Hughes and Crawford, 2012; Crawford et al., 2014).

Whether weighted or non-weighted regression was considered, close slope and gradient values were observed from three methods (Table 4.1). Rainfall stable isotopes are characterized by strong seasonal variations with depleted average values in winter months (December, January, February:  $-43.2\text{‰}$  to  $-47.7\text{‰}$  for  $\delta\text{D}_p$  and  $-6.9\text{‰}$  to  $-7.5\text{‰}$  for  $\delta^{18}\text{O}_p$ ) and enriched average values during summer months (June, July, August:  $-27.8\text{‰}$  to  $-31.5\text{‰}$  for  $\delta\text{D}_p$  and  $-4.6\text{‰}$  to  $-5.1\text{‰}$  for  $\delta^{18}\text{O}_p$ ) (Appendix Table 1).

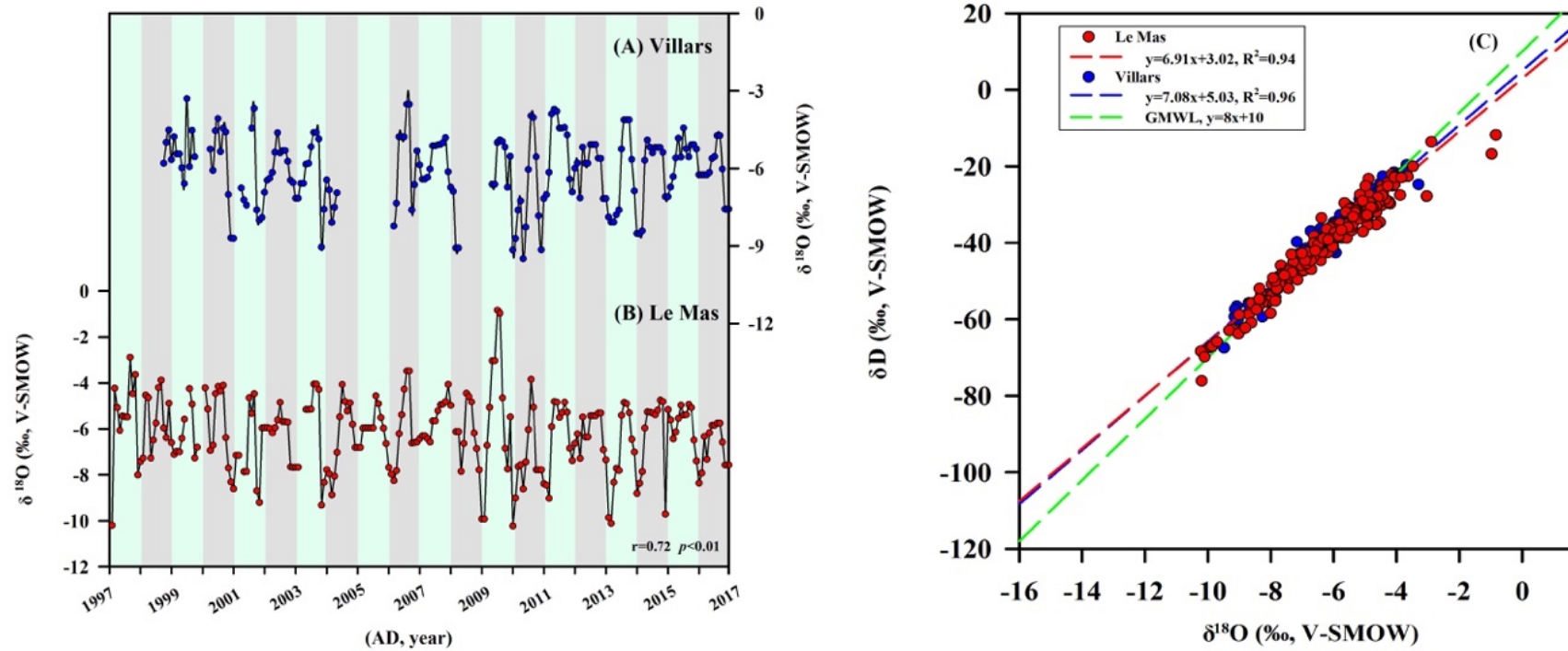


Figure 4. 1 Time series of monthly rainfall  $\delta^{18}\text{O}_p$  at Villars (A) and Le Mas (B) stations. (C) Local meteoric water line (LMWL) for Le Mas (red), and Villars (blue) based on the linear regression. The Global Meteoric Water Line (GMWL) in green (Craig, 1961) is plotted for comparison.

On a monthly timescale,  $\delta^{18}\text{O}_p$  and local temperature show a positive correlation at Villars ( $R=0.61$ ,  $p<0.0001$ ) and Le Mas ( $R=0.62$ ,  $p<0.0001$ ) for the considered period (1996-2016) (Figure 4.2A) with a  $T$ - $\delta^{18}\text{O}_p$  gradient of  $0.17\text{‰}/^\circ\text{C}$  and  $0.15\text{‰}/^\circ\text{C}$  respectively. This indicates that the  $\delta^{18}\text{O}_p$  in SW-France is mainly affected by local temperature. Compared with observed (Fricke and O'Neill, 1999; Alley and Cuffey, 2001) and modelled (Jouzel et al., 1997; Schmidt et al., 2007)  $T$ - $\delta^{18}\text{O}_p$  gradient over the global-scale, ranging from  $0.17\text{‰}/^\circ\text{C}$  to  $0.9\text{‰}/^\circ\text{C}$ , the  $T$ - $\delta^{18}\text{O}_p$  gradient in the Le Mas and Villars stations are close to the lowest values. On the contrary,  $\delta^{18}\text{O}_p$  and local precipitation do not exhibit a significant correlation:  $R=0.19$  at Le Mas and  $R=0.29$  at Villars, with a gradient of  $-0.7\text{‰}/100\text{mm}$  and  $-0.8\text{‰}/100\text{mm}$ , respectively (Figure 4.2B).

In order to assess local  $\delta^{18}\text{O}_p$  records in SW-France whether or not can be sensitive to regional parameters variations, correlations between  $\delta^{18}\text{O}_p$  from Le Mas and Villars stations and European temperatures with  $5^\circ \times 5^\circ$  global grids were calculated on the seasonal timescale for the 1996-2016 period. Results show that significant correlations are mostly found for winter (DJF) and spring (MAM) (Figures 4.3A, 4.3B, 4.3E, 4.3F). At Le Mas station, the time-series of  $\delta^{18}\text{O}_p$  displays positive correlation with Northern Europe temperatures and negative ones with the temperature of South Europe and Mediterranean area (Figures 4.3A). A similar pattern also occurs for the Villars station, although these correlations are weaker (Figures 4.3E) possibly due to a lack of some monthly data in Villars (Figures 4.3E; Appendix data). Moreover, during spring (MAM), the correlation of  $\delta^{18}\text{O}_p$  and regional temperature shows positive (Northwest Europe) and negative (North Africa and Mediterranean area) relationships at both stations (Figures 4.3B & 4.3F). Unlike the high correlation between local temperature and  $\delta^{18}\text{O}_p$  on all months, this regional relationship is only reflected in winter and spring (Figures 4.3A & 4.3B).

Table 4. 1. Parameters of the fitting for LMWL, OLSR and PWLSR methods for Le Mas and Villars, SW-France and then for all stations (The method refer to [Hughes and Crawford, 2012](#)).

		N	a	SD	b	SD	$r^2$
Le-Mas	LMWL	239	6.91	0.12	3.02	0.74	0.94
	OLSR	239	6.95	0.11	3.35	0.73	0.94
	PWLSR	239	6.96	0.11	3.52	0.74	0.94
Villars	LMWL	179	7.08	0.1	5.03	0.64	0.96
	OLSR	179	7.06	0.1	4.93	0.63	0.96
	PWLSR	179	7.01	0.1	4.67	0.67	0.96

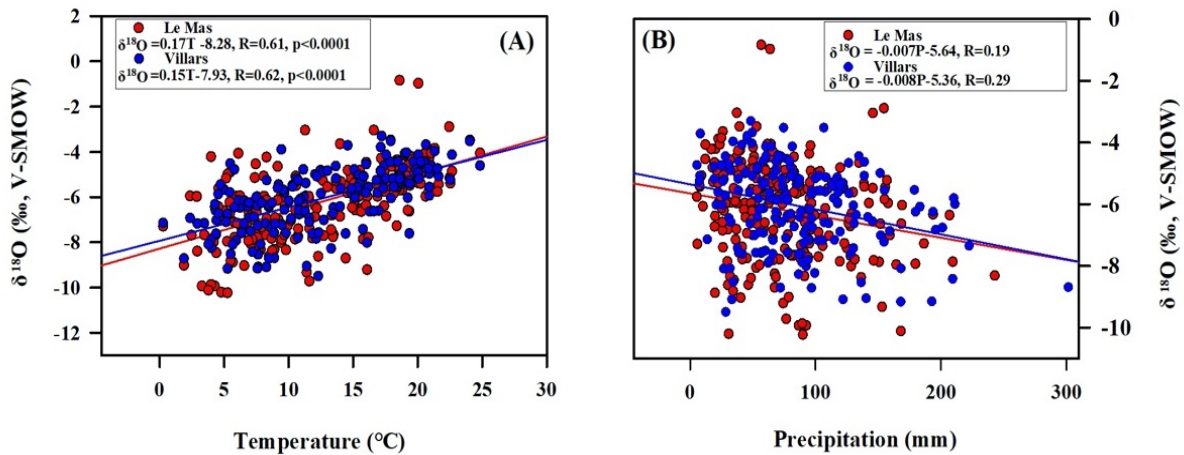


Figure 4. 2 (A) Correlation between  $\delta^{18}O_p$  and local monthly temperature for the 1997-2016 period. (B) Correlation between  $\delta^{18}O_p$  and local monthly precipitation for the 1997-2016 period.

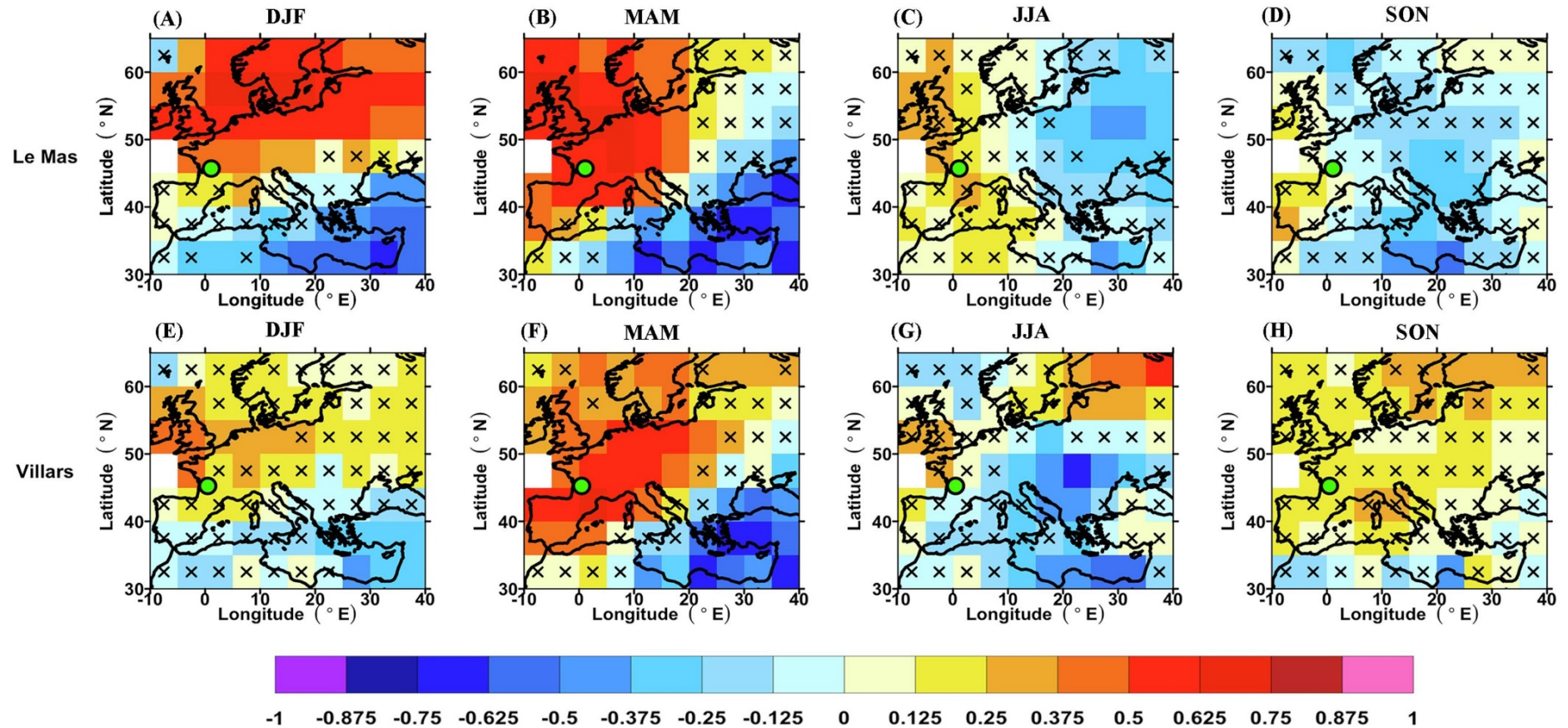


Figure 4. 3 Seasonal correlation maps between  $\delta^{18}\text{O}_p$  from Le Mas (top panel) and Villars (bottom panel) and temperatures over Europe during the period of 1997-2016 (Some disconnected data is not considered). (A, E) DJF, (B, F) MMA, (C, G) JJA, (D, H) SON. Black crosses indicate grid points where the correlation is not significant at the 90% confidence level. However, the discontinuities of  $\delta^{18}\text{O}_p$  data were excluded in some years ([Appendix data](#)). The figure was produced using the programming language R.

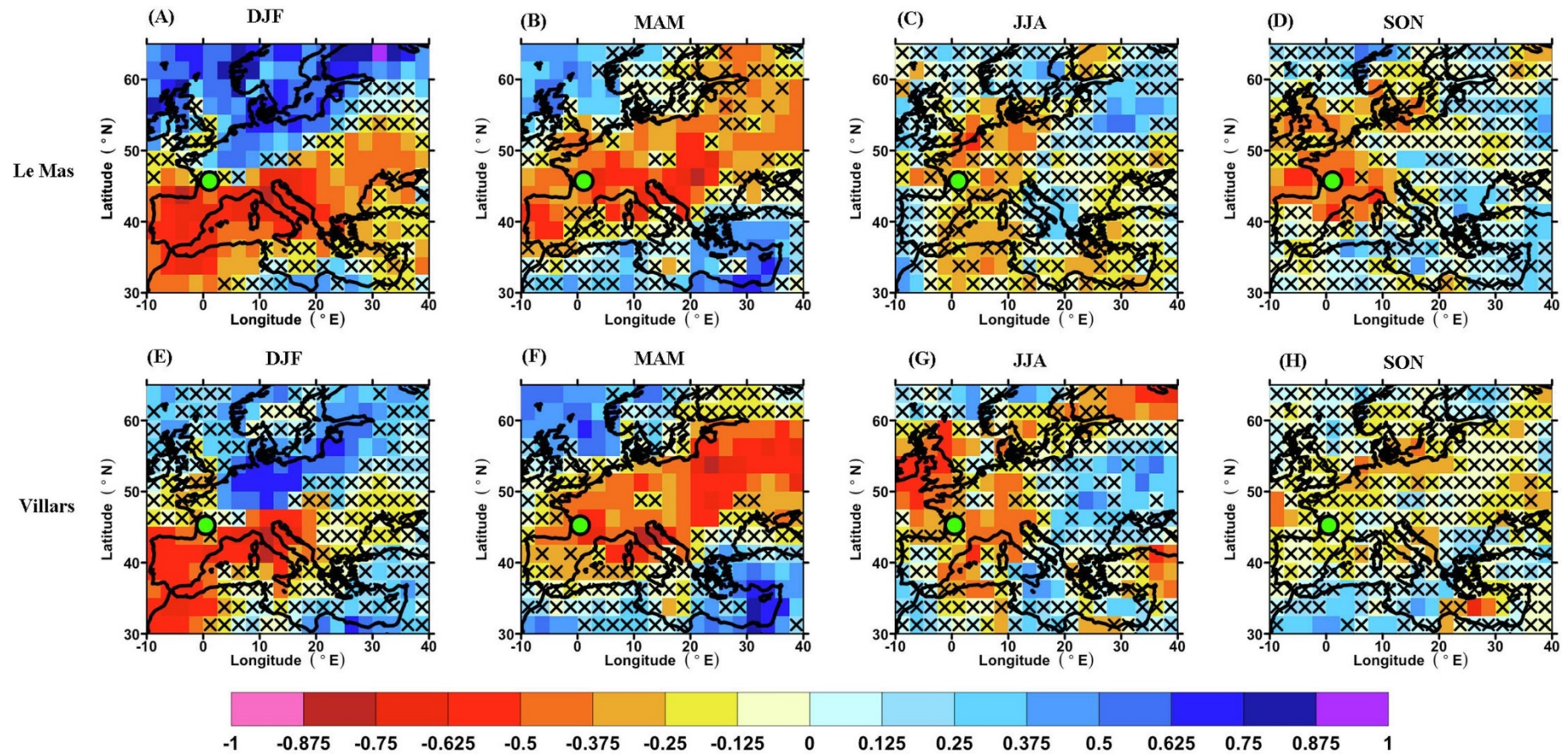


Figure 4. 4 Seasonal correlation maps between  $\delta^{18}O_p$  from Le Mas (top panel) and Villars (bottom panel) and precipitation over Europe during the period of 1997–2016 (Some disconnected data is not considered). (A, E) DJF, (B, F) MMA, (C, G) JJA, (D, H) SON. Black crosses indicate grid points where the correlation is not significant at the 90% confidence level. However, the discontinuities of  $\delta^{18}O_p$  data were excluded in some years ([Appendix data](#)). The figure was produced using the programming language R.

The relationship between regional precipitation and  $\delta^{18}\text{O}_p$  for all the seasons was also considered (Figures 4.4). Despite the globally much weaker correlations, we observe that, in winter, regional precipitation with  $2.5^\circ \times 2.5^\circ$  global grids and  $\delta^{18}\text{O}_p$  shows a similar spatial pattern between regional temperature and  $\delta^{18}\text{O}_p$  (Figures 4.3A and 4.3E, 4.4A and 4.4E). During spring (MAM), the link between  $\delta^{18}\text{O}_p$  and regional precipitation shows a positive pattern with North Europe and North African and Mediterranean Sea and a negative one all over the European continent (Figures 4.4B and 4.4F). During summer (JJA) and autumn (SON) seasons, no or less significant correlations were observed between temperature/precipitation and  $\delta^{18}\text{O}_p$  for both stations (Figures. 4.3C, 4.3D, 4.3G, 4.3H, 4.4C, 4.4D, 4.4G, 4.4H).

The degrees of freedom corrections were calculated between the two 20-year time-series of  $\delta^{18}\text{O}_p$  from SW-France (Le Mas and Villars) and the Atlantic SST with  $5^\circ \times 5^\circ$  global grids (Figure 4.5). The results show that  $\delta^{18}\text{O}_p$  values are positively correlated with SST in the Gulf Stream of Mexico (Figures 4.5B, 4.5F), and opposite to SST in northern and southern of North Atlantic, inducing a tripolar SST distribution in the North Atlantic in spring. However, during other seasons, no or less significant correlations were observed between SST and  $\delta^{18}\text{O}_p$  for both stations (Figure 4.5A, 4.5C, 4.5D, 4.5E, 4.5G, 4.5H).

Note that whether we consider the pattern of  $\delta^{18}\text{O}_p$  and European temperature or precipitation in Le Mas and Villars stations in winter and spring, it is similar to the spatial pattern between NAO phase and European temperature and precipitation (Cassou et al., 2004; Baldini et al., 2008; Figures 4.3A, 4.3E, 4.4A, 4.4E). The link between NAO index and  $\delta^{18}\text{O}_p$  seems to be confirmed by their high correlations ( $p < 0.01$  or  $p < 0.05$ ) in winter ( $R=0.45$  and  $R=0.42$ ) and spring ( $R=0.33$  and  $R=0.36$ ) (Figures 4.6A, 4.6B, 4.6C, 4.6D).

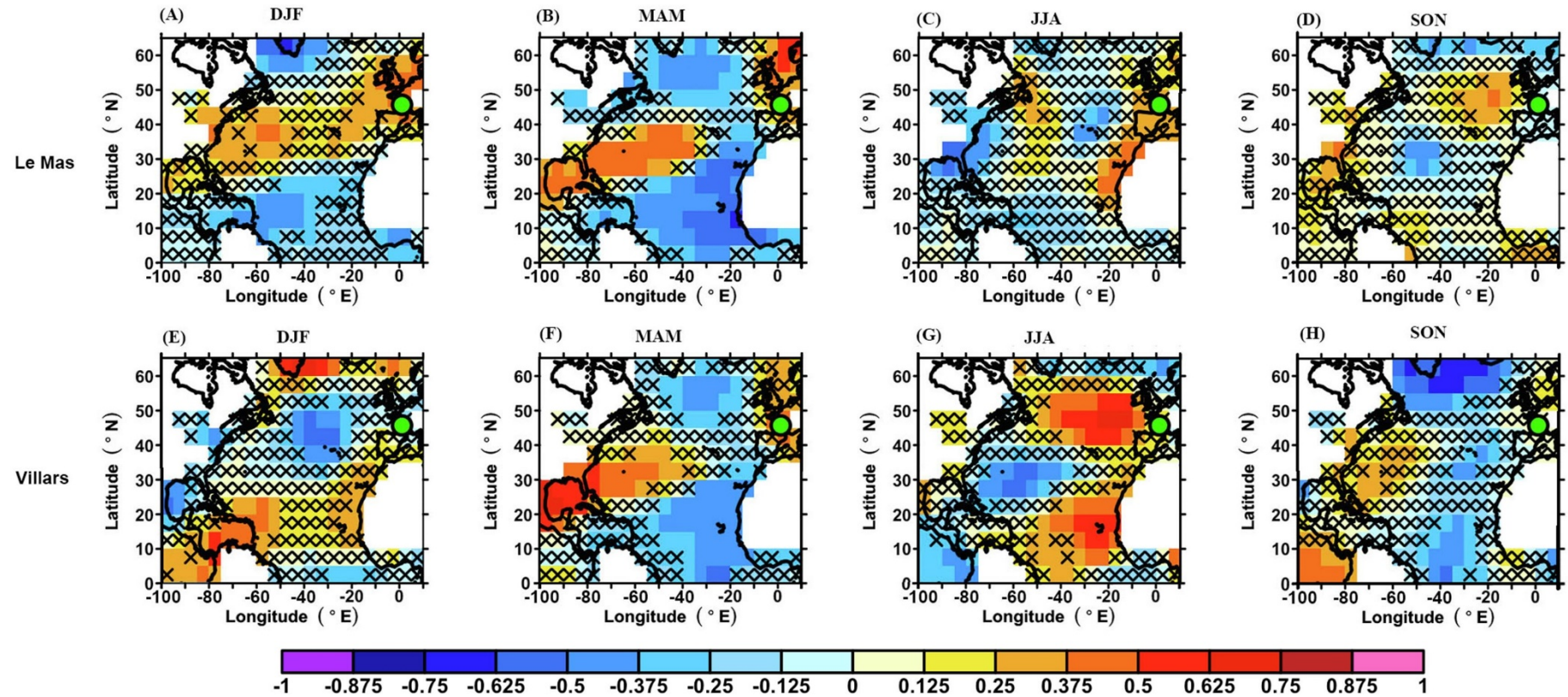


Figure 4. 5 Seasonal correlation maps between  $\delta^{18}\text{O}_p$  from Le Mas (top panel) and Villars (bottom panel) stations and SST in North Atlantic during the 1997–2016 period (Some disconnected data is not considered). (A, E) DJF, (B, F) MMA, (C, G) JJA, (D, H) SON. Black crosses indicate grid points where the correlation is not significant at the 90% confidence level. However, the discontinuity of  $\delta^{18}\text{O}_p$  data were excluded in some years (Appendix data). The figure was produced using R programming language. The degrees of freedom corrections were calculated by time-series autocorrelations (McCarthy et al., 2015).



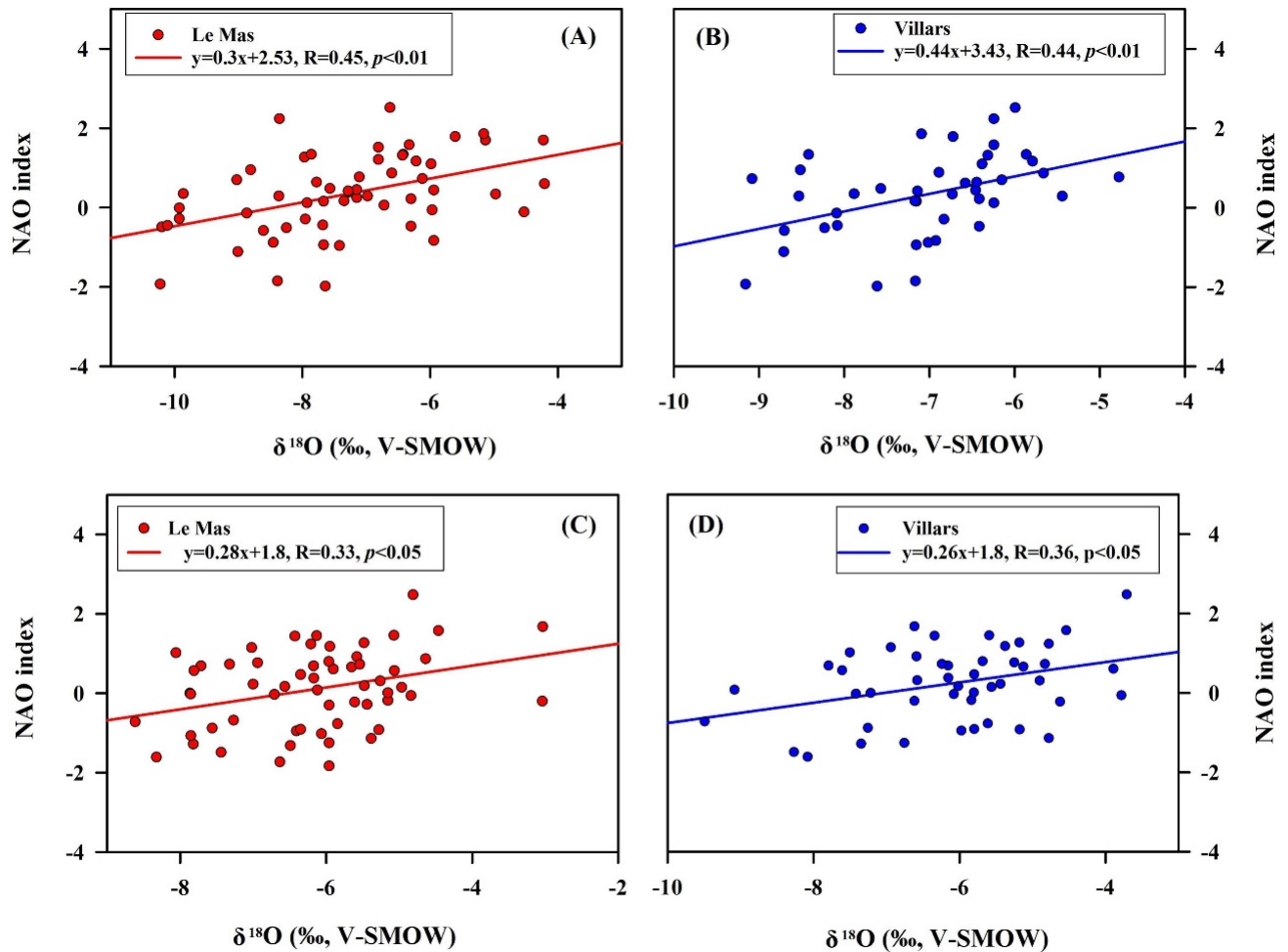


Figure 4.6 Correlation between  $\delta^{18}\text{O}_p$  and NAO index at Le Mas and Villars (A) Correlation between  $\delta^{18}\text{O}_p$  and NAO index at Le Mas during the winter period of 1997–2016. (B) Correlation between  $\delta^{18}\text{O}_p$  and NAO index at Villars during the winter period of 1997–2016. (C) Correlation between  $\delta^{18}\text{O}_p$  and NAO index at Le Mas during the spring period of 1997–2016. (D) Correlation between  $\delta^{18}\text{O}_p$  and NAO index at Villars during the winter period of 1997–2016.

#### 4.1.2 Relationship between $\delta^{18}\text{O}_p$ and initial moisture source on a monthly timescale

In order to localize the moisture sources of the rainfall (the percentage of initial moisture, PIMS) that occur above Villars's station, we first used the HYSPLIT software for periods of high (summer) and low (winter)  $\delta^{18}\text{O}_p$  (Figure 4.7). Results show a clear seasonal variability in the back trajectories with a much longer pathway in December, January and February compared to the summer months (June, July and August)

(Figure 4.7). During winter, some vapor sources reach areas clearly beyond the 60° W meridian, while in summer the extreme west source is significantly closer to Villars, around the extreme east of Canada (Figures 4.7D, 4.7E, 4.7F). But when replaced in the spatial pattern of Figure 1, and looking at the actual percentages given by the software calculation (Table 4.2), then it appears that water vapor source in winter is mostly distributed in the region of NAGR (West North Atlantic: North America and Greenland) characterized by a longer transportation (Table 4.2; Figures 4.7A, 4.7B, 4.7C), while, in summer, it is mostly from the closest source (PAWE: Proximal Atlantic and West Europe) (Table 4.2; Figures 4.7D, 4.7E, 4.7F).

These results show that the sources (characterized by the PIMS) and rainfall  $\delta^{18}\text{O}_p$  in SW-France are characterized by a well-marked seasonality: negative  $\delta^{18}\text{O}_p$  excursions occur in winter when there is the longer initial moisture location (e.g., NAGR) (Table 4.2; Figures 4.7A, 4.7B, 4.7C). On the contrary, the  $\delta^{18}\text{O}_p$  in summer shows a positive  $\delta^{18}\text{O}_p$  excursion, which coincides with the closer initial moisture location (e.g., PAWE) (Table 4.2; Figures 4.7D, 4.7E, 4.7F).

During spring and autumn, there is no obvious contrasted PIMS (Figure 4.8). We note however that PIMS in the near summer months (e.g., May and September) is derived from the increased closer moisture source (PAWE), and decreased longer moisture source (NAGR), corresponding to heavier values of  $\delta^{18}\text{O}_p$  and  $\delta\text{D}_p$  (Table 4.2 and Appendix Table 2; Figure 4.8C, 4.8D). In contrast, in the near winter months (e.g., March and November), PIMS from the closer source (e.g., PAWE) is decreased, and longer sources is increased (e.g., NAGR) (Table 4.2; Figures 4.8A, 4.8F), which indicates that the change of PIMS can regulate the  $\delta^{18}\text{O}_p$  on the monthly timescale in SW-France.

**Table 4. 2** Variation of monthly PIMS for Le-Mas and Villars for all months of the year for 1997-2016 period.

	Months	PAWE	NA	ME	DA	NAGR	NENA
	Dec	23%	0%	5%	24%	<b>44%</b>	0%
Winter	Jan	26%	14%	0%	5%	<b>55%</b>	0%
	Feb	19%	6%	0%	23%	<b>53%</b>	0%
	Mar	14%	17%	12%	12%	44%	0%
Spring	Apr	27%	25%	0%	15%	18%	0%
	May	50%	24%	0%	21%	4%	0%
	Jun	<b>50%</b>	19%	0%	21%	9%	0%
Summer	Jul	<b>50%</b>	35%	0%	0%	13%	0%
	Aug	<b>51%</b>	24%	0%	10%	15%	0%
	Sep	60%	6%	0%	3%	32%	0%
Autumn	Oct	34%	15%	0%	13%	39%	0%
	Nov	0%	14%	9%	22%	54%	0%

*Note: The proportion of three trajectories varies between 99% and 101%, which is attributed to software error.*

These results highlight the close relationships between PIMS and  $\delta^{18}\text{O}_p$  values at Villars (and Le Mas). A high PIMS from closer regions (e.g., PAWE and NA) is related to heavier  $\delta^{18}\text{O}_p$  values while high PIMS from farther regions (e.g., NAGR) is related to lower  $\delta^{18}\text{O}_p$  values (Table 4.2; Appendix Table 2). Linear equations have been established, for Le Mas and Villars stations, to quantify the relationship between  $\delta^{18}\text{O}_p$  and PIMS (Table 4.3). Results show a positive relationship ( $p < 0.01$  or  $p < 0.05$ ) between  $\delta^{18}\text{O}_p$  and PIMS in the region of PAWE and NA, and a negative relationship ( $p < 0.01$ ) between  $\delta^{18}\text{O}_p$  and PIMS in the region of NAGR, whereas the rest of the regions (ME and DA) have much less impact on  $\delta^{18}\text{O}_p$  values (Table 4.3).

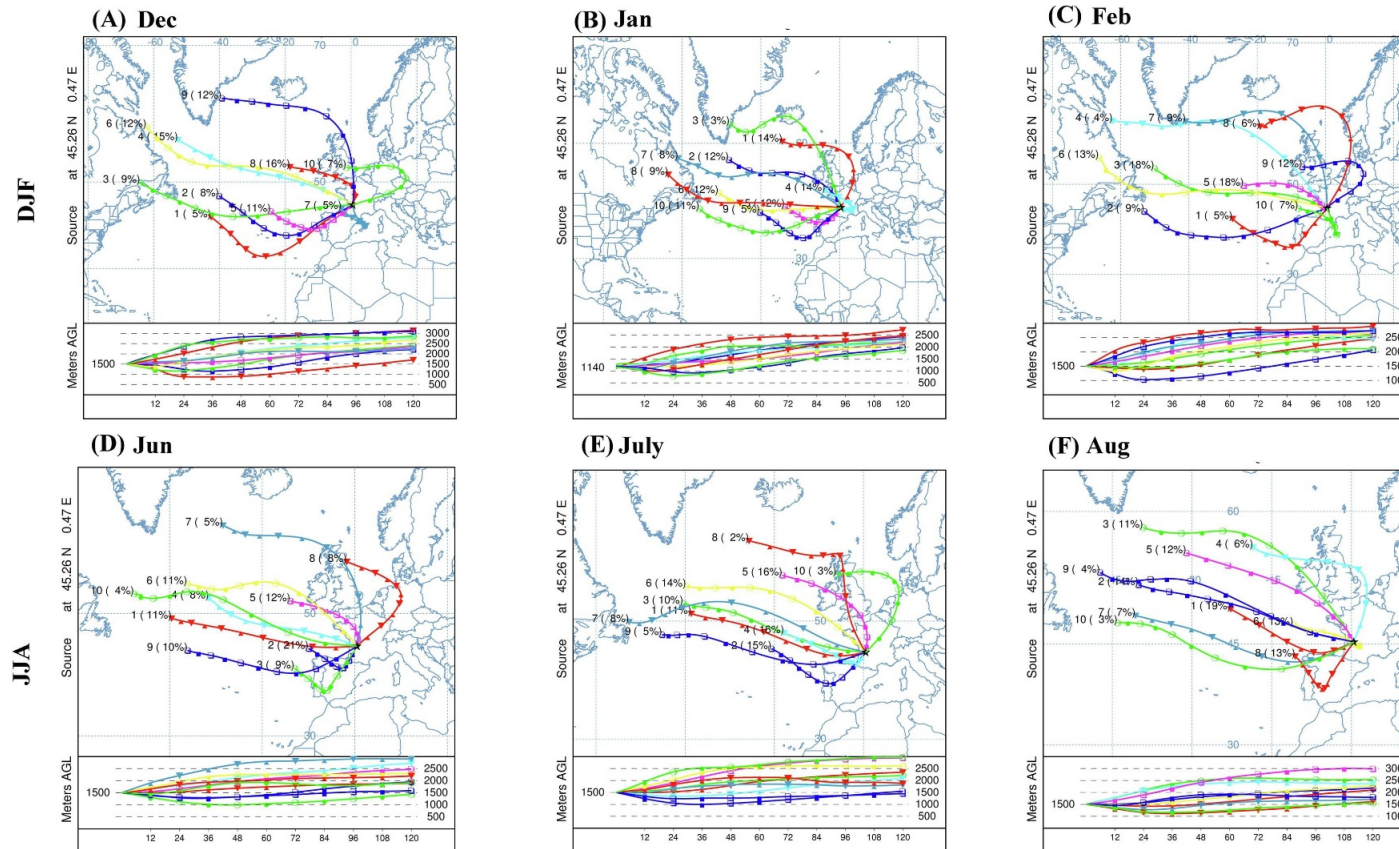


Figure 4. 7 Back trajectories for contrasted seasons, winter (December (A), January (B), February (C)) and summer (June (D), July (E), August (F)). The star indicates the location of Villars, and the detailed data of PIMS are listed in Table 2. The air mass history was calculated at 1500 m a.g.l over the past 120 h, and every 6 h outputted a trajectory, then we integrated all of calculated data into ten trajectories. The back trajectories are presented for monthly variations for the period of 1997–2016.

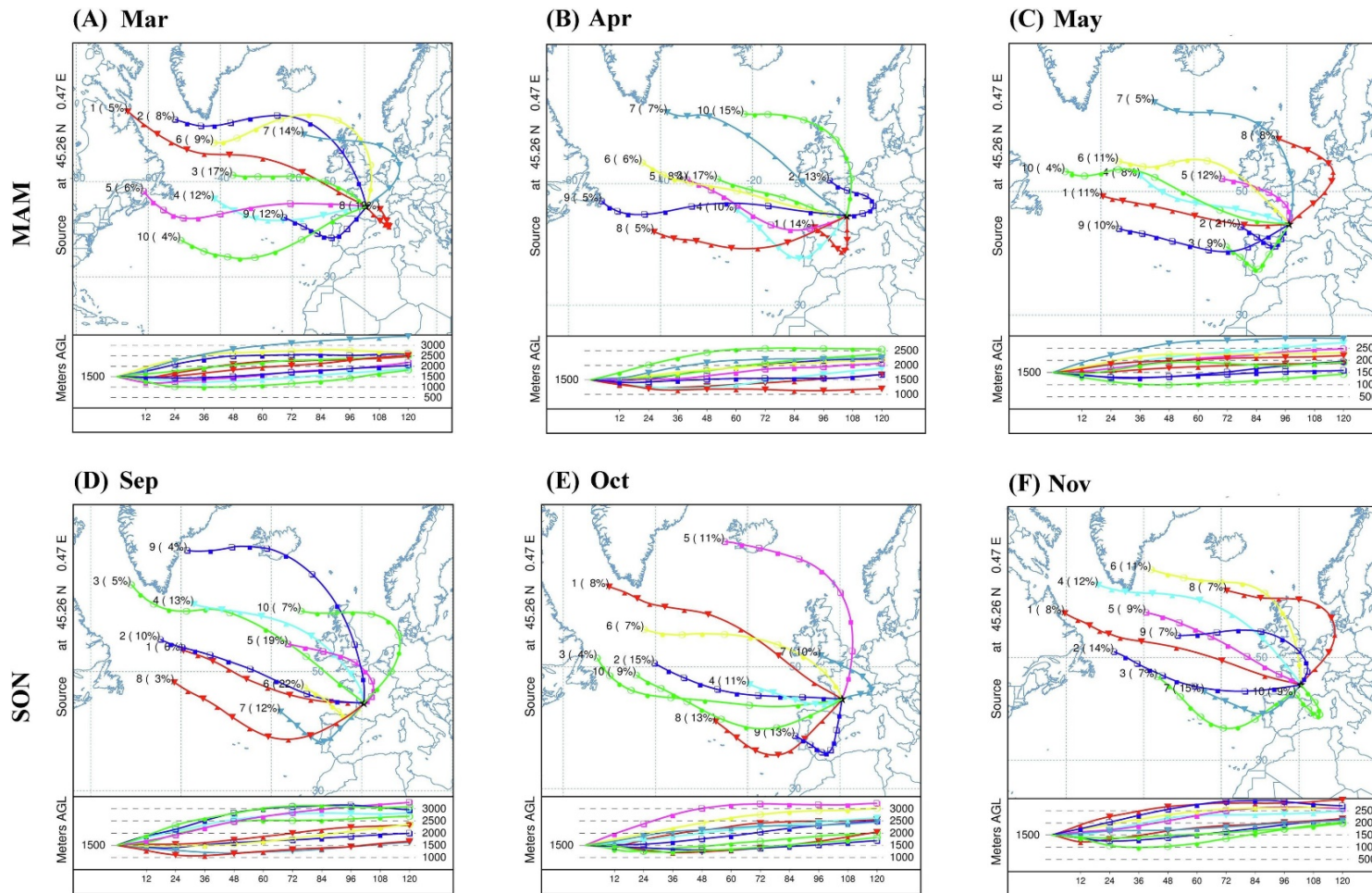


Figure 4. 8 Back trajectories for March (A), April (B), May (C), September (D), October (E) and November (F). The star indicates the location of Villars, and the detailed data of moisture source is listed in Table 1. The air mass history was calculated at 1500 m a.g.l over the past 120 hours, and every 6 hours outputted a trajectory, then we integrated all of the calculated data into ten trajectories.

Table 4. 3 Linear correlations between monthly  $\delta^{18}\text{O}_p$  with monthly PIMS and temperature.

	Le Mas	Villars
PAWE	$\delta^{18}\text{O}_p = 0.0427 \cdot \text{PAWE} - 7.6386$ , $R = 0.7653$ , $p < 0.01$	$\delta^{18}\text{O}_p = 0.0396 \cdot \text{PAWE} - 7.4094$ , $R = 0.8068$ , $p < 0.01$
NA	$\delta^{18}\text{O}_p = 0.0780 \cdot \text{NA} - 7.4936$ , $R = 0.7364$ , $p < 0.01$	$\delta^{18}\text{O}_p = 0.0633 \cdot \text{PAWE} - 7.1253$ , $R = 0.6795$ , $p < 0.05$
ME	$\delta^{18}\text{O}_p = -0.0940 \cdot \text{ME} - 5.9964$ , $R = 0.3827$	$\delta^{18}\text{O}_p = -0.0865 \cdot \text{ME} - 5.8876$ , $R =$ $0.4003$
DA	$\delta^{18}\text{O}_p = -0.0474 \cdot \text{DA} - 5.5318$ , $R = -0.3835$	$\delta^{18}\text{O}_p = -0.0509 \cdot \text{DA} - 5.3583$ , $R = -$ $0.4674$
NAGR	$\delta^{18}\text{O}_p = -0.0472 \cdot \text{NAGR} - 4.7043$ , $R = -$ $0.8684$ , $p < 0.01$	$\delta^{18}\text{O}_p = -0.0400 \cdot \text{NAGR} - 4.8079$ , $R = -0.8362$ , $p < 0.01$
Temperature	$\delta^{18}\text{O}_p = 0.17 \cdot \text{T} - 8.28$ , $R = 0.61$ , $p < 0.0001$	$\delta^{18}\text{O}_p = 0.15 \cdot \text{T} - 7.93$ , $R = 0.62$ , $p < 0.0001$

Table 4. 4 Variation of annual PIMS for Le-Mas and Villars stations based on the integration of annual trajectories.

Year	PAWE	NA	ME	DA	NAGR	NENA
1997	26%	26%	0%	21%	26%	0%
1998	28%	19%	0%	16%	37%	0%
1999	19%	12%	6%	8%	55%	0%
2000	29%	45%	8%	0%	18%	0%
2001	29%	20%	3%	17%	38%	0%
2002	33%	18%	0%	16%	27%	5%

2003	38%	11%	0%	18%	10%	8%
2004	12%	33%	9%	2%	42%	0%
2005	32%	14%	0%	0%	34%	19%
2006	24%	20%	4%	9%	42%	0%
2007	28%	17%	0%	14%	28%	13%
2008	27%	0%	5%	13%	56%	0%
2009	20%	0%	0%	37%	43%	0%
2010	26%	10%	0%	22%	43%	0%
2011	11%	13%	6%	32%	38%	0%
2012	24%	25%	0%	13%	39%	0%
2013	18%	10%	0%	32%	36%	4%
2014	23%	16%	0%	13%	45%	8%
2015	20%	12%	0%	26%	43%	0%
2016	11%	22%	0%	33%	34%	0%
Average	24%	17%	2%	17%	37%	3%

Note: The proportion of three trajectories varies between 99% and 101%, which is attributed to software error.

### 4.1.3 Relationship between $\delta^{18}\text{O}_p$ , d-excess and initial moisture source/local climate parameters on the annual and inter-annual timescale

On the annual timescale, a positive relationship ( $p < 0.05$ ), in both Le Mas and Villars stations, is observed between the annual average  $\delta^{18}\text{O}_p$  ( $\delta^{18}\text{O}_{ap}$ ) and annual mean temperature, with a  $T$ - $\delta^{18}\text{O}_{ap}$  gradient of  $0.42\text{‰}/^\circ\text{C}$  and  $0.51\text{‰}/^\circ\text{C}$ , respectively. These values fall in the range of gradients observed from global continental, marine and polar sites ( $0.17\text{‰}/^\circ\text{C}$  to  $0.9\text{‰}/^\circ\text{C}$ ; [Clark and Fritz, 1999](#); [Figures 4.9A, 4.9B](#)). At

the opposite,  $P\text{-}\delta^{18}\text{O}_{ap}$  gradients are low:  $-0.1\text{‰}/100\text{mm}$  and  $-0.07\text{‰}/100\text{mm}$  for Le Mas and Villars, and no significant correlation ( $p>0.1$ ) was observed (Figures 4.9C, 4.9D).

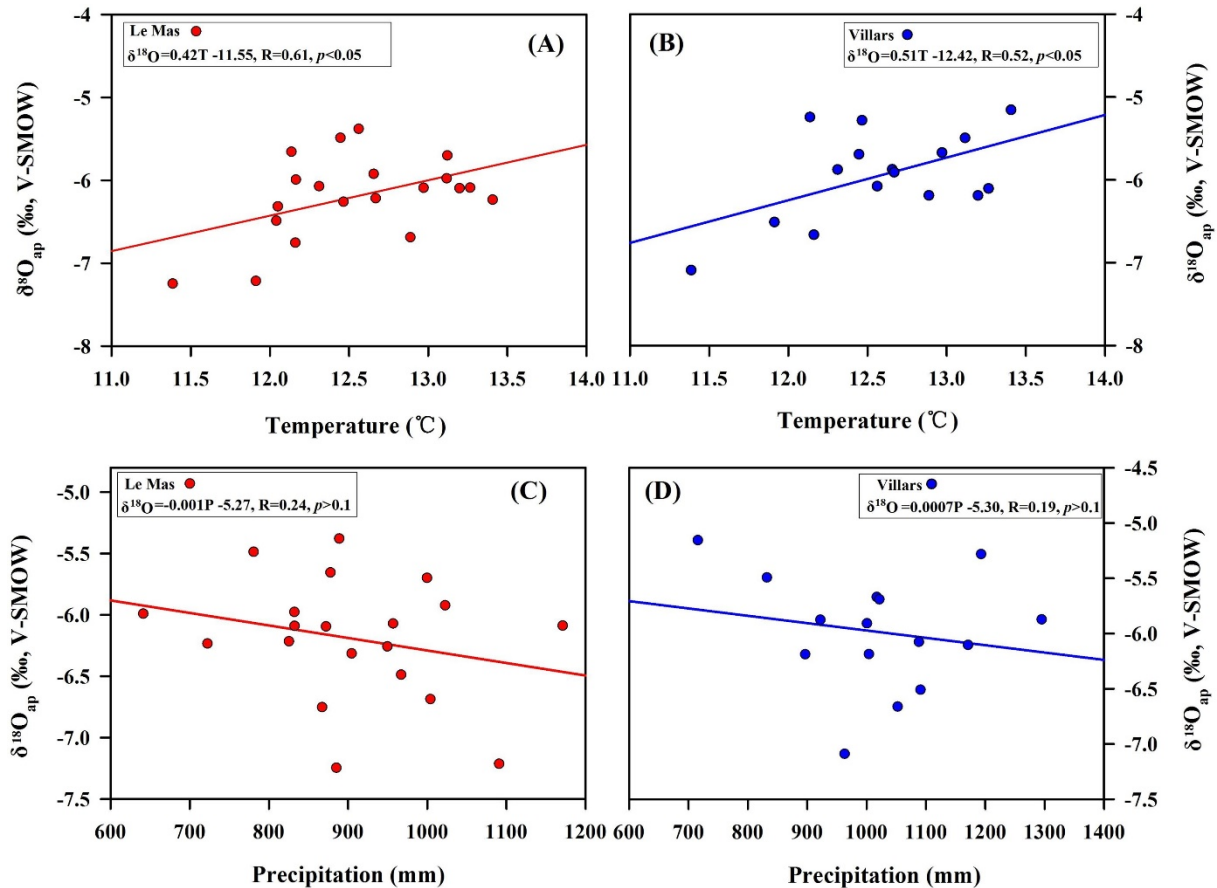


Figure 4. 9 Correlation between annual mean precipitation  $\delta^{18}\text{O}$  ( $\delta^{18}\text{O}_{ap}$ ) and local annual mean temperature and precipitation at Le Mas and Villars. (A) Correlation between annual mean precipitation  $\delta^{18}\text{O}$  ( $\delta^{18}\text{O}_{ap}$ ) and local annual mean temperature at Le Mas. (B) Correlation between  $\delta^{18}\text{O}_{ap}$  and local annual mean temperature at Villars. (C) Correlation between  $\delta^{18}\text{O}_{ap}$  and local annual mean precipitation at Le Mas. (D) Correlation between  $\delta^{18}\text{O}_{ap}$  and local annual mean precipitation at Villars.

The locations of PIMS were determined using 5 days' reconstruction of air mass history during 1997-2016 (Table 4.4; Figure 4.10). Curiously, the most distant areas (NAGR and PAWE) are the principal moisture sources (i.e., roughly >60%), while NA and DA are substantial contributors (i.e., roughly 34%), and the rest of the regions (ME and NESAs) have little impact, at least for the 1997-2016 period (Table 4.4; Figure 4.10). On the annual timescale, annual average values for  $\delta^{18}\text{O}$  and  $\delta\text{D}$  ( $\delta^{18}\text{O}_{ap}$  and  $\delta\text{D}_{ap}$ )



were calculated for the same period (Figure 4.11A; Appendix Table 3). Annual  $\delta^{18}\text{O}_{\text{ap}}$  value at Le Mas and Villars stations varies from -5.38 ‰ to -7.24 ‰ and -5.16 ‰ to -7.09 ‰, respectively (Appendix Table 3). The annual weighted  $\delta^{18}\text{O}_{\text{p}}$  means ( $\delta^{18}\text{O}_{\text{w}}$ ) range from -4.63 ‰ to -7.00 ‰ and -4.69 ‰ to -6.79 ‰ for Le Mas and Villars respectively (Appendix Table 3). Whereas the  $\delta^{18}\text{O}_{\text{p}}$  has a significant variation at the monthly timescale, it is much lower on the inter-annual timescale (Appendix Tables 2 & 3).

We also determine the correlation between PIMS and mean annual precipitation isotope composition ( $\delta^{18}\text{O}_{\text{ap}}$  and  $\delta^{18}\text{O}_{\text{w}}$ ) for the 1997-2016 period (Figure 4.11; Table 4.4 and Appendix Table 2). Results show clear trends in the time-series of stable isotopes in Le Mas and Villars (Figures 4.11A, 4.11B):  $\delta^{18}\text{O}_{\text{w}}$  and  $\delta^{18}\text{O}_{\text{ap}}$  display a decreasing trend (for both stations Le Mas and Villars) on the 1997-2016 studied period, which coincides to i) a decreasing trend of the initial moisture source (PIMS) of closer regions (e.g., PAWE and NA) (Figures 4.11C, 4.11D), and ii) to an increasing trend of PIMS of longer pathways (e.g., DA and NAGR) (Figures 4.11E, 4.11F). However, weak or less inter-annual variations for local temperature and precipitation were observed over the past 20 year (Figures 4.11G, 4.11H). In consequence, it appears that most of the inter-annual variability of rainfall isotopic composition ( $\delta^{18}\text{O}_{\text{p}}$ ) is controlled by the variation of the proportion of the different sources characterized by the PIMS trends. indicate the trends for the changes on the inter-annual timescale.

The term of d-excess was firstly defined by Dansgaard (1964) as the following equation:  $\text{d-excess} = \delta\text{D} - 8 \cdot \delta^{18}\text{O}$ , illustrating the degree of deviation from the equilibrium of isotopic fractionation caused by the kinetic fractionation in the evaporation of vapor (Dansgaard, 1964). Rainfall d-excess exhibited a weak inter-annual increasing trend

in Villars and Le Mas over the past 20 year, and the value range from 17.6 ‰ to -9.0 ‰ with the average value being 10.6 ‰ for Le Mas, and 17.6 ‰ to 1.7 ‰ with the average value being 9.5 ‰ for Villars, respectively (Figures 4.12A, 4.12B), which is close to the value of 10 ‰ for the average of global precipitation. Annual variation of d-excess coincides to an increasing trend of PIMS of longer pathways (e.g., DA and NAGR) and a weak increasing trend in local temperature (Figures 4.12A, 4.12B, 4.12C, 4.12D, 4.12E).

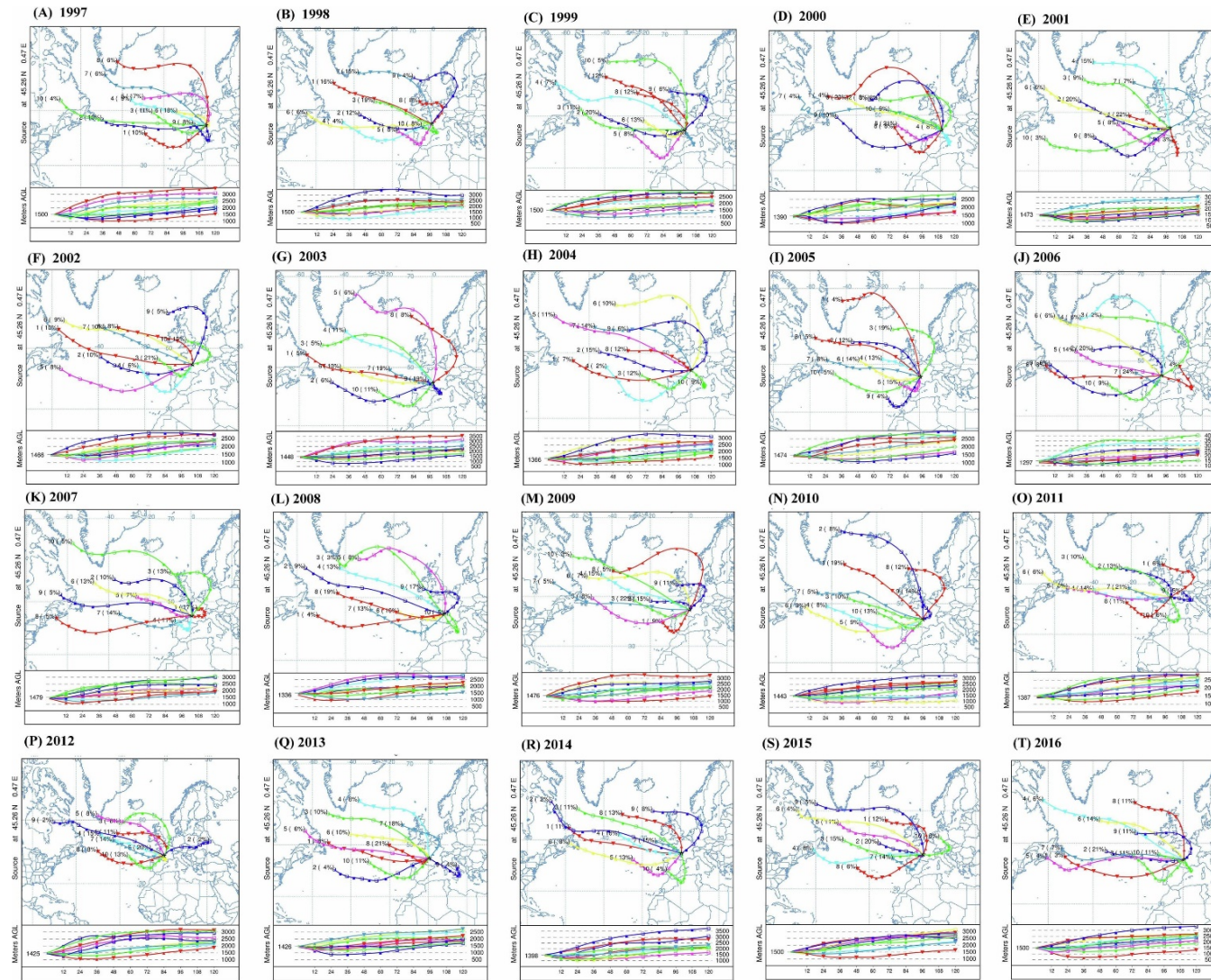


Figure 4. 10 Back trajectories for initial moisture sources for the 1997–2016 period. The star indicates the location of Villars, and the detailed data of moisture source were listed in Appendix Table 2.

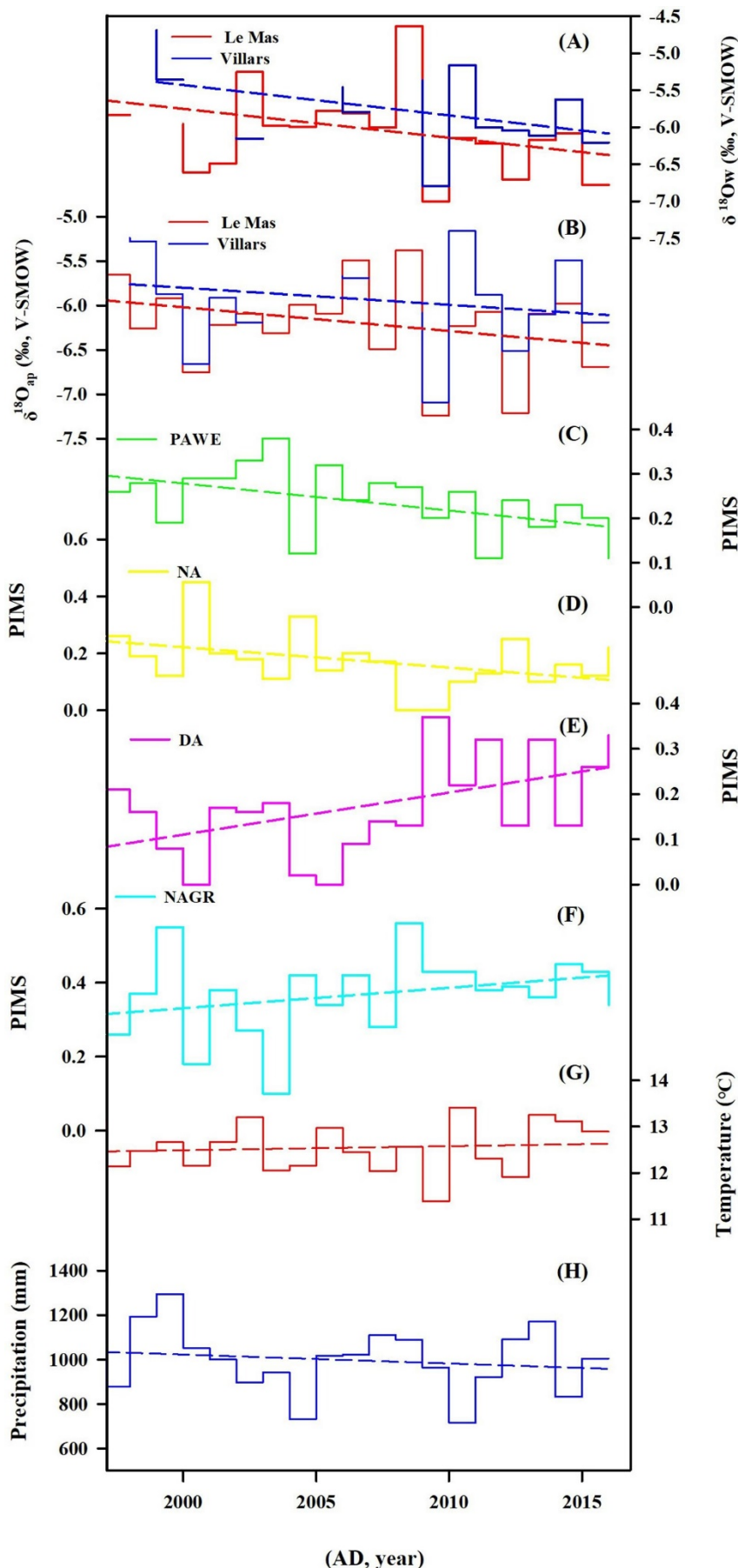


Figure 4. 11 Comparisons of  $\delta^{18}\text{O}_{ap}$  and the percentage of initial moisture sources (PIMS) and local annual mean temperature and precipitation at Le Mas and Villars on the inter-annual timescale.

(A) the inter-annual variation of average weighted precipitation  $\delta^{18}\text{O}$  ( $\delta^{18}\text{O}_w$ ), (B) the inter-annual average variation of precipitation  $\delta^{18}\text{O}$  ( $\delta^{18}\text{O}_{ap}$ ), (C) the inter-annual variation of PAWE, (D) the inter-annual variation of NA, (E) the inter-annual variation of DA, (F) the inter-annual variation of NAGR. (G) the inter-annual variation of local annual mean temperature in Villars. (H) the inter-annual variation of local annual mean precipitation in Villars. The fitting dashed lines indicate the trends for the changes on the inter-annual timescale.

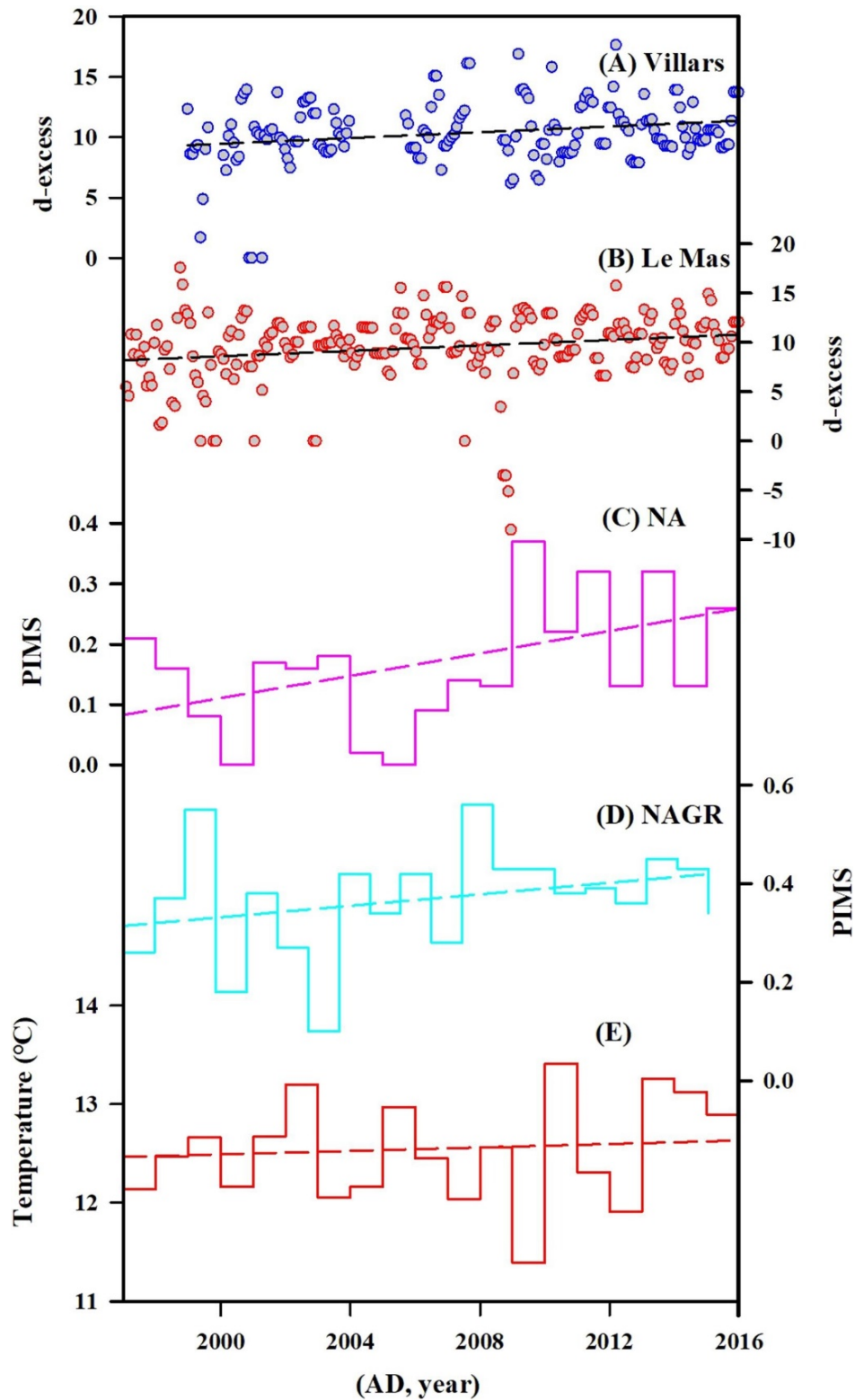


Figure 4. 12 Comparisons of the  $d$ -excess with the percentage of initial moisture sources (PIMS) and the local annual mean temperature at Le Mas and Villars on the inter-annual timescale. (A) the inter-annual variation of the  $d$ -excess at Villars, (B) the inter-annual variation of the  $d$ -excess at Le Mas, (C) the inter-annual variation of DA, (D) the inter-annual variation of NAGR. (E) the inter-annual variation of local annual mean temperature in Villars. The fitting dashed lines

## 4.2. Discussion

### 4.2.1 Causes of the variations of precipitation isotope ( $\delta^{18}\text{O}_p$ , $\delta\text{D}_p$ ) in SW-France

Whether considering monthly or inter-annual timescale, it appears that  $\delta^{18}\text{O}_p$  of both Le Mas and Villars stations follow variations of PIMS and local temperature. Several factors may be raised to explain the  $\delta^{18}\text{O}_p$  variability: **i)** the length of the water vapor transport route which plays an important role on the Rayleigh fractionation process; **ii)** the initial mean seawater  $\delta^{18}\text{O}$  ( $\delta^{18}\text{O}_{\text{sw}}$ ) values which may be different; **iii)** the removal of moisture from an air mass which is temperature-dependent during Rayleigh fractionation, and the progressive condensation of the vapor requires the cooling of the air mass from the vapor of cloud to the falling rain (IAEA working group, 2000).

#### 4.2.1.1 “amount effect” and “temperature effect” controls

Compared with global meteoric water line (GMWL:  $\delta\text{D}=8\delta^{18}\text{O}+10$ ) (Craig, 1961; Dansgaard, 1964), we observed that there is a lower slope and a lower intercept in the LMWL of the two monitoring sites (Le Mas and Villars) (Figure 4.1C) (Genty et al., 2014a). This is a general case for continental stations (IAEA working group, 2000) and may be attributed to evaporation during the precipitation under the clouds and various complex phenomena linked to the history of rainfall (Dansgaard, 1964; Stewart, 1975; Gat, 1996; Peng et al., 2005; Yamanaka et al., 2007; Lachniet, 2009; Pang et al., 2011; Chen et al., 2015; Figure 4.1C).

A positive correlation is observed between  $\delta^{18}\text{O}_p$  and local monthly/annual mean temperature (Figures 4.2A, 4.2B) in Le Mas and Villars. The main reason is that the air

mass, after leaving from the moisture source, is dominated by Rayleigh fractionation processes, temperature and “rain-out” dependent (Dansgaard, 1954, 1964; Bowen, 2008). Water vapor in the atmosphere is difficult to isothermally condense, and any progress of atmospheric precipitation is caused by a temperature cooling (Dansgaard, 1954, 1964). When the condensed water is formed, then leaving water vapor immediately, the stable isotope ratio is depleted in the condensed water with the decrease of temperature (Dansgaard, 1964; Rozanki et al., 1993; Lachniet, 2009).

No significant correlation is observed between mean annual precipitation and  $\delta^{18}\text{O}_p$ , suggesting no “amount effect” at the Le Mas and Villars stations (Figures 4.2B; Genty et al., 2014a). Additionally, Keklec and Domínguez-Villar (2014) who conducted a monitoring of  $\delta^{18}\text{O}_p$  in central Spain, proposed that all climate parameters with a seasonal cycle’s characterization would exhibit a certain link with  $\delta^{18}\text{O}_p$ , however, when monitoring the relationship between single precipitation event with  $\delta^{18}\text{O}_p$ , these links are not visible (Keklec and Domínguez-Villar, 2014), further indicating that the amount of precipitation is not affecting the  $\delta^{18}\text{O}_p$ .

#### 4.2.1.2 Moisture source effect

The transportation distance between moisture source and the monitoring site (latitude effect) has already shown an important control on the  $\delta^{18}\text{O}_p$  (Aggarwal et al., 2004; Breitenbach et al., 2010; Chen and Li, 2018). Based on the Rayleigh fractionation process governing these links, the increased moisture transportation distances may result in depleted  $\delta^{18}\text{O}_p$  value (Rindsberger et al., 1983; Field, 2010; Krklec and Domínguez-Villar, 2014; Krklec et al., 2018).

In winter months, the principal initial moisture sources derive from a longer source (NAGR) in comparison with the summer season characterized by a closer moisture

source (PAWE) (Figure 4.7). The precipitations that occur during the migration of moisture are enriched in  $^{18}\text{O}$  leading to an impoverishment of remaining vapor and then resulting in a lower  $\delta^{18}\text{O}_p$  (Araguás-Araguás et al., 2000; Breitenbach et al., 2010; Cai et al., 2016). Therefore, the longer the depression pathway, the lower  $\delta^{18}\text{O}_p$  value (Araguás-Araguás et al., 2000; Lee & Fung, 2008; Risi et al., 2008; Lachniet et al., 2009; Kurita, 2013; Cai et al., 2017). The mechanism is similar with “continental effect” where the rainout above the continent is the cause of impoverishment of the  $\delta^{18}\text{O}$  with increasing distance from the ocean, but in fact very variable, i.e., from region to region and from season to season (IAEA working group, 2000).

Besides, the discrepancy of initial mean sea water  $\delta^{18}\text{O}_{\text{sw}}$  values is also an important factor controlling the variation of  $\delta^{18}\text{O}_p$  values in SW-France (Rozanski et al., 1993; Clark and Fritz, 1997; Cole et al., 1999; Friedman et al., 2002). Most of the moisture sources in Villars and Le Mas come from two main areas: NAGR in winter and PAWE in summer. Because the mean  $\delta^{18}\text{O}_{\text{sw}}$  in the NAGR area (-4.0 ‰ to 0 ‰) (LeGrande and Schmidt, 2006) is lower than the one in the PAWE area (from 0 ‰ to 1.5 ‰) (LeGrande and Schmidt, 2006), it may also be a significant contribution to the observed  $\delta^{18}\text{O}_p$  variation.

An important phenomenon appears at the inter-annual timescale where changes of the  $\delta^{18}\text{O}_w$  and  $\delta^{18}\text{O}_{\text{ap}}$  follow the inter-annual initial location of moisture source (Figure 4.11), which is attributed to Rayleigh fractionation process and initial moisture sources (Figures 4.10 and 4.11). Previous works have revealed that the  $\delta^{18}\text{O}_d$  (drip-water  $\delta^{18}\text{O}$ ) inherited the signal of atmospheric precipitation on the monthly timescales, and the influence of the “mixing effect” with “old water” in the epikarst zone (Pape et al., 2010; Li et al., 2011; Partin et al., 2013; Zhang & Li, 2019) seriously damp or even suppress the rainfall seasonal characteristics (e.g., heavier in summer and lighter in winter)



(Genty et al., 2014a). However, other studies indicated that the  $\delta^{18}\text{O}_d$  and  $\delta^{18}\text{O}_c$  can respond to the signal of  $\delta^{18}\text{O}_w$  on the interannual timescale (Chen and Li, 2018; Ellis et al., 2020). Our results show that the inter-annual  $\delta^{18}\text{O}_p$  and  $\delta\text{D}_p$  variations are controlled by the mean annual change of the initial location of moisture source, which provides new insights to explain climatic significance of oxygen isotope of drip water and stalagmites on the interannual timescale in Villars Cave.

#### 4.2.2 Variations of d-excess on the annual timescale

It is generally believed that d-excess is sensitive to moisture source conditions (Pfahl and Wernli, 2008; Pfahl and Sodemann, 2014), therefore, which is suitable for assessing the origin of water vapor. Moreover, some studies have proposed that high and increasing d-excess values reflect fast evaporation (low RH) and stronger kinetic isotope effects during evaporation (Clark and Fritz, 1997; Dublyansky et al., 2018).

The linear variation of d-excess and PIMS of longer pathways (DA and NAGR) exhibits an increasing trend in Le Mas and Villars (Figures 4.12A, 4.12B, 4.12C, 4.12D), reflecting enhanced evaporations and stronger kinetic isotope effects in the transportation of vapor while moisture from longer pathways was increased over the entire period of observation (Clark and Fritz, 1997; Pfahl and Wernli, 2008; Dublyansky et al., 2018). The increase of air temperature at the monitoring stations over the past 20 years leads to the enhancement of water vapor evaporation, inducing the rising change of precipitation d-excess (Figures 4.12A, 4.12B, 4.12E). Hence, our results suggest that the d-excess variations in paleo-record (e.g., ice cores) should be adapted to reflect moisture source characterized by atmospheric circulation and local temperature.

### 4.2.3 Links between NAO and $\delta^{18}\text{O}_p$ in SW-France

During a positive phase of the NAO, a large pressure gradient between the Azores (High Pressure) and Iceland (Low Pressure) across the North Atlantic creates higher winter temperatures and precipitation over the Atlantic and Northern Europe while it is lower over Mediterranean Sea and North Africa (Hurrell, 1995, 1996; Uvo, 2003). The exactly opposite pattern in negative NAO phase is found when the pressure gradient between Azores and Iceland decreases by shifting southwards the northern hemisphere westerly jet-stream (Hurrell, 1995).

NAO in different phase plays an important role in the length of water vapor transport in winter and spring (Baldini et al., 2008). When winter and spring NAO index is in positive excursion, warmer westerly winds will carry  $^{18}\text{O}$  moisture with shorter transportation distance, resulting in heavier  $\delta^{18}\text{O}_p$  values in SW-France (Baldini et al., 2008; Langebroek et al., 2011), therefore NAO index and  $\delta^{18}\text{O}_p$  exhibit a positive correlation (Figures 4.6A, 4.6B, 4.6C, 4.6D). However, NAO only take a strengthened or weakened effect on the length of water vapor transport in winter (Baldini et al., 2008), which will not change the fact that most of winter moisture source distributed in the region of longer distance (West North Atlantic: North America and Greenland) (Section 4.2; Krklec and Domínguez-Villar, 2014). The isotopic time series at the seasonal timescales show correlations with NAO index, providing a useful NAO proxy ( $\delta^{18}\text{O}_p$ ) to indicate the variation in seasonal paleo-NAO index. However, when it comes to the relationship between NAO and  $\delta^{18}\text{O}_p$  in the inter-annual timescale, a particularly weak correlation ( $p > 0.1$ ) was found.

#### 4.2.4 Quantifying the relationship between PIMS/temperature and $\delta^{18}\text{O}_p$ in SW-France

The variations of PIMS and local temperature have been identified as important contributors for the observed  $\delta^{18}\text{O}_p$  changes in SW-France. Therefore, combining the links between PIMS/temperature and  $\delta^{18}\text{O}_p$ , several equations were established using multiple linear regression analysis methods as followed:

$$\text{EQ (1) for Le Mas station: } \delta^{18}\text{O}_p = 0.038 * \text{PAWE} + 0.046 * \text{NA} + 0.054 * \text{ME} + 0.02 * \text{DA} + 0.025 * \text{NAGR} + 0.119 * \text{T} - 10.929, R = 0.965, p < 0.01$$

Where  $\delta^{18}\text{O}_p$  indicates precipitation  $\delta^{18}\text{O}$  (V-SMOW), and T ( $^{\circ}\text{C}$ ) indicate the local monthly temperature in Le Mas.

EQ (2) for Villars's station:

$$\delta^{18}\text{O}_p = 0.035 * \text{PAWE} + 0.031 * \text{NA} + 0.054 * \text{ME} - 0.001 * \text{DA} + 0.005 * \text{NAGR} + 0.049 * \text{T} - 8.637, R = 0.942, p < 0.05$$

Where  $\delta^{18}\text{O}_p$  indicates precipitation  $\delta^{18}\text{O}$  (V-SMOW), and T ( $^{\circ}\text{C}$ ) indicate the local monthly temperature in Villars.

These two equations allow to evaluate the importance of the factors (PIMS, Temperature) variability on the  $\delta^{18}\text{O}_p$  variability. Results show that the following factors influence the  $\delta^{18}\text{O}_p$  in the order on importance: Temperature > NAGR > PAWE > NA > DA > ME at the monthly timescale. We use the SPSS software to calculate the variance of contribution rate, and the proportion in the four main principal components are 60.6% (Temperature), 16.6% (NAGR), 15.4% (PAWE), 6.2% (NA), the rest of two-component (DA and ME) is <2%. Therefore, in any case, considering the range of variability of various contributions from different moisture source regions and local temperature, it is obviously found that local temperature is the principal

variable controlling the oxygen isotope composition of precipitation in the continental European at a monthly timescale.

The use of HYSPLIT model for tracking moisture source is providing a good example for how to accurately calculate the relationship between  $\delta^{18}\text{O}_p$  and moisture sources. Different from regional/general circulation models of the  $\delta^{18}\text{O}_p$  (Cruz- San Julián et al., 1992; Celle-Jeanton et al., 2001; Sodemann et al., 2008; Baldini et al., 2010; Gao et al., 2011; Bershaw et al., 2012), this study not only provides the quantified mathematical equations based among the longest isotopic isotope time series and the variations of PIMS (over 20 years), but also determines the extent of the impact on the monthly timescale.

Additionally, the speleothem  $\delta^{18}\text{O}$  in the Villars Cave, also recorded a series of abrupt climatic events on the centennial-millennial timescales, such as Dansgaard-Oeschger, Heinrich and 8.2 ka events (Genty et al., 2001, 2003, 2006; Genty, 2008; Wainer et al., 2009, 2010, 2013; Genty et al., 2014a). In this study, the long monitoring-based work established a link between local climate parameters and the  $\delta^{18}\text{O}_p$ , which can be used for interpreting the significance of speleothem  $\delta^{18}\text{O}$ . No or less correlation was observed between the  $\delta^{18}\text{O}_p$  and local precipitation, indicating that speleothem  $\delta^{18}\text{O}$  in Villars Cave likely cannot reconstruct local precipitation. In contrast, change in  $\delta^{18}\text{O}_p$  can be linked to both the change of moisture source and to the local temperature variation.

### 4.3 Conclusions

Based on the observations and models on  $\delta^{18}\text{O}_p$  and  $\delta\text{D}_p$ , moisture sources, and regional/local climate parameters during the 1997-2016 period at the Le Mas and Villars meteorological stations, SW-France, the following conclusions can be drawn:

(1) Based on HYSPLIT model, we have quantified the percentage of initial moisture source (PIMS) for different months and found shorter transportation distances during summer months and longer ones during winter, which is consistent with the observed seasonal variations of  $\delta^{18}\text{O}_p$ .

(2) The variation of temperature and PIMS are important factors that are the main causes on the seasonal variation of the  $\delta^{18}\text{O}_p$ . In the order of importance, the following factors influence the  $\delta^{18}\text{O}_p$ : Temperature>NAGR>PAWE>NA>DA>ME, and the proportion of the four main principal components are 60.6% (Temperature), 16.6% (NAGR), 15.4% (PAWE), 6.2% (NA) on the monthly timescale.

(3) On the annual timescale,  $\delta^{18}\text{O}_p$  maintains a positive relationship with local mean annual temperature, however, no evidences for its “amount effect” has been observed.

(4) On a longer timescale, an important result shows that an inter-annual decreasing trend was observed for the  $\delta^{18}\text{O}_p$  ( $\delta^{18}\text{O}_{ap}$  and  $\delta^{18}\text{O}_w$ ), following the variation of annual PIMS. We observed, over the past 20 years, that the percentage of a farther moisture source region (NAGR) was increased, at the opposite, there is a decreasing trend for the closer source (PAWE).

(5) The linear variation trend over the past 20 years of d-excess coincides to the variations of PIMS in longer pathways (DA and NAGR) and local temperature on the inter-annual timescale, which is likely due to the global temperature increase and the change of moisture source characterized by atmospheric circulation in SW-France.

(6) The variation of moisture distribution regions should be considered when interpreting the climatic significance for speleothem oxygen isotopic records in SW-France.

**Chapter 5 - Hydrological characterizations of the karst  
unsaturated zone by using a reservoir-flow model –  
Simulations of present day and future infiltration  
characterizations**

---

## Introduction

Based on the HYSPLIT model, we have quantified the percentage of the initial moisture source (PIMS) using isotopes, but the infiltration processes of rainwater into the unsaturated zone is still largely unclear. Based on the isotopic variation of rainwater at previous rainfall stations Le Mas and Villars sites, we simulate rainfall infiltration flow and drip water  $\delta^{18}\text{O}$  using the KarsFor reservoir-flow model for Villars Cave site.

This model, among several other parameters, needs to set the number of reservoirs and their sizes. For that, we used ERT (electrical resistivity tomography) results to obtain the most reasonable pattern of reservoir and flow settings as well as their connections with our dripping points in Villars Cave. The long duration of the rainfall and drip water time series (>20 years) is a key point as it allows us to compare confidently hydrological climate factors to rainfall and drip water variations. This research is a continuation of the earlier work presented by [Genty et al. \(2014a\)](#) in that it extends  $\delta^{18}\text{O}_r$  and  $\delta^{18}\text{O}_d$  of Villars Cave after 2014 A.D., and it uses a more complex model to simulate the infiltration based on reservoirs geometry from a geophysical survey.

More specifically, the study motivations are developed in the following questions: (1) How are the responses of stable isotopes and the infiltration drip flows from the different reservoirs identified in the ERT profile in the KarstFor (karst hydrological model) model? (2) How is the coherency between the modeled drip rates and stable isotope composition of the different dripping stations compared to the measurements?

Our first research on the sources of rainfall above Villars Cave is further explored in the following article, which specifically examines the processes by which this rainfall infiltrates the cave and reaches the dripping stations that feed stalagmites.



**Article 2:** *Jian Zhang, Dominique Genty, Colette Sirieix, Cécile Verdet, Sylvain Mateo, Ludovic Devaux, Giovanni Sgubin, Stéphane Bujan, Bénédicte Minster, Edouard Régnier, Ting-Yong Li, François Bourges, Ming-Qiang Liang, Chaojun Chen. **Data-model comparisons of isotopic and hydrological variability of the karst vadose zone above Villars Cave, SW-France: implications for speleothem paleoclimate records.** Chemical geology (under review, revised)*

## **Abstract**

Because of the great heterogeneity of the limestone fissures, conduits, and reservoirs in karst areas, the understanding of the infiltration in caves and karst terrains is complicated. The time delays observed between rainfall and the various flows into caves, such as shaft flow and seepage flow, exhibit significant variability. To better understand the infiltration above a typical shallow cave, Villars Cave, South-west France, we used both a very long monitoring (>20 years) isotopic data set of rainfall and drip rates at two different cave gallery levels (14 m and 36 m below cave surface, respectively) in Villars Cave and a conceptual model (KarstFor) that mix water flows and isotopes. The time-lapse electrical resistivity tomography (ERT) image enabled us to determine the most appropriate reservoir and flow settings, which were incorporated into the KarstFor model. The modeled variations in storage water and infiltration flow align with the observed dripping discharge rates, indicating seasonal variability and a distinct time delay between water excess ( $\text{Rainfall} - \text{Evapotranspiration} > 0$ ) and drip rates in different cave level. The fact that the model strikingly simulates the small, but constant, isotopic difference of drip water  $\delta^{18}\text{O}$  ( $\delta^{18}\text{O}_d$ ) values between the upper and the lower galleries of Villars Cave. On an inter-annual scale, the observed  $\delta^{18}\text{O}_d$  values follow the variation of the water excess and the cave temperature, showing a long-term trend, possibly due to climatic change above the studied cave. All these results are not

only important to better understand the infiltration in karstic zones, but also are important to better interpret the speleothem  $\delta^{18}\text{O}$  records widely used in paleo-climate studies.

## 5.1 Results

### 5.1.1 Rainfall and drip water $\delta^{18}\text{O}$ time series

Rainfall  $\delta^{18}\text{O}$  showed apparent seasonal changes, with less negative values in summer and more negative values in winter (Figure 5.1A; Genty et al. 2014a). Based on the  $\delta^{18}\text{O}$  and  $\delta\text{D}$  values of the rainwater samples above the Villars Cave, we established an updated equation of the local meteoric water line (LMWL):  $\delta\text{D}=7.01\delta^{18}\text{O}+ 4.7$ ;  $n = 201$ , with a correlation coefficient  $R = 0.98$  ( $p < 0.01$ ) (Figure 5.2; Table 5.1; Zhang et al., 2020). In order to verify the reliability of the LMWL equation, we also used other different methods, including ordinary least squares regression (OLSR) and precipitation-weighted least squares regression (PWLSR) (Hughes and Crawford, 2012, Crawford et al., 2014). Whether weighted or non-weighted regressions were considered, the close slopes and gradients were observed from three methods (Table 5.2). In the drip water, the high  $\delta^{18}\text{O}$  variability from  $-5.37\text{‰}$  to  $-6.76\text{‰}$  which sometimes appears to be seasonal was only observed in one of the dripping stations from the upper gallery (Vil-#10A) (Figure 5.1B), while the other three cave  $\delta^{18}\text{O}_d$  time-series display almost no fluctuations and without any visible seasonal variability (Figure 5.1C). The mean difference between lower and upper galleries is about  $0.2\text{‰}$ , the lower gallery stations  $\delta^{18}\text{O}_d$  having the lowest values:  $-6.35\text{‰}$  (SD=0.08,  $n=106$ ) and  $-6.36\text{‰}$  (SD=0.08;  $n = 112$ ) for Vil-#1A and Vil-#1B (lower gallery), and  $-6.13\text{‰}$  (SD=1.33;  $n=129$ ) and  $-6.19\text{‰}$  (SD=0.21‰;  $n=96$ ) for Vil-#10A

and Vil-#10B (upper gallery) (Table 5.2). A difference of 0.2‰ falls within the stated analytical uncertainty of  $\pm 0.05\text{‰}$  for the  $\delta^{18}\text{O}$  values (Figure 5.1C). While a difference of 0.2‰ may appear small, it can be visually apparent in Figure 5.1C.

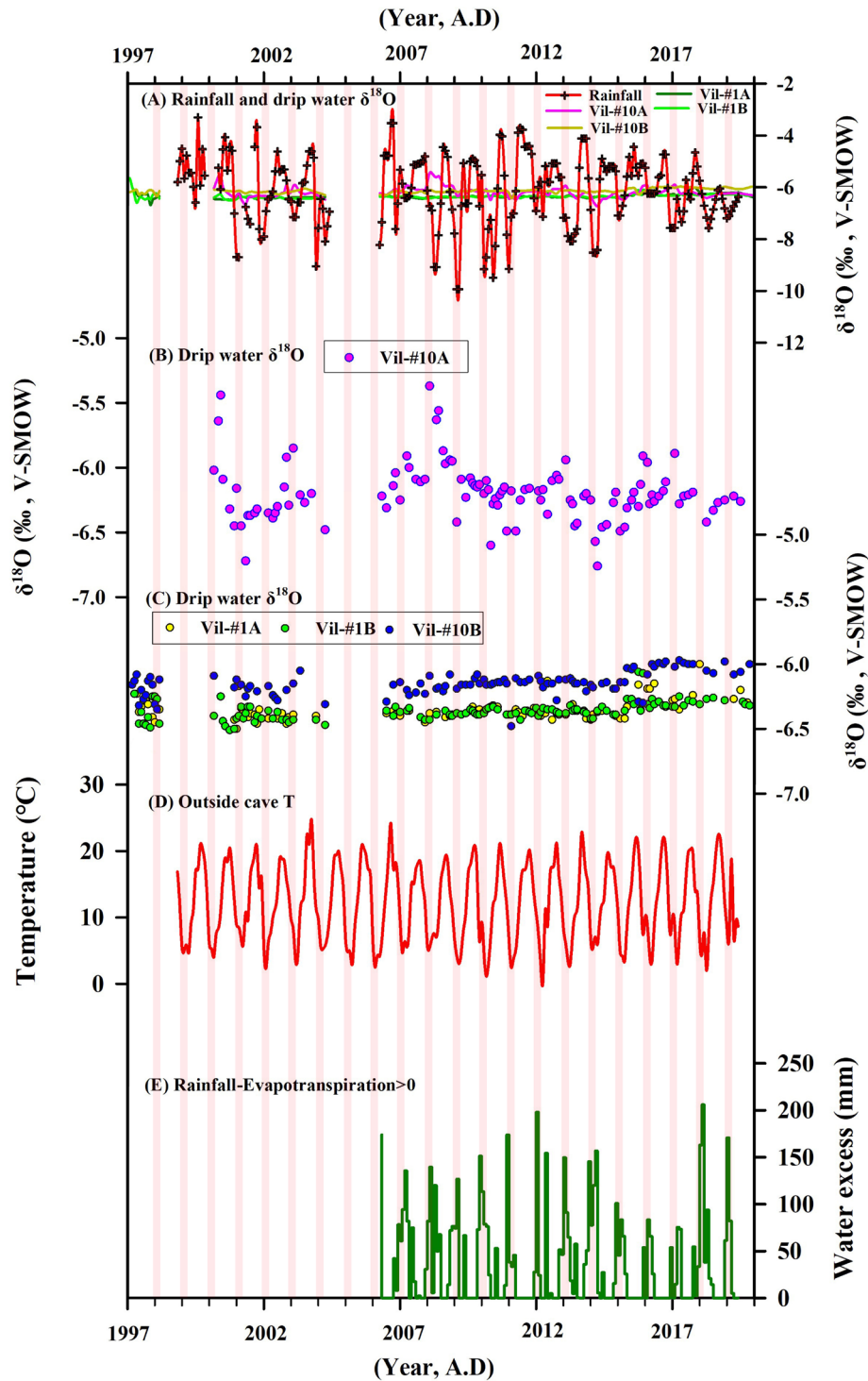


Figure 5. 1 The combined time series of meteoric conditions and isotope hydrology of

waters in Villars Cave. (A) Comparison with rainfall and drip water  $\delta^{18}\text{O}$  values of sites (Vil#1A, Vil#1B, Vil#10A and Vil#10B) in Villars Cave. (B) A separate zoom figure was created to display the  $\delta^{18}\text{O}$  values for Vil-#10A. (C) A separate zoom figure was created to display the  $\delta^{18}\text{O}$  values for Vil-#1A, Vil-#1B, and Vil-#10B in Villars Cave. (D) The monthly average air temperature outside of Villars Cave. (E) Water excess outside Villars Cave. The pink shading represents the winter months.

It is interesting to note that the upper gallery Vil-#10A drip station, which has the most variable  $\delta^{18}\text{O}_d$  values, displays a similar slope to the rainfall isotopic  $\delta^{18}\text{O}_d$  (slope= 6.83; [Figure 5.2A](#); [Table 5.1](#)). In Vil-#10A may be controlled by less reservoirs, directly from the soil/epikarst zone. Other stations are gathered in a small set of  $\delta^{18}\text{O}_d$ - $\delta\text{D}$  values, even if we can observe a larger  $\delta\text{D}$  variation compared to the  $\delta^{18}\text{O}_d$  one ([Figure 5.2B](#); [Table 5.2](#)). All these values show clearly a large damping of the rainfall isotopic signal that is the consequence of the mixing of the recharged water for several months to several years as explained before ([Genty et al., 2014a](#); [Jean-Baptiste et al., 2019](#)).

*Table 5. 1 Parameters of the fitting for LMWL, OLSR, and PWLSR methods for Villars, SW-France (The method refers to [Hughes and Crawford, 2012](#))*

		N	a	SD	b	SD	$r^2$
	LMWL	201	7.01	0.12	4.7	0.74	0.94
Rainfall	OLSR	201	7.06	0.12	4.62	0.75	0.94
	PWLSR	201	7.01	0.12	4.27	0.77	0.94
Drip water (Vil-#10A)	LMWL	129	6.84	0.33	4.93	2.04	0.77
Drip water (Vil-#10B)	LMWL	96	7.37	0.87	8.21	5.31	0.44
Drip water (Vil-#1A)	LMWL	106	5.83	1.2	-2.17	7.56	0.19
Drip water (Vil-#1B)	LMWL	112	3.09	0.94	-19.76	5.96	0.09

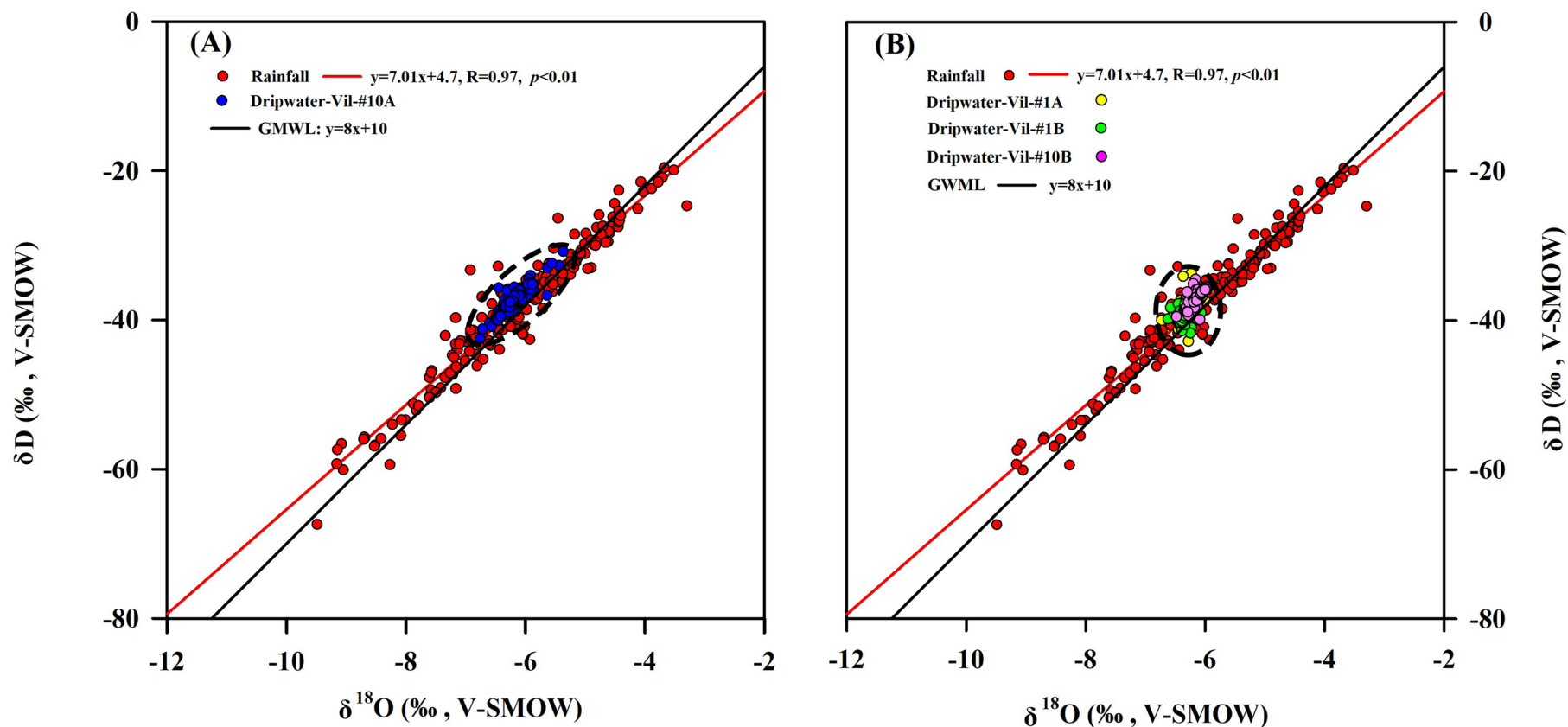


Figure 5. 2 Local meteoric water line (LMWL) (red solid line) based on the  $\delta^{18}\text{O}$  and  $\delta\text{D}$  values of rainfall outside of Villars Cave. (A) The  $\delta^{18}\text{O}$  and  $\delta\text{D}$  values for drip waters (Vil-#10A) in Villars Cave are distributed around the LMWL. (B) The  $\delta^{18}\text{O}$  and  $\delta\text{D}$  values for drip waters (Vil-#1B, Vil-#10A and Vil-#10B) in Villars Cave with a depressed amplitude as compared to that of precipitation. The Global Meteoric Water Line (GMWL) in black (Craig, 1961) is plotted for comparison.

## 5.1.2 Rainfall amount, evapotranspiration, and drip rate relationships

The climate around the Villars Cave exhibits a temperate and maritime characteristic. The local monthly precipitation shows that there is no significant seasonality above the Villars Cave. The mean annual value is 1014 mm in the 1997-2019 period (SD =192 mm). There is a strong seasonal signal in the quantity of water that infiltrates the karst, which can be estimated by the efficient rainfall ((Rainfall amount-ETP) >0)) also called water excess (Figure 5.1E). On the opposite, seasonality is well marked on the outside air temperature (Figure 5.1D) and then on the ETP (potential evapotranspiration) with an annual value of 836.7 mm (SD = 58 mm).

Between October 2013 and April 2019, drip loggers recorded a large variability at different scales but are characterized by a well-marked seasonality (Figure 5.3). The averaged drip rates over the entire hydrological years at the three drip water sites (Vil-#10A, Vil-#10B, Vil-#1B) are 21, 3.5, and 16.5 drip/mins, respectively, with a variability characterized by their standard deviation values (SD) of 28.4, 3.7 and 13.9 drip/min, respectively (Figure 5.3).

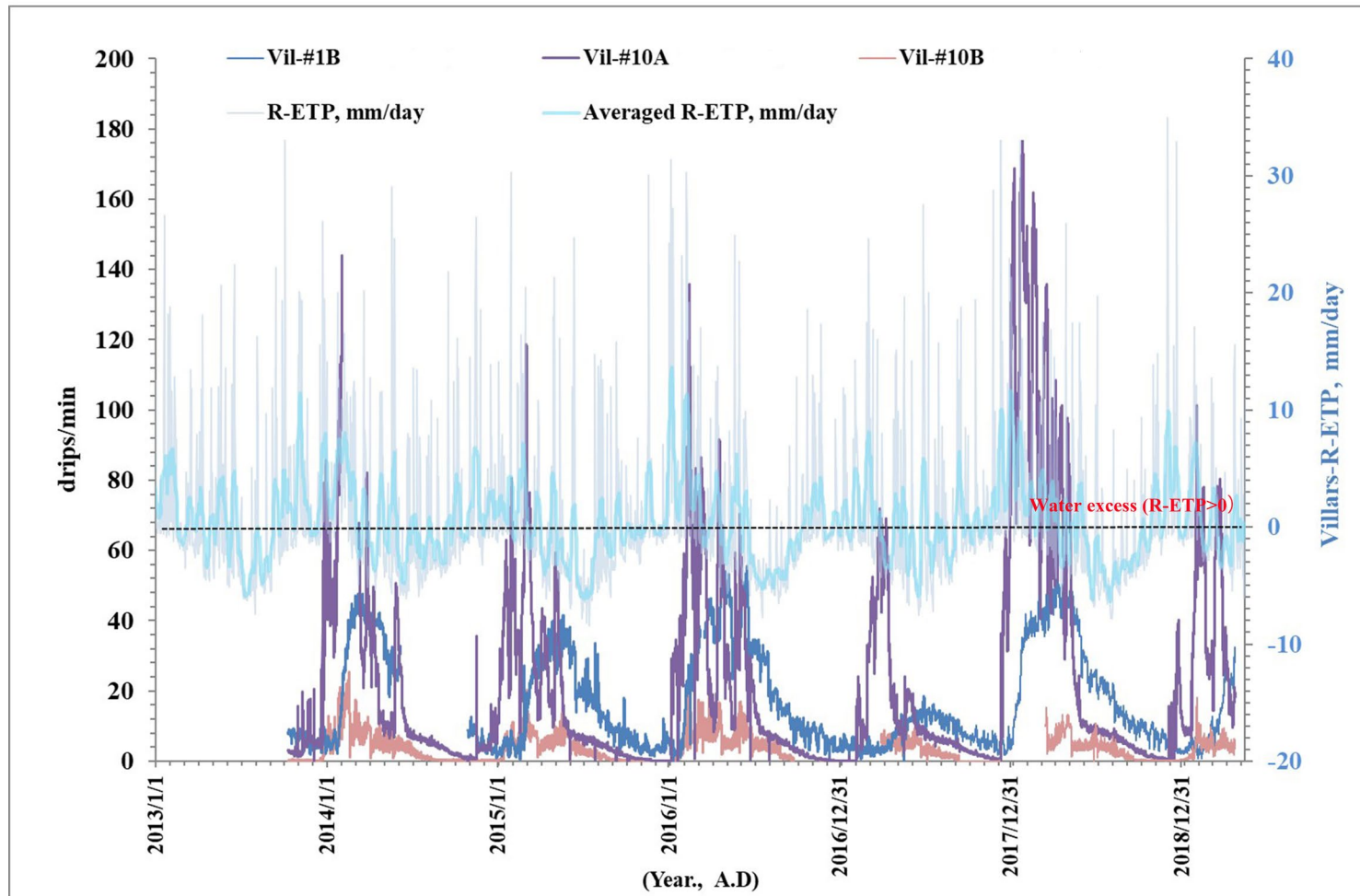


Figure 5. 3 Comparison of the variability of daily rainfall amount, R-ETP and drip-water rates during 2013-2019. A smoothed (10 points) average to R-ETP in blue line was applied, making it easier to identify daily variabilities.

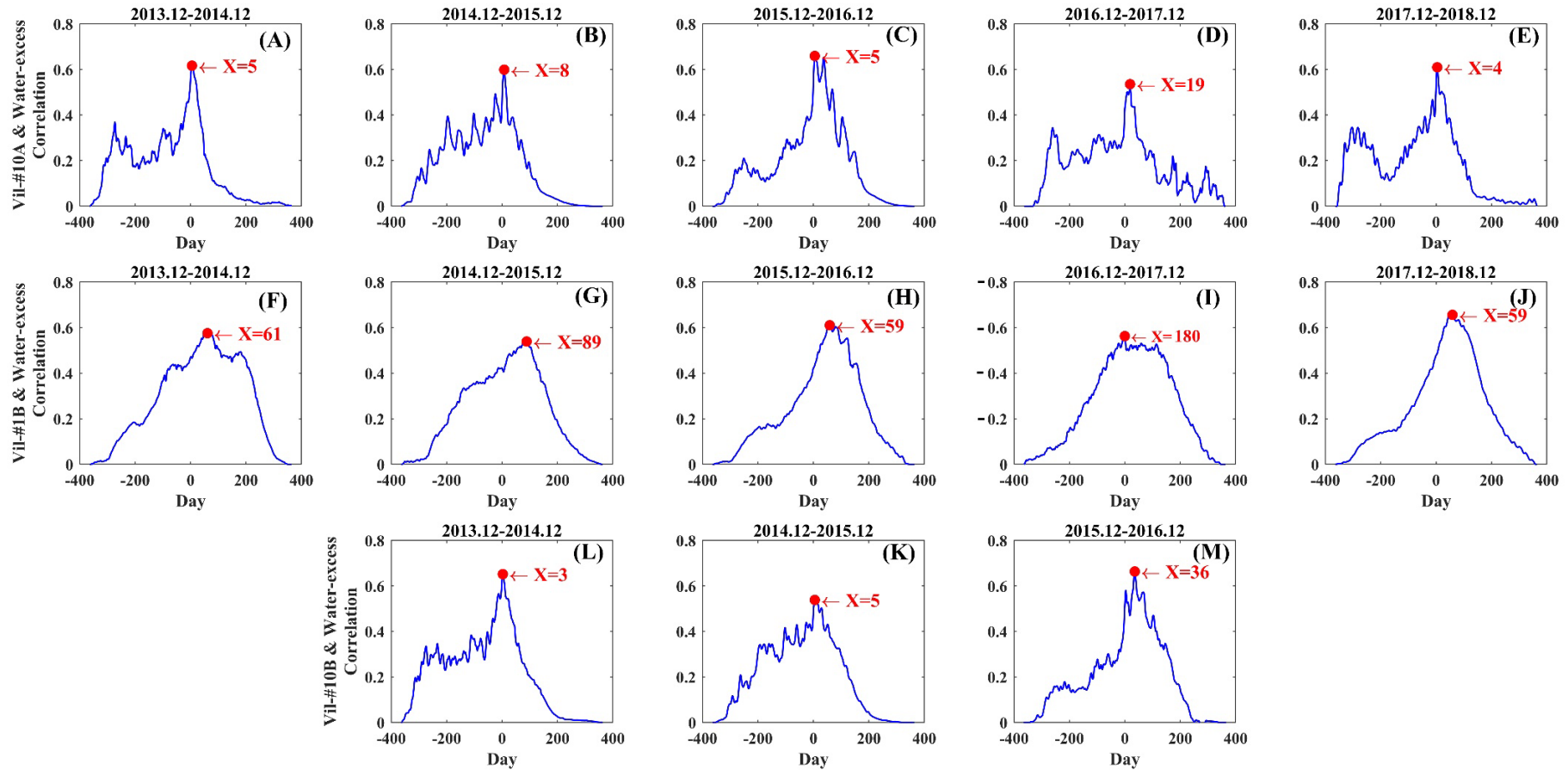


Figure 5. 4 The delay time between drip-water rates and water excess after the threshold the percolation threshold ( $R-EPT > 0$ ) during 2014-2018 using Pearson's linear correlation coefficient in the MATLAB coherence package. (A-E) Vil-#1A & Water-excess, (F-J) Vil-#1B & Water-excess, (L-M) Vil-#10B & Water-excess.



Looking at the details, during the first cycle of 2014-2015, it was observed that there was a local water excess of more than zero in mid-September 2014 in Vil-#10A (Figure 5.5). It takes approximately two to three months for the reservoirs' water to be filled up and reached the percolation threshold, which then enables water to start moving down into the cave, forming drip water. Consequently, there was a rise in the drip water rate for December 2014, which persisted until around May 2015 in Vil-#10A (Figure 5.5).

The time delay between the water that infiltrates after reaching the percolation threshold, quantified here by the water excess, and the drip rates have been estimated by cross-correlations (Figure 5.4). Results show that the time lag is in the interval of 59-180 days for Vil-#1B station located in the lower gallery, 3-36 days for Vil-#10B, and 4-19 days for Vil-#10A located in the upper gallery (Figure 5.4 and Table 5.3), showing that time lags go from a few days to several months depending on the depth of the drip stations and of its inertia linked to reservoir behaviors. We perform a manual one-to-one comparison by comparing peaks of the different time series of water excess and drip rate in different years (Figures 5.5 and 5.6) to verify the cross-correlation results. Results, clearly visible on time series, show that the lag time at Vil-10A# (upper gallery) with water excess is about 3-18 days, consistent with our cross-correlation results (4-19 days). For the Vil-#1B (lower gallery), the peaking of water-excess is about January to February every year, and the peak of drip rate is about March to April to May every year. For Vil-#1B station, the delay is generally more than three months depending on different years (Figure 5.5 and Figure 5.6).

*Table 5. 2. Average and range for the  $\delta^{18}O/\delta D$  values for rainfall and drip water (Vil-#10A, Vil-#10B, Vil-#1A, Vil-#1B) in Villars Cave.*

---

Rainfall	Vil-#10A	Vil-#10B	Vil-#1A	Vil-#1B
----------	----------	----------	---------	---------

---

$\delta^{18}\text{O}$	Average	-6.13	-6.19	-6.14	-6.35	-6.36
	SD	1.33	0.21	0.09	0.08	0.08
	Max	-3.30	-5.37	-5.97	-6.00	-6.06
	Min	-9.93	-6.76	-6.48	-6.73	-6.62
$\delta\text{D}$	Average	-37.99	-37.43	-37.03	-39.24	-39.44
	SD	9.37	1.68	0.97	1.15	0.76
	Max	-19.60	-30.81	-34.50	-33.70	-36.20
	Min	-67.40	-42.50	-39.90	-42.80	-41.70

*Table 5. 3 The delay time between drip-water rates and water excess during 2013-2019.*

Date	Vil-#1B& Water	Vil-#10A& Water	Vil-#10B& Water
	excess	excess	excess
2013/11/14-			
2014/11/18	38 days	7 days	3 days
2014/11/18-			
2015/12/25	63 days	8 days	5 days
2015/12/25-2017/2/7	60 days	5 days	36 days
2017/2/7-2017/12/14	180 days	19 days	--
2017/12/14-			
2018/12/20	28 days	4 days	--
Average lag time	74 days	9 days	15 days

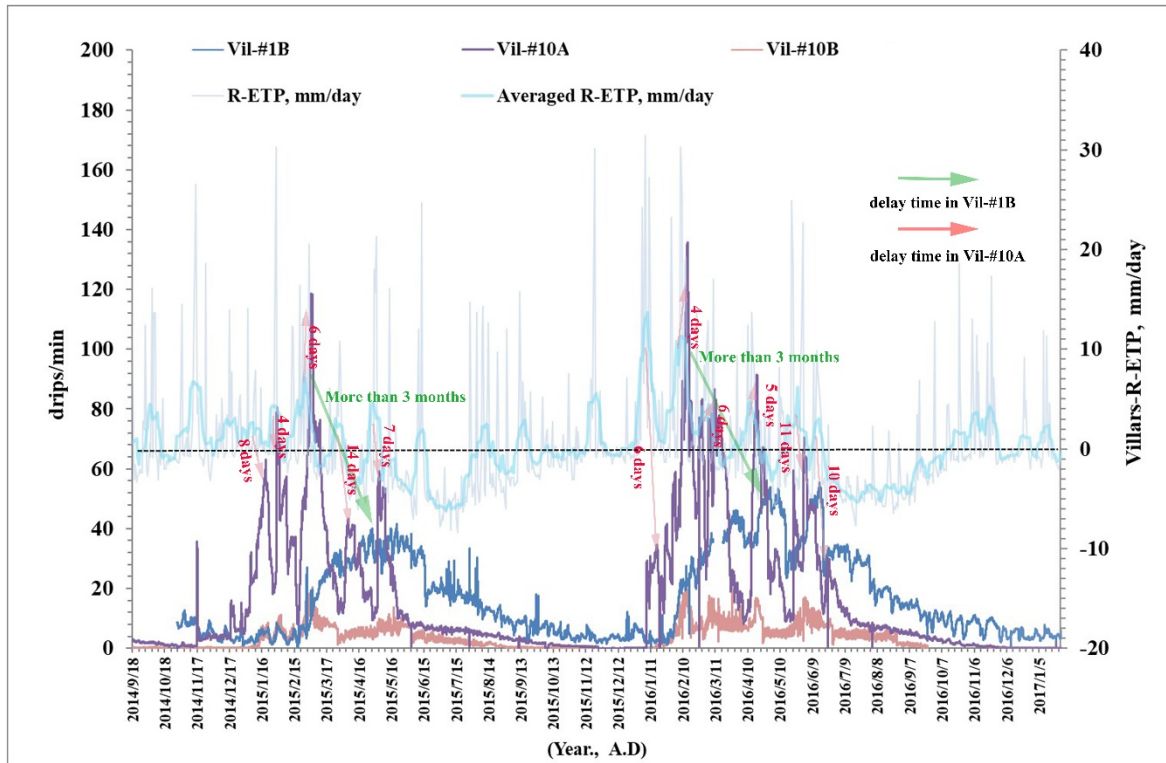
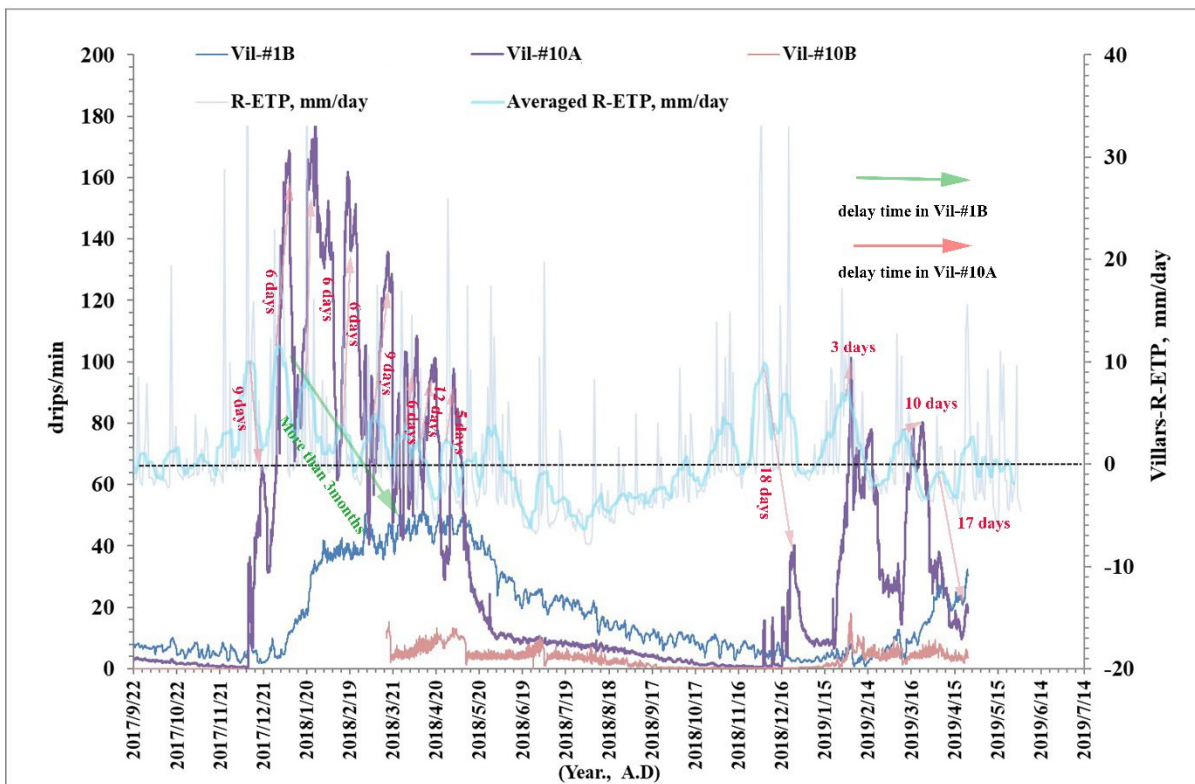


Figure 5. 5 Comparison of the variability of daily rainfall amount, R-ETP and drip-water rates during 2014-2016. Red arrows indicate the delay days between Vil-#10A and water excess.



*Figure 5. 6 Comparison of the variability of daily rainfall amount, R-ETP and drip-water rates during 2017-2019. Red arrows indicate the delay days between Vil-#10A and water excess.*

### 5.1.3 ERT gives a realistic image of the reservoirs

In this section, we present only one ERT image which is used here to verify the coherency between the pattern of the hydrological-isotopic model and the reality in terms of reservoir numbers and depths (Figure 5.7). Made on the 7th of January 2021 (Figure 5.7), this ERT resistivity model shows different karst zones above the Villars Cave that gives a broad image of the cave galleries and karst reservoirs more or less saturated. The following information is found in this image: (1) The resistivity which is higher than  $1000 \Omega \cdot m$  may be related to the unsaturated limestone. This value increases over  $3240 \Omega \cdot m$  in three red high resistivity zones (altitude: 165-175 m), which may be related to the upper galleries of Villars Cave (Figure 5.7); (2) The low green resistivity ranges from  $48 \Omega \cdot m$  to  $550 \Omega \cdot m$ , indicating the areas that can be filled with more water than the rock mass in winter, likely soil, epikarst, and some reservoir zones.

When comparing the cave topographical map with ERT image (Figures 2.1C& 5.7), we observe a very good agreement between cave galleries (map) and high resistivity zones (ERT). It is evident that Figure 5.7 shows three red zones (Zones A-C) with high resistivity values, which correspond to the three cave galleries depicted in Figure 2.1C. However, the ERT image does not provide precise information about the exact location of the lower gallery stations (Vil-#1A and Vil-#1B) (Figures 3.1C& 5.7). These stations are situated in a lower vertical section, potentially located near the side of Karst Store 1 and at a greater depth (Figure 3.1C).

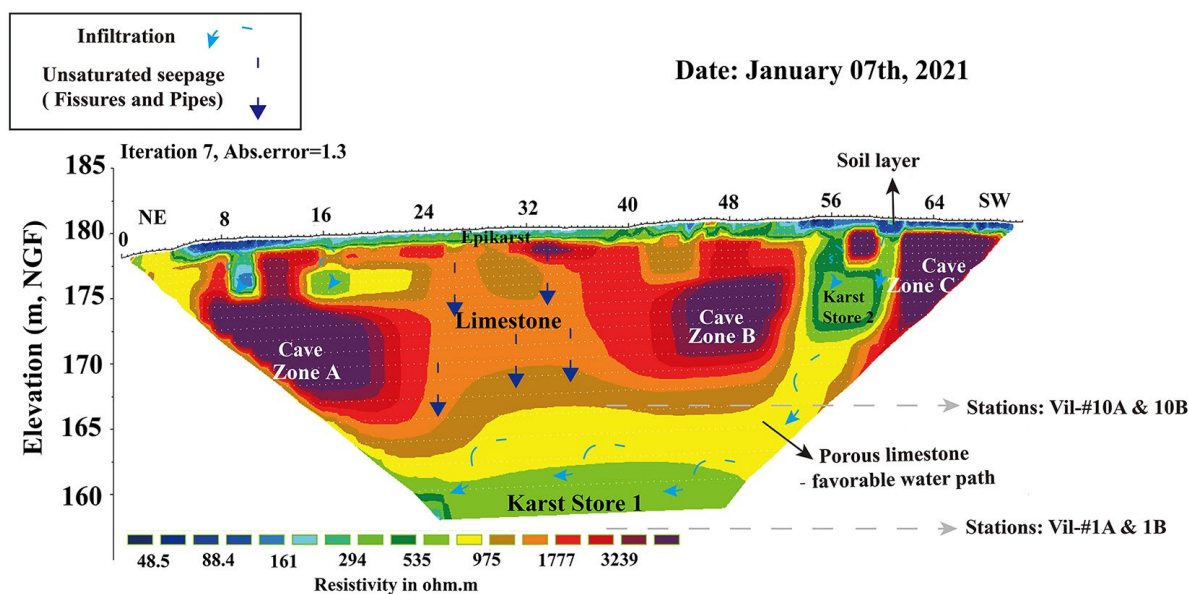


Figure 5. 7 The resistivity model of 07th/January 2021 with an electrode spacing of 1 m. The inversion was performed based on the concatenation of the data of all the two arrays (Gradient Array and Pole-Dipole Array), using Res2Dinv software to process data. The ERT image is well coupled with the simulation results of the isotope model. The dashed lines are the possible locations of the monitoring points.

#### 5.1.4 Simulations of the flowing rate of drip water

The links between different flow paths and water reservoirs can be described as follows: (1) F1 flow is from Soil Store, and outflows to Epikarst. (2) Karst store 2 can receive water flow from F4 and F8 and outflows in F7. (3) Karst store 1 can receive water flow from F7 and drain in F5. Modeled variations of the quantity of water stored in each reservoir during the 2006-2019 simulation period are plotted in Figures 5.8C, 8D, 8E. Results show, firstly, that there are considerable differences in water storage dynamics between individual water reservoirs. Secondly, the seasonal flowing successfully simulates higher/lower hydrological response discharge, agreeing with observed seasonal drip rates. Both reach a maximum drip rate, following winter water excess high values (Figures 5.3 & 5.8).

To assess the reliability of the model output, we conducted a correlation analysis between the simulated flux and the observed drip rate. This correlation is based on monthly values for all the studied periods from 2013-2019 (Figure 5.9). Results show that the correlations between Vil-#10A and F4 flow (from soil and epikarst stores), between Vil-#10B and F7 flow (from Karst store 2), and between Vil-#1B and F5 flow (from Karst store 1), are significant ( $p < 0.01$ ) with a high coefficient of correlation:  $R = 0.8$ ,  $R = 0.75$  and  $R=0.61$ , respectively (Figures 5.9A& 5.9B& 5.9C).

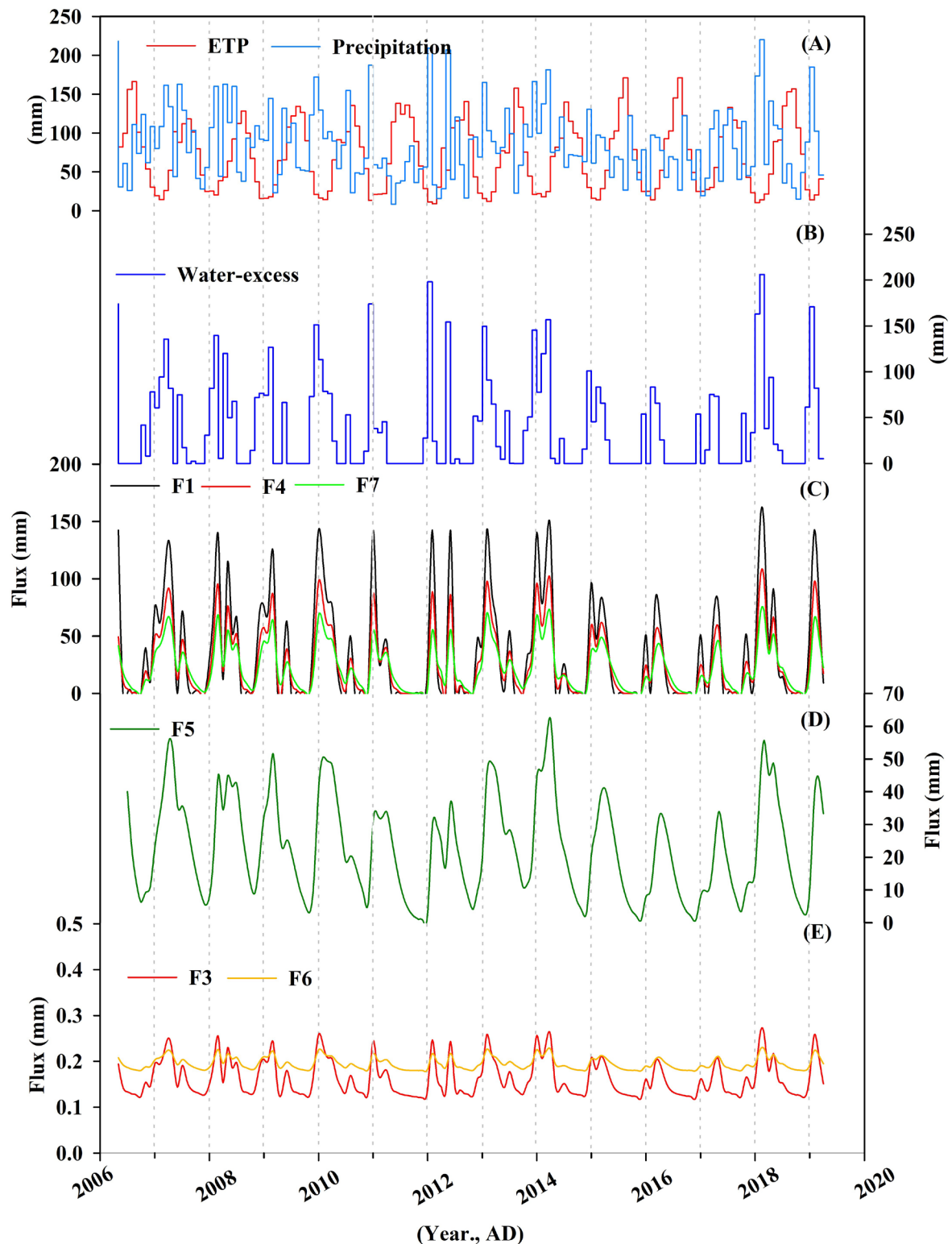


Figure 5.8 Model hydrological output for 2006-2019. (A) Comparison of local precipitation and ETP in Villars Cave. (B) Water excess (Precipitation minus potential evapotranspiration ( $P-ETP$ ) $>0$ ). (C) The modeled discharge (F1, F4, F7) in the unsaturated zone of Villars Cave. (D) The modeled discharge (F5) in the unsaturated zone of Villars Cave. (E) The modeled discharge (F3, F6) in the unsaturated zone of Villars Cave. Hydrological output is implemented as a python module. Examples are

provided for using it from <https://github.com/agriff86/karstolution>.

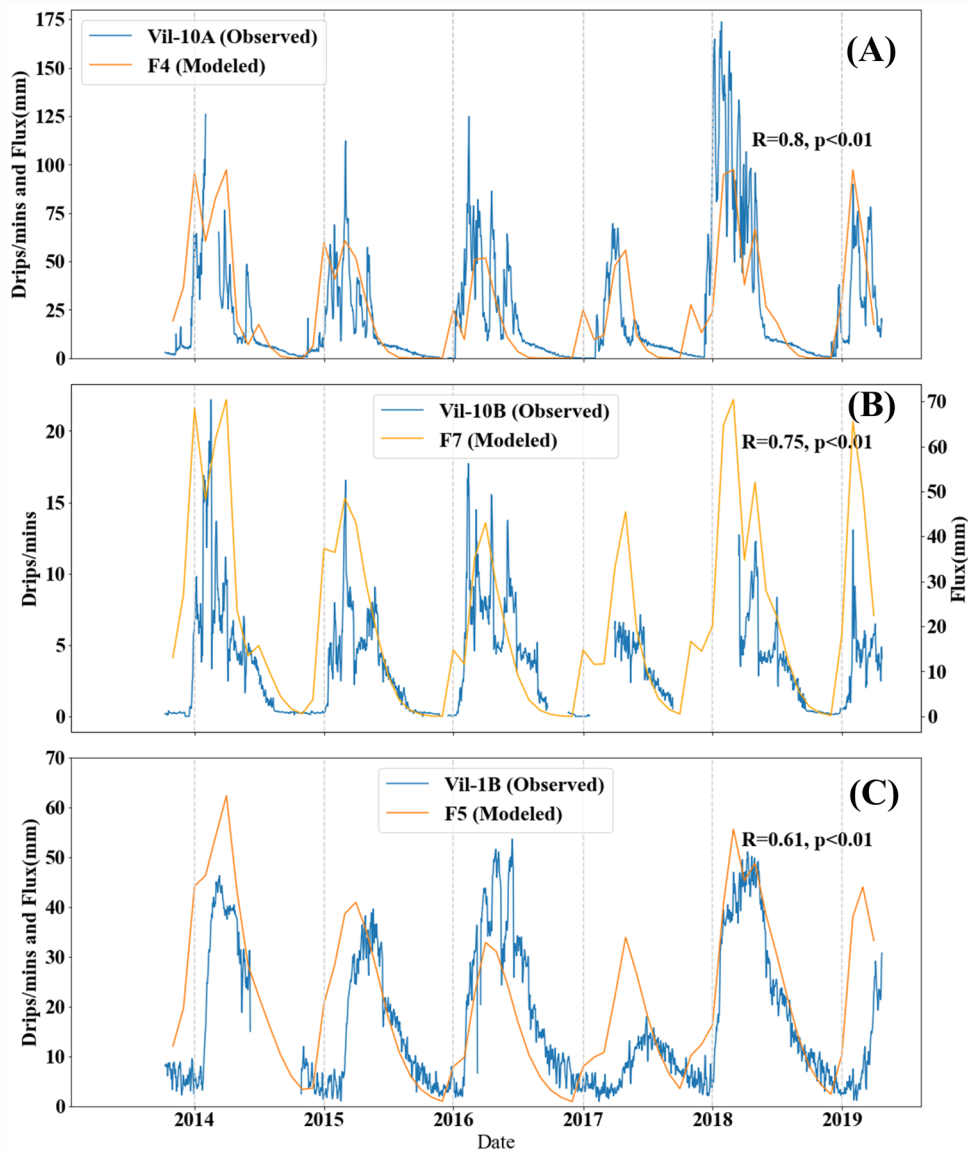


Figure 5. 9 Correlation and comparison between the simulated flux and the observed drip rate during 2013-2019. (A) Vil-#10A& F4 flow, (B) Vil-#1B & F5 flow, (C) Vil-#10B& F7 flow. Correlation is calculated on a monthly scale.

Compared to the behavior of the different reservoirs (Figure 5.10), the modeled output with the same vertical axis shows differences in the relative magnitude of individual water fluxes and obvious seasonal variability in all reservoirs.



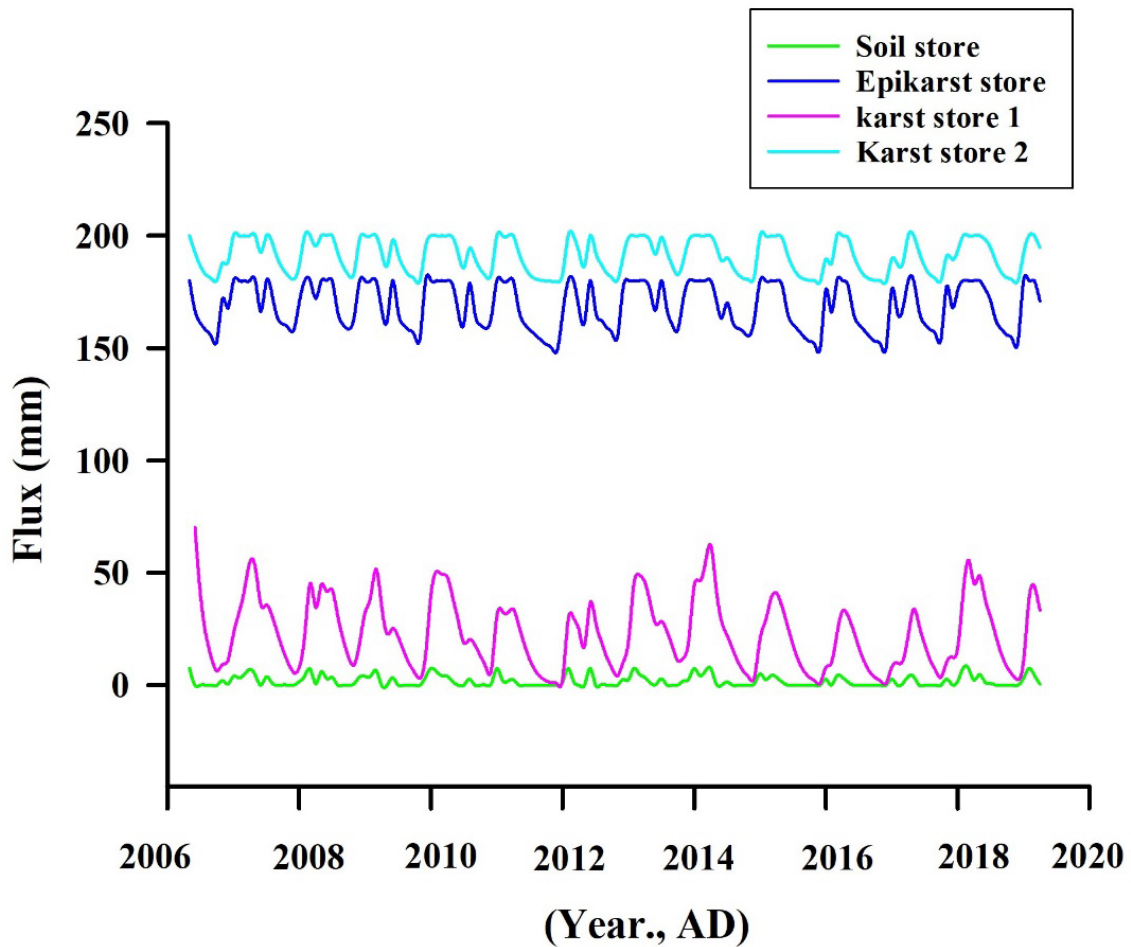


Figure 5. 10 The variability of modeled fluxes in the soil store, Epikarst store, and Karst store 2 and 1 with the same vertical axis.

In order to understand the hydrological variability of each reservoir separately, the water storage of Soil Store is very variable, with a magnitude from 0 to 9 mm (Figure 5.11A). Karst Store 1 shows a seasonal variation from 0 to 60 mm, and the magnitude variability of the Epikarst Store (from 150 to 180 mm) and of the Karst Store 2 (from 180 to 200 mm) is between the initial and maximum setting storage capacity (Figure 5.11B & 5.11C). Once the maximum storage capacity is exceeded, water infiltration overflows to the next reservoirs, explaining the flat shape of maximum flow periods (Figure 5.11B & 5.11C).

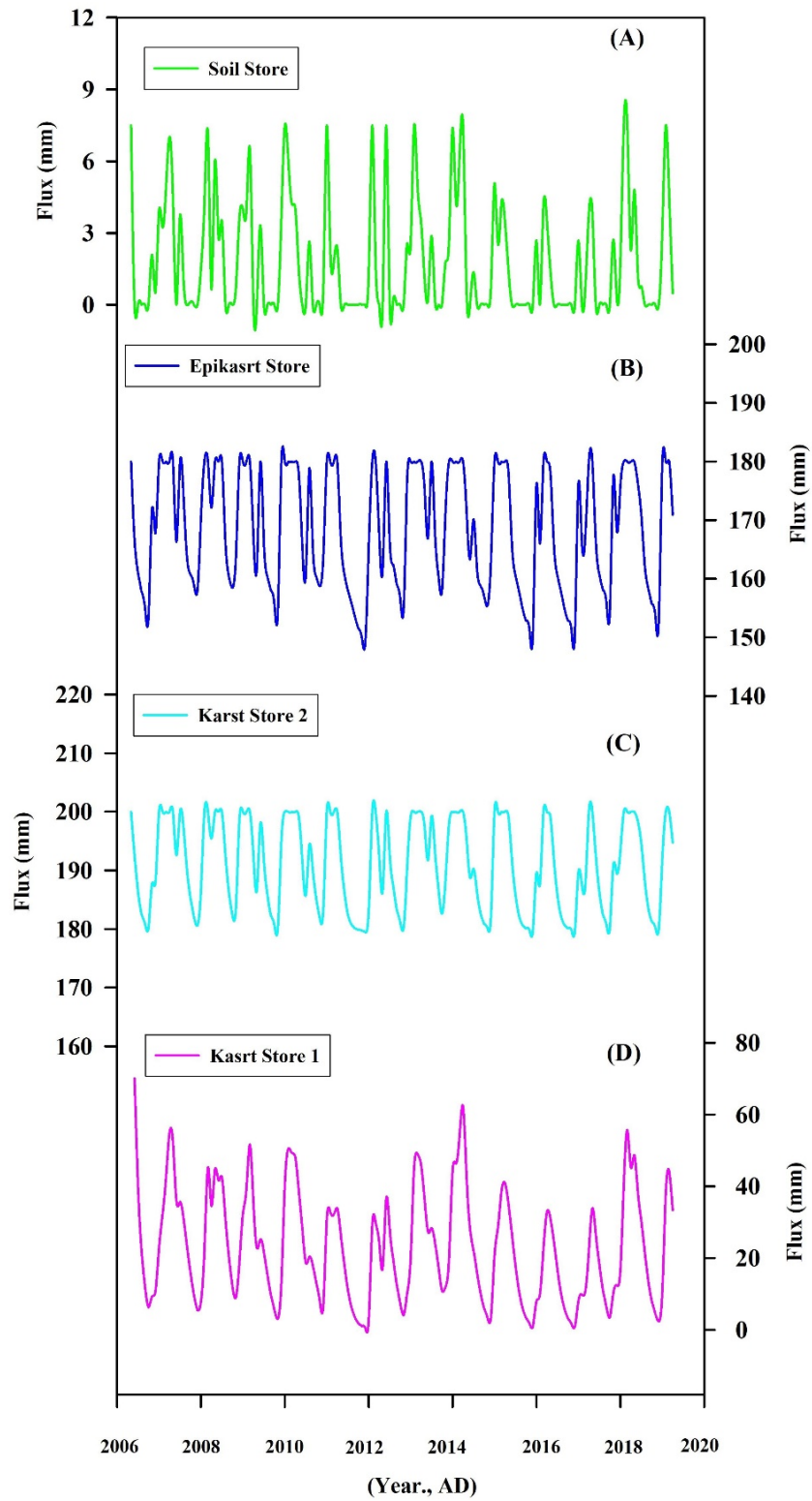


Figure 5. 11 The variability of modeled fluxes in the soil store (A), Epikarst store (B), and Karst store 2 (C) and 1 (D).

### 5.1.5 Simulations of isotopes in drip water

The Epikarst  $\delta^{18}\text{O}$  display different isotope variability amplitudes, when we set different F1 and Epicap value (Figure 5.12A). The amplitude is reduced when we set F1=0.1 and Epicap value=160, leading to values close to the observed at Vil-#10A station (about 1.5 ‰ maximum amplitude) (Figure 5.12A). When we test F1 = 0.95/0.5 and Epicap values = 100/50, the modeled Epikarst has a much larger variance (Figure 5.12A). We evaluated the impact of evapotranspiration (ETP) on Epikarst  $\delta^{18}\text{O}$  by examining the proportion of karst water ( $k_{\text{eevap}}$ ) across varying parameters (0.1, 0.04, 0.01). By applying a correction factor ( $K_{\text{d18O\_Epi}}= 0.04$ ) to account for the effects of ETP, we were able to generate a mean value of Epikarst  $\delta^{18}\text{O}$ , as illustrated in Figure 5.13.

Karst Store 2 simulation suggests that water feeding the Vil-#10B station (mean value=-6.14‰, SD=0.09 ‰) has a low variability amplitude (Figure 5.12B). Modeled data are in agreement with observed  $\delta^{18}\text{O}_d$  when the low F4 (F4=0.1) and high Ovicap value (Ovicap=180) were set in models (Figures 5.12B). Here too, when we test at F4 = 0.95/0.5 and Ovicap values = 100/50, the modeled Karst Store 2 has a much larger variance (Figure 5.12B). At Karst Store 1, the simulated  $\delta^{18}\text{O}_d$  gives a similar trend with lower gallery dripping points (Vil-#1A and Vil-#1B stations, mean value=-6.35, SD=0.08), when the low F5 value (F5=0.1) and high Ovicap value (Ovicap=180) were considered (Figure 5.12C).

Table 5. 4 The observed mean  $\delta^{18}\text{O}_d$  and mean drip rates in the different monitoring sites

		Cave monitoring sites	Observed mean $\delta^{18}\text{O}$ (‰)	SD	Mean drip rates (drip/mins)	SD
All-year infiltration	Weighted Rainfall		-6.24	0.56		
	Upper Gallery	Vil-#10A	-6.19	0.21	20.93	28.4
		Vil-#10B	-6.14	0.09	3.48	3.66
	Lower Gallery	Vil-#1A	-6.35	0.08	--	--
		Vil-#1B	-6.36	0.08	16.5	13.9
High infiltration (Nov-April year)	Weighted Rainfall		-6.75	0.78		
	Upper Gallery	Vil-#10A	-6.20	0.25	35.4	33
		Vil-#10B	-6.12	0.08	5.2	4.2
	Lower Gallery	Vil-#1A	-6.33	0.07	--	--
		Vil-#1B	-6.35	0.04	29.2	13.07

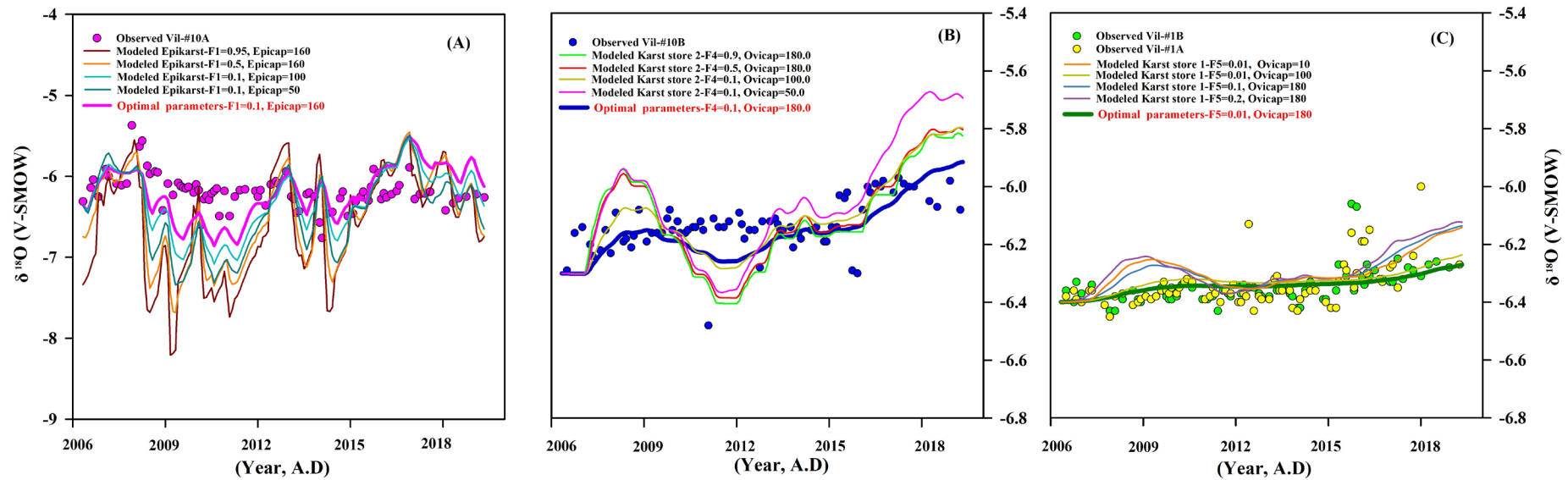


Figure 5.12 Optimization and the sensitivity test using different parameters in path processes ( $F$ ) and overflow ( $Epicap$  and  $Ovicap$ ) based on KarstFor model for Villars Cave. (A) Comparisons of modeled epikarst  $\delta^{18}\text{O}$  and observed Vil-#10A (upper gallery) in Villars Cave based on adjusting in  $F1$  and overflow ( $Epicap$ ) in Epikarst. (B) Comparisons of modeled Karst store 2  $\delta^{18}\text{O}$  and observed Vil-#10B (upper gallery) by adjusting in  $F4$  and overflow ( $Ovicap$ ) in karst store 2 in Villars Cave. (C) Comparisons of modeled Karst store 1  $\delta^{18}\text{O}$  and observed Vil-#1A and #1B by adjusting in  $F5$  and overflow ( $Ovicap$ ) in karst store 2 in Villars Cave (lower gallery). There is a temperature difference of 1 °C between different galleries with the upper gallery of 12.5°C and the lower gallery of 11.5°C; therefore, we set different evaporation ( $k\_d18O\_epi$ ) parameters in upper galleries (Vil-#1B) in a high value: 0.06‰ and in a lower value: 0.04‰ in low galleries (Vil-#1A and #1B). We did not consider the influence of humidity as it remained above 90% saturation throughout.

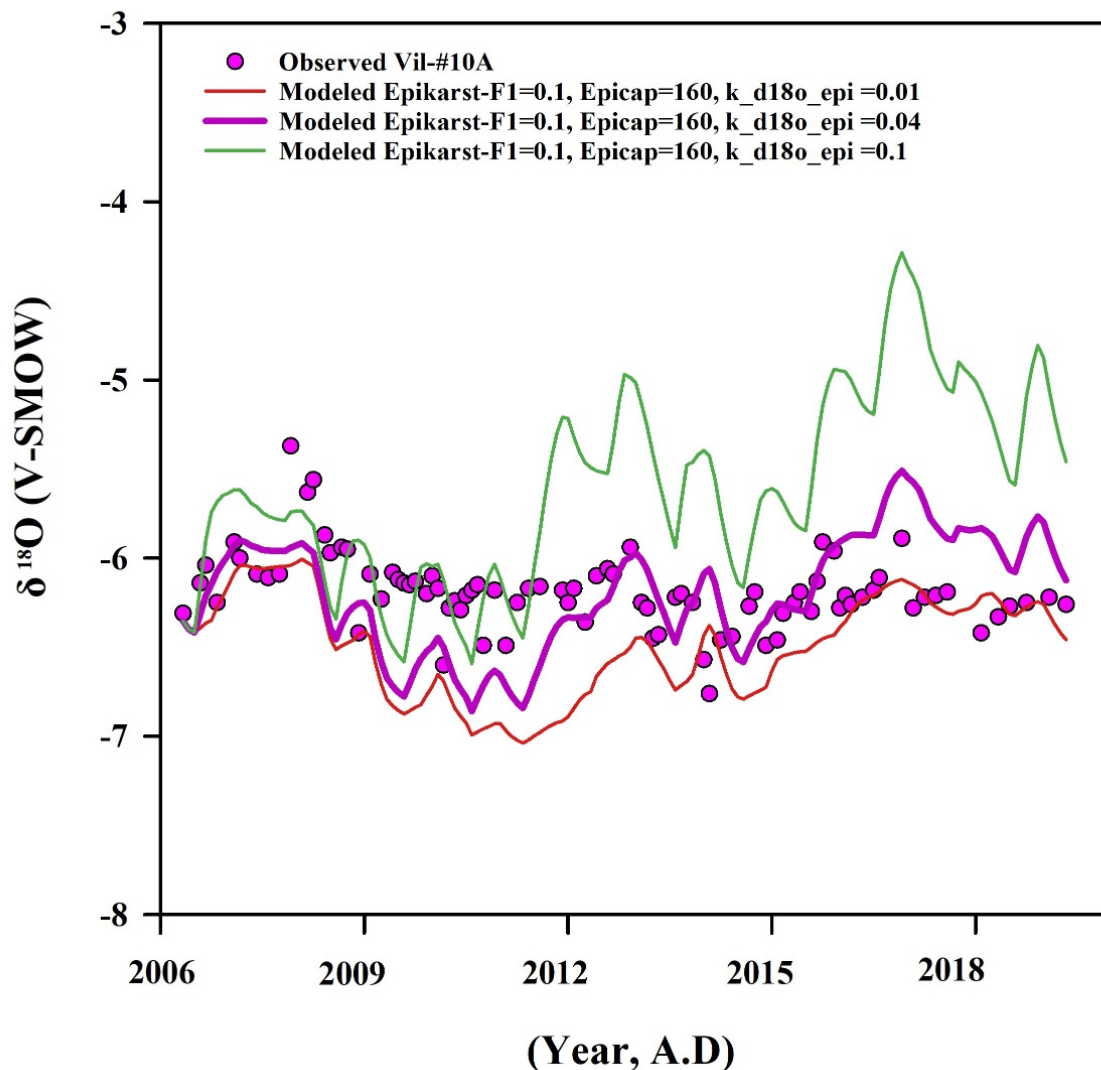


Figure 5.13 Optimization and the sensitivity test using different  $k_{d18O\_epi}$  parameters in path processes ( $F1=0.1$ ) and overflow ( $Epicap=160$ ) based on KarstFor model for Villars Cave.

## 5.2 Discussion

### 5.2.1. Linking observed drip stations to ERT image and KarstFor model

One challenging question is to attribute each dripping station in Villars Cave to a specific reservoir exit or flux conduit in the KarstFor model pattern. We utilized the time series of drip rates, where the variability indicates its more or less connected to water

excess variability. In this way, Vil-#10A is the only dripping station that exhibits a highly variable drip rate, which can be attributed to its direct connection to the Soil or Epikarst store (Figures 3.1 & 5.7). Therefore, we propose to locate the Vil-#10A station at the drainage exit of the Epikarst reservoir (F4 flow; Figures 3.1 & 5.7).

The upper ERT image, characterized by low resistivity values, suggests reservoirs that can be assimilated to Karst Store 2 (Figures 3.1 & 5.7). According to the drip rate change of Vil-#10B, more damped flows are observed compared to Vil-#10A. For this reason, we suggest to put it at the exit of the Karst Store 2 reservoir (F7; Figures 3.1 & 5.3& 5.7). The deepest part of the ERT profile (below 162m NGF) with low resistivity values (Figure 5.7), which may be explained by the presence of a deeper reservoir storage area, can be eventually connected to the lower gallery dripping stations Vil-#1A and Vil-#1B. However, Vil-#1B dripping station never stop, even during dry seasons. Therefore, we proposed that this site should be put at the drainage exit of the Karst Store 1 reservoir (F5 flow; Figures 3.1 & 5.3& 5.7).

Actually, the presented ERT image does not yet accurately reveal the exact location of the lower gallery stations (Vil-#1A and Vil-#1B), which are located in a different vertical section, possibly near the left side of Karst Store 1 and at a deeper position (Figure 5.7). In fact, the lower cave gallery (Vil-#1B) is situated beneath Karst Store 1, receiving its water supply from Karst Store 1 (Figure 5.7). By doing these attributions, we not only validate the modeled flowing processes but we show that, even at the same depth and close to each other in the upper gallery, two drip stations may be supplied by different flow paths and reservoir systems (Vil-#10A and Vil-#10B for example).

## 5.2.2. Present and future long-term changes of Villars Cave drip

### water $\delta^{18}\text{O}$

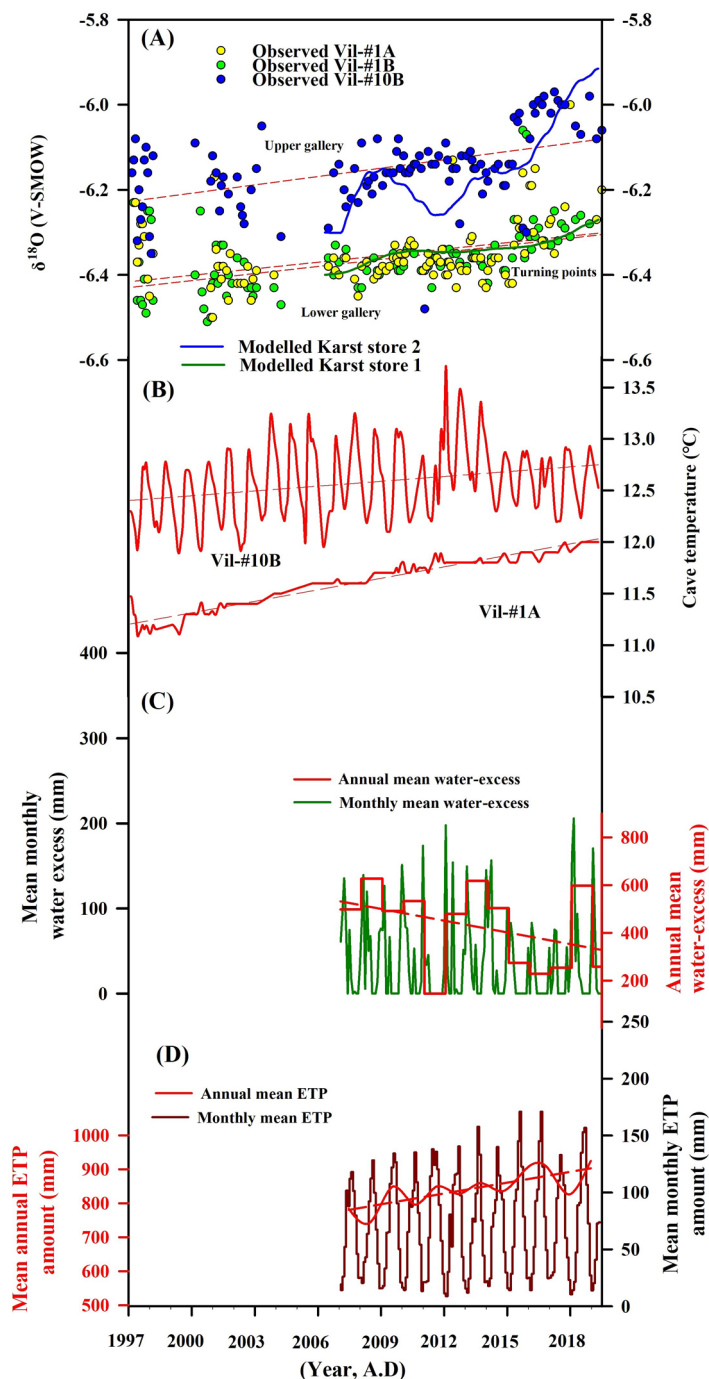


Figure 5. 14 (A) Modeled  $\delta^{18}\text{O}$  in the Karst store 1 & 2 and observed Vil-#10B (Upper gallery) and Vil-#1A/#1B (lower gallery) in Villars Cave. (B) Inside cave temperature (Vil-#1B and Vil-#10B), (C) Mean annual outside water excess calculated on a monthly scale. (D) Mean annual outside ETP calculated on a monthly scale. The red-fitted linear



*regression indicates its inter-annual change trend.*

The modelled and observed data of  $\delta^{18}\text{O}_d$  show a long-term increasing trend between 2006 and 2019 at an inter-annual scale, as depicted in [Figure 5.14A](#). The enriched trend of drip water  $\delta^{18}\text{O}$  is parallel to the interannual decline of the water excess ([Figure 5.14C](#)) due to the increasing trend of the potential evapotranspiration (ETP) ([Figure 5.14D](#)). This finding suggests that this  $\delta^{18}\text{O}_d$  trend may be the consequence of temperature increase due to global warming.

To give an insight into the possible future evolution of Villars Cave drip water, we used climate data from the dynamically downscaled and de-biased CNRM-CM5 global model under the RCP8.5 scenario as input for the KarstFor model to simulate  $\delta^{18}\text{O}_d$  until 2100 ([Figure 5.15](#)). The scope of such an analysis aim to preliminary characterize the future trend of  $\delta^{18}\text{O}_d$ , without accounting for the uncertainty associated with the climate projections, which would require a multi-model analysis. Nevertheless, this preliminary investigation confirms our physical interpretation made through the use of observed data: as temperature increases ( $3^\circ\text{C}/100$  years, [Figure 5.15B](#)), the rainfall of Villars Cave decrease ( $-15\text{mm}/100$  years, [Figure 5.15C](#)) the evaporation of Villars Cave intensifies ( $25\text{mm}/100$  years, [Figure 5.15D](#)), leading to a reduction in water-excess ( $-40\text{mm}/100\text{years}$ , [Figure 5.15E](#)). Similarly, to input rainfall oxygen isotopes ([Figure 5.15A](#)) in the KarstFor model, we used the equation  $\delta^{18}\text{O}=0.15T-7.93$  ([Zhang et al., 2020](#)) to simulate the rainfall oxygen isotopes during the next 100 years in Villars Cave. Based on these inputs KarsFor model outputs show a well-marked increase in isotopes in several reservoirs, including Epikarst, Karst store 1, and Karst store 2 ([Figure 5.15A](#)).

We believe that two main reasons may explain this increasing trend in the isotopes observed in the various reservoirs, linking with the different Villars dripping stations. Firstly, a positive correlation is observed between rainwater isotopes and temperature

at Villars (Zhang et al., 2020). As global warming continues over the next 100 years, there will be a rise (enrichment) in rainwater oxygen isotopes that enter the soil and the epikarst (Figure 5.15A). Secondly, this increase also is likely accompanied by a possible increase in soil isotope fractionation because of higher ETP in the future (Figure 5.15D).

The fact that the water excess will decrease in the next 100 years (-40 mm/100 years) (Figure 5.15E), which should theoretically decrease the  $\delta^{18}\text{O}$  of the infiltrated water. This is because water excess will only occur during the colder months under the context of global warming, during which the  $\delta^{18}\text{O}_r$  is the lowest which would typically lead to a depletion in the  $\delta^{18}\text{O}$  value of the infiltrated water as input. However, we observe the opposite, which is an increase in the reservoir  $\delta^{18}\text{O}$  values (Figure 5.15A). As a consequence, we can say that the main factor that drives the future evolution of the infiltrated  $\delta^{18}\text{O}$  is the rainfall  $\delta^{18}\text{O}$ , which will increase in the future because of the increase in the temperature and possible fractionations due to the ETP increase.

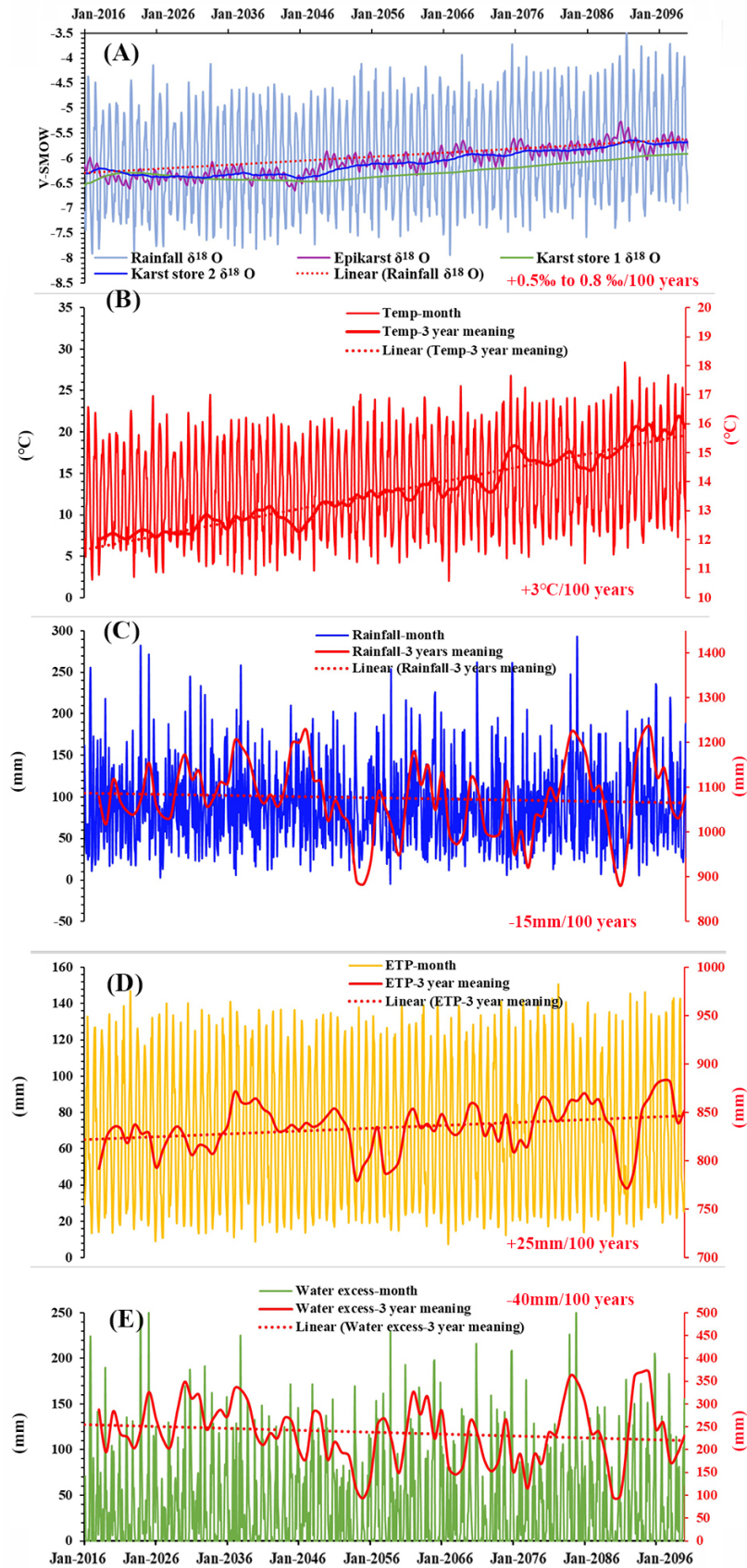


Figure 5. 15. (A) Modeled and predicted  $\delta^{18}\text{O}$  in the Karst store 1 & 2 and Epikarst in Villars Cave from 2016 to 2100. (B) Outside cave temperature a monthly (left axis) and

annual (right axis) from 2016 to 2100, (C) Mean outside rainfall amount calculated on an annual scale from 2016 to 2100. (D) Mean outside ETP calculated on a monthly (left axis) and annual (right axis) scale from 2016 to 2100. (E) Mean outside water-excess ( $\text{Rainfall}-\text{ETP}>0$ ) calculated on a monthly (left axis) and annual (right axis) from 2016 to 2100. The fitted linear regression indicates its inter-annual change trend. To input rainfall oxygen isotopes in the KarstFor model, we used the equation  $\delta^{18}\text{O}=0.15T-7.93$  (Zhang et al., 2020) to simulate the rainfall oxygen isotopes in the next 100 years in Villars Cave, and temperature data is based on monthly outside cave temperature. We set the proportion of karst evaporation water ( $k_{\text{eevap}} = 0.016$ ) to predict reservoir  $\delta^{18}\text{O}$  according to the ERT trend in next 100 year.

### 5.2.3 Infiltration “time delay” versus isotopic mixing process

The karst hydrological model results suggest that the drip water at different monitoring sites comes from different reservoirs. In the upper gallery, the Vil-#10A dripping station is controlled by fewer reservoirs connected to the fracture zone from the ERT image (Figure 3.1 & 5.7). Consequently, Vil-#10A has the largest variable  $\delta^{18}\text{O}_d$  values (Figure 5.1B). Vil-#10B from the upper gallery and Vil-#1A and Vil-#1B from the lower gallery support the initial hypothesis that these reservoirs are distinct (Genty et al., 2014a; Jean-Baptiste et al., 2019). Regarding low variability of the drip  $\delta^{18}\text{O}$ , we think that the long infiltration mixing isotopic process would produce very stable  $\delta^{18}\text{O}$  drip values at upper and lower dripping stations on the annual timescale as we observed over a very long period (> 20 years) (Figure 5.1C and Figure 5.14A).

As mentioned before, one of the Villars characteristics is the small (0.2 ‰), but significant, difference between the upper and lower gallery  $\delta^{18}\text{O}_d$  (Vil-#10B and Vil-#1A/1B) (Figure 5.14A; Table 5.4). This difference might be controlled by reservoir overflows in the infiltration zone as suggested by Genty et al., (2014). Lower values of rainfall  $\delta^{18}\text{O}$  occur during the high recharge period in winter. The reservoir storage exceeds the water level and activates the overflow to supply water to the deeper reservoir, causing the overflow to mix with the Karst store 1 water to supply the lower gallery drip stations (Vil-#1A and Vil-#1B). Conversely, during summer, the  $\delta^{18}\text{O}_r$  is

much higher, coinciding with a low recharge period leading to the absence of low  $\delta^{18}\text{O}_d$  overflow.

The time delays between the water excess and the drip rates are a few days to several months. What we need to clarify is that “time delay” is not the actual time of the water infiltration, but rather the time is necessary to “fill” the karst reservoirs and “push” the water downwards towards the dripping stations in a “piston flow” system. Actually, the actual mean age of the drip water is much older ([Genty et al., 2014a](#); [Jean-Baptiste et al., 2019](#)).

To resolve this apparent inconsistency between infiltration “time delay” and isotopic mixing time, we have to imagine a piston flow system in which the change in drip rate is due to a change in hydraulic charge related to the filling of the reservoir that feeds the dripping station. Then, hydraulic pressure, linked to water excess changes, determines the dripping rate variations. However, the mixing process and overflow determine the isotope values of the water, which is always mixing with “old water” inside the reservoirs. Consequently, we can distinguish the “time delay” that applies to the water excess/drip-rate variations, while the “isotopic mixing transit time” concerns the mean age of the water that infiltrates through the reservoirs ([Genty et al., 2014a](#)).

#### **5.2.4. Implications for speleothem records**

The karst hydrological model that we used here allows us to simulate and to understand the sensitivity of the dripping stalactites feeding stalagmites to the rainfall input signal. Consequently, it could be used to assess whether speleothems from different sampling points in the cave are suitable for reconstructing paleoclimate change. For example, if a stalagmite is fed by a very variable dripping point with a highly seasonal isotopic signal, we should be able to reconstruct past seasonal climatic

signals. On the opposite, if the feeding of a stalagmite is well-damped, with no seasonality in the  $\delta^{18}\text{O}_d$ , then it will be more adapted to study longer climatic trends.

Model simulations show that deeper drip stations fed by reservoir overflows are subject to isotopically biased low values, which is important for palaeoclimatological studies. More tests on actively growing calcite from different levels of Villar Cave will shed new light on this issue. The hydrological modeling method we used here also made a quantitative assessment of the relative importance of temperature, precipitation, and water balance changes, especially for the time and amount of groundwater recharge, which is of first importance for the interpretation of the speleothem  $\delta^{18}\text{O}$ .

Understanding processes and variability of the dripping isotopic composition water has consequences on the interpretation of speleothem fluid inclusions. In the case of a well-mixed seepage reservoir supplying a dripping station, there is no seasonal variation in the  $\delta^{18}\text{O}$  of cave drip water, implying that fluid inclusions should represent the average annual (or multi-year) rainfall water composition. Moreover, local isotopic differences in the drip water, like the one observed and modeled in Villars Cave between lower and upper galleries ( $-0.2\text{‰}$ ), will produce differences in the isotopic composition of contemporaneous speleothems, adding more variabilities to other factors like kinetics fractionations.

KarstFor model helps to understand the infiltration and to put reasonable hypotheses about the presence of reservoirs and their connection. With the help of ERT, we get a realistic image of the conduits and reservoirs above the Villars Cave. In this case, the KarstFor model can be used to simulate the answer of the local karst system by setting different parameter inputs, such as infiltration into the reservoir water more or less seasonally, more or fewer periods of heavy rainfall, allowing us to

understand the reason why the variability in dripping rate and isotopic are different. The forecasting using models may even go further and, for example, simulate the stalagmite isotopic composition by using an inside-process model as suggested by [Deininger and Scholz, 2019](#) (ISOLUTION model). Under future global warming, the oxygen isotopes of drips and stalagmites may be slightly enriched due to the reduction of water excess based on KarstFor model.

## 5.3 Conclusions

Based on a long hydrological and isotopic monitoring of the rainfall and drip waters in the Villars Cave, we were able to study, with the help of a hydrological-isotopic conceptual model, the behavior of the rainfall infiltration in a karst environment. The Villars Cave is an ideal study case because its dripping stations, which have been monitored for more than 20 years, are situated at different depths in the cave, and have different hydrological characteristics fed by different pathways and reservoirs. The geometry of the first direct images of the reservoirs obtained with ERT measurements above the cave, combined with the geometry of the conceptual model, helped us to attribute each dripping station to a specific place. After having fixed the parameters used in the karst hydrological model ([Bradley et al., 2010](#); [Baker et al., 2013](#); [Treble et al., 2013](#); [2019](#)), simulation outputs lead to the following conclusions:

- (1) the seasonality of the rainfall infiltration characterized by the water excess (or efficient rainfall) is well simulated in epikarst zones and the different reservoir overflows; the closest dripping station, Vil-#10A, does show the highest isotopic variability demonstrating its connection to these sub-surface reservoirs;
- (2) the “apparent” time delay between water excess and the different dripping stations calculated by a cross-correlation method reveals that the time lags go from a few days to several months depending on the depth of the station and its inertia linked to reservoir behaviors; this “apparent” time delay was correctly simulated by the KarstFor model, it is the consequence of the recharge that push the infiltrated water in a “piston flow” system; actual water transit time is much longer as proved by former studies;



- (3) the small but constant isotopic difference between the upper and lower galleries' drip water, suggests that the -0.2 ‰ lower isotopic values found in the deeper gallery are due to overflows that are likely to occur during the winter season when the  $\delta^{18}\text{O}_r$  is lower; here too model simulation and observations are coherent;
- (4) the drip stations in the two galleries show a  $\delta^{18}\text{O}_d$  long-term variation, likely due to the  $\delta^{18}\text{O}_r$  change and possibly also controlled by a higher global external temperature leading to more ETP. Our future simulations suggest that global warming will likely lead to an increase in  $\delta^{18}\text{O}_d$  over the next 100 years.

The combination of a long drip rate and isotope monitoring, and modeling linked to an actual pattern of reservoirs seen by ERT measurements, is a novel and promising approach to studying the origin of differences observed in the flows and the isotopic compositions of dripping sites in caves. Indeed, this approach appears useful to estimate the consequences of any modifications of the climatic conditions above a cave, especially changes in rainfall intensities, seasonality, and temperatures, due to climatic changes.

# **Chapter 6 - Using Time-lapse electrical resistivity tomography to visualize the karst unsaturated zone**

---

## Introduction

Understanding the dynamics and geometry of karst reservoirs is critical for the knowledge of hydrological processes in cave systems and their impact on the isotopic composition of drip water. Previous studies conducted in Villars Cave have shed light on the seasonal infiltration patterns using isotopic and drip rate analyses ([Genty et al., 2014a](#)) and rainfall sources ([Zhang et al., 2020](#)). However, several significant questions related to the dynamics and geometry of karst reservoirs still need to be addressed. These questions include the determination of the size, number, and shape of unsaturated karst reservoirs, as well as their dynamics ([Genty et al., 2014a](#)).

Villars Cave is a shallow cave developed in Jurassic limestone characterized by covered at some surface places by thin quaternary sediments and some weathered limestone zones that may affect the drip flow rate and geophysical signals, making it an ideal site for geophysical research. In this study, we applied the 2D Time-Lapse Electrical Resistivity Tomography (TL-ERT) method to investigate and monitor the subsurface geological features above Villars Cave, over a monitoring period of 3 years (February 2020 to January 2023). The purpose of this study is: (1) to visualize and locate water reservoirs, wetting fronts, soil layers, and precise cave galleries and also to document their seasonal resistivity variations, (2) to explore the relationship between resistivity and hydrological changes in the seepage zone above the

cave galleries, (3) to identify the preferential water flow paths above the unsaturated zone of Villars Cave.

**Chapter 6 is divided into two parts:**

- (1) The first part presents the results of ERT with a 1-meter spacing, which allows the visualization of unsaturated areas, reservoirs, caves, and topsoil layers as well as their seasonal changes. This part of the chapter 6-1 is linked to the article 3.
- (2) The second part of the chapter presents the results of ERT with a 1.5-m spacing, which can visualize hydrological changes as deep as 30 m. The outcomes obtained from the ERT conducted with a spacing of 1.5 meters confirmed the results in HAC method utilized in Part I.

**Article 3:** *Jian Zhang, Colette Sirieix, Dominique Genty, Cécile Verdet, Fabien Salmon, Shan Xu, Sylvain Mateo, Marie Larcanché, Stéphane Bujan, Ludovic Devaux. Imaging hydrological dynamics in karst unsaturated zones by time-lapse electrical resistivity tomography. Science of the Total Environment (under review)*

## Chapter 6-Part I ERT measurement with a 1m spacing

### Abstract

The hydrodynamics of karst terrain are highly complex due to the diverse fractures and reservoirs within limestone formations. The time delay between rainfall events and subsequent flow into reservoirs exhibits significant variability. Unfortunately, these hydrological processes are not easily visualized in karst topography. However, subsurface geophysics, specifically 2D time-lapse electrical resistivity tomography (ERT), provides an effective method for studying the relationships between hydrological and geophysical features. In our research, we applied ERT in the Karst Critical Zone (KCZ) to visualize specific karstic zones, including cave galleries, water storage reservoirs, wetting fronts, soil layers, and potential preferential flow paths down to a depth of 20 meters. To capture spatial and seasonal variations in resistivity, we presented a comprehensive approach by combining seventeen inversion models obtained between February 2020 and January 2023 above Villars Cave in SW-France—a well-known prehistorical cave. We used a multi-dimensional statistical technique called Hierarchical Agglomerative Clustering (HAC) to create a composite model that divided the synthetic ERT image into eight clusters representing different karst critical zones. The ERT image clearly visualized the cave gallery as areas with high resistivity values that remained consistent throughout the seasons. Through our analysis, we discovered a

close seasonal relationship between water excess and resistivity variations in most infiltration zones, with time delays increasing with depth. The karst reservoirs, located at significant depths compared to other clusters, displayed sensitivity to changes in water excess but were primarily affected by fluctuations in water conductivity, particularly during summer or dry periods. These findings have significant implications for predicting rainwater infiltration pathways into caves, thus aiding in the conservation and preservation of prehistoric caves and their cultural heritage.

## **6.1 Results**

### **6.1.1 ERT measurements**

The initial electrical resistivity tomography (ERT) survey conducted in Villars on February 18th, 2020 involved testing various array configurations, including Dipole-Dipole, gradient, and Pole-Dipole arrays, both in forward and reverse array. After evaluation, we ultimately opted to use the concatenation of Pole-Dipole with gradient array, employing an electrode spacing of 1 meter above the Villars Cave. This particular array configuration was chosen because it offered better visualization of deeper regions and provided more accurate imaging of the shallow layers ([Appendix Figures 1-4](#)).

Main measurement results are gathered in 17 ERT images made from February 2020 to January 2023 ([Figure 6.1](#)). The ERT profile, from northeast

(NE) to southwest (SW) on a 71 m-long profile, covers the Bajocian and Bathonian limestone formations (Figure 2.1C). Here, strong resistivity contrasts are observed, giving a broad picture of the cave galleries and karst reservoirs, which are more or less saturated (Figure 6.1).

The distribution of the relative frequency (Figure 6.2) suggests that the resistivity data are mainly concentrated between 245  $\Omega\cdot\text{m}$  and 9772  $\Omega\cdot\text{m}$ , accounting for 91 % of the whole type data set. However, the resistivity above 9772  $\Omega\cdot\text{m}$  accounts for less than 4% of the entire type of data-set (Figure 6.2). The highest values (165–178 m NGF) correspond to the cave, and the lower values (<245  $\Omega\cdot\text{m}$ ) correspond to the top-soil. According to the frequency analysis of resistivity presented in Figure 6.2, the median resistivity of the limestone in Villars Cave is 1521  $\Omega\cdot\text{m}$ , which is higher than the resistivity of the nearby well-investigated geophysical site (Lascaux Cave) with a median of 556  $\Omega\cdot\text{m}$  (Coniacian and Santonian limestone) (Xu et al., 2016; Verdet et al., 2020). This difference suggests that the limestone in Villars Cave has undergone less weathering compared to the limestone in Lascaux Cave.

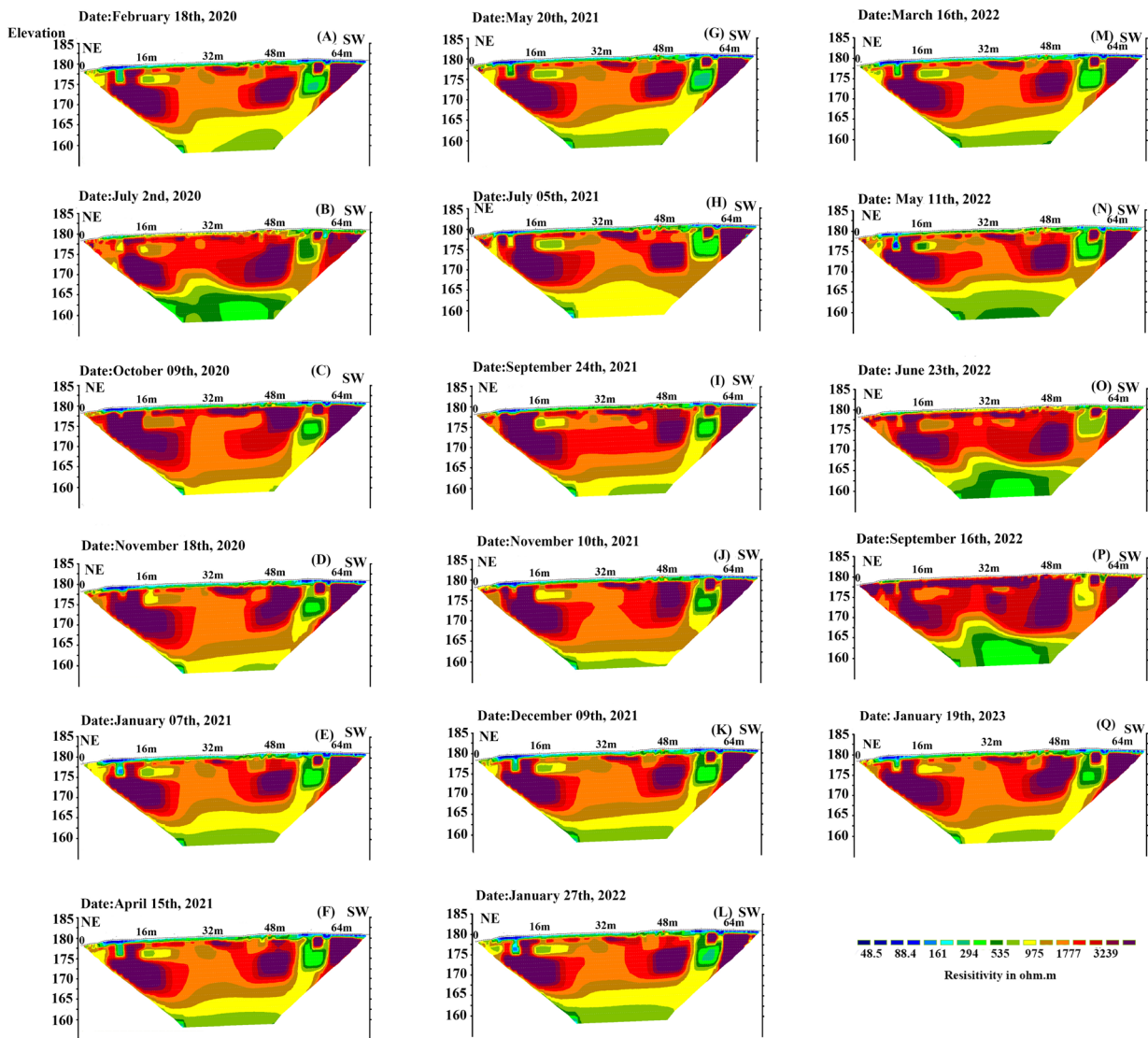


Figure 6. 1 The specific electrical resistivity distribution of line 71 m above Villars Cave from Feb/2020 to Jan/2023. The inversion was performed based on the concatenation of the data of the two arrays (Gradient Array and Pole-Dipole Array), using Res2Dinv software to process data.



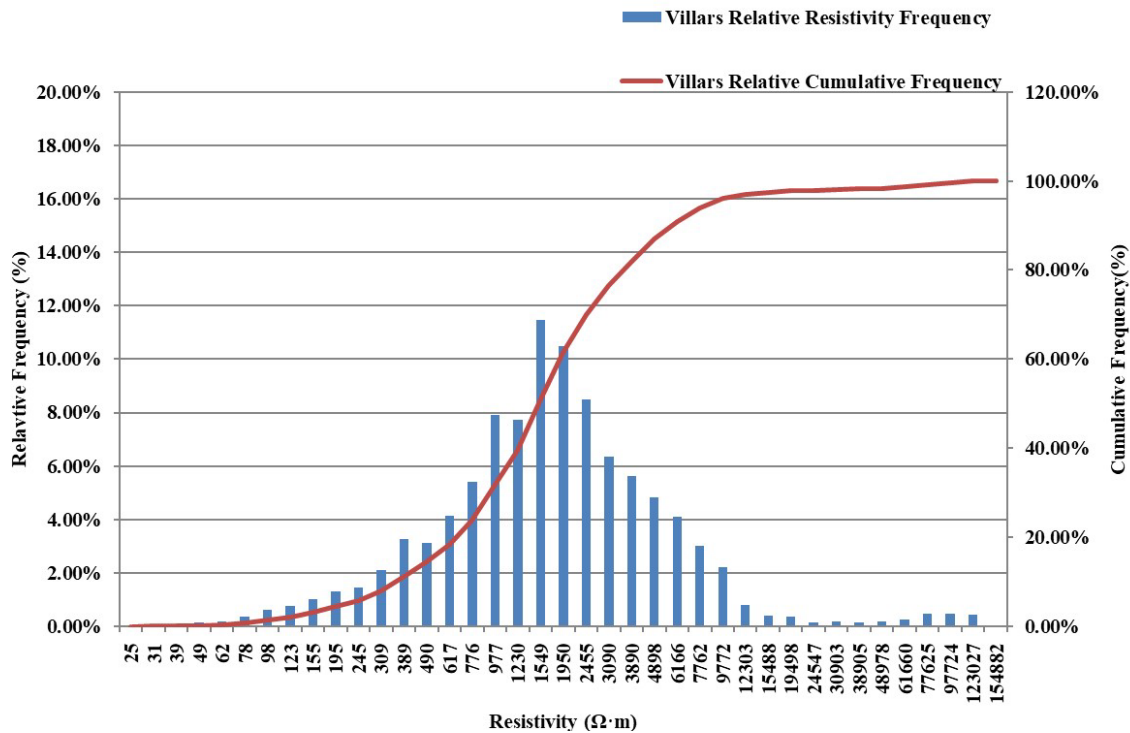


Figure 6. 2 Relative frequency and cumulative frequency of the concatenation of two arrays (Gradient Array and Pole-Dipole Array) for the whole data set.

A detailed case study was used to show the details of the different ERT properties in the image at the Villars site on 7th/January 2021 (Figure 6.3). The following information can be extracted from this ERT image: (1) The resistivity exceeds 3240  $\Omega \cdot m$  in three red high-resistivity zones (168–178 m NGF), possibly corresponding to the three galleries of Villars Cave (Figure 6.3; Figure 2.1C). (2) The low green resistivity of the conductive part ranges from 161  $\Omega \cdot m$  to 535  $\Omega \cdot m$ , indicating that these zones may contain more water or clay content, possibly reservoirs and wetting fronts (Figure 6.3). (3) It is worth noting that, at the surface, the resistivity decreases quickly on the right part of the profile (blue colors near the surface) between 5-13 m and about 52-71 m (NE-SW direction) along the profile, with an average resistivity of less than 100  $\Omega \cdot m$  (Figure 6.3).

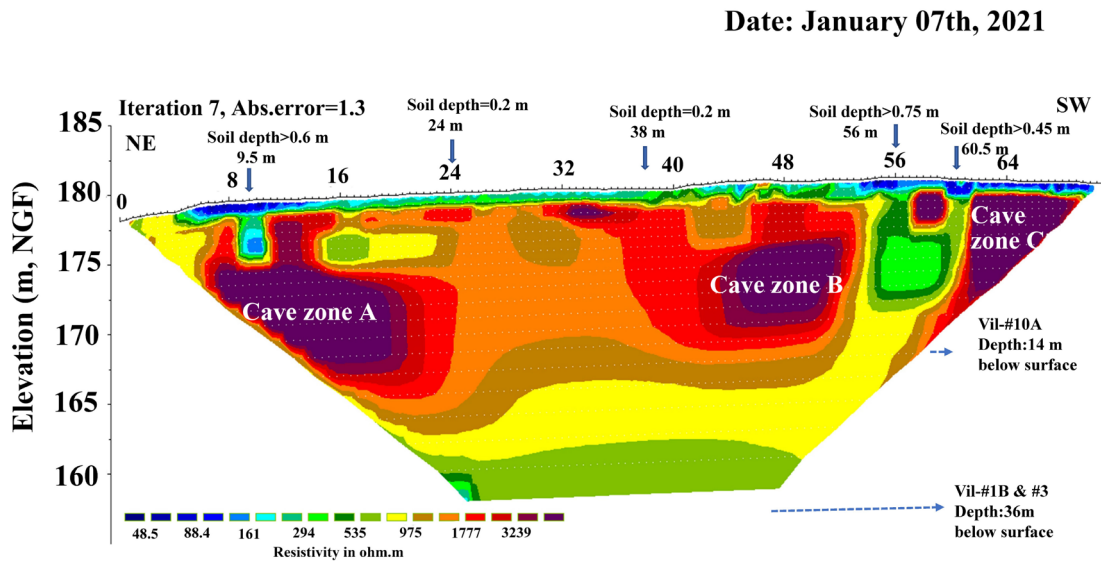


Figure 6. 3 The resistivity model of 07/January 2021 with an electrode spacing of 1 m above the Villars Cave. The Zone A-C of the images corresponding to the identified three cave galleries in Figure 3.1C.

The study presented in [Appendix Figure 5](#) utilized Res2DMod software for model configuration and we use Res2Dinvx64 software for inversion. The ERT observation data of Villars Cave was simulated by incorporating three high-resistivity zones and low-resistivity zones representing the surface and subsurface layers ([Appendix Figure 5](#)). By comparing the simulated results with the observed data, similar trends and patterns were observed in [Figure 6.3](#), indicating that the model effectively replicated the resistivity distributions in Villars Cave. Additionally, an experiment was conducted by increasing the resistivity value in the surface layer, revealing that these changes did not affect the resistivity values in the deeper layers ([Appendix Figure 6](#)). Furthermore, [Appendix Figure 7](#) was conducted by removing the low resistivity values in the deeper layer to investigate the impact on the inversion results. Interestingly, the

changes in the resistivity of the deeper layer were found to correspond with the modifications made in our modeling approach. This suggests that the lower part of the model reflects the actual subsurface resistivity distribution in ERT monitoring image in [Figure 6.3](#).

### **6.1.2 HAC method applied to ERT image classifications**

The HAC method we used with Minitab® version (19) is based on a correlation matrix through the normalized original resistivity data. Each resistivity image consists of 21 levels, and two, three, or more clusters can be classified ([Xu et al., 2017](#)). The electrical similarity of blocks between different clusters decreases with time as the distance at which they merge increases. Conversely, blocks belonging to clusters are merged at very low distances, exhibiting similar electrical behaviors (also see Method section). The statistical parameters for each cluster are summarized in [Figure 6.4A](#). Here, the classification line corresponding to the high distance is selected to highlight the main characteristic research zones of stratigraphic structures. The dendrogram shows three distinct primary clusters (clusters A, B, and C) ([Figure 6.4A](#)). Clusters A, B, and C with median resistivity in all ERT measurements, ranging from 2321  $\Omega\cdot\text{m}$  to 100054  $\Omega\cdot\text{m}$ , 80  $\Omega\cdot\text{m}$  to 1277  $\Omega\cdot\text{m}$ , 493  $\Omega\cdot\text{m}$  to 2635  $\Omega\cdot\text{m}$ , respectively, which may be composed of karst structural systems with completely different geological characteristics ([Figure 6.4A](#)).

To get as much detail as possible to highlight potential sub-regions, we decided to make more cutoffs (classification lines), classifying in eight clusters (see dashed lines in [Figure 6.4A](#)) as follows:

Cluster A, consisting of clusters 1, 7, and 8, shows the highest median value for electrical resistivity ([Figure 6.4B](#)). Blocks with the largest resistivity values were collected in cluster A (clusters 7& 8, altitude: 165-178 m) ([Figure 6.4B](#)), with the high median values, ranging from 5001 to 8245  $\Omega\cdot\text{m}$  and from 3471  $\Omega\cdot\text{m}$  to 100054  $\Omega\cdot\text{m}$ , respectively ([Table 6.1](#)). However, compared to clusters 7& 8, cluster 1 with a slightly lower median value, ranging from 2321  $\Omega\cdot\text{m}$  to 4957  $\Omega\cdot\text{m}$  ([Table 6.1](#)), is distributed around clusters 7 & 8 ([Figure 6.4B](#)).

Cluster B, consisting of clusters 2 and 4, shows the lowest median values, ranging from 261  $\Omega\cdot\text{m}$  to 1277  $\Omega\cdot\text{m}$  and 80  $\Omega\cdot\text{m}$  to 534  $\Omega\cdot\text{m}$ , respectively, with most conductive areas mainly distributed on the soil surface and probably in weathered limestone zones (from NE to SW direction) at 50–60 m of the ERT profile ([Table 6.1](#); [Figures 6.4A & 6.4B](#)).

Cluster C, including clusters 3, 5, and 6, with median values ranging from 775  $\Omega\cdot\text{m}$  to 1763  $\Omega\cdot\text{m}$ , 1432  $\Omega\cdot\text{m}$  to 2635  $\Omega\cdot\text{m}$ , and 493  $\Omega\cdot\text{m}$  to 1133  $\Omega\cdot\text{m}$ , respectively ([Table 6.1](#)), is located in the middle zone between 165 m and 177 m NGF (clusters 3 and 5) and lower zones deeper than 165 m NGF (cluster 6) of the ERT profile ([Figure 6.4B](#)).

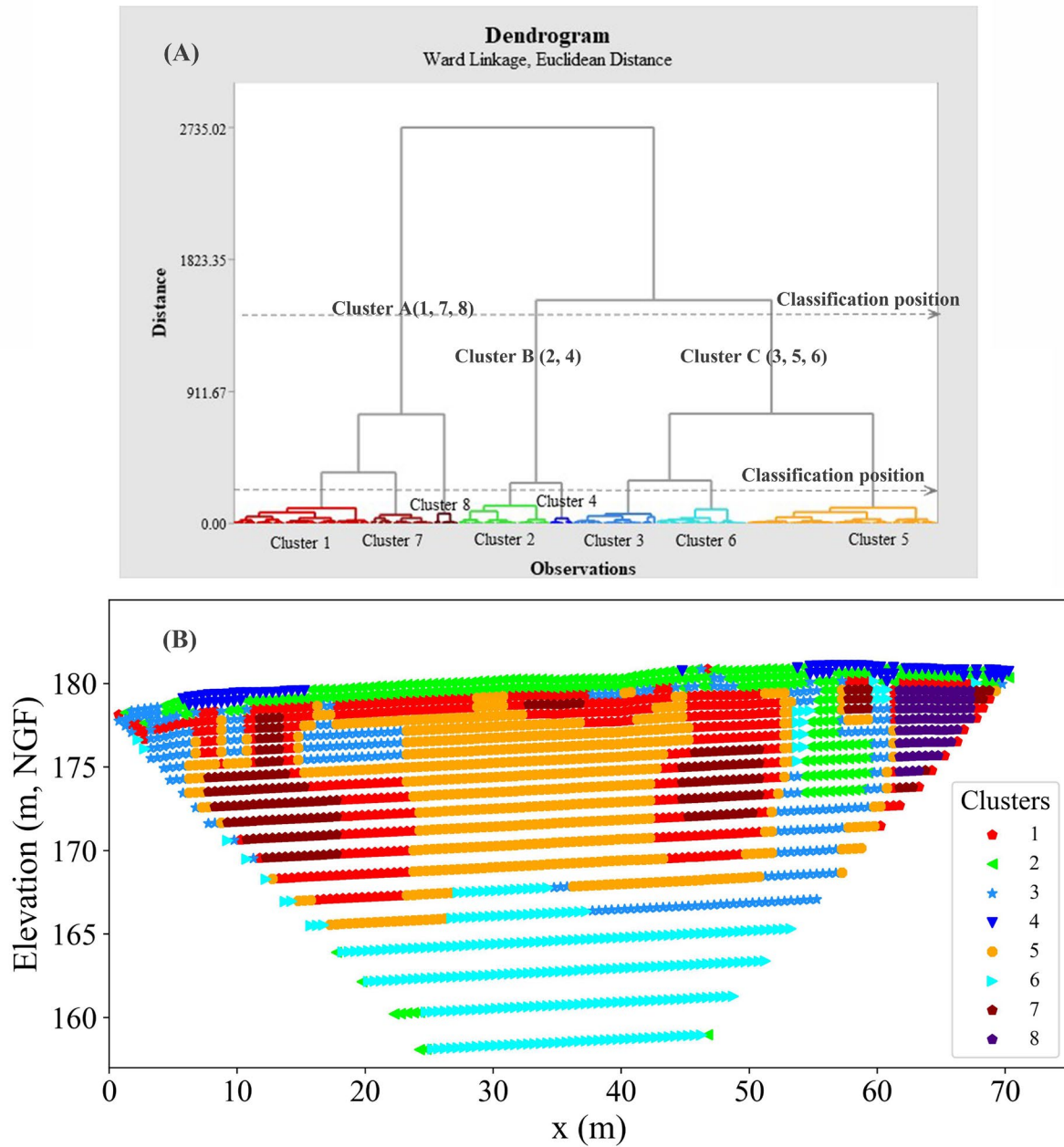


Figure 6. 4 Results of the Hierarchical Agglomerative Classing (HAC) for all monitoring periods for the profile (71m) above Villars Cave. (A) Dendrogram create three and eight clusters. (B) Distribution of blocks taking into account their clusters.

**Table 6. 1** Statistical parameter: for the resistivity of each cluster in ERT-1m spacing (Median and Standard Deviation (SD), Average value)

	Cluster 1			Cluster 2			Cluster 3			Cluster 4			Cluster 5			Cluster 6			Cluster 7&8		
	median	SD	average	median	SD	average	median	SD	average	median	SD	average	median	SD	average	median	SD	average	median	SD	average
2020/2/18	2592	1199	2871	289	119	299	803	262	788	94	30	90	1442	455	1565	781	194	831	8521	38310	28029
2020/7/2	2821	1481	3217	626	292	722	1277	684	1434	297	110	310	2079	666	2059	493	175	526	4610	2012	4922
2020/10/9	4249	2582	5007	342	219	390	1051	967	1405	94	35	98	1801	1087	2126	1133	343	1198	7762	36587	26594
2020/11/18	3557	1472	3596	274	195	337	979	572	1066	89	34	90	1571	767	1841	1028	682	1145	6505	29441	20534
2021/1/7	2321	988	2502	296	121	304	841	242	802	88	31	92	1440	522	1579	815	188	808	7331	13138	13553
2021/4/15	2763	1053	2874	306	115	313	840	254	841	97	34	99	1539	435	1619	848	209	860	7137	35945	25528
2021/5/20	2713	1388	2928	270	124	287	775	196	749	82	27	84	1447	481	1540	792	255	835	7797	36811	26502
2021/7/5	3212	1811	3483	331	158	354	955	597	1069	113	45	114	1571	556	1691	877	181	902	8706	27297	22180
2021/9/24	3461	1816	3839	399	271	456	998	834	1275	119	49	119	1841	641	1892	989	387	1073	7397	40900	29570
2021/11/10	3395	1355	3629	339	154	351	975	368	1057	106	32	97	1758	460	1807	1018	315	1056	7723	23464	19976
2021/12/9	2765	1022	2773	261	113	279	796	266	813	80	25	79	1501	502	1580	851	221	871	7252	23548	18736
2022/1/27	2527	1596	2863	295	143	320	802	241	768	90	30	90	1524	524	1597	750	255	801	8357	24816	20659
2022/3/16	2753	1093	2906	263	114	277	779	224	778	83	26	82	1432	387	1543	860	231	868	7047	25115	19151
2022/5/11	2454	1223	2877	408	160	444	876	307	883	144	61	160	1605	578	1663	633	169	666	9420	3960	9914
2022/6/23	3394	2112	3867	703	445	828	1318	683	1448	300	88	277	2110	633	2174	541	362	610	5620	3460	6981
2022/9/16	4957	3813	6208	1277	1168	1764	1763	2744	2707	534	181	551	2635	973	2621	531	230	583	5055	3118	5981
2023/1/19	3122	1415	3264	364	137	362	927	563	987	100	42	115	1618	640	1832	908	240	945	6556	30333	21983
Median	3043	1968	3453	351	493	476	939	951	1110	106	136	150	1647	694	1808	817	351	858	7135	27844	18870
Maximum	4957	3813	6208	1277	1168	1764	1763	2744	2707	534	181	551	2635	1087	2621	1133	682	1198	9420	40900	29570
Minimum	2321	988	2502	261	113	277	775	196	749	80	25	79	1432	387	1540	493	169	526	4610	2012	4922

### 6.1.3 Rainfall amount, evapotranspiration, and drip rate

Daily hydroclimatic parameters of the Villars Cave are presented in [Figure 6.5](#), including rainfall (R) and rainfall minus evapotranspiration (R-ETP), which is considered efficient rainfall or water-excess when it is greater than 0. We observed that the change of the water-excess has a seasonal signal, with a maximum in winter and a minimum in summer-autumn ([Figure 6.5](#) and [Table 6.2](#)). The total annual value of the water-excess is 836.4 mm in 2020 and 902.7 mm in 2021, respectively ([Figure 6.5](#)). During the year 2022, R-ETP remained below 0 from May to October, indicating almost no rainfall during this period ([Figure 6.5](#)), and this anomaly is attributed to an unusually dry year, as shown in [Figure 6.5](#).

*Table 6. 2 Calculate the monthly average drip rate and Water-excess (Total monthly amount).*

Date	VIL-1B (Average Monthly drips/min)	VIL-10A (Average Monthly drips/min)	VIL-#3 (Average Monthly drips/min)	Water excess (Monthly amount, mm)
October-2019	8.71	2.41	0.09	117.40
November-2019	8.11	80.65	13.16	226.10
December-2019	28.52	120.85	18.41	161.90
January-2020	46.87	40.12	3.51	72.20
February-2020	51.69	62.73	9.28	68.70
March-2020	51.70	89.83	15.52	88.60
April-2020	39.66	12.44	3.59	80.60
May-2020	34.94	34.94	8.39	48.20

June-2020	25.37	9.31	2.81	46.30
July-2020	19.57	6.97	1.31	0.00
August-2020	14.58	5.02	0.56	23.60
September-2020	10.01	2.81	0.37	55.30
October-2020	7.61	2.90	0.50	157.40
November-2020	5.14	5.78	0.33	26.10
December-2020	4.61	57.31	9.05	169.40
January-2021	8.17	71.19	7.14	142.50
February-2021	49.19	108.15	19.78	83.70
March-2021	35.45	18.28	1.73	20.70
April-2021	28.22	10.58	1.42	15.20
May-2021	21.54	32.87	1.77	98.00
June-2021	28.23	17.67	0.70	108.80
July-2021	21.80	13.09	0.31	96.30
August-2021	17.91	9.13	0.82	7.80
September-2021	14.26	6.90	0.47	62.70
October-2021	10.31	4.94		52.40
November-2021	8.77	3.63	Instrument stopped	54.10
December-2021	7.61	47.68		160.50
January-2022	17.96	56.49	3.38	36.40
February-2022	28.37	41.11	5.32	36.40
March-2022	43.30	52.76	4.22	37.50
April-2022	44.05	51.24	5.03	75.80
May-2022	34.16	21.45	2.76	4.70
June-2022	23.17	7.81	1.77	66.10
July-2022	14.96	5.88	1.49	5.80
August-2022	11.71	5.21	1.04	12.50
September-2022	8.26		0.72	7.10
October-2022	4.02		0.46	



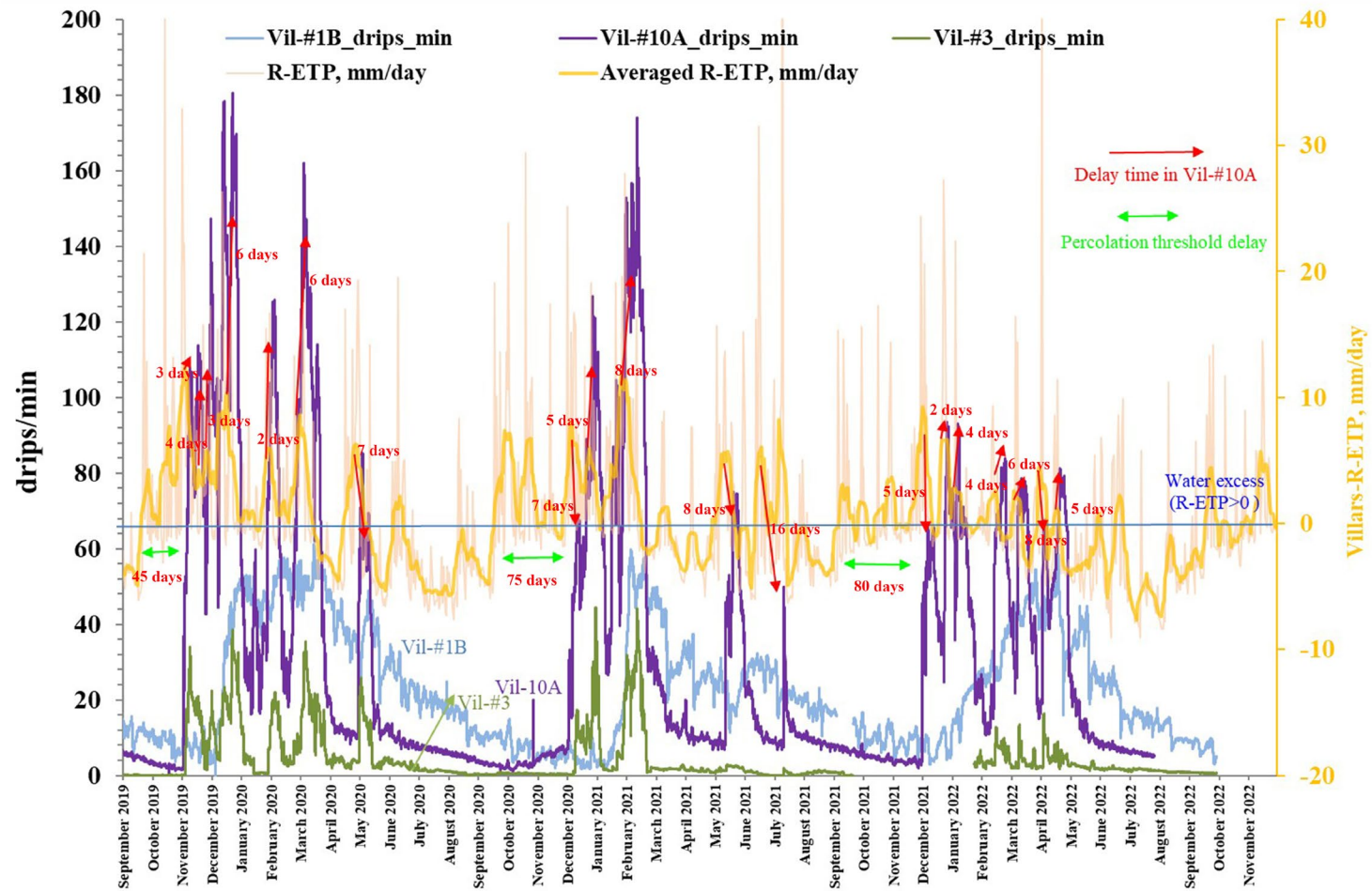


Figure 6. 5 Comparison of the variability of daily R-ETP (rainfall minus evapotranspiration) and drip-water rates (Vil-#3, Vil-#1B, Vil-#10A) during September/2019- September/2022.

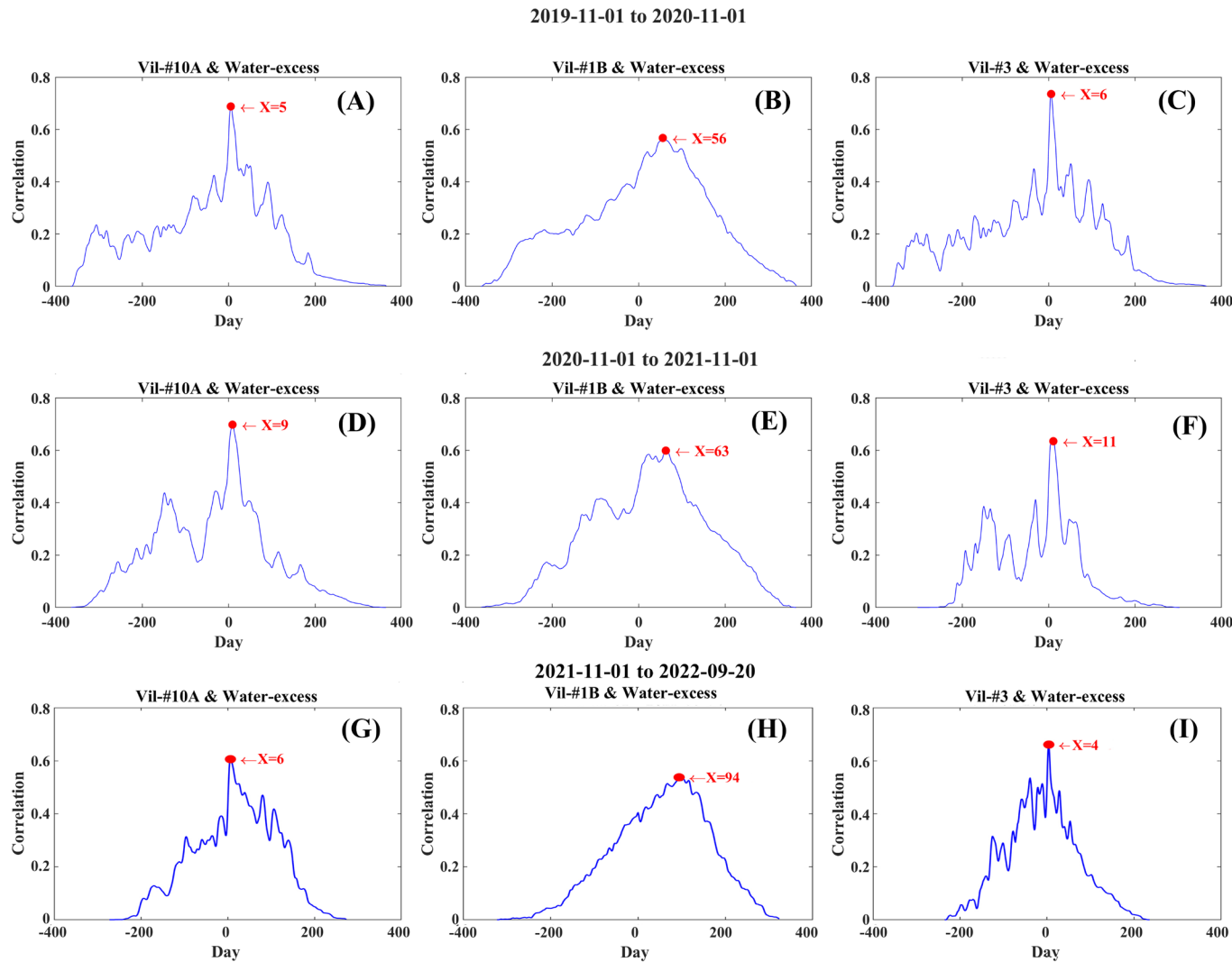


Figure 6. 6 Using Pearson's linear correlation coefficient in the MATLAB coherence package, the delay time between drip-water rates and water excess ( $R-EPT > 0$ ) during 2020-2022. (A, D, G) Vil-#10A & Water-excess, (B, E, H) Vil-#1B & Water-excess, (C, F, I) Vil-#3 & Water-excess. The delay days (X is the highest value) have been exhibited in the diagram too. We performed a five-day smoothing on water excess and drip-water rates to remove small peak effects.

To characterize the variability of cave drip water, we conducted the drip-rate monitoring between September 2019 and September 2022 A.D. by using STALAGMATE drip counters under three drip stations located at different depths as described in section 3.3.4 (Figure 6.5). The three drip water sites (Vil-#10A: depth 14m, Vil-#1B, and Vil-#3: depth 36m) have discharges ranging from 0.60 to 180.67 (SD: 37.43) drips/min (Vil-#10A), 1.6 to 61.1 (SD: 15.29) drips/min (Vil-#1B) and 0 to 44.4 (SD: 6.96) drips/min (Vil-#3). We also note that the drip rate of Vil-#10A and Vil-#3 stations are more variable than Vil-#1B (Figure 6.5).

During the first cycle of 2019-2020, water-excess starts to be significantly more than 0 since mid-September 2019 (Figure 6.5). Infiltration takes about 45 days for the reservoirs' water to be filled up and reach the percolation threshold, allowing the water to move down into the cave (Figure 6.5). As a result, there is an increase in the dripping rate in November 2019 in stations Vil-#10A and Vil-#3, and in December in station Vil-#1B. Drip rates remain high until approximately May 2020, displaying a general decrease until December 2020. During the humid period, there is a systematic link between the water-excess and the drip rate variations in Vil-#10A, with a time delay of several days as we depicted in Figure 6.5. During the 2020-2021 year, the hydrological cycle of Vil-#10A and Vil-#3 dripping stations began to increase in December 2020, lasting approximately until August 2021 (Figure 6.5). The fact

that the beginning of the cycle at the Vil-#1B dripping station occurs later than Vil-#10A and Vil-#3, close to January or February, implies that there are distinct pathways and reservoirs involved in the infiltration process across the different sites (Figure 6.5).

To quantify the time delay between the water-excess and drip rates after the percolation threshold, we performed a cross-correlation analysis at the three monitoring sites Vil-#10A, Vil-#3, and Vil-#1B. The mean lag time has been determined in the interval of 5-9 days for Vil-#10A station (Figures 6.6A & 6.6D & 6.6G), 56-94 days for Vil-#1B station (Figures 6.6B & 6.6E & 6.6H), and 4-11 days for Vil-#3 station (Figures 6.6C & 6.6F & 6.6I). In summary, these results show the following:

(1) Vil-#10A and Vil-#3 have a similar water-excess/dripping time delay even though they are located at different levels (14m deep for Vil-#10A and 36 m deep for Vil-#3).

(2) From the time series, the Vil-#3 station has a much more dampened dripping amplitude despite a similar time delay with the Vil-#10A station.

(3) At the dripping point of Vil-#1B station, located in the lower gallery, we observe a much longer time lag and lower mean drip rate compared to Vil-#10A.

## 6.2 Discussion

### 6.2.1 Recognition of soil layers and cave zones from ERT images

The superficial part of the ERT images shows low resistivity values corresponding to clusters 2 and 4 (Figure 6.4B). Cluster 4 has a median value of  $106 \Omega \cdot \text{m}$ , with a range between  $80 \Omega \cdot \text{m}$  to  $534 \Omega \cdot \text{m}$  (Table 6.1) at the 5-13 m and 52-71 m on the ERT profile (from NE to SW), characterized by a highly variable resistivity by the HAC method (Figure 6.4B). The specific resistivity values observed at these locations on the ERT profile, as evidenced by the results of our soil drillings, can be attributed to the nature of the soil (clay and organic matter), which has an upper layer consisting of a mix of weathered limestone and exceeds thicknesses of 0.6 m, 0.75 m, and 0.45 m at the locations of 9.5 m, 56 m, and 60.5 m, respectively (Figure 6.7).

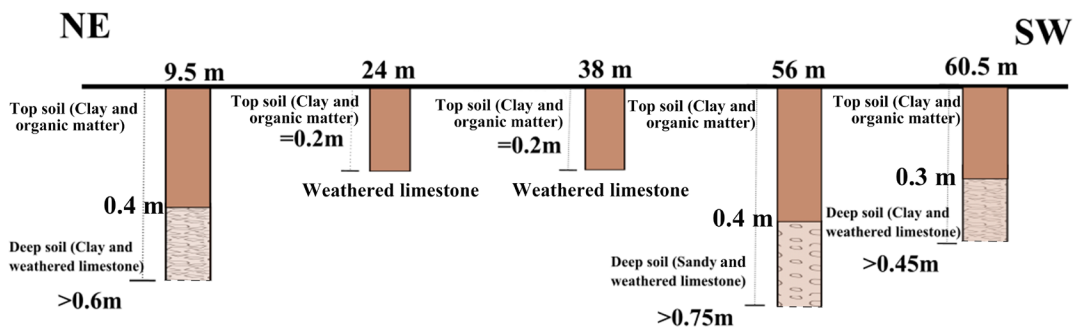


Figure 6. 7 The soil depth and soil type of the ERT profile at 9.5 m, 24 m, 38 m, 56 m, 60.5 m.

Cluster 2 has a median resistivity value of  $351 \Omega \cdot m$ , ranging from  $261 \Omega \cdot m$  to  $1277 \Omega \cdot m$  (Figure 6.4B; Table 6.1). It is situated on the surface, specifically between 15 m and 50 m on the ERT profile line (from NE to SW), as well as in a deeper zone (altitude: 172 to 177 m, NGF) that can be seen between 50 m and 60 m on the ERT profile (Figure 6.4B). We further divide cluster 2 into two distinct sub-clusters, namely clusters 2.1 and 2.2 (Figure 6.8A):

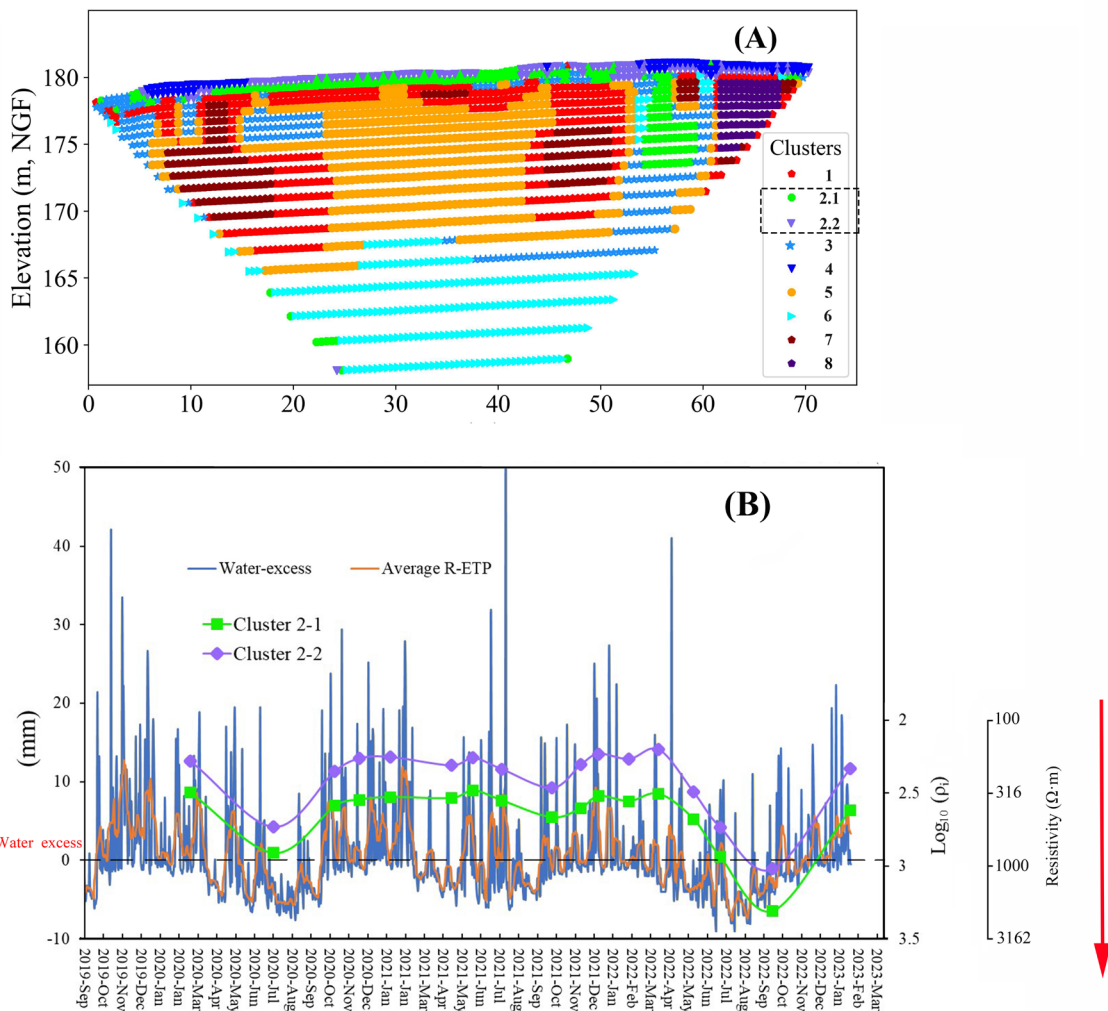


Figure 6. 8 (A) Cluster 2 is divided into clusters 2.1 and 2.2, (B) Comparison between median resistivity variations for clusters 2.1 and 2.2 and water excess.

- (1) Cluster 2.2, located in the superficial part of the ERT profile (Figure 6.8A), shows a median electrical resistivity value of  $219 \Omega \cdot \text{m}$ , with a range from  $160 \Omega \cdot \text{m}$  to  $1047 \Omega \cdot \text{m}$  (Figure 6.8B). The median resistivity value of cluster 2.2 is slightly higher but comparable to the median resistivity value of cluster 4 ( $106 \Omega \cdot \text{m}$ , top-soil). Cluster 2.2 displays seasonal variations, which are commonly linked to water-excess (Figures 6.8A and 6.8B). The surface in cluster 2.2 is confirmed to be the top-soil about 0.2 m thick, as observed at two locations situated at 24 m and 38 m on the ERT profile (Figure 6.7).
- (2) The median electrical resistivity of cluster 2.1 is  $403 \Omega \cdot \text{m}$ , ranging from  $304 \Omega \cdot \text{m}$  to  $2029 \Omega \cdot \text{m}$ , which is higher than cluster 2.2 (Figure 6.8B). Cluster 2.1 is associated with the soil layer situated below the layer of cluster 2.2 and also in the deeper section between 50 m to 60 m of the ERT profile (altitude: 172 m to 177 m, NGF) (Figure 6.8A). Cluster 2.1 exhibits the seasonal fluctuations that are associated with the water excess (Figures 6.8A and 6.8B). Notably, it has been observed in the soil digging that the limestone zones have undergone weathering (small limestone blocks mixed with sandy soil) between depths of 0.4 m and over 0.75 m (56 m on the ERT profile in Figure 6.7). Therefore, it is possible that cluster 2.1 could represent a mixture of weathered limestone with sandy soils with high porosity. However, due to the

limitations of the manual auger, it was not possible to excavate deeper to determine the exact boundary ( $>0.75$  m) (Figure 6.7).

Clusters 7 and 8 exhibits a consistently high median resistivity ( $7168 \Omega \cdot \text{m}$ ) (Figure 6.4B) that does not show seasonal variations over time (Figures 6.9A & 6.9H). The comparison of the location of these clusters with the cave plan map allowed us to attribute these zones to the cave galleries (Figures 2.1C & 6.4B). It shows that: (1) Cluster 7 (Figure 6.4B) has high resistivity zones located on the ERT profile at 6-22 m and 40-54 m (from NE to SW, vertical altitude: 168 m-178 m, NGF) in the ERT profile. These zones are precisely corresponding to the cave plan map (Figure 2.1C). (2) Cluster 8, located at a vertical altitude of 168 m-178 m NGF, displays a high resistivity signal observed at 60-71 m on the ERT profile (Figures 2.1C & 6.4B), indicating the presence of an undiscovered cave gallery or a sinkhole collapse.

### **6.2.2 Clustering resistivity variabilities with local water-excess**

According to Archie's law (Archie, 1942), if the electrical resistivity of a rock formation varies with time, it implies that the degree of saturation ( $S_w$ ) or the resistivity of water ( $\rho_w$ ) is changing with time, as the porosity ( $\phi$ ) is assumed to be constant. Therefore, changes in the electrical resistivity of the rock over time can reflect changes in the water content of the rock, responding to local water-excess (Xu et al., 2017).



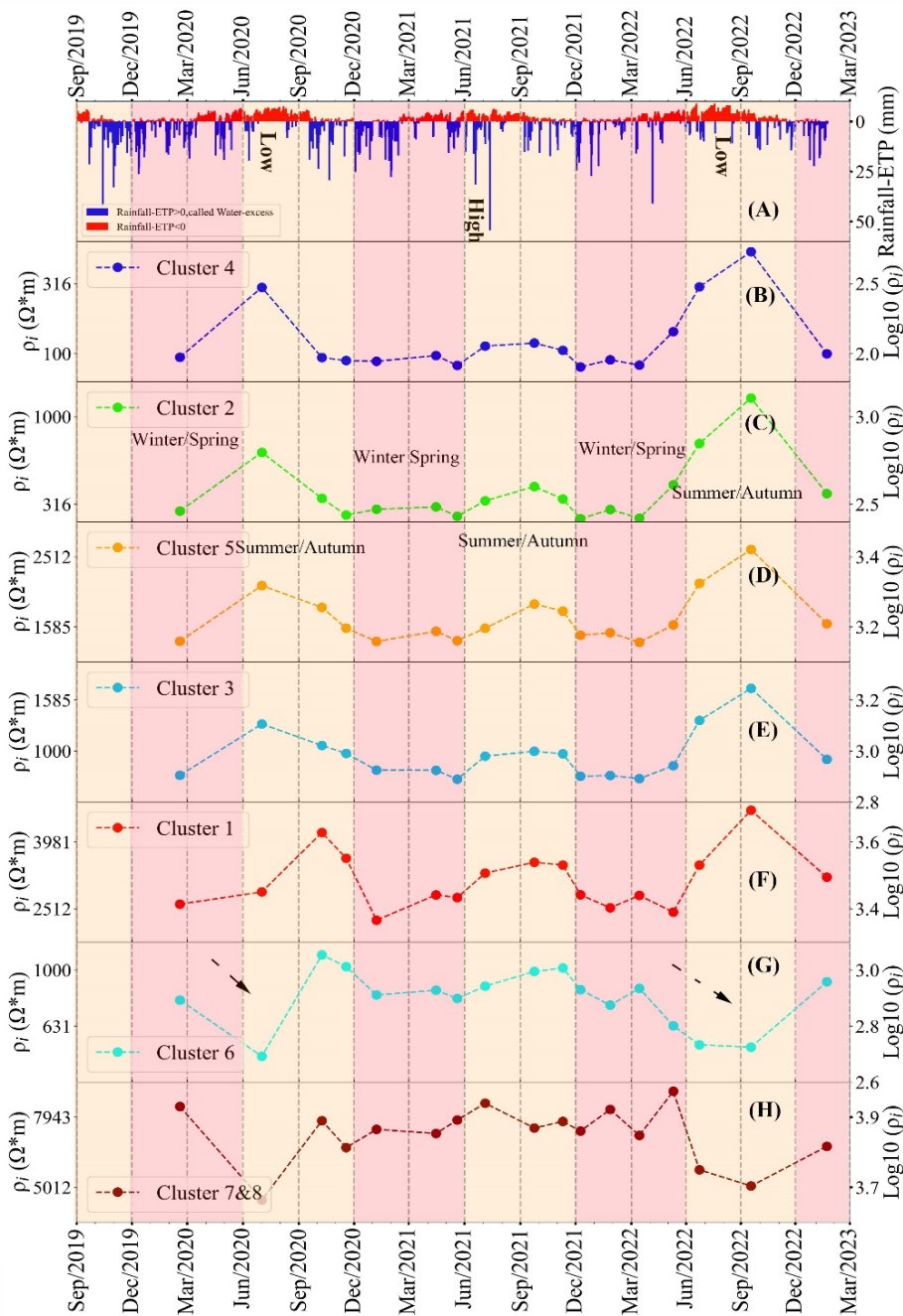


Figure 6. 9 Evolution of the median resistivity of clusters 1-8 with local water excess. The individual blocks from the synthetic model were associated with a similar resistivity seasonal variability gathered into 6 clusters (1-6). However, Clusters 7 and 8 only exhibit high resistivity without obvious seasonal variability. The arrows indicate the resistivity in cluster 6 decreased in the dry/summer periods.

As observed in Figure 6.9, there is a strong correlation between water-excess (blue part in Figure 6.9A) and resistivity over time, as shown by the

sharp increase in resistivity, more or less time-delayed depending on the cluster, after water-excess increases. Here roughly, we observe a well-marked seasonality over time, and the resistivity in clusters 1 to 5 increases in summer and autumn, and decreases in winter and spring (Figures 6.9B-6.9F). Furthermore, it is worth noting that each cluster displays a distinct range of resistivity values, despite any seasonal similarities that may exist between them (Figures 6.9B-6.9F).

To facilitate a point-to-point comparison of water-excess and resistivity variability, we have plotted them on the same graph for each cluster (Figures 6.10). The superficial part of the ERT images (essentially cluster 4 and cluster 2) displays obvious seasonal changes than represent a relatively quasi-synchronous response to the local water-excess (Figure 6.10A). We also note a high variability of resistivity where the highest median value is 534  $\Omega\cdot\text{m}$ , and the lowest median value is 80  $\Omega\cdot\text{m}$  (cluster 4, Figure 6.10A). Assuming that resistivity of water ( $\rho_w$ ) and porosity ( $\phi$ ) remained constant, we can estimate that the top-soil water saturation varied approximately 2.6 times in cluster 4. In addition, the surface soil layers responded to the local drought periods of July 2020 and July-September 2022 (Rainfall-ETP<0) as high resistivity values were observed (Figure 6.10A). In more detail, we observed a minimum water-excess of 46.30 mm during June and July 2020 (Table 6.2 and Figure 6.10A). As a result, the relative frequency distribution of resistivity observed in the top-soil

layer does not show some values less than  $245 \Omega \cdot m$  compared to the other months (Figure 6.11B). Similarly, from May 2022 to September 2022, the water-excess decreased to 96.2 mm (Table 6.2 and Figure 6.10A). This led to a shift in the relative resistivity frequency to higher value zones as high as  $2563 \Omega \cdot m$  for the median value, with the resistivity below  $245 \Omega \cdot m$  disappeared (Figure 6.11H).

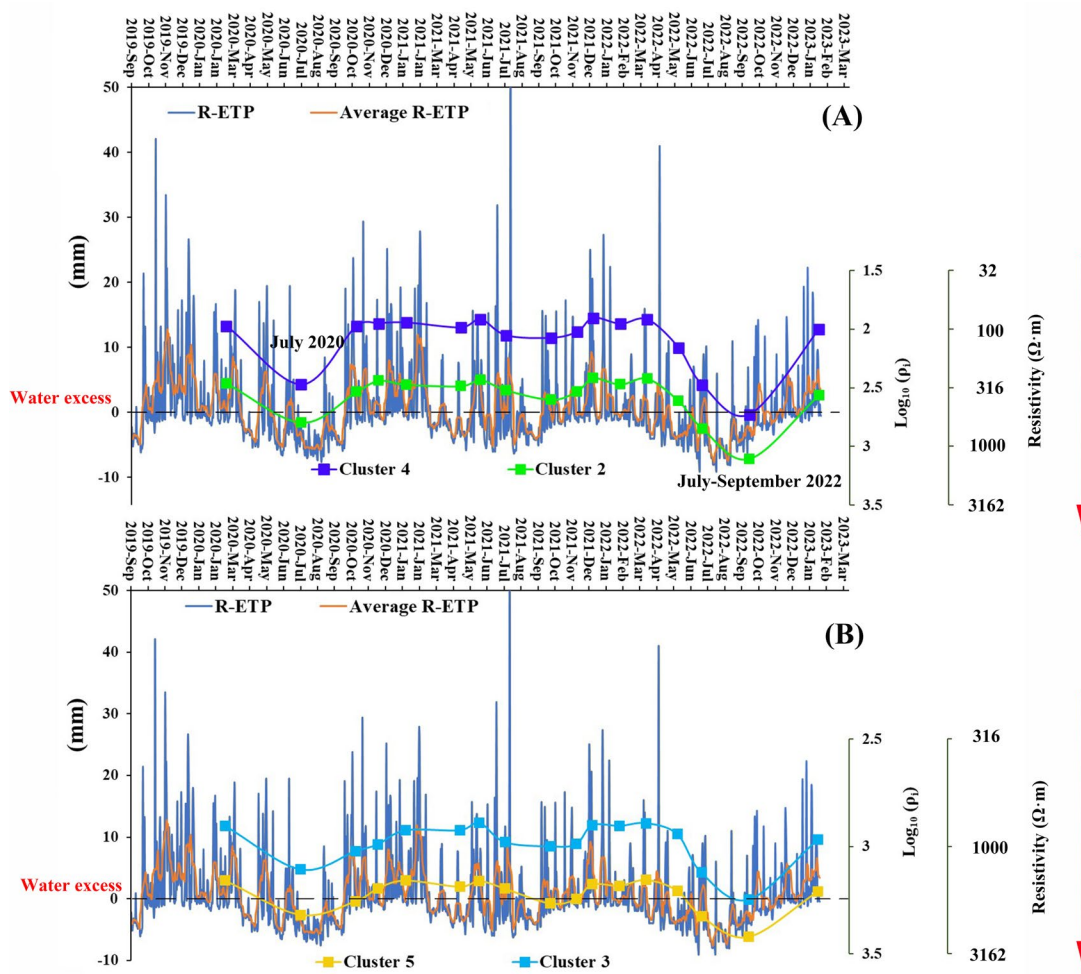


Figure 6. 10 Comparison between median resistivity of clusters 2-5 and water-excess ( $R-ETP > 0$ ) (A) Evolution of the median resistivity of clusters 2&4 with local water excess (B) Evolution of the median resistivity of clusters 3&5 with local water excess. A similar resistivity seasonal variability gathered into 4 clusters (2-5) with no or few days delays with a local water excess.

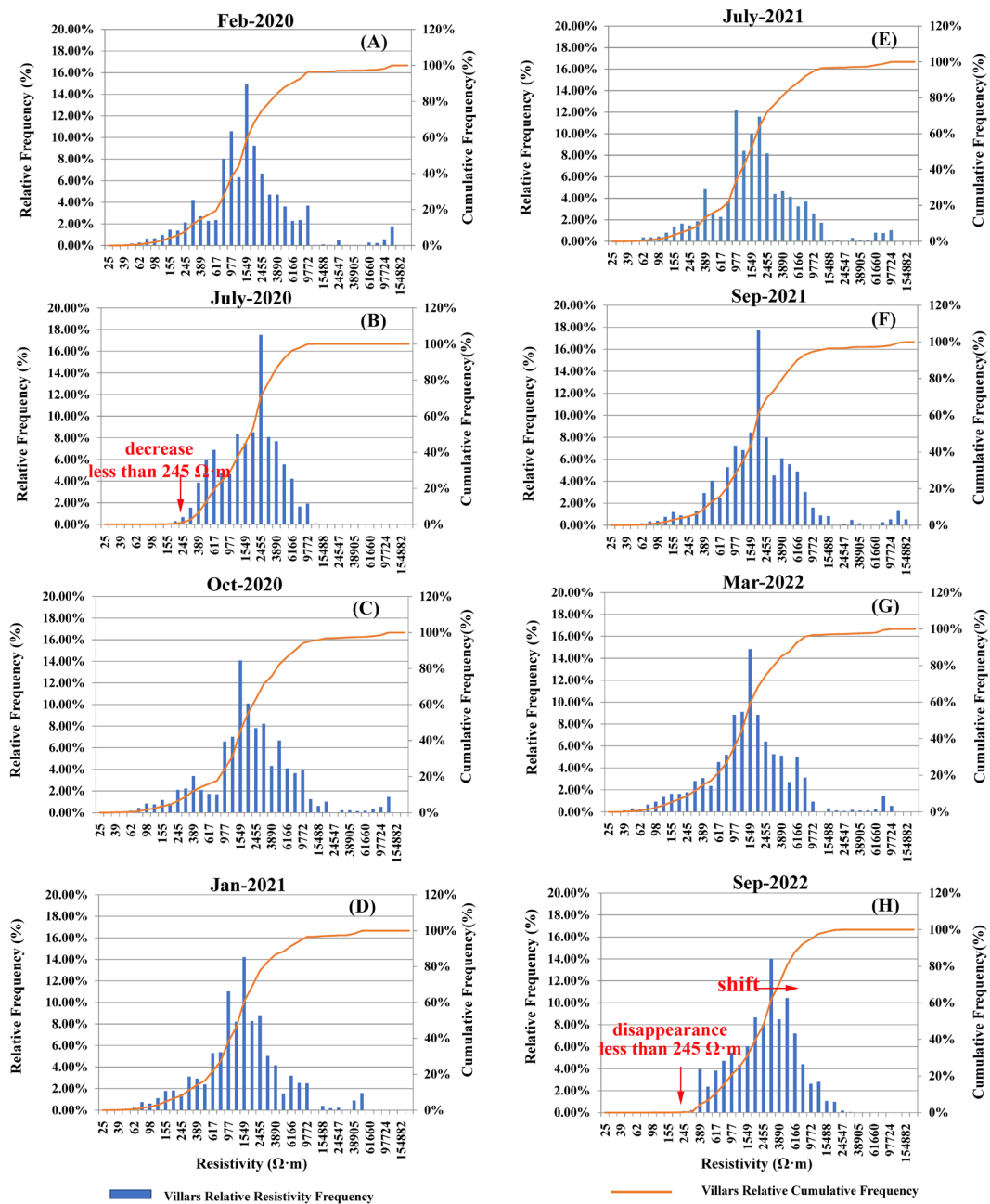


Figure 6. 11. Relative frequency and cumulative frequency for the month data set.

Cluster 5 is also sensitive to water-excess with a median resistivity of 1647  $\Omega \cdot m$ , with a range between 1432  $\Omega \cdot m$  to 2635  $\Omega \cdot m$  (Figure 6.10B). The time lag between cluster 5 and water-excess appears slightly higher than for sub-surface clusters 2 and 4 (Figures 6.10A&10B). However, the variability of

water saturation in cluster 3 over time is basically the same as cluster 5 (Figure 6.10B). We suggest that cluster 5 likely corresponds to the Bajocian and Bathonian limestone, where seasonal variation may be due to water filling or draining of the fissure network.

Cluster 3, with a median resistivity value of 939  $\Omega\cdot\text{m}$ , ranging from 775  $\Omega\cdot\text{m}$  to 1763  $\Omega\cdot\text{m}$ , is located at the same altitude (165-178 m, NGF) of cluster 5 (Figures 6.10B & 6.4B). Similarly, cluster 3 also experiences only a few days or one month of time delay with water-excess (Figure 6.10B). The observation worth mentioning is that cluster 3 has a lower median resistivity value than cluster 5, indicating a comparatively higher porosity (Figure 6.10B). Based on the above observation, it can be concluded that cluster 3 serves as a preferred water pathway due to its higher porosity, functioning as a transmission belt (located on the right side of Figure 6.10B), which supplies water to deeper zones linked with cluster 6.

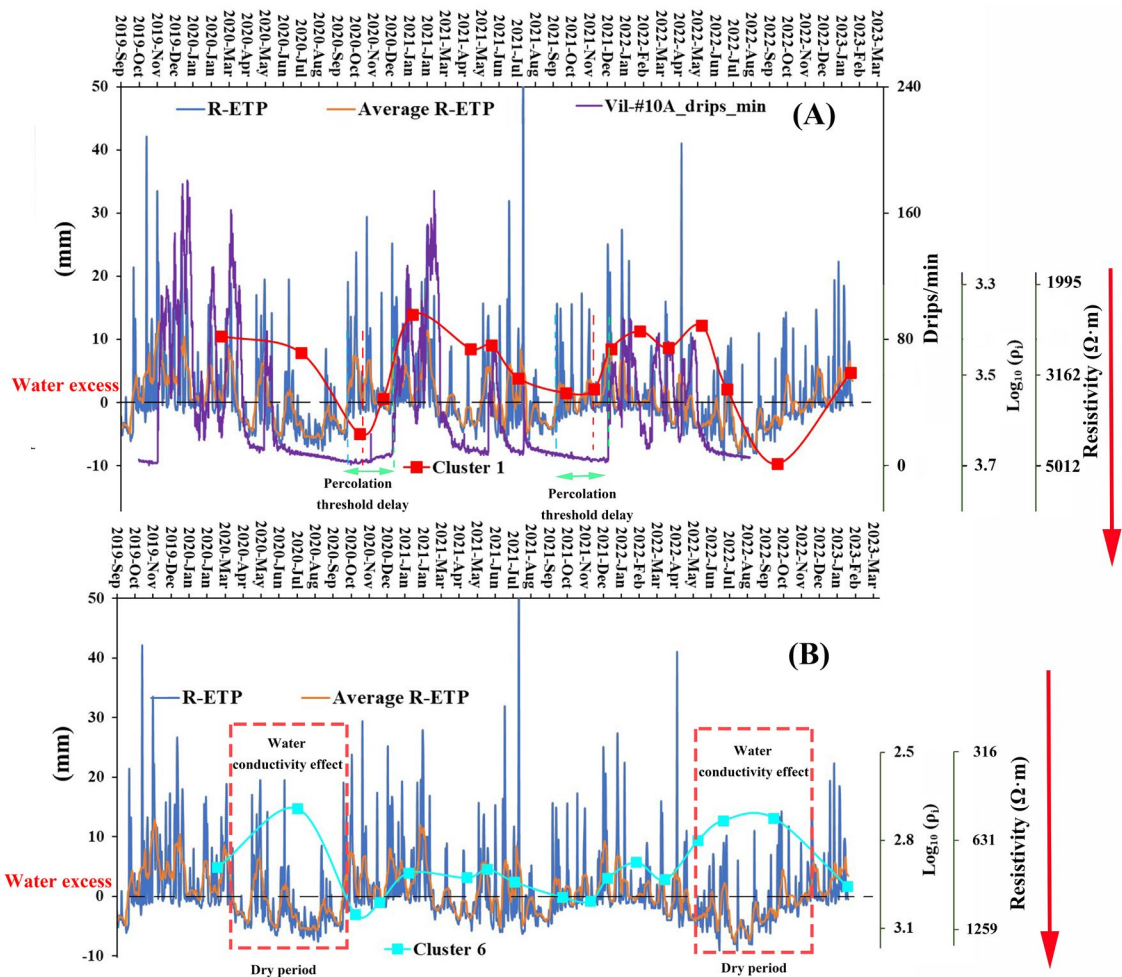


Figure 6. 12 Comparison between median resistivity (clusters 1 and 6) and water-excess ( $R-ETP > 0$ ) (A) Evolutions of the median resistivity of cluster 1. (B) Evolutions of the median resistivity of cluster 6.

Cluster 1 has a median resistivity value of 3043  $\Omega \cdot m$ , ranging from 2321  $\Omega \cdot m$  to 4957  $\Omega \cdot m$  (Figure 6.12A), which is a higher resistivity value than cluster 5 (1647  $\Omega \cdot m$ ). Cluster 1 is mainly distributed around the cave gallery and along the 10-50 m section of the ERT profile (at an altitude of 176 m-178 m, NGF) (Figure 6.4B). The cluster 1 resistivity increases in summer/autumn and decreases in winter/spring, basically in the same pattern or ahead of the cave dripping rate (Vil-#10A) (Figure 6.12A). We observe a time delay of about 1-2 months for cluster 1 in response to local water-excess (Figure 6.12A). It is

hypothesized that this delay may be associated with the percolation threshold between water-excess and drip rate as described in section 6.1.3 (Figure 6.12A). The bulk resistivity is directly inversely proportional to the conductivity of the water based on Archie's law, called "water conductivity effect" (Archie, 1942). However, the field monitoring carried out in previous research between 1996 and 1997 shows that the electrical conductivity of the water varied a little and was around 356  $\mu\text{S}/\text{cm}$  (summer months) and 372  $\mu\text{S}/\text{cm}$  (winter months) at station Vil-#10A (cluster 1) in the upper gallery (Baker et al., 2000; Genty et al., 2001). Therefore, based on the observations and results obtained in Vil-#10A, it can be concluded that the upper gallery does not exhibit any significant "water conductivity effect", as the conductivity of the water in this zone remains stable and does not change with time.

Cluster 6, located at the lowest altitudes of ERT profiles, has a median resistivity value of 817  $\Omega\cdot\text{m}$ , ranging from 493  $\Omega\cdot\text{m}$  to 1133  $\Omega\cdot\text{m}$  (Figure 6.12B). Resistivity values in cluster 6 are lower than in cluster 5 (1647  $\Omega\cdot\text{m}$ ), suggesting higher water content. In wet periods, cluster 6 median resistivity displays seasonal variability linking with water excess, but it appears to be much more time delayed to water-excess than other clusters (Figure 6.12B). However, there are two long-term inconsistent excursions with water-excess in the dry periods (May-October 2020 and April-October, 2022), especially in summer (Figure 6.12B). Unlike cluster 1, the resistivity of cluster 6, situated in the deeper

sections of the profiles (below 165 m NGF), appears to be predominantly influenced by the “water conductivity effect” in the dry/summer periods (Archie, 1942). The conductivity of water in lower gallery station Vil-#1B, which is situated close to the altitude of cluster 6, is higher and varied seasonally from 600  $\mu\text{S}/\text{cm}$  (summer months) to 460  $\mu\text{S}/\text{cm}$  (winter months) (Baker et al., 2000; Genty et al., 2001). We interpret the resistivity variability of cluster 6 as the result of a “piston flow” infiltration system, where during the summer/dry periods, the infiltration water has a much higher conductivity due to its long residence time leading to a more intense mineralization of the water in fissures and micro-fissures.



### 6.2.3 Schematic diagram of the unsaturated karst zone around Villars Cave

According to the geophysical analysis and hydrological knowledge of the studied region, we propose a schematic geo-electrical synthetic model (Figure 6.13). The boundaries in the geo-electrical structures are inferred from the HAC method (Figure 6.4B). The model delineates the limestone, top-soil, weathered limestone, privileged feeding zone, and storage zones based on their resistivity values and temporal resistivity variations linked to cave water drip rate (Figures 6.9& 6.10& 6.12).

From this synthetic image, it is possible to draw a schematic diagram of the groundwater movement pathways in the critical karst zone (KCZ) above Villars Cave (Figure 6.13). We can speculate that most of the water flow is transported from soil layers and inter-connected epikarst reservoirs and then moves deeper into the porous limestone zone (cluster 3). However, precipitation can also infiltrate vertically through fracture networks in the Bajocian and Bathonian limestone (cluster 5, Figure 6.13). The rapid water circulation observed in cluster 2 is highly sensitive to local rainfall, which is compounded with the superficial top-soil and weathered limestone zones mixed with sand on the surface and between 50-60 m (altitude: 172 m to 177 m, NGF) of the ERT profile (Figure 6.13).

In regards to storage zones in Villars, cluster 6 is capable of acting as a water reservoir from a quick fissure network transport of water in cluster 5 and a transport of water from cluster 3 and cluster 2.1 (Figure 6.13). Similarly, it appears that cluster 1 also acts as a storage zone with a hydrological behavior closely linked to the dripping rate in the upper gallery (Vil-#10A) (Figure 6.12A). Cluster 1 stores local

rainwater and regulate its release over time which can have important implications for feeding upper galleries' stalagmites in Villars Cave.

In summary, the cluster characteristics and behaviors are not randomly distributed but they highlight the structures of the infiltration zone which can be interpreted as reservoirs, preferential rapid or slow infiltration zones.

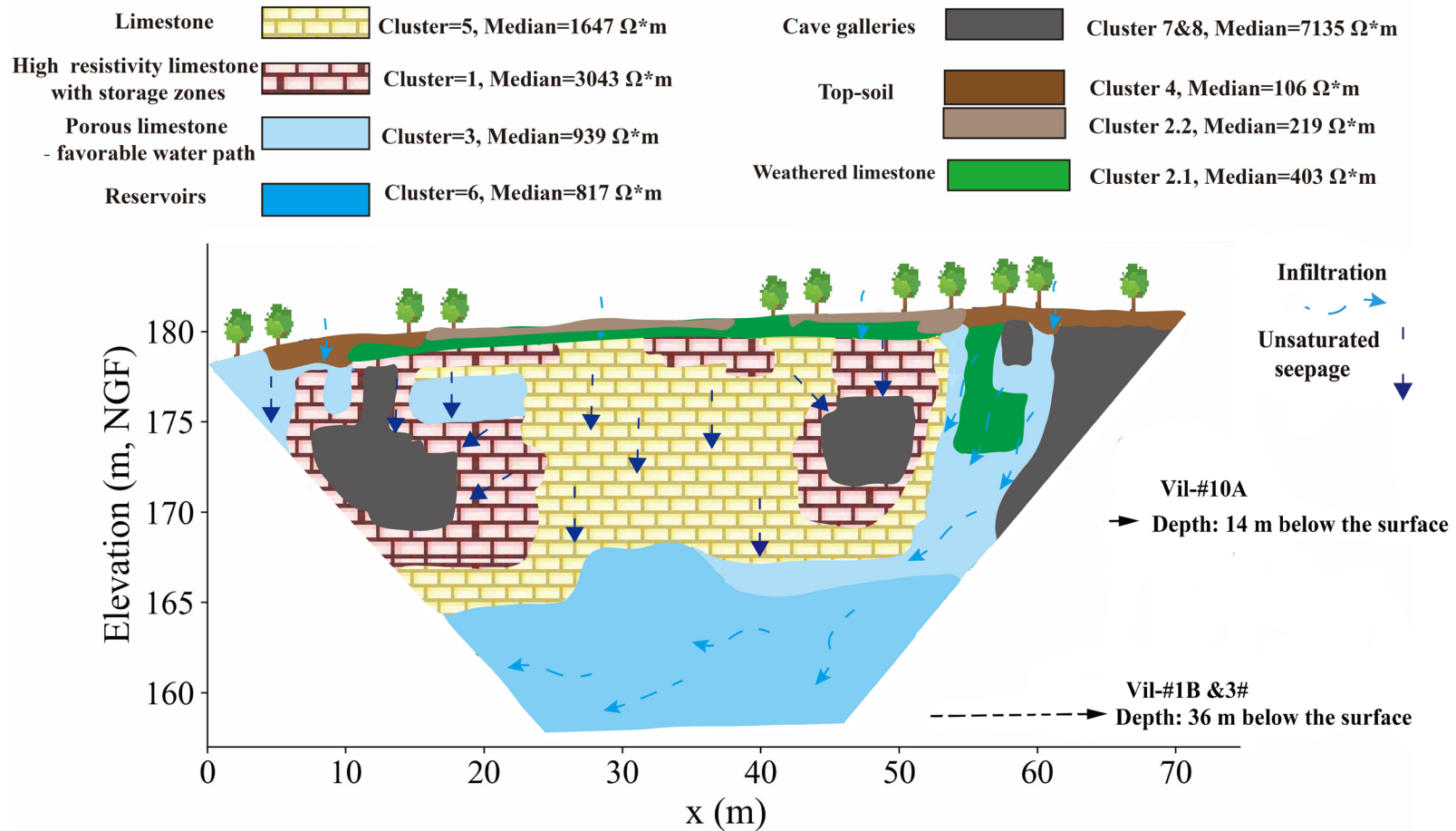


Figure 6. 13 Schematic geo-electrical model of the ERT survey line in ERT-1m spacing. The wiggly arrows represent preferential flow, straight arrows represent vertical infiltrations in karst fracture.

### 6.3 Conclusions

The 3-year long-term ERT monitoring of the karst vadose zone overlying Villars Cave, SW-France, combined with drip rate monitoring inside the cave, not only reveals the geometry and the different structures of the infiltration zone but also shows a well-marked seasonal dynamics of aquifer recharge processes.

Regarding the ERT-1m spacing, ERT images allow the identification of distinct clusters using the Hierarchical Agglomerative Clustering (HAC) method that shows a contrasting evolution in eight different resistivity zones (clusters 1 to 8), some of them being associated with the source of the drip water within the Villars Cave. The different karst critical zones (KCZ), including cave galleries and water storage reservoirs, top-soil layers, and potential preferential flow paths, were visualized by seventeen ERT images. The main conclusions can be summarized as follows:

(1) the resistivity variations in clusters 2 and 4, which are situated in the superficial layer of ERT profiles and consist of top-soil (clusters 4 and 2.2) and weathered limestone in a slightly deeper zone (cluster 2.1), are directly related to water-excess variations and local droughts.

(2) clusters 5, located in the middle layers of the ERT images, show well-marked seasonal resistivity changes. It is directly related to water-excess changes with a short delay (a few days/one month), likely due to the more or

less filling of the fissures and micro-fissures.

(3) cluster 3, mostly located on the right side of ERT images and characterized by a slightly lower resistivity, seems to act as a preferential infiltration pathway toward deeper reservoirs. Similar to Cluster 5, cluster 3 also demonstrates a delay of a few days or one month after water-excess.

(4) at the deeper part of the ERT profile, cluster 6 also show the seasonal variability with water excess during wet periods. However, it displays low resistivity values during summer/dry periods likely due to higher mineralized infiltration waters.

(5) cluster 1, distributed in the surrounding of the cave galleries, consists of high-resistivity limestone, connected to cave dripping hydrology (Vil-#10A) with a delay of 1-2 months with water-excess due to the percolation threshold, feeding the cave stalagmites in Villars.

(6) clusters 7 and 8 exhibit extremely high resistivity that does not show seasonal variations. These areas coincide with the cave galleries or the collapse of the sinkhole.

Overall, these results open new opportunities for understanding karst systems, which are often considered “black boxes”. Characterizing the sources of drip rate signals routinely monitored in cave systems can help to better understand the hydrodynamic behavior of the karst subsurface. In particular, the combined analysis of time-lapse ERT results and drip water measurements

is not only a novel and promising method to study the origin of different flow types in caves and their lithological and geological structural constraints, but also to better understand karst aquifer recharge processes that provide the knowledge base for cave studies and have implications for paleoclimate studies.

## Chapter 6-Part II ERT measurement with a 1.5m spacing

In order to visualize hydrological and geophysical changes in the deeper zones of the Villars cave, we conducted eight ERT-1.5m spacing surveys from July 2021 to January 2023 along an extended length of 106.5 m.

### 6.4 ERT measurement-1.5m spacing results

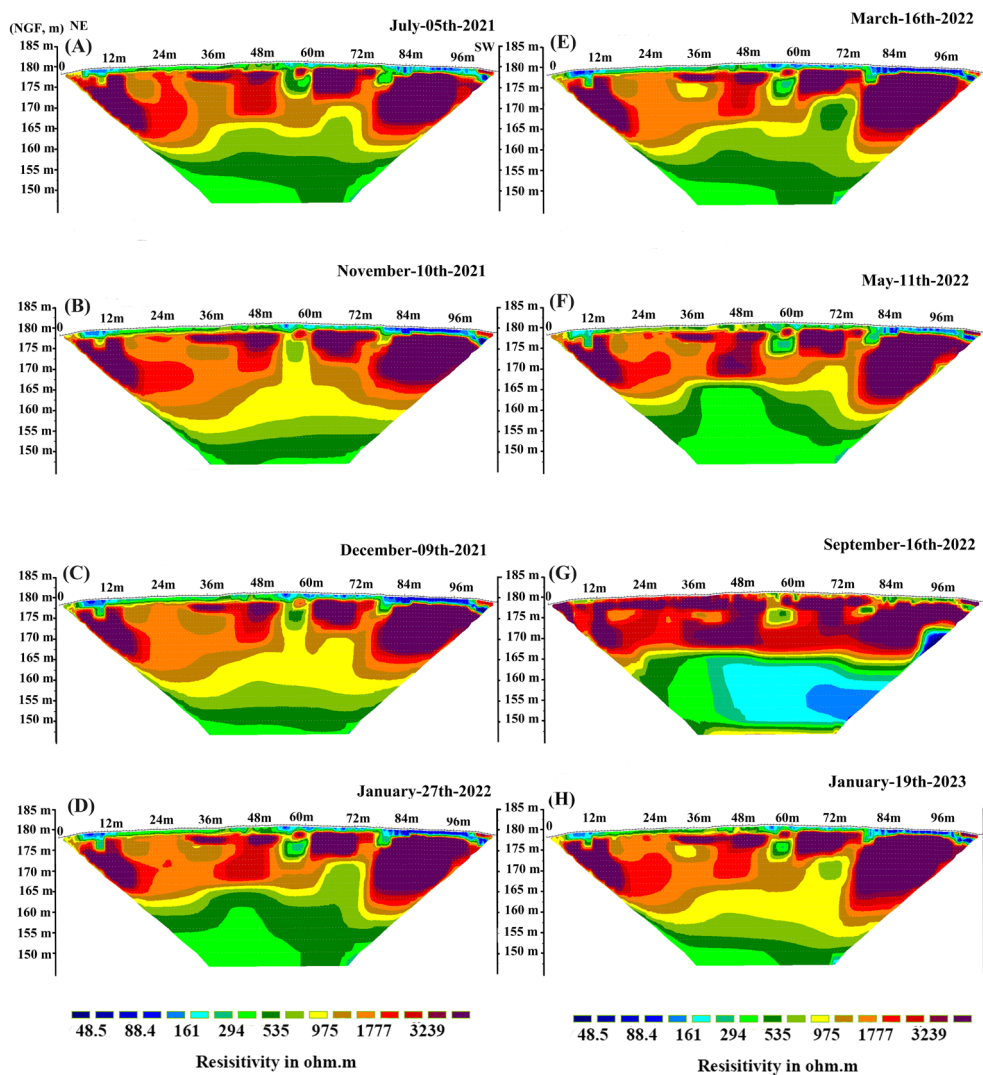


Figure 6. 14 Electrical resistivity 106.5 m profile above the Villars Cave from July/2021 to January/2023. The inversion was performed based on the concatenation of the data of the two arrays (Gradient Array and Pole-Dipole Array), using Res2Dinv software to process data.

Similar to the findings with a 1m spacing, the ERT with a 1.5m spacing reveals a strong seasonal resistivity contrast in low-resistivity zones (Figure 6.14). However, there is no significant seasonal variation observed in high-resistivity zones (red zones) over the period (Figure 6.14).

On January 27th, 2022, a case study was conducted above Villars Cave to illustrate ERT resistivity distributions on a long profile (1.5 m spacing). The survey revealed that the surface layer has low resistivity values of less than 294  $\Omega\cdot\text{m}$ , consisting of top-soil with high water contents (Figure 6.15B). The limestone zones were found to have moderate resistivity values ranging from 535  $\Omega\cdot\text{m}$  to 3239  $\Omega\cdot\text{m}$ , while high resistivity values over 3239  $\Omega\cdot\text{m}$  were observed in several red zones in the ERT survey, specifically around 160-168 m (NGF), indicating the presence of air-filled caves or sinkhole collapse in the area (6.15B).

In general, both the 1m and 1.5m spacing for ERT exhibit similar patterns of resistivity distributions in January 27th, 2022 (Figures 6.15A and 6.15B). However, the ERT-1m spacing may provide higher resolution imaging of subsurface resistivity characteristics. For instance, in Figure 6.15A, the 1m spacing ERT is able to capture details such as the preferential zones (yellow zones, in 54 m to 60 m from NE-SW direction), which may not be as clearly visible with a 1.5m spacing (Figure 6.15B). Additionally, the ERT 1m-spacing image may reveal clear geological structure, such as cave galleries, at ERT



profile of 40-50 m (from NE to SW direction). This indicates that using a smaller spacing, such as 1m, can potentially offer enhanced resolution for identifying subsurface resistivity characteristics in detail.

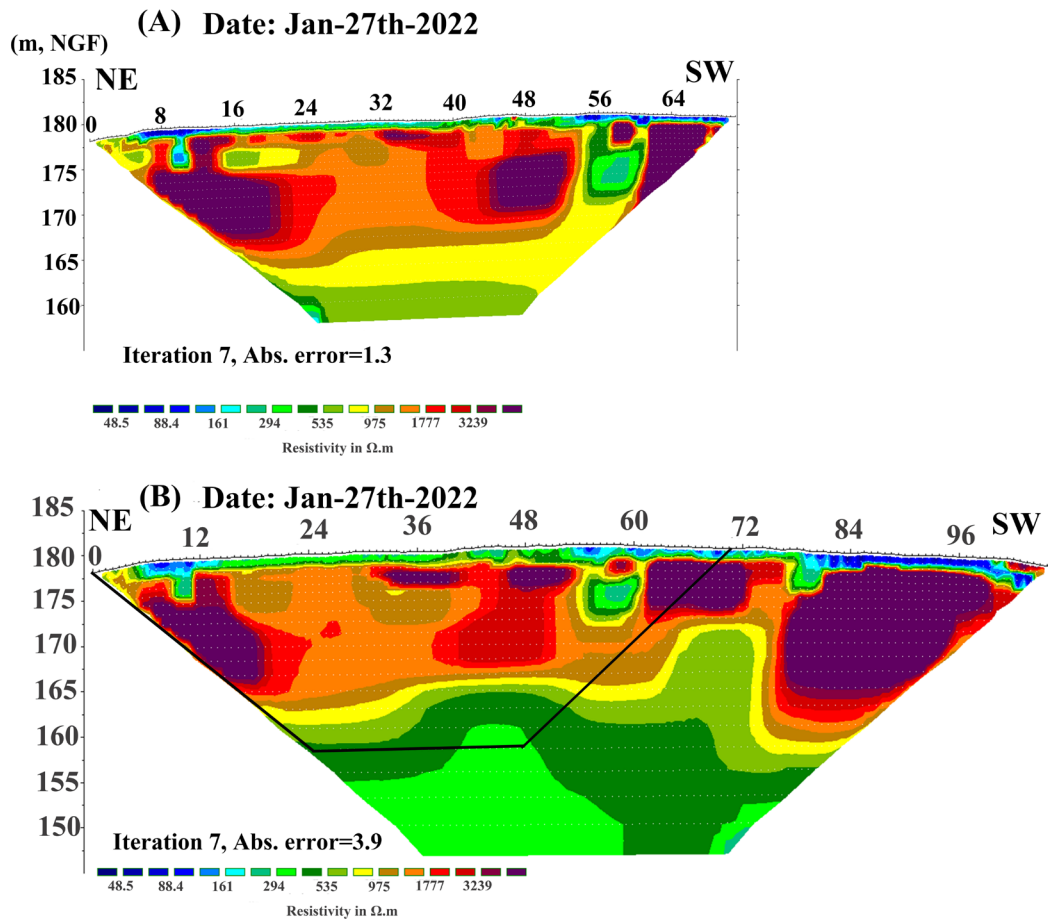


Figure 6. 15 (A) The resistivity model of 27th/January 2022 with an electrode spacing of 1 m above Villars Cave. (B) The resistivity model of 27th/January 2022 with an electrode spacing of 1.5 m above Villars Cave.

The relative frequency and cumulative frequency for the whole data in ERT-1.5m spacing indicate that the resistivity data are mainly concentrated between  $389 \Omega\cdot m$  and  $9772 \Omega\cdot m$ . However, the resistivity above  $9772 \Omega\cdot m$  accounts for less than 9% of the entire type of data set (Figure 6.16). The high values correspond to the cave galleries (165–178 m, NGF), whereas the lower

values correspond to the top-soil (clay and organic matter). Compared to the ERT conducted with a 1-meter spacing, the ERT with a 1.5-meter spacing revealed higher frequency values between 389 and 977  $\Omega \cdot m$ , which correspond to a new identified reservoir zone (cluster 6-1.5m, Figure 6.17B). Additionally, the higher frequency of resistivity values exceeding 9772  $\Omega \cdot m$  suggests the existence of a cave gallery or sinkhole on the right side of the ERT image (cluster 8-1.5m, Figure 6.17B).

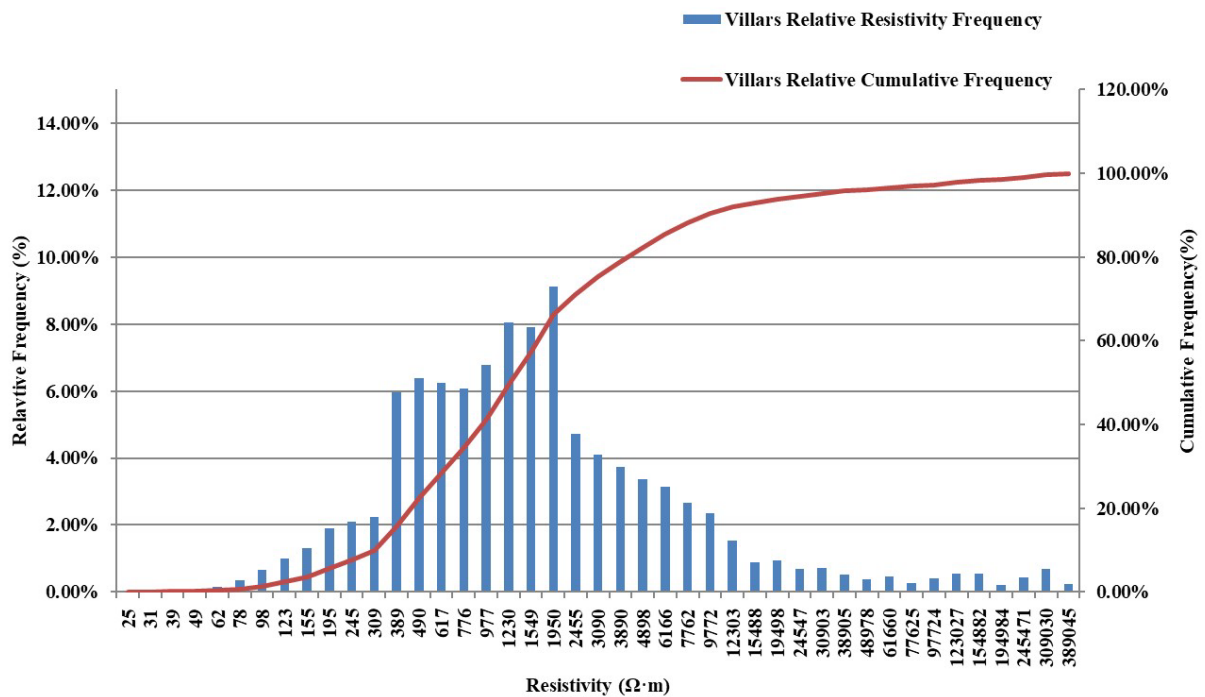


Figure 6. 16 Relative frequency and cumulative frequency of the concatenation of two arrays (Gradient Array and Pole-Dipole Array) for the whole data set in 1.5 spacing.

## 6.5 HAC in ERT images-1.5 m spacing

The dendrogram producing the different clusters (Figure 6.17A) shows four distinct main clusters (clusters A, B, C and D). In order to obtain as much detail as possible and to compare with the ERT-1m spacing, we decided on a

cutoff line (classification line), which yielded eight sub-clusters (see dashed line in Figure 6.17A). Clusters A, B, C, and D, with median resistivities from 486  $\Omega\cdot\text{m}$  to 2619  $\Omega\cdot\text{m}$ , 2359  $\Omega\cdot\text{m}$  to 9122  $\Omega\cdot\text{m}$ , and 11531  $\Omega\cdot\text{m}$  to 162381  $\Omega\cdot\text{m}$ , and 95  $\Omega\cdot\text{m}$  to 2242  $\Omega\cdot\text{m}$ :

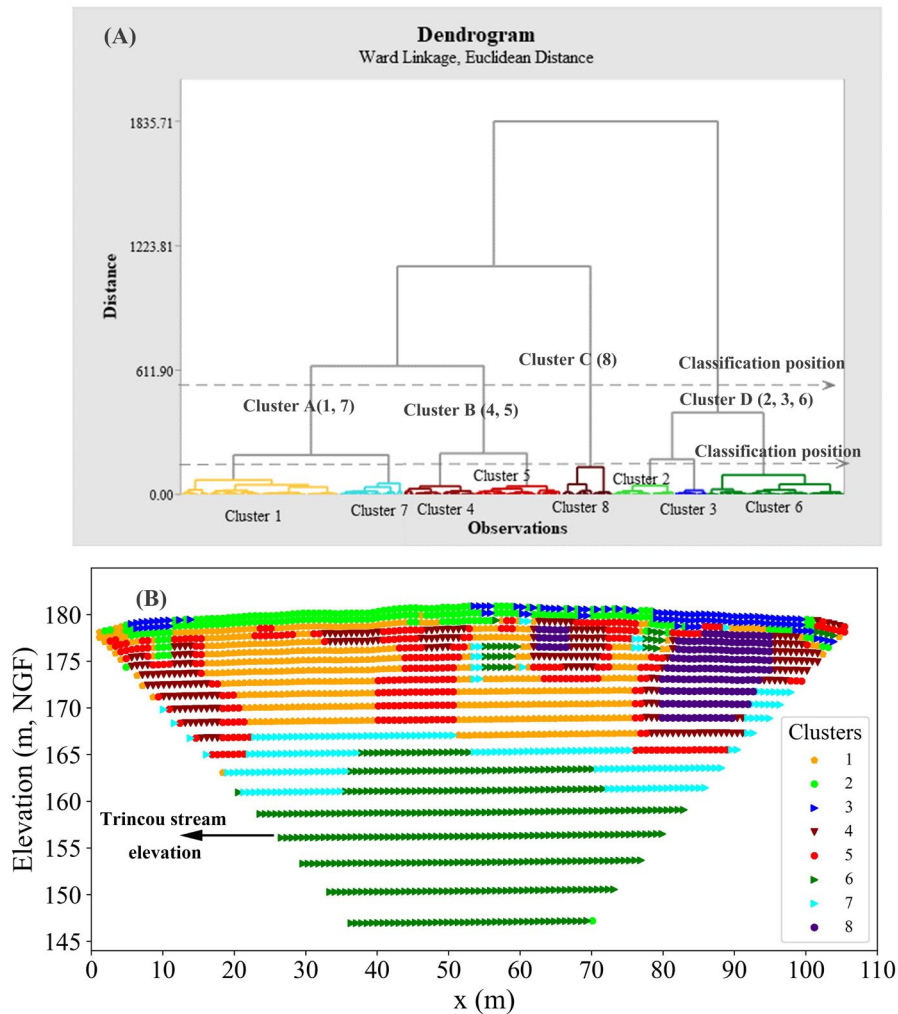


Figure 6. 17 Results of the Hierarchical Agglomerative Classing (HAC) for all monitoring periods for the ERT-1.5m profile (106.5m) above Villars Cave. (A) Dendrogram creates four and eight clusters. (B) Distribution of blocks taking into account their clusters.

- (1) Cluster A, including clusters 1 and 7, ranges from 1178  $\Omega\cdot\text{m}$  to 2619  $\Omega\cdot\text{m}$  and 486  $\Omega\cdot\text{m}$  to 1520  $\Omega\cdot\text{m}$ , respectively (Table 6.3; Figure 6.17A).

- (2) Cluster B, consisting of clusters 4 and 5, shows median values, ranging from 5646  $\Omega\cdot\text{m}$  to 9122  $\Omega\cdot\text{m}$  and 2359  $\Omega\cdot\text{m}$  to 4348  $\Omega\cdot\text{m}$ , respectively (Table 6.3; Figure 6.17A).
- (3) Cluster C, consisting of cluster 8 (Figure 6.17A) in the right section of the HAC image (165 m to 175 m NGF) (Figure 6.17B), shows the highest median value of resistivity from 11531  $\Omega\cdot\text{m}$  to 162381  $\Omega\cdot\text{m}$  (Table 6.3; Figure 6.17A).
- (4) Cluster D, with the low resistivity zone, including in clusters 2, 3, and 6 (Figure 6.17A), ranges from 278  $\Omega\cdot\text{m}$  to 2242  $\Omega\cdot\text{m}$ , 95  $\Omega\cdot\text{m}$  to 615  $\Omega\cdot\text{m}$ , 213  $\Omega\cdot\text{m}$  to 690  $\Omega\cdot\text{m}$ , respectively (Table 6.3).

In comparison to the ERT conducted with the 1m-spacing, the ERT with a 1.5m spacing reveals extremely high resistivity values in the right part of the HAC image (purple zones, Figure 6.17B). As a result, a separate cluster, labeled cluster 8-1.5m, is classified to indicate this distinct area (a new cave gallery or sinkhole collapse) with unusually high resistivity values (Figure 6.17B; Table 6.3). These higher values may be due to the fact that the profile is exactly above the gallery and integrated much more air volume. Currently, these cave zones are not visible on the cave plan map because we are unable to access this gallery (Figure 2.1C). In addition, the new 1.5 m-spacing classification highlights a previously unidentified reservoir area, labeled as cluster 6-1.5m (Figure 6.17B).

**Table 6. 3 Statistical parameters for the resistivity of each cluster (Median and Standard Deviation (SD), Average value) in the ERT-1.5m spacing.**

	Cluster 1			Cluster 2			Cluster 3			Class 4			Cluster 5			Cluster 6			Cluster 7			Cluster 8		
Date	medi an	SD	avera ge	medi an	SD	avera ge	medi an	S D	avera ge	medi an	SD	avera ge	medi an	SD	avera ge	medi an	S D	avera ge	medi an	SD	avera ge	medi an	SD	avera ge
2021/7/5	1270	465	1360	379	177	416	150	65	167	6195	315 1	6945	2741	127 0	2932	478	13 3	505	1109	248 5	1746	5369 4	5096 8	69851
2021/11/10	1358	407	1370	353	185	389	125	41	132	5969	258 1	6483	2499	112 6	2811	681	23 7	700	1440	128 6	1713	2496 3	1660 9	29860
2021/12/9	1186	341	1195	280	102	294	95	28	101	6034	486 0	6805	2359	792	2387	656	19 6	646	1262	135 6	1555	3585 0	3573 1	48184
2022/1/27	1285	401	1274	319	127	344	110	44	114	7135	350 5	7576	2680	152 1	2881	415	10 8	445	1160	251 1	1693	1134 46	1008 07	14009 3
2022/3/16	1178	437	1202	278	166	316	102	47	105	8402	607 2	9806	2518	244 1	3120	517	14 0	517	1282	403 6	2072	1623 81	1141 75	17184 3
2022/5/11	1401	419	1381	502	174	510	170	61	172	6095	246 7	6560	2593	128 6	2940	378	13 0	427	949	125 7	1358	6442 0	7913 3	92988
2022/9/16	2619	177 3	2955	2242	120 4	2420	615	21 9	634	5646	859 2	6864	4348	281 3	4600	213	23 5	324	486	255	534	1153 1	9794	13717
2023/1/19	1319	113 4	1498	402	491	491	132	87	141	9122	109 06	11898	3024	389 6	3864	690	25 0	667	1520	448 4	2498	1615 02	1283 39	19601 3
Median	1364	990	1529	378	827	648	132	19 2	196	6541	626 3	7867	2678	223 2	3192	484	22 3	529	987	244 9	1332	4833 0	1010 62	95319
Maximum	2619	177 3	2955	2242	120 4	2420	615	21 9	634	9122	109 06	11898	4348	389 6	4600	690	25 0	700	1520	448 4	2498	1623 81	1283 39	19601 3
Minimum	1178	341	1195	278	102	294	95	28	101	5646	246 7	6483	2359	792	2387	213	10 8	324	486	255	534	1153 1	9794	13717

## 6.6 Comparisons of variabilities in resistivity in ERT-1.5m and ERT-1m spacing

### 6.6.1 Mutually-validated HAC clusters in ERT-1.5m and ERT-1m spacing

Further comparison of two different ERT spacing (1m and 1.5m spacing) of these clusters could provide valuable insights and verifications into ERT data interpretations. Generally, the HAC results show similar resistivity distributions (Figure 6.18) and significant seasonal changes linked with local water excess (Figures 6.19 and 6.20).

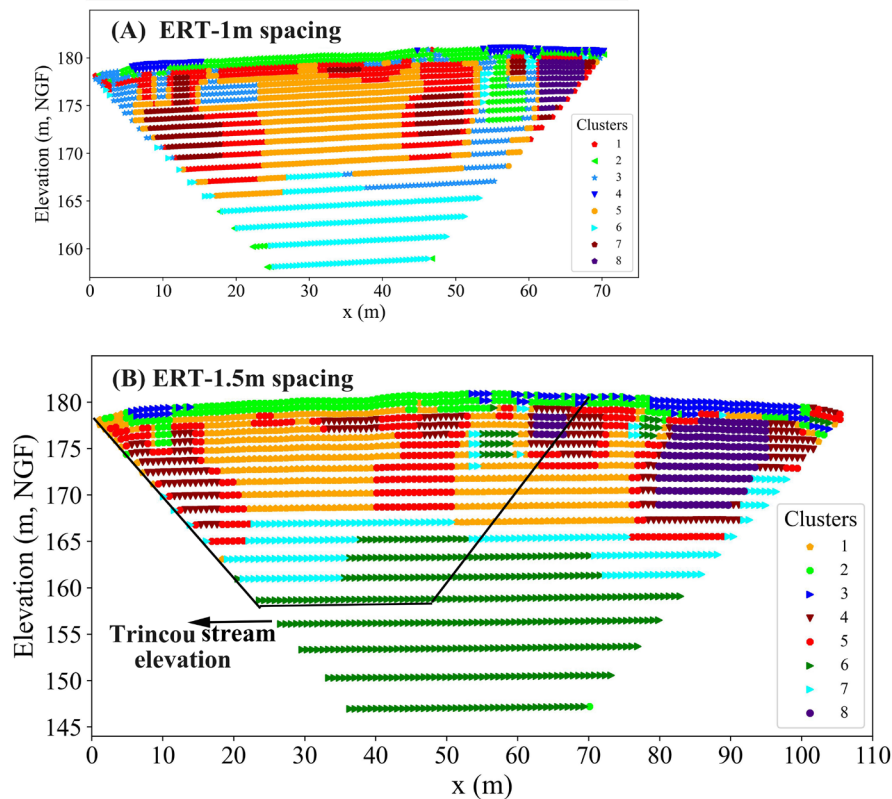


Figure 6. 18 Dendrogram creates eight clusters in 1 m and 1.5 m spacing.

The similar clusters corresponding to 1m and 1.5m spacing are listed as follows:

### **(1) Cluster 3-1.5m and Cluster 4-1m**

Cluster 3-1.5m and cluster 4-1m both exhibit similar median resistivity values. In cluster 3-1.5m, the median resistivity is 132  $\Omega\cdot\text{m}$ , with a range of 95  $\Omega\cdot\text{m}$  to 615  $\Omega\cdot\text{m}$  (Figure 6.19A and Table 6.3), located at 5-13 m and around 52-71 m and at 78-100 m (from NE-SW direction) of the ERT profile (Figure 6.18B). Similarly, cluster 4-1m (Figure 6.18A) has a median resistivity of 106  $\Omega\cdot\text{m}$ , with a range of 80  $\Omega\cdot\text{m}$  to 534  $\Omega\cdot\text{m}$  (Table 6.1), located in same place as cluster 3-1.5m (Figure 6.18B). The median resistivity values in both clusters are linked to water excess, showing seasonal variation with an increase in summer and autumn, and a decrease in winter and spring (Figure 6.19A). These clusters are mainly composed of surface clay and organic matter as the borehole confirmed (Figure 6.7).

### **(2) Cluster 2-1.5m and Cluster 2-1m**

In cluster 2-1.5m, the median resistivity value is 378  $\Omega\cdot\text{m}$ , with a range of 278  $\Omega\cdot\text{m}$  to 2242  $\Omega\cdot\text{m}$  (Figure 6.19B and Table 6.3), mainly located between 15 m and 50 m (on the ERT profile from NE to SW) and situated the below of cluster 3-1.5 m of the ERT profile (Figure 6.18B). This cluster displays a similar median resistivity value with cluster 2-1m (median value: 351  $\Omega\cdot\text{m}$ ). The seasonal resistivity pattern of cluster 2-1.5m is comparable to that of cluster 2-

1m (Figure 6.19B). Both clusters contain a small amount of top-soil mixed with weathered limestones as borehole confirmed in Figure 6.7.

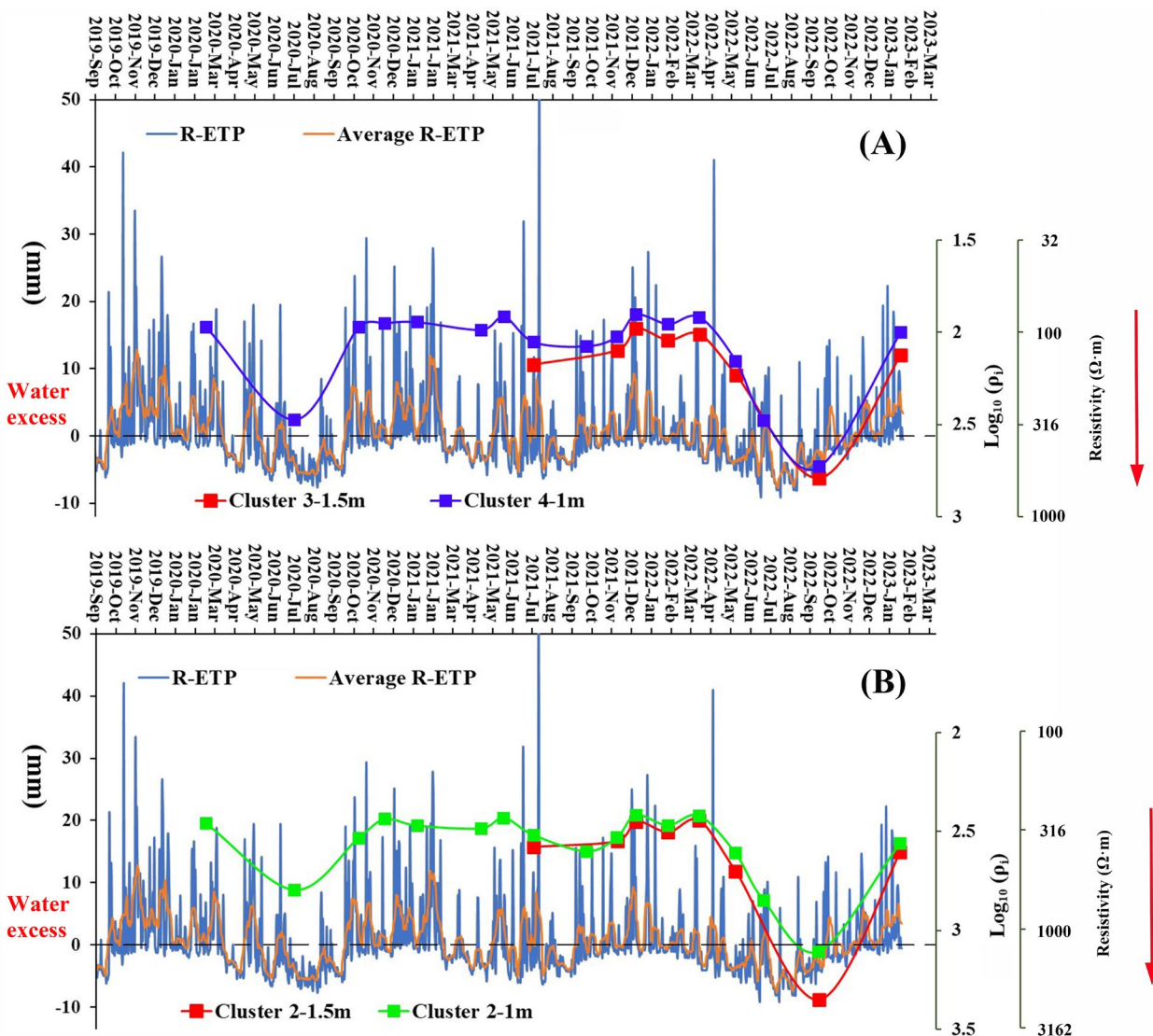


Figure 6. 19 Comparison between median resistivity and water-excess ( $R-ETP > 0$ ) (A) Cluster 3-1.5m and cluster 4-1m. (B) Cluster 2-1.5m and cluster 2-1m.



### (3) Cluster 1-1.5m and Cluster 5-1m

Cluster 1-1.5m has a median resistivity value of 1364  $\Omega \cdot m$ , ranging from 1178  $\Omega \cdot m$  to 2619  $\Omega \cdot m$  (Figure 6.20A and Table 6.3), located in the middle layer of the ERT profile (165-178 m, NGF) (Figure 6.18B). This is relatively close to the median resistivity value (1647  $\Omega \cdot m$ ) of cluster 5-1m, corresponding to the zone of fractured limestones in the fissure network.

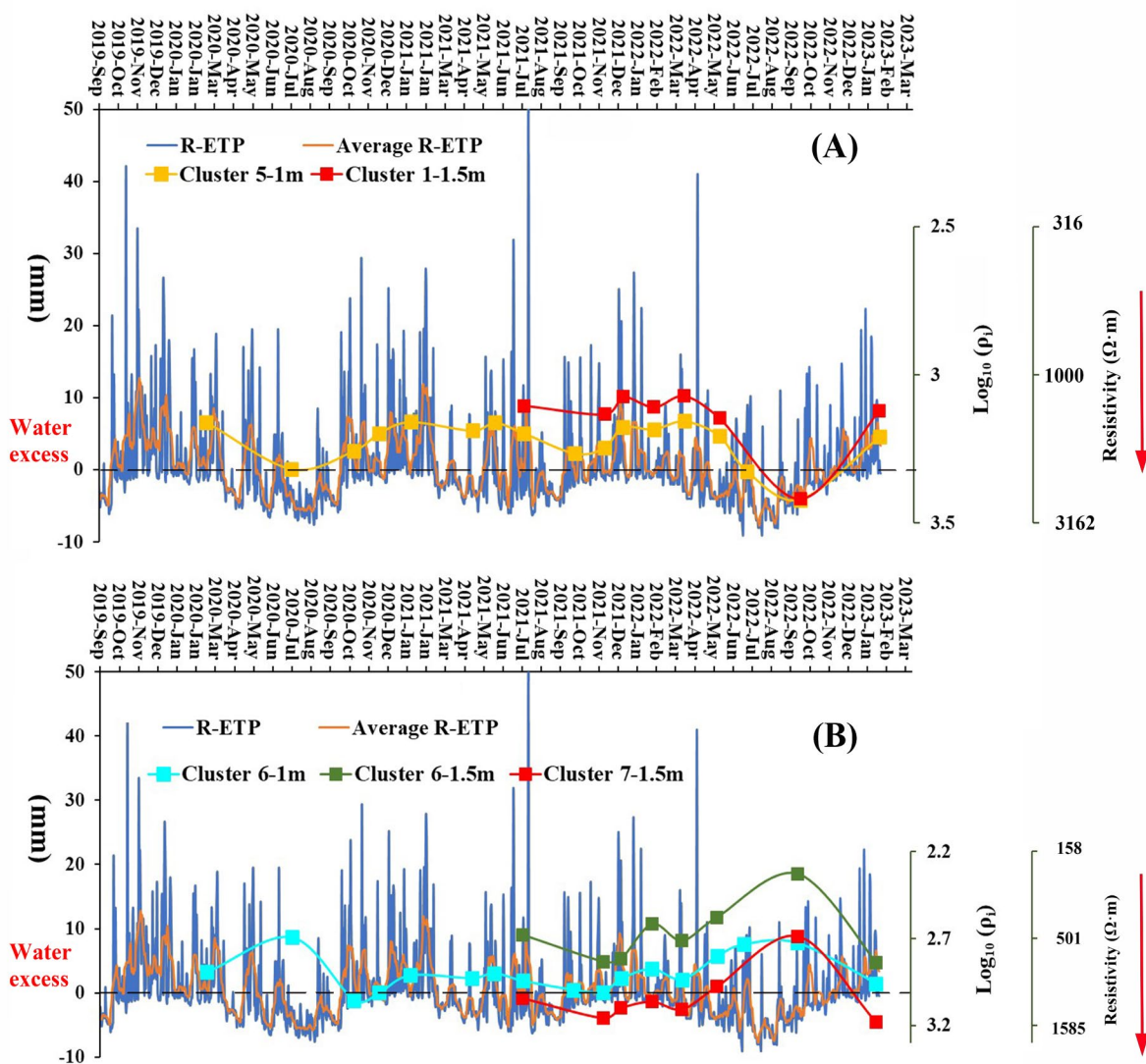


Figure 6. 20 Comparison between median resistivity and water-excess ( $R-ETP > 0$ ) (A) Cluster 5-1m and cluster 1-1.5 m (B) Cluster 6-1m, cluster 6-1.5m, and cluster 7-1.5 m.

#### (4) Clusters 7-1.5 m and Cluster 6-1m

The median value of cluster 7-1.5 m is 987  $\Omega \cdot m$ , ranging from 486  $\Omega \cdot m$  to 1520  $\Omega \cdot m$  (Figure 6.20B and Table 6.3), respectively, located in the below 165 m (NGF) (Figure 6.18B). Cluster 7-1.5 is almost situated in the same location as cluster 6-1m, exhibiting a closer median resistivity value with cluster 6-1m (817  $\Omega \cdot m$ ). Similarly, during summer, cluster 7-1.5 m may be influenced by the conductivity of underground water, which was discussed in section 6.2.2.

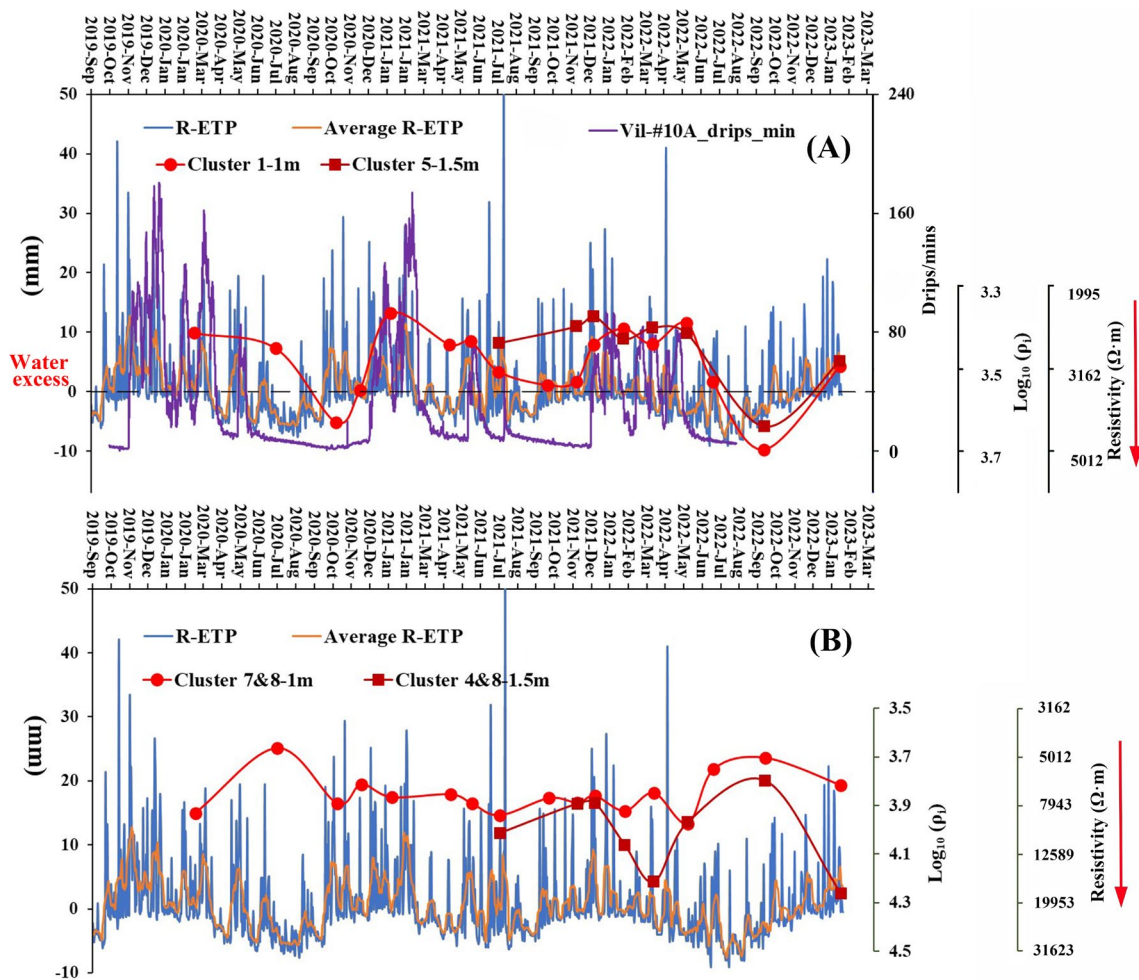


Figure 6. 21 Comparison between median resistivity and water-excess (R-ETP > 0) (A) Cluster 5-1.5m and cluster 1-1m; (B) Cluster 4&8-1.5m and cluster 7&8-1m.

#### (5) Cluster 5-1.5m and Cluster 1-1m

The median value of cluster 5-1.5m is 2678  $\Omega\cdot\text{m}$ , and the range of resistivity values is from 2359  $\Omega\cdot\text{m}$  to 4348  $\Omega\cdot\text{m}$  (Figure 6.21A), which is mainly distributed around cave galleries (Figure 6.18B). This area is close to cluster 1-1m, which has a median value of 3043  $\Omega\cdot\text{m}$ , ranging from 2321  $\Omega\cdot\text{m}$  to 4957  $\Omega\cdot\text{m}$  (Table 6.1). These clusters are linked with the cave dripping water rate (Vil-#10A) (Figure 6.21A), acting as storing local rainwater feeding cave stalagmites in Villars Cave as we also explained in section 6.2.2.

#### **(6) Cluster 4&8-1.5m and Cluster 7&8-1m**

The red zones at 160-168 m (NGF) in cluster 4&8-1.5 m (Figure 6.18B) spacing show a high median resistivity ( $>6000 \Omega\cdot\text{m}$ ) without seasonal variabilities (Figure 6.21B; Table 6.2), corresponding in cluster 7&8-1m spacing (Figure 6.18A); they can be attributed to cave gallery area.

### **6.6.2 Unvalidated HAC clusters: Cluster 3-1m and Cluster 6-1.5m**

The unvalidated clusters in cluster 3-1m spacing and cluster 6-1.5m spacing in the two ERT measurements are discussed in detail. Here are some possible points to consider:

(1) The discovery of cluster 3-1m in the ERT measurements, which is not visualized on the 1.5m spacing image (Figure 18). It is hypothesized that the inability to visualize cluster 3-1m on the 1.5m spacing image may be attributed to the lower resolution of the image compared to the 1m spacing.

(2) Cluster 6-1.5 m, located in the lowest layers in the ERT image below cluster 6-1m (Figure 6.18B), exhibits a median resistivity value of 484  $\Omega\cdot\text{m}$  with a range of 213  $\Omega\cdot\text{m}$  to 690  $\Omega\cdot\text{m}$ , which is lower than the median resistivity value of cluster 6-1m (817  $\Omega\cdot\text{m}$ ) (Figure 6.20B). This suggests that the resistivity variations in cluster 6-1.5m are influenced by factors other than changes in water conductivity. Moreover, cluster 6-1.5m also located at the same altitude with the Trincou stream as shown in Figure 6.18B, suggests that the quantity of water in cluster 6-1.5m may remain more saturated due to its greater depth.

## 6.7 Summary

Two different measurements were conducted with 1m and 1.5m spacing using the same ERT profile to compare the variabilities in resistivity. The clusters corresponding to 1m and 1.5m spacing were compared, and the results showed similar resistivity variations, and possibly with seepage water conductivity at some places. The clusters and their characteristics are as follows:

(1) Cluster 3-1.5m and Cluster 4-1m: both clusters exhibit similar median resistivity values, linked to water excess, showing seasonal variation with an increase in summer and autumn and a decrease in winter and spring. These clusters are mainly composed of surface clay and organic matter.

(2) Cluster 2-1.5m and Cluster 2-1m: these clusters display a similar median resistivity value and a comparable seasonal resistivity pattern. Both clusters contain a small amount of top-soil mixed with weathered limestones.

(3) Cluster 1-1.5m and Cluster 5-1m: cluster 1-1.5m and cluster 5-1m has a median resistivity value in the middle layer of ERT, corresponding to the zone of fractured limestones in the fissure network.

(4) Cluster 6-1m and Cluster 7-1.5m: clusters 6-1.5m and 7-1.5m serve as storage reservoirs. However, during summer/dry period, cluster 7-1.5m may be influenced by the conductivity of underground water.

(5) Cluster 6-1.5m, located at the lowest layers in the ERT image, exhibits lower resistivity and greater depth compared to cluster 6-1m, suggesting influences other than changes in water conductivity. Cluster 6-1.5m, located at the same altitude with the Trincou stream, further suggests that it may remain more saturated due to river water and greater depths.

Overall, the comparison of variabilities in resistivity in ERT-1.5m and ERT-1m spacing provides valuable insights and verifications into ERT data interpretations.

## General conclusion

The study of the hydrology and geophysics of karst systems is a complex but essential field of research that requires the use of various techniques and tools. The three studies presented here highlight the importance of using long-term monitoring and modeling approaches to better understand the links between meteorological conditions, the source of rainfall, water infiltration, and cave drip rates and isotopic compositions. The results obtained using different methods, including stable isotopes, electrical resistivity tomography, and modeling, provide valuable information on the dynamics and behavior of karst systems. By testing and validating ERT/hydrology/isotope methods in this particular site which is the Villars Cave, we hope to deepen the understanding of typical karst sites hydrological behavior. This, in turn, could help to improve our ability to manage and protect sensitive karst environments. The main conclusions as follows:

- (1) Origins of precipitation isotopic signature, by using HYSPLIT model, has shed light on the complex relationship between stable isotopes of precipitation, moisture sources, and local climate parameters in Southwest France. We concluded to shorter transportation distances during summer months and longer ones during winter, which is consistent with the observed seasonal variations of  $\delta^{18}\text{O}_p$ . Our results have provided important insights into the factors controlling the oxygen isotope composition of precipitation in this region, with the percentage of initial moisture sources being a key factor. Furthermore, this study has highlighted the importance of long-term monitoring in detecting decadal trends and changes in rainfall sources.
- (2) Valuable insights into the dynamics of infiltration and karst reservoirs behavior above Villars Cave, have been made by using both a long-term monitoring

isotopic data set and the KarstFor conceptual model. Results show a well-marked seasonal variability and a moderate time delay between water excess and drip rates. It also reveals the impact of multiple infiltration routes and karst reservoir dynamics on the drip water  $\delta^{18}\text{O}$ . Furthermore, our findings indicate that the observed stalactite dripping  $\delta^{18}\text{O}$  follows the variation of the water excess and the cave temperature on an inter-annual scale, revealing a long-term trend possibly due to climatic change above the studied cave. The simulated trends for the future 100 years also show a significant increase in  $\delta^{18}\text{O}_d$ , mainly due to the rainfall  $\delta^{18}\text{O}$  and outside temperature increase.

(3) Time-lapse electrical resistivity tomography (TL-ERT) has been used to monitor the karst vadose zone overlying Villars Cave during 3 years. Results showed significant seasonal dynamics of aquifer recharge processes and allowed the visualization of different karst critical zones, including cave galleries and water storage reservoirs, top-soil layers, and potential preferential flow paths. This study identified distinct clusters with contrasting resistivity variations, directly related to water-excess changes, local droughts, and preferential infiltration pathways. These findings highlight the interest of using subsurface geophysics, particularly TL-ERT to visualize and to study hydrological and geophysical features in karst terrains.

All these results have implications not only for the scientific understanding of karst systems but also for the management and conservation of caves and their natural heritage. The ability to predict water infiltration pathways and to understand the factors controlling drip rates and isotopic compositions can help in the development of effective conservation and management strategies. Overall, the combination of multiple techniques and approaches is crucial for gaining a

comprehensive understanding of the complex hydrological and geophysical processes in karst systems.

Since cave morphology and network geometry are the results of long-term geological, geomorphological and hydrogeological evolution, it is important to determine how they were formed and their subsequent evolution. Field observations associated with the 2D/3D ERT analysis will help to characterize the cave evolution and to establish an accurate cave framework.

Future plans can be developed as follows:

- (1) 3D ERT observation will be used in the unsaturated zones in Villars Cave. In future DECACLIM project (ANR project), 3D ERT will be used to i) distinguish between superficial lithologies, fractures, and underlying vadose zones with high resistivity associated with cave galleries and/or weathered zones, and ii) identify recharge zones. iii) quantify the volume of each cluster.
- (2) by combining Ground penetrating radar (GPR) and ERT images, we hope to better identify the geometry of the cave galleries.
- (3) by applying the KarstFor and Hysplit models, we will predict changes in cave hydrology and isotopes in the context of global warming under various Representative Concentration Pathway (RCP) scenarios for the next hundred years.



## Acknowledgments

I am extremely grateful to have the opportunity to pursue a doctoral degree at the University of Bordeaux, and I would like to express my heartfelt thanks to everyone who has supported and cared for me, including my teachers, classmates, friends, and family.

First of all, special acknowledgement is given to my respectable supervisors, Dominique Genty and Colette Sirieix, whose patient instructions and constructive suggestions are beneficial to me a lot. They have given me great instructions and encouragement throughout the entire process of the Ph.D. period.

I want to express my deepest gratitude to Konstantinos Chalikakis, Bruno Lartiges, Laurent Bruxelles, and François Bourges for serving as my dissertation defense committee. Thank the entire EPOC and I2M lab team for their help. In particular, I would like to thank Olivier Le Roux, Joëlle Riss and Frédérique Eynaud for their advice for my thesis supervisory. I would like to thank Isabelle Lecomte, Cécile Verdet, Fabien Salmon, Sylvain Mateo, Marie Larcanché, Stéphane Bujan, and Ludovic Devaux for their help in the field in Villars. I would like to thank my colleagues: Charlotte Clément, Manon Sabourdy, Héloïse Barathieu, Ali Boukham, Mohamed Amine Es-Soufi, and Amal Rebhi. I want to thank my Chinese friends: Shuai Liu, Tong Shen, Hanyu Ye, Panpan Ma, Xuewen Zhou, Xiaowen Quan, Limeng Ruan, Shuning Han, Xinrui Li, Jiaming Huang, Xiangzhuo Liu, Jiabao Lin, Jiwang Fang and so on.

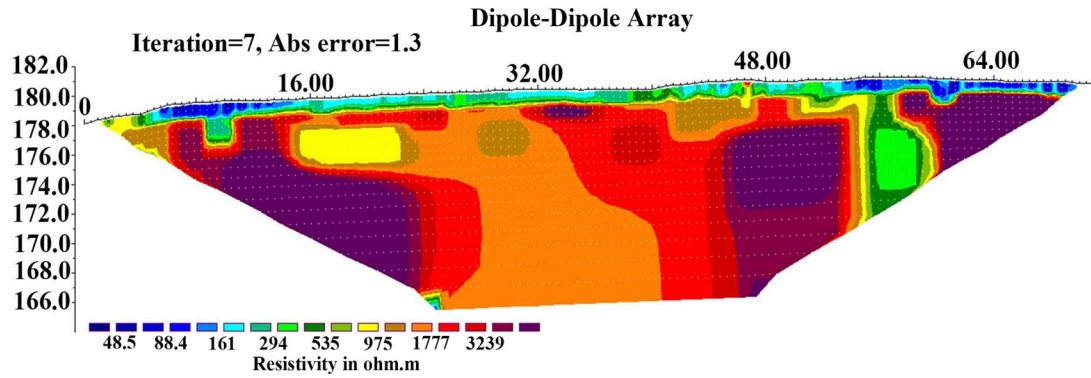
We thank the Versaveaud family, who are always interested in our research, and their constant help makes the long-term monitoring work in Villars Cave possible. We would like to express sincere thanks to Olivier Mestre for their help with meteorological data. We thank Thierry Baritaud for his help in data collecting and field trips. We thank Daniel Chailloux, Laurent Magne, Gilles Souchet for their help in determining the drip sites.

Last but not least, I want to express my deepest gratitude to my family, especially my parents, without whom I would not be where I am today. They have been my greatest source of support throughout these four years, and I hope to create a better life for them as I move forward in my career. To all those I love and who love me, I wish you good health and happiness.

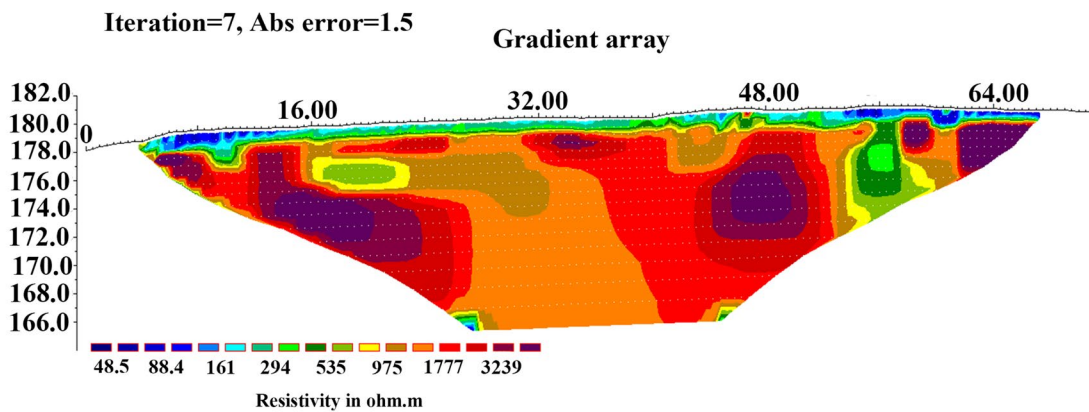
This work was supported by I2M programs on decorated caves for geophysical surveys. This research was also supported by the China Scholarship Council (CSC) to Jian. Zhang (201906990014). This long monitoring work (DG) has been funded, since 1996, by several programs from the CNRS (INSU), and three laboratories (GEOPS, Orsay, Paris-Saclay University; Laboratoire des Sciences du Climat et de l'Environnement, LSCE, CEA/CNRS/UVSQ and Environnements et Paléoenvironnements Océaniques et Continentaux, EPOC, University of Bordeaux, France). Villars Cave is part of the sites that are studied by the CNRS GIS group called GEMS "Groupe d'Etude des Milieux Souterrains", dir. B. Lartiges GET Toulouse". The rainfall stable isotope data from the Le-Mas and Villars stations is included as part of the National Observatory SNO RENOIR (CNRS, Elisabeth GIBERT-BRUNET). Department of Environmental Sciences, University of Bordeaux, has financially supported this project

## Appendix Figures

The first ERT array testing in Villars using Dipole-Dipole, Gradient, Pole-Dipole with forward and reverse array in 18th/Feb 2020:

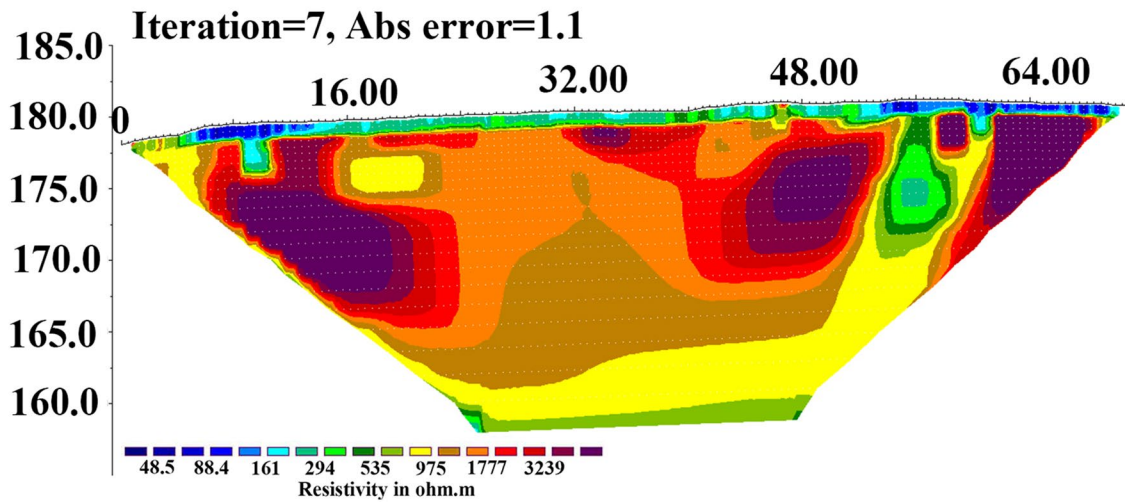


*Appendix Figure 1. The resistivity model of 18th/Feb 2020 using Dipole and Dipole with an electrode spacing of 1 m above the Villars Cave.*



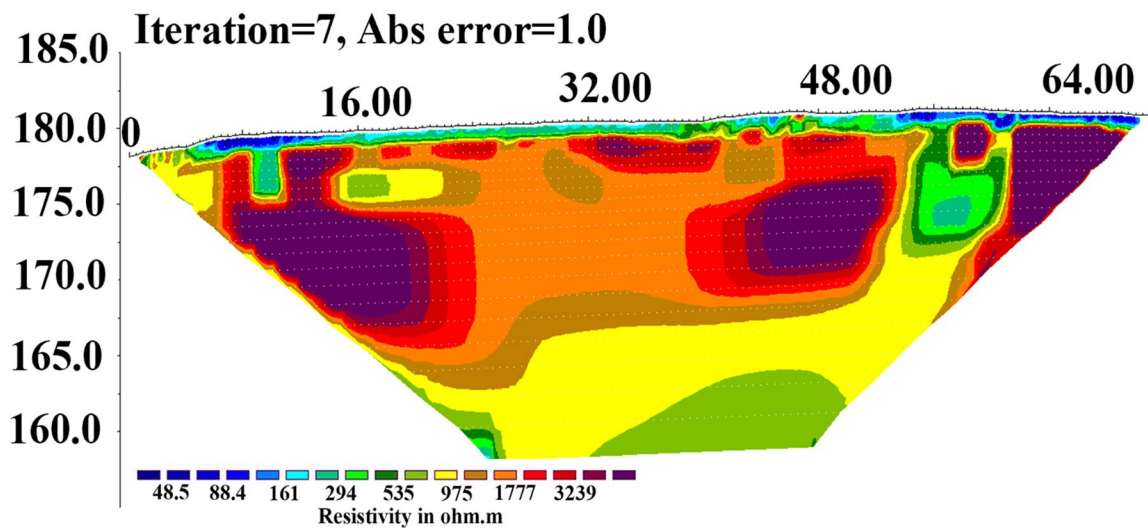
*Appendix Figure 2. The resistivity model of 18th/Feb 2020 using gradient array with an electrode spacing of 1 m above the Villars Cave.*

### Pole-Dipole-Forward and Reverse Array

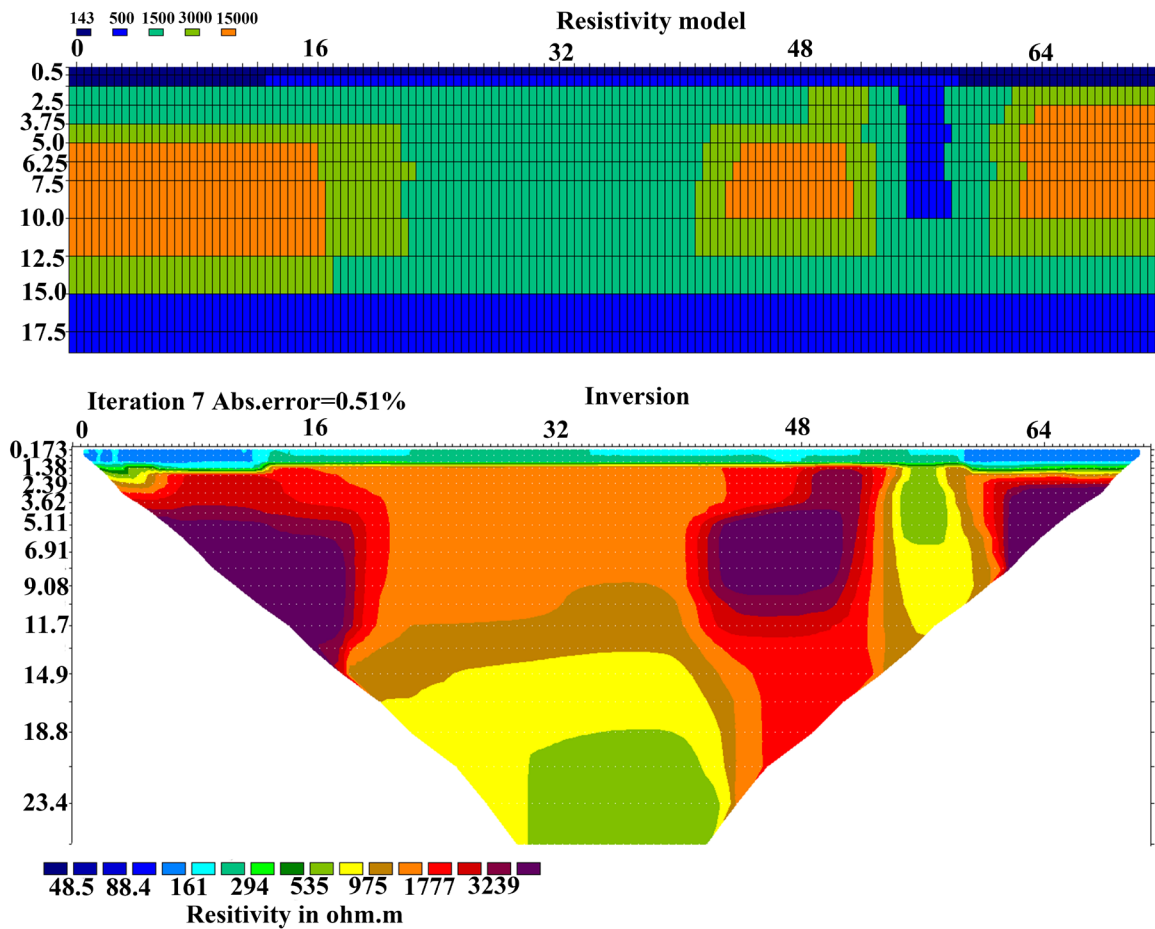


Appendix Figure 3. The resistivity model of 18th/Feb 2020 using pole-dipole forward and reverse array with an electrode spacing of 1 m above the Villars Cave.

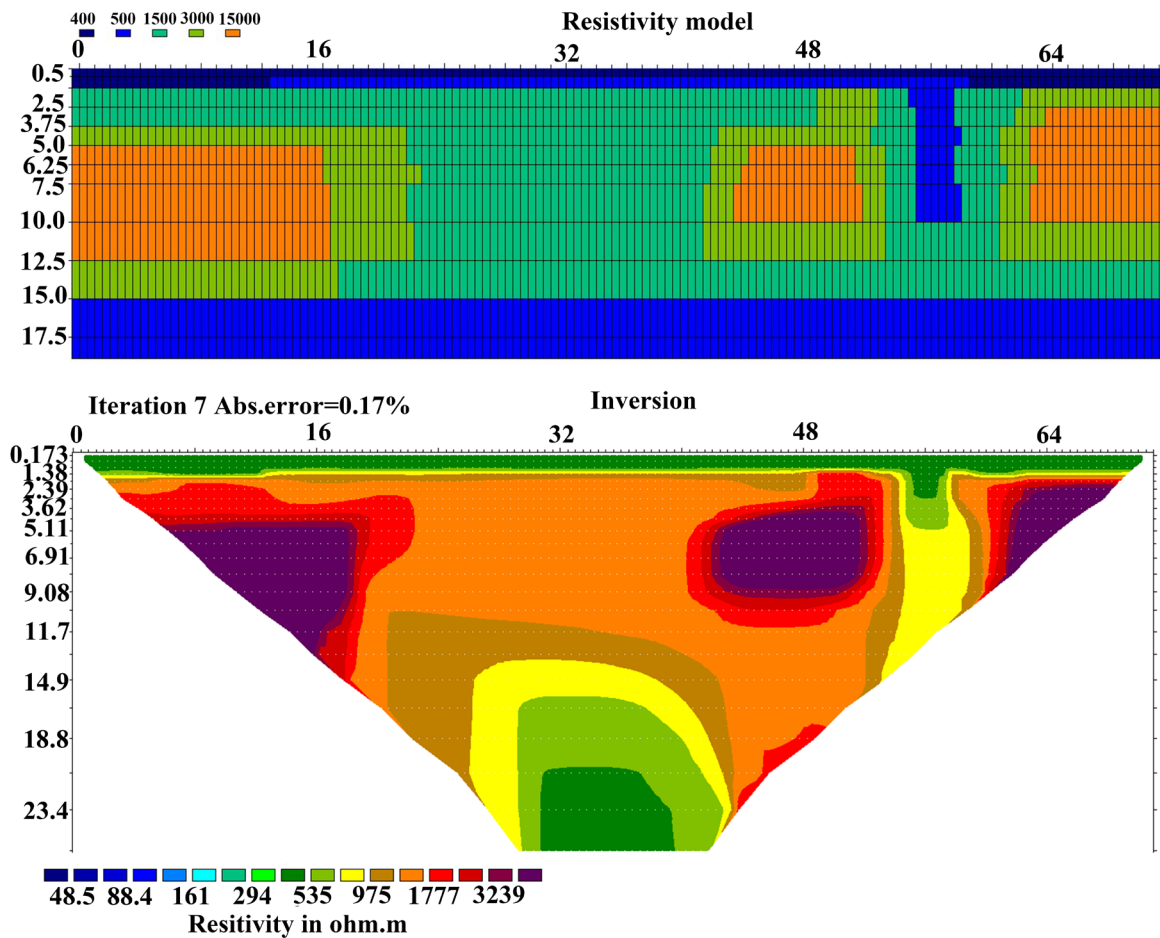
### Concatenating Pole-Dipole and Gradient array



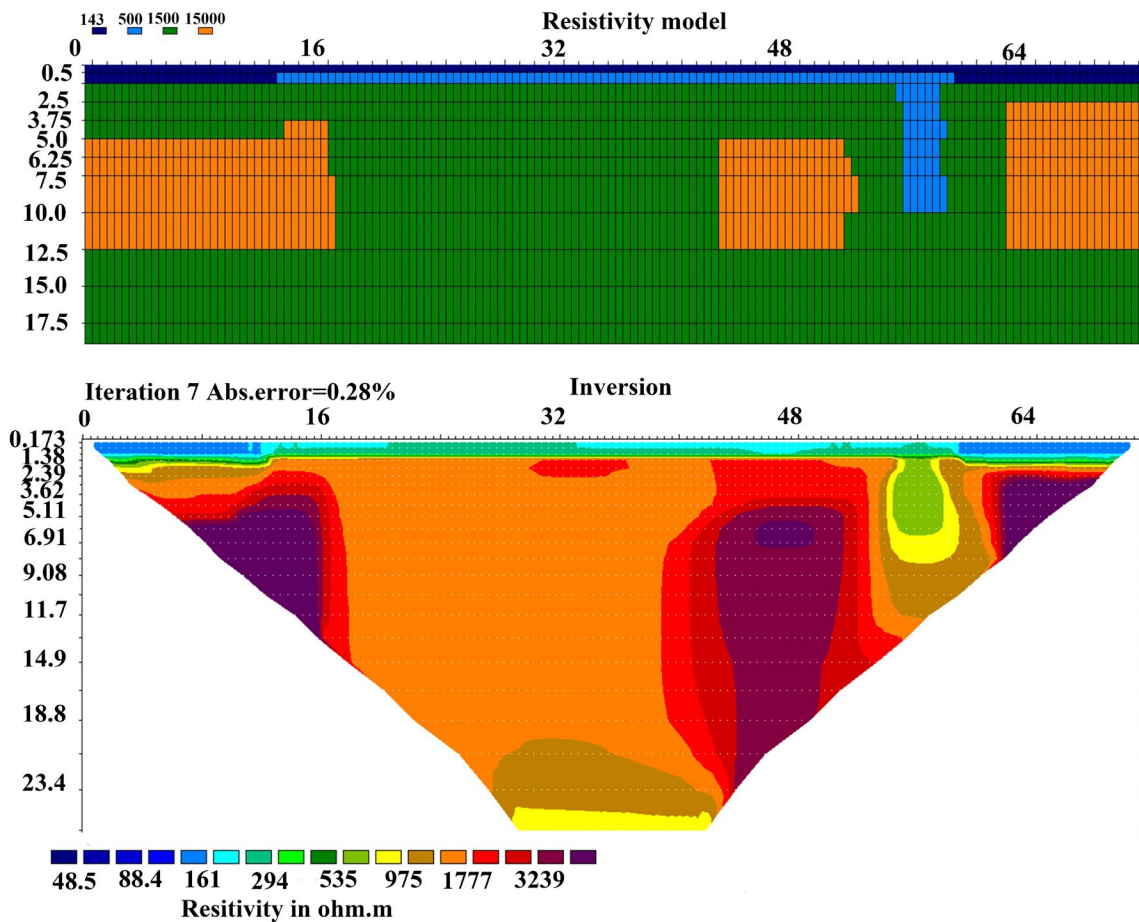
Appendix Figure 4. The resistivity model of 18th/Feb 2020 using concatenating pole-dipole with gradient array with an electrode spacing of 1 m above the Villars Cave.



Appendix Figure 5 shows the model configuration using Res2DMod, and the inversion results using Res2Dinvx64 are also displayed. In this study, we set three high-resistivity zones, as well as low-resistivity zones representing the surface and subsurface layers, to simulate the ERT observation data of Villars Cave. By comparing the simulated results with our observed data, as shown in Figure 6.3, we found similar patterns or trends. This suggests that the model and inversion used in our study are capable of reproducing the resistivity observed in Villars Cave.



Appendix Figure 6 displays the model configuration using Res2DMod. The inversion results obtained using Res2Dinvx64 are also presented. We conducted an experiment by increasing the resistivity value in the surface layer to examine the impact on the inversion results. We found that the changes in surface resistivity did not affect the resistivity values in the deeper layers.



Appendix Figure 7 shows the model configuration using Res2DMod, and the corresponding inversion results obtained through Res2Dinvx64 are displayed. An experiment was conducted by removing the low resistivity values in the deeper layer to investigate the impact on the inversion results. Interestingly, the changes in the resistivity of the deeper layer were found to correspond with the modifications made in our modeling approach.

## Appendix Data

*Appendix Table. 1 Average values for  $\delta^{18}O_p$ ,  $\delta D_p$  and their standard deviation (SD) for different months at Le Mas and Villars stations from 1997 to 2016 A.D.*

	Le Mas				Villars			
	$\delta^{18}O$ (‰, V- SMOW)	SD	$\delta D$ (‰, V- SMOW)	SD	$\delta^{18}O$ (‰, V- SMOW)	SD	$\delta D$ (‰, V- SMOW)	SD
Dec	-7.5	1.4	-47.4	11.8	-7.1	1	-44	7.6
Jan	-7.4	1.4	-47.7	11.2	-6.9	1	-43.2	8.1
Feb	-7.1	1.2	-46.1	10.2	-7.2	1	-45.8	7.3
Mar	-6.5	1	-42.1	7.1	-6.5	1.3	-40.6	8.9
Apr	-6.2	1.3	-41.2	9.8	-6.1	1.3	-39.2	10.5
May	-5.7	1.2	-36.8	8.6	-5.8	1.3	-37.2	10.5
Jun	-5	1.1	-31.5	6.8	-5.1	0.8	-31.3	6.1
Jul	-4.6	1.1	-29.7	5.5	-4.8	0.6	-29.4	5.2
Aug	-4.7	0.5	-29.5	4.5	-4.6	0.6	-27.8	4.4
Sep	-5.9	1.1	-36.6	8.7	-5.5	1.6	-34	10.7
Oct	-6.7	2	-42.2	13.5	-6.5	1.3	-40	9.6
Nov	-7.1	1.3	-45.3	10.9	-6.8	2.1	-41.1	14
Winter	-7.3	1.4	-47.1	11.1	-7.1	1	-44.3	7.7
Spring	-6.1	1.2	-40.1	8.5	-6.1	1.3	-39	10
Summer	-4.8	0.9	-30.2	5.6	-4.8	0.6	-29.5	5.2
Autumn	-6.5	1.5	-41.4	11	-6.3	1.7	-38.4	11.5

*Appendix Table. 2 Average values for  $\delta^{18}O_p$ ,  $\delta D_p$  and their SD for 1997-2016 at Le Mas*

and Villars stations.

Villars						Le mas				
	$\delta^{18}\text{O}_{\text{ap}}$	SD	$\delta^{18}\text{O}_w$ (‰,	$\delta\text{D}_{\text{ap}}$ (‰,	SD	$\delta^{18}\text{O}_{\text{ap}}$	SD	$\delta^{18}\text{O}_w$ (‰,	$\delta\text{D}_{\text{ap}}$ (‰,	SD
	(‰, V-		V-	V-		(‰, V-		V-	V-	
	SMOW)		SMOW)	SMOW)		SMOW)		SMOW)	SMOW)	
1997.00	-5.70	2.02	-5.52	-37.71	16.74					
1998.00	-5.65	1.19	-5.83	-36.23	7.50	-5.24	0.60		-30.80	5.39
1999.00	-6.26	1.08	-5.12	-41.69	6.00	-5.28	0.97	-4.69	-33.97	6.93
2000.00	-5.92	1.72	-5.96	-37.50	12.53	-5.87	1.72	-5.36	-36.61	12.04
2001.00	-6.75	1.60	-6.61	-45.57	12.80	-6.66	1.54	-5.35	-41.25	12.27
2002.00	-6.22	0.93	-6.49	-39.66	6.90	-5.91	0.73	-6.15	-37.22	4.61
2003.00	-6.09	1.97	-5.25	-38.44	15.16	-6.19	1.33	-6.16	-39.07	9.34
2004.00	-6.31	1.50	-5.98	-40.63	11.93					
2005.00	-5.99	0.82	-5.99	-38.03	4.37					
2006.00	-6.09	1.64	-5.78	-38.07	11.82	-5.67	1.61	-5.46	-35.35	11.76
2007.00	-5.49	0.79	-5.81	-32.00	5.70	-5.69	0.70	-5.79	-34.38	4.56
2008.00	-6.49	1.62	-6.01	-41.98	12.38					
2009.00	-5.38	3.10	-4.63	-37.92	17.61	-6.08	1.39	-5.37	-37.95	9.40
2010.00	-7.24	1.52	-7.00	-47.25	11.07	-7.09	1.85	-6.79	-46.38	13.89
2011.00	-6.23	1.44	-6.15	-39.78	11.18	-5.16	1.25	-5.16	-31.23	8.87
2012.00	-6.07	0.78	-6.22	-38.20	5.17	-5.88	0.83	-6.00	-34.65	5.52
2013.00	-7.21	1.87	-6.70	-47.42	14.08	-6.51	1.74	-6.05	-41.78	12.44
2014.00	-6.09	1.63	-6.17	-38.56	11.82	-6.10	1.32	-6.11	-38.18	9.48
2015.00	-5.98	1.05	-6.09	-37.31	6.77	-5.49	0.66	-5.62	-33.58	5.14
2016.00	-6.69	0.85	-6.78	-42.69	5.29	-6.19	0.99	-6.21	-38.51	6.28



*Appendix Table. 3 The equations of multiple linear regression between  $\delta^{18}\text{O}_p$  and different sources/local temperature (T) by adding different variables step by step at Le Mas and Villars stations.*

	Le Mas	Villars
Local Temperature	$\delta^{18}\text{O}_p=0.17* T-8.28$ , R= 0.61, p<0.01	$\delta^{18}\text{O}_p=0.15* T-7.93$ , R= 0.62, p<0.01
PAWE+T	$\delta^{18}\text{O}_p=0.15* T+0.07*PAWE-8.33$ , R= 0.94, p<0.01	$\delta^{18}\text{O}_p=0.1* T+0.02*PAWE-7.873$ , R= 0.91, p<0.01
NAGR+T	$\delta^{18}\text{O}_p=0.187* T+0.006*NAGR-7.610$ , R= 0.942, p<0.01	$\delta^{18}\text{O}_p=0.13* T-0.003*NAGR-7.610$ , R= 0.89, p<0.01
NA+T	$\delta^{18}\text{O}_p=0.155* T+0.01*NA-8.319$ , R= 0.944, p<0.01	$\delta^{18}\text{O}_p=0.131* T+0.006*NA-7.824$ , R= 0.91, p<0.01
NA+PAWE+T	$\delta^{18}\text{O}_p=0.112* T+0.013*PAWE+0.021*NA-8.374$ , R= 0.953, p<0.01	$\delta^{18}\text{O}_p=0.055* T+0.022*PAWE+0.025*NA-7.921$ , R= 0.924, p<0.01
ME+NA+PAWE+T	$\delta^{18}\text{O}_p=0.096* T+0.022*PAWE+0.026*NA+0.043*ME-8.673$ , R= 0.96, p<0.01	$\delta^{18}\text{O}_p=0.033* T+0.035*PAWE+0.031*NA+0.056*ME-8.308$ , R= 0.941, p<0.01
DA+ME+NA+PAWE+T	$\delta^{18}\text{O}_p=0.104* T+0.02*PAWE+0.022*NA+0.04*ME-0.004*DA-8.563$ , R= 0.961, p<0.01	$\delta^{18}\text{O}_p=0.046* T+0.031*PAWE+0.026*NA+0.051*ME-0.004*DA-8.141$ , R= 0.942, p<0.01
NAGR+ME+NA+PAWE+T	$\delta^{18}\text{O}_p=0.038*PAWE+0.046*NA+0.054*ME+0.02*DA+0.025*NAGR+0.119*T-10.929$ , R=0.965, p<0.01	$\delta^{18}\text{O}_p= 0.035*PAWE+0.031*NA+0.054*ME-0.001*DA+0.005*NAGR+0.049*T-8.637$ , R=0.942, p<0.05

*Appendix Table. 4 Number of remaining electrodes after removing points of filtering and rejecting gapfiller in the measurements of all sequences (1m)*

Date	Sequence	Number of points	Remove points after filtering	Remove points after rejecting gapfiller	Sequence	Number of points	Remove points after filtering	Remove points after rejecting gapfiller	Sequence	Number of remaining electrodes
18th/Feb/2020	PD-72-1-F-R-250ms	6218	0	742	Grad-72-1-500ms	8223	0	0	Concatenating PD-250ms and GD-500ms	13699
02th/July/2020	PD-72-1-F-R-500ms	6218	0	742	Grad-72-1-v3-250ms	6042	13	0	Concatenating PD-500ms and GD-250ms	11505
09th/Oct/2020	PD-72-1-F-R-500ms	6218	0	742	Grad-72-1-v3-250ms	6042	0	0	Concatenating PD-500ms and GD-250ms	11518
18th/Nov/2020	PD-72-1-F-R-500ms	6218	0	742	Grad-72-1-v3-250ms	6042	0	0	Concatenating PD-500ms and GD-250ms	11518
07th/Jan/2021	PD-72-1-F-R-500ms	6218	0	742	Grad-72-1-v3-250ms	6042	0	0	Concatenating PD-500ms and GD-250ms	11518
15th/Apr/2021	PD-72-1-F-R-500ms	6218	0	742	Grad-72-1-v3-250ms	6042	0	0	Concatenating PD-500ms and GD-250ms	11518
20th/May/2021	PD-72-1-F-R-500ms	6218	4 (Deviation>5)	740	Grad-72-1-v3-250ms	6042	0	0	Concatenating PD-500ms and GD-250ms	11516
05th/July/2021	PD-72-1-F-R-500ms-1m	6218	0	742	Grad-72-1-v3-250ms	6042	0	0	Concatenating PD-500ms and GD-250ms	11518

Appendix

24th/Sep/2021	PD-72-1-F-R- 500ms	6218	0	742	Grad-72-1- v3-250ms	6042	0	0	Concatenating ms and GD-250ms	PD-500	11518
10th/Nov/2021	PD-72-1-F-R- 500ms-1m	6218	0	742	Grad-72-1- v3-250ms	6042	0	0	Concatenating ms and GD- 250ms	PD-500	11518
09th/Dec/2021	PD-72-1-F-R- 500ms-1m	6218	0	742	Grad-72-1- v3-250ms	6042	0	0	Concatenating ms and GD- 250ms	PD-500	11518
27th/Jan/2022	PD-72-1-F-R- 500ms-1m	6218	0	742	Grad-72-1- v3-250ms	6042	0	0	Concatenating ms and GD- 250ms	PD-500	11518
16th/Mar/2022	PD-72-1-F-R- 500ms-1m	6218	0	742	Grad-72-1- v3-250ms	6042	0	0	Concatenating ms and GD- 250ms	PD-500	11518
11th/May/2022	PD-72-1-F-R- 500ms-1m	6218	0	742	Grad-72-1- v3-250ms	6042	0	0	Concatenating ms and GD- 250ms	PD-500	11518
27th/Jun/2022	PD-72-1-F-R- 500ms-1m	6218	0	742	Grad-72-1- v3-250ms	6042	0	0	Concatenating ms and GD- 250ms	PD-500	11518
16th/Sep/2022	PD-72-1-F-R- 500ms-1m	6218	0	742	Grad-72-1- v3-250ms	6042	0	0	Concatenating ms and GD- 250ms	PD-500	11518
19th/Jan/2023	PD-72-1-F-R- 500ms-1m	6218	0	742	Grad-72-1- v3-250ms	6042	0	0	Concatenating ms and GD- 250ms	PD-500	11518

**Appendix Table. 5** Number of remaining electrodes after removing points of filtering and rejecting gapfiller in the measurements of all sequences (1.5 m)

Date	Sequence	Number of points	Remove points after filtering	Remove points after rejecting gapfiller	Sequence	Number of points	Remove points after filtering	Remove points after rejecting gapfiller	Sequence	Number of remaining electrodes
05th/July/2021	PD-72-1-F-R- 500ms-1m	6218	0	742	Grad-72-1- v3-250ms	6042	0	0	Concatenating PD-500 ms and GD- 250ms	11518
10th/Nov/2021	PD-72-1-F-R- 500ms-1m	6218	0	742	Grad-72-1- v3-250ms	6042	0	0	Concatenating PD-500 ms and GD- 250ms	11518
09th/Dec/2021	PD-72-1-F-R- 500ms-1m	6218	0	742	Grad-72-1- v3-250ms	6042	0	0	Concatenating PD-500 ms and GD- 250ms	11518
27th/Jan/2022	PD-72-1-F-R- 500ms-1m	6218	0	742	Grad-72-1- v3-250ms	6042	0	0	Concatenating PD-500 ms and GD- 250ms	11518
16th/Mar/2022	PD-72-1-F-R- 500ms-1m	6218	0	742	Grad-72-1- v3-250ms	6042	0	0	Concatenating PD-500 ms and GD- 250ms	11518
11th/May/2022	PD-72-1-F-R- 500ms-1m	6218	0	742	Grad-72-1- v3-250ms	6042	0	0	Concatenating PD-500 ms and GD- 250ms	11518
16th/Sep022	PD-72-1-F-R- 500ms-1m	6218	1(Deviation>5)	742	Grad-72-1- v3-250ms	6042	0	0	Concatenating PD-500 ms and GD- 250ms	11517
19th/Jan/2023	PD-72-1-F- R- 500ms- 1m	6218	0	742	Grad-72- 1-v3-250ms	6042	0	0	Concatenating PD-500 ms and GD- 250ms	11518

**Appendix Data 1. The original data for  $\delta^{18}\text{O}_p$ ,  $\delta D_p$  and local precipitation/ temperature for the period 1997-2016 at Le Mas and Villars stations.**

date	Le Mas				Villars			
	precipitation (mm)	temperature (°C)	$\delta D$ (‰ V-SMOW)	$\delta^{18}\text{O}$ (‰ V-SMOW)	precipitation (mm)	temperature (°C)	$\delta D$ (‰ V-SMOW)	$\delta^{18}\text{O}$ (‰ V-SMOW)
1997/1/15	30.8	4.8	-76.1	-10.20				
1997/2/15	64.9	8.3	-29.2	-4.23				
1997/3/15	8.9	10.5	-29.8	-5.07				
1997/4/15	10.2	11.6	-39.7	-6.06				
1997/5/15	155.5	15.8	-32.7	-5.44				
1997/6/15	122.3	17.0	-35.1	-5.47				
1997/7/15	110.1	19.4	-35.7	-5.48				
1997/8/15	154.5	22.4	-13.5	-2.89				
1997/9/15	63.3	18.0	-30.1	-4.47				
1997/10/15	26.1	14.0	-22.7	-3.64				
1997/11/15	128.3	9.4	-58.4	-8.01				
1997/12/15	124.8	6.4	-49.4	-7.42				
1998/1/15	94.9	6.3	-46.4	-7.27				
1998/2/15	12.0	7.4	-34.6	-4.53				
1998/3/15	40.8	9.1	-35.2	-4.64				
1998/4/15	186.4	9.9	-48.9	-7.27				
1998/5/15	48.6	15.7	-42.3	-6.49				
1998/6/15	70.3	17.5	-38.7	-5.75				
1998/7/15	20.4	19.5	-29.7	-4.20				
1998/8/15	22.4	20.7	-27.5	-3.88				
1998/9/15	142.5	16.9	-35.2	-5.96	114.4	16.9	-35.6	-5.80
1998/10/15	93.7	12.0	-33.5	-6.38	151.5	12.0	-28.4	-4.99
1998/11/15	75.7	5.5	-23.2	-4.89	60.3	5.5	-24.4	-4.51
1998/12/15	70.0	5.0	-39.5	-6.60	76.8	5.0	-34.9	-5.66
1999/1/15	65.9	5.8	-44.0	-7.11	80.0	5.8	-25.9	-4.77
1999/2/15	77.8	4.7	-43.9	-6.98	121.5	4.7	-34.9	-5.44
1999/3/15	50.2	9.2	-47.4	-7.00	74.3	9.2	-34.9	-5.44
1999/4/15	106.2	11.2	-44.6	-6.41	117.5	11.2	-38.6	-5.98

Appendix

1999/5/15	88.3	17.0	-38.7	-5.58	106.9	17.0	-43.4	-6.59
1999/6/15	46.9	17.2			48.3	17.2	-24.7	-3.30
1999/7/15	39.7	20.9	-29.4	-4.25	117.6	20.9	-42.6	-5.93
1999/8/15	96.1	20.4	-35.4	-4.92	77.0	20.4	-27.2	-4.53
1999/9/15	122.9	18.4	-45.1	-7.27	97.0	18.4	-33.6	-5.55
1999/10/15	58.5	13.3	-46.7	-6.80	57.6	13.3		
1999/11/15	65.1	6.1			62.1	6.1		
1999/12/15	132.0	5.3			233.3	5.3		
2000/1/15	16.8	4.0	-24.6	-4.21	29.5	4.0		
2000/2/15	97.6	7.4	-32.3	-5.14	172.5	7.4		
2000/3/15	45.3	8.3	-47.2	-6.94	56.9	8.3	-33.5	-5.25
2000/4/15	127.6	10.9	-46.9	-6.71	183.2	10.9	-41.4	-6.08
2000/5/15	82.8	16.0	-25.1	-4.46	71.0	16.0	-26.2	-4.54
2000/6/15	50.1	19.0	-22.0	-4.15	41.2	19.0	-21.5	-4.07
2000/7/15	95.0	18.4	-28.6	-4.36	84.7	18.4	-33.3	-5.35
2000/8/15	96.0	20.5	-25.0	-4.10	72.4	20.5	-27.5	-4.45
2000/9/15	19.9	17.4	-40.3	-6.38	58.2	17.4	-28.3	-4.59
2000/10/15	102.3	12.7	-49.1	-7.70	151.9	12.7	-42.9	-7.01
2000/11/15	242.8	8.9	-53.3	-8.31	301.5	8.9	-55.8	-8.69
2000/12/15	46.4	8.5	-55.7	-8.61	72.0	8.5	-55.7	-8.70
2001/1/15	94.8	6.8	-49.7	-7.15	127.8	6.8		
2001/2/15	36.3	6.0	-49.7	-7.15	49.2	6.0		
2001/3/15	144.1	10.8			201.2	10.8	-43.2	-6.76
2001/4/15	150.7	9.5	-54.3	-7.87	154.5	9.5	-47.3	-7.22
2001/5/15	29.7	15.8	-54.2	-7.86	37.7	15.8	-49.1	-7.42
2001/6/15	19.4	18.0	-32.0	-4.65	43.1	18.0		
2001/7/15	138.5	19.7	-32.6	-5.33	134.5	19.7	-25.4	-4.44
2001/8/15	36.8	20.6	-26.2	-4.47	49.5	20.6	-19.6	-3.68
2001/9/15	67.3	14.4	-58.8	-8.69	41.7	14.4	-50.3	-7.61
2001/10/15	74.2	16.1	-62.7	-9.21	92.4	16.1	-53.4	-8.01
2001/11/15	43.5	5.9		-5.96	62.2	5.9		-7.90
2001/12/15	31.9	2.4	-35.6	-5.94	58.4	2.4	-41.7	-6.92
2002/1/15	32.5	6.2	-35.6	-5.94	31.0	6.2	-41.7	-6.46

Appendix

2002/2/15	73.5	7.6	-36.3	-5.98	77.1	7.6	-41.3	-6.38
2002/3/15	42.9	10.0	-39.5	-6.17	55.0	10.0	-40.2	-6.16
2002/4/15	51.8	11.3	-38.2	-5.95	57.8	11.3	-34.8	-5.38
2002/5/15	129.9	13.7	-36.4	-5.61	138.9	13.7	-29.5	-4.62
2002/6/15	48.3	18.8	-30.0	-4.85	73.7	18.8		-5.40
2002/7/15	37.0	18.8	-35.4	-5.69	60.0	18.8	-32.8	-5.31
2002/8/15	58.0	18.6	-35.4	-5.69	121.8	18.6	-32.8	-5.31
2002/9/15	59.7	15.7		-5.71	28.2	15.7	-34.2	-5.73
2002/10/15	82.8	13.5	-49.8	-7.66	96.7	13.5	-38.7	-6.46
2002/11/15	127.8	9.7	-49.8	-7.67	145.3	9.7	-39.4	-6.55
2002/12/15	81.1	8.2	-49.8	-7.67	115.0	8.2	-44.0	-7.15
2003/1/15	81.5	3.5	-49.8	-7.67	94.6	3.5	-44.0	-7.15
2003/2/15	56.3	4.3			72.7	4.3	-40.7	-6.58
2003/3/15	45.8	10.8			32.6	10.8	-40.7	-6.58
2003/4/15	52.7	12.5	-31.6	-5.16	71.7	12.5	-37.3	-5.84
2003/5/15	65.8	14.8	-31.6	-5.16	66.7	14.8	-37.1	-5.80
2003/6/15	63.3	22.5	-31.5	-5.14	99.7	22.5	-32.3	-5.16
2003/7/15	64.4	21.0	-22.5	-4.05	68.5	21.0	-28.1	-4.61
2003/8/15	61.6	24.8	-22.5	-4.05	38.8	24.8	-28.1	-4.61
2003/9/15	65.8	17.2	-24.3	-4.28	54.6	17.2	-29.9	-4.86
2003/10/15	153.0	11.4	-62.9	-9.32	140.3	11.4	-60.1	-9.05
2003/11/15	91.1	9.8	-55.9	-8.33	88.5	9.8	-49.4	-7.58
2003/12/15	70.8	5.8	-52.0	-7.78	67.8	5.8	-41.2	-6.45
2004/1/15	164.3	5.2	-53.7	-7.95	195.8	5.2	-44.6	-6.83
2004/2/15	19.8	5.7	-62.4	-8.87	26.8	5.7	-55.5	-8.09
2004/3/15	52.6	7.1	-55.2	-8.06	59.9	7.1	-49.7	-7.50
2004/4/15	110.8	10.2	-45.9	-7.02	90.8	10.2	-44.2	-6.94
2004/5/15	72.0	14.3	-34.9	-5.48	59.6	14.3		
2004/6/15	12.2	19.0	-24.8	-4.07	16.8	19.0		
2004/7/15	69.3	19.4	-29.9	-4.81	63.1	19.4		
2004/8/15	156.9	20.0	-32.6	-5.22	139.2	20.0		
2004/9/15	24.8	17.4	-27.4	-4.87	50.5	17.4		
2004/10/15	95.2	14.5	-34.9	-5.80	99.3	14.5		

2004/11/15	30.1	6.9	-43.0	-6.81	36.8	6.9		
2004/12/15	96.5	4.8	-43.0	-6.81	103.6	4.8		
2005/1/15	36.8	4.7	-43.0	-6.81	41.9	4.7		
2005/2/15	28.3	2.9	-38.8	-5.97	43.6	2.9		
2005/3/15	48.6	8.1	-38.8	-5.96	52.0	8.1		
2005/4/15	157.8	11.6	-38.8	-5.96	107.6	11.6		
2005/5/15	62.8	15.4	-38.8	-5.96	26.7	15.4		
2005/6/15	22.4	20.6	-38.8	-5.96	60.1	20.6		
2005/7/15	31.9	20.5	-29.5	-4.56	38.2	20.5		
2005/8/15	21.0	19.5	-32.5	-4.91	44.6	19.5		
2005/9/15	49.1	17.2	-35.0	-5.51	71.0	17.2		
2005/10/15	37.4	16.1	-36.4	-5.97	63.8	16.1		
2005/11/15	53.3	6.9	-40.1	-6.64	58.2	6.9		
2005/12/15	91.8	2.5	-45.9	-7.68	124.8	2.5		
2006/1/15	55.3	4.2	-50.8	-7.97	83.3	4.2		
2006/2/15	67.3	4.1	-55.6	-8.25	99.3	4.1	-54.0	-8.23
2006/3/15	146.3	8.7	-52.2	-7.82	222.4	8.7	-47.7	-7.35
2006/4/15	27.0	11.1	-39.4	-6.21	26.4	11.1	-29.1	-4.78
2006/5/15	85.0	15.1	-33.3	-5.38	53.4	15.1	-29.1	-4.78
2006/6/15	38.2	19.9	-25.1	-4.27	19.4	19.9	-29.1	-4.78
2006/7/15	39.3	24.0	-20.0	-3.48	106.6	24.0	-19.9	-3.52
2006/8/15	52.9	17.9	-20.0	-3.48	74.5	17.9	-19.9	-3.52
2006/9/15	126.3	19.4	-38.2	-6.62	128.1	19.4	-50.3	-7.61
2006/10/15	59.5	16.3	-40.0	-6.60	47.9	16.3	-42.7	-6.63
2006/11/15	91.2	10.5	-42.1	-6.57	86.9	10.5	-32.6	-5.32
2006/12/15	44.1	4.5	-40.0	-6.42	68.8	4.5	-34.4	-5.86
2007/1/15	69.1	6.9	-38.3	-6.30	87.5	6.9	-36.3	-6.41
2007/2/15	128.6	8.4	-38.3	-6.30	141.6	8.4	-36.3	-6.41
2007/3/15	77.5	8.5	-39.5	-6.43	132.3	8.5	-37.2	-6.34
2007/4/15	48.2	15.2	-40.0	-6.57	20.8	15.2	-40.9	-6.02
2007/5/15	61.9	15.7	-29.6	-5.65	117.3	15.7	-31.7	-5.13
2007/6/15	84.8	18.4	-29.6	-5.65	108.3	18.4	-31.7	-5.13
2007/7/15	60.5	18.5	-30.2	-5.21	81.6	18.5	-31.0	-5.09



---

2007/8/15	82.9	18.6	-30.6	-4.95	102.8	18.6	-30.6	-5.07
2007/9/15	36.1	15.4	-30.3	-4.92	43.5	15.4	-29.8	-5.01
2007/10/15	41.1	12.5	-29.4	-4.81	30.9	12.5	-27.6	-4.81
2007/11/15	23.7	6.1	-22.9	-4.06	58.6	6.1	-37.4	-6.13
2007/12/15	66.3	5.3	-25.1	-4.98	96.3	5.3	-41.9	-6.73
2008/1/15	114.1	7.0			119.6	7.0	-42.9	-6.89
2008/2/15	25.1	8.3	-36.0	-6.12	33.2	8.3	-56.6	-9.08
2008/3/15	94.6	7.6	-36.0	-6.12	121.8	7.6	-56.6	-9.08
2008/4/15	119.3	10.5	-55.2	-7.85	104.8	10.5		
2008/5/15	151.7	15.6	-43.7	-6.63	115.3	15.6		
2008/6/15	50.9	18.2	-27.7	-4.45	67.1	18.2		
2008/7/15	49.8	19.2	-28.1	-4.59	53.0	19.2		
2008/8/15	55.9	19.1	-29.3	-4.83	102.3	19.1		
2008/9/15	49.9	15.1	-42.5	-6.18	84.9	15.1		
2008/10/15	92.1	12.0	-45.4	-6.86	113.0	12.0		
2008/11/15	71.1	7.5	-50.7	-7.78	108.5	7.5		
2008/12/15	92.5	4.3	-67.3	-9.93	85.3	4.3		
2009/1/15	86.5	3.3	-67.3	-9.93	146.7	3.3		
2009/2/15	19.5	5.5	-44.6	-6.72	23.0	5.5		
2009/3/15	38.5	8.1	-37.1	-5.07	38.9	8.1		
2009/4/15	145.6	11.3	-27.8	-3.04	130.8	11.3	-43.2	-6.62
2009/5/15	37.2	16.6	-27.8	-3.03	110.4	16.6	-43.2	-6.62
2009/6/15	56.7	18.6	-11.8	-0.83	82.6	18.6	-31.1	-5.00
2009/7/15	63.7	20.0	-16.7	-0.97	32.4	20.0	-33.0	-4.90
2009/8/15	134.5	20.9	-30.3	-4.65	44.5	20.9	-33.1	-4.96
2009/9/15	25.9	17.6	-43.2	-6.84	38.3	17.6	-31.4	-5.18
2009/10/15	45.3	13.4	-48.7	-7.75	93.8	13.4	-36.9	-6.73
2009/11/15	145.6	10.3	-31.4	-5.48	178.8	10.3	-30.4	-5.53
2009/12/15	89.8	5.3	-68.3	-10.23	167.9	5.3	-59.3	-9.16
2010/1/15	78.6	1.9	-58.8	-9.01	96.7	1.9	-56.0	-8.71
2010/2/15	80.0	4.4	-48.1	-7.64	86.5	4.4	-47.7	-7.61
2010/3/15	91.0	7.6	-48.1	-7.56	90.7	7.6	-47.1	-7.26
2010/4/15	30.1	12.3	-60.9	-8.62	28.4	12.3	-67.4	-9.49

---

2010/5/15	75.5	13.3	-51.9	-7.44	86.5	13.3	-59.4	-8.27
2010/6/15	168.9	17.9	-41.0	-6.03	130.1	17.9	-41.9	-6.04
2010/7/15	24.9	21.3	-22.9	-3.85	34.2	21.3	-22.3	-3.97
2010/8/15	26.6	19.1	-30.7	-5.06	49.3	19.1	-22.8	-4.03
2010/9/15	41.6	16.2	-49.3	-7.78	38.5	16.2	-36.2	-5.55
2010/10/15	88.2	12.1	-49.3	-7.78	63.5	12.1	-52.1	-7.83
2010/11/15	131.3	7.6	-49.3	-7.78	192.6	7.6	-57.4	-9.15
2010/12/15	48.5	2.9	-56.7	-8.39	66.0	2.9	-46.3	-7.16
2011/1/15	34.9	4.4	-57.5	-8.46	51.1	4.4	-45.5	-7.01
2011/2/15	40.3	6.6	-63.7	-9.03	56.2	6.6	-41.2	-6.15
2011/3/15	35.9	9.4	-38.6	-5.90	45.6	9.4	-22.4	-3.89
2011/4/15	17.9	14.6	-29.9	-4.81	8.1	14.6	-20.9	-3.71
2011/5/15	59.5	17.1	-30.1	-4.84	45.5	17.1	-21.5	-3.78
2011/6/15	93.7	17.9	-34.8	-5.50	28.1	17.9	-26.9	-4.44
2011/7/15	95.5	18.5	-33.1	-5.29	60.6	18.5	-26.7	-4.43
2011/8/15	50.6	20.5	-29.5	-4.84	70.0	20.5	-26.0	-4.41
2011/9/15	18.3	18.9	-31.3	-5.27	30.8	18.9	-27.4	-4.71
2011/10/15	66.2	14.0	-42.5	-6.85	53.6	14.0	-38.9	-6.42
2011/11/15	41.3	11.6	-46.4	-7.38	55.0	11.6	-42.7	-6.91
2011/12/15	168.3	7.5	-40.1	-6.63	211.1	7.5	-34.6	-5.99
2012/1/15	49.5	5.4	-36.4	-6.22	63.6	5.4	-32.7	-5.79
2012/2/15	5.7	0.3	-45.0	-7.28	13.6	0.3	-44.0	-7.14
2012/3/15	34.7	10.6	-31.1	-5.48	19.3	10.6	-28.5	-5.18
2012/4/15	206.8	9.7	-42.4	-6.35	210.1	9.7		-5.80
2012/5/15	99.2	16.0	-42.4	-6.35	54.6	16.0		-5.80
2012/6/15	138.8	18.7	-36.8	-5.43	138.8	18.7	-31.2	-5.08
2012/7/15	66.2	18.6	-36.8	-5.43	66.2	18.6	-31.2	-5.08
2012/8/15	7.8	21.6	-36.8	-5.43	7.8	21.6	-31.2	-5.08
2012/9/15	22.2	17.4	-31.5	-5.31	22.2	17.4	-32.4	-5.61
2012/10/15	118.0	14.0	-31.5	-5.31	118.0	14.0	-32.5	-5.61
2012/11/15	102.3	9.0	-44.6	-6.91	102.3	9.0	-43.2	-7.17
2012/12/15	105.6	6.5	-43.0	-7.35	105.6	6.5	-39.7	-7.17
2013/1/15	89.3	4.0	-67.0	-9.86	89.3	4.0	-51.2	-7.88

---

2013/2/15	168.0	3.8	-69.8	-10.11	168.0	3.8	-53.4	-8.08
2013/3/15	31.8	7.8	-54.7	-8.33	31.8	7.8	-53.4	-8.08
2013/4/15	94.1	10.7	-50.5	-7.71	94.1	10.7	-51.5	-7.79
2013/5/15	65.9	11.8	-52.0	-7.81	65.9	11.8	-50.4	-7.61
2013/6/15	115.2	16.8	-35.7	-5.41	115.2	16.8	-33.9	-5.25
2013/7/15	81.4	22.7	-31.4	-4.85	81.4	22.7	-25.1	-4.12
2013/8/15	60.2	20.1	-30.7	-4.90	60.2	20.1	-25.1	-4.12
2013/9/15	64.7	17.6	-31.5	-5.30	64.7	17.6	-25.1	-4.12
2013/10/15	126.7	14.9	-40.8	-6.46	126.7	14.9	-34.2	-5.65
2013/11/15	159.2	7.3	-42.7	-7.01	159.2	7.3	-41.4	-6.87
2013/12/15	34.3	5.5	-62.2	-8.81	34.3	5.5	-56.8	-8.52
2014/1/15	136.3	7.6	-54.7	-8.37	136.3	7.6	-56.9	-8.53
2014/2/15	209.3	7.2	-50.0	-7.86	209.3	7.2	-55.9	-8.42
2014/3/15	96.7	9.6	-37.4	-5.96	96.7	9.6	-34.9	-5.68
2014/4/15	68.8	12.6	-32.7	-5.26	68.8	12.6	-29.3	-4.90
2014/5/15	86.7	13.7	-32.4	-5.28	86.7	13.7	-31.6	-5.18
2014/6/15	113.0	19.4	-32.0	-5.31	113.0	19.4	-33.4	-5.40
2014/7/15	87.2	20.1	-35.1	-5.39	87.2	20.1	-32.2	-5.19
2014/8/15	73.4	18.1	-33.7	-5.18	73.4	18.1	-32.2	-5.19
2014/9/15	27.0	18.6	-30.7	-4.75	27.0	18.6	-32.2	-5.19
2014/10/15	119.6	15.5	-30.7	-4.81	119.6	15.5	-33.8	-5.38
2014/11/15	76.6	11.6	-65.8	-9.71	76.6	11.6	-42.8	-7.09
2014/12/15	76.4	5.2	-27.4	-5.16	76.4	5.2	-42.8	-7.09
2015/1/15	82.8	4.6	-31.9	-5.61	82.8	4.6	-41.3	-6.72
2015/2/15	80.2	4.3	-40.3	-6.43	80.2	4.3	-39.6	-6.31
2015/3/15	107.7	9.1	-38.8	-6.13	107.7	9.1	-34.8	-5.59
2015/4/15	53.3	13.0	-35.9	-5.54	53.3	13.0	-30.0	-4.83
2015/5/15	102.0	15.3	-33.2	-4.97	102.0	15.3	-35.4	-5.56
2015/6/15	70.5	20.2	-33.2	-5.40	70.5	20.2	-22.6	-4.44
2015/7/15	7.4	22.5	-33.2	-5.38	7.4	22.5	-31.2	-5.24
2015/8/15	103.6	20.9	-32.7	-4.93	103.6	20.9	-34.6	-5.55
2015/9/15	80.4	15.8	-29.0	-5.08	80.4	15.8	-31.0	-5.09
2015/10/15	49.6	12.2	-40.4	-6.49	49.6	12.2	-31.0	-5.08

---

2015/11/15	26.2	10.7	-47.2	-7.40	26.2	10.7	-32.2	-5.25
2015/12/15	68.4	8.7	-51.9	-8.36	68.4	8.7	-39.4	-6.24
2016/1/15	179.6	6.9	-49.1	-7.93	179.6	6.9	-39.4	-6.24
2016/2/15	193.7	6.9	-38.9	-6.33	193.7	6.9	-39.4	-6.24
2016/3/15	88.3	7.9	-47.7	-7.32	88.3	7.9	-39.4	-6.24
2016/4/15	95.4	10.8	-39.2	-6.17	95.4	10.8	-38.9	-6.16
2016/5/15	63.2	14.9	-38.3	-5.84	63.2	14.9	-35.8	-5.61
2016/6/15	154.9	18.1	-38.2	-5.84	154.9	18.1	-35.2	-5.54
2016/7/15	24.6	20.8	-36.6	-5.75	24.6	20.8	-28.5	-4.73
2016/8/15	5.4	21.5	-36.6	-5.75	5.4	21.5	-28.5	-4.73
2016/9/15	25.7	19.2	-42.0	-6.58	25.7	19.2	-36.8	-6.03
2016/10/15	38.9	12.3	-48.5	-7.57	38.9	12.3	-46.8	-7.57
2016/11/15	77.9	8.8	-48.5	-7.57	77.9	8.8	-46.8	-7.57
2016/12/15	56.4	6.4	-48.5	-7.57	56.4	6.4	-46.8	-7.57

---

Note: A similarity checked method (referred to section 3.2 from [Genty et al., 2014a](#)) was applied to adjust the  $\delta^{18}\text{O}_p$  to obtain a unified time series and corresponding  $\delta^{18}\text{O}_p$  sequence values.

**Appendix Data 2. The original data for  $\delta^{18}\text{O}_p$  of drip water for the period 1997-2019 at Villars Cave.**

Sampling date	Vil#10A $\delta^{18}\text{O}$	Sampling date	Vil#10B $\delta^{18}\text{O}$	Sampling date	Vil#1A $\delta^{18}\text{O}$	Sampling date	Vil#1B $\delta^{18}\text{O}$
2000/2/18	-6.02	1997/2/11	-6.16	1997/3/8		1997/3/8	-6.23
2000/4/3	-5.64	1997/3/8	-6.13	1997/4/12	-6.23	1997/4/12	
2000/5/8	-5.44	1997/4/12	-6.08	1997/5/10	-6.37	1997/5/10	-6.46
2000/6/20	-6.09	1997/5/10	-6.32	1997/6/5	-6.33	1997/6/5	-6.37
2000/9/27	-6.32	1997/6/5	-6.20	1997/7/21	-6.28	1997/7/21	-6.46
2000/12/4	-6.45	1997/7/21	-6.27	1997/8/18	-6.28	1997/8/18	-6.47
2000/12/29	-6.16	1997/8/18	-6.24	1997/9/18	-6.31	1997/9/18	-6.41
2001/2/14	-6.45	1997/9/18	-6.13	1997/10/25		1997/10/25	-6.49
2001/4/8	-6.72	1997/10/25	-6.10	1997/11/22	-6.41	1997/11/21	-6.25
2001/5/24	-6.37	1997/11/22	-6.16	1997/12/24	-6.45	1997/12/24	-6.25
2001/6/30	-6.37	1997/12/24	-6.31	1998/1/24	-6.35	1998/1/24	-6.27
2001/8/17	-6.35	1998/1/24	-6.35	1998/2/18	-6.35	1998/2/18	-6.46
2001/9/12	-6.32	1998/2/18	-6.12	2000/11/2	-6.43	2000/2/18	-6.4
2001/11/2		2000/2/18	-6.09	2000/12/4	-6.5	2000/5/8	-6.25
2001/12/26		2000/12/4	-6.18	2000/12/29	-6.17	2000/6/20	-6.44
2002/2/23	-6.35	2000/12/29	-6.12	2001/2/14	-6.34	2000/7/21	-6.48
2002/4/9	-6.39	2001/2/14	-6.16	2001/2/14	-6.38	2000/9/7	-6.51
2002/5/28	-6.35	2001/4/8	-6.25	2001/4/8		2000/11/2	-6.5
2002/6/30	-6.30	2001/5/24	-6.19	2001/5/24	-6.41	2000/12/4	-6.42
2002/9/28	-6.15	2001/6/30	-6.17	2001/6/30	-6.38	2000/12/4	-6.58
2002/10/15	-5.92	2001/9/12	-6.21	2001/8/17	-6.39	2000/12/29	-6.4
2002/11/26	-6.29	2001/11/2		2001/9/11	-6.46	2001/2/14	-6.33
2003/1/30	-5.85	2002/2/23	-6.17	2001/11/2	-6.35	2001/2/14	-6.42
2003/4/8	-6.21	2002/4/9	-6.24	2001/12/29		2001/4/8	-6.38
2003/6/18	-6.27	2002/5/28	-6.26	2002/2/25	-6.42	2001/5/24	-6.33
2003/9/22	-6.20	2002/6/30	-6.28	2002/4/9	-6.42	2001/6/30	-6.33
2004/3/18	-6.48	2002/9/28		2002/6/30	-6.42	2001/8/16	-6.45
2006/3/24	-6.22	2002/10/15	-6.20	2002/8/28	-6.38	2001/9/11	-6.40
2006/3/24	-6.24	2002/11/26		2002/10/6	-6.46	2001/11/2	

2006/6/26	-6.31	2003/1/30	-6.15	2002/10/6	-6.47	2001/12/26	-6.42
2006/6/27	-6.27	2003/6/18	-6.05	2002/11/26	-6.41	2002/2/25	-6.36
2006/9/8	-6.14	2004/3/18	-6.31	2003/1/30	-6.39	2002/4/9	-6.42
2006/10/12	-6.04	2006/6/26	-6.29	2003/11/19	-6.40	2002/6/30	-6.37
2006/12/4	-6.25	2006/9/8	-6.16	2004/3/18		2002/8/28	-6.43
2007/3/20	-5.91	2006/12/4	-6.14	2006/6/27	-6.38	2002/10/6	-6.43
2007/4/25	-6.00	2007/3/20	-6.20	2006/9/8	-6.36	2002/10/6	-6.45
2007/7/10	-6.09	2007/4/25	-6.24	2006/10/2	-6.39	2002/11/26	-6.45
2007/9/25	-6.11	2007/7/10	-6.22	2006/12/4	-6.40	2003/1/30	-6.43
2007/11/19	-6.09	2007/9/25	-6.15	2007/3/20	-6.36	2003/11/19	-6.43
2008/1/22	-5.37	2007/11/19	-6.23	2007/4/25	-6.36	2004/3/18	-6.47
2008/4/2	-5.63	2008/1/22	-6.09	2007/9/25	-6.41	2006/6/27	-6.36
2008/5/27	-5.56	2008/4/2	-6.19	2007/11/19	-6.45	2006/9/8	-6.40
2008/7/4	-5.87	2008/5/27	-6.18	2008/1/22	-6.38	2006/10/12	-6.33
2008/8/18	-5.97	2008/7/4	-6.21	2008/4/2	-6.37	2006/12/4	-6.37
2008/10/18	-5.94	2008/8/18	-6.17	2008/8/19	-6.41	2007/3/20	-6.36
2008/11/27	-5.95	2008/10/18	-6.08	2008/10/18	-6.40	2007/4/25	-6.34
2009/1/29	-6.42	2008/11/27		2008/11/27	-6.39	2007/9/25	-6.41
2009/3/19	-6.09	2009/1/29	-6.19	2009/1/29	-6.38	2007/11/19	-6.43
2009/5/28	-6.23	2009/3/19	-6.16	2009/3/19	-6.39	2008/1/22	-6.43
2009/7/10	-6.08	2009/5/28	-6.16	2009/5/28	-6.38	2008/4/2	-6.39
2009/7/17	-6.13	2009/7/10	-6.16	2009/7/10	-6.36	2008/8/19	-6.36
2009/7/2	-6.19	2009/9/14	-6.11	2009/8/4	-6.33	2008/10/18	-6.39
2009/8/4	-6.12	2009/10/25	-6.08	2009/9/14	-6.36	2008/11/27	-6.40
2009/9/9	-6.14	2009/11/27	-6.15	2009/10/21	-6.37	2009/1/29	-6.38
2009/9/14	-6.12	2010/1/14	-6.12	2009/11/27	-6.35	2009/3/19	-6.39
2009/9/17	-6.20	2010/2/25	-6.16	2010/1/14	-6.37	2009/5/28	-6.38
2009/10/21	-6.15	2010/4/2	-6.16	2010/2/26	-6.35	2009/7/10	-6.35
2009/10/25	-6.08	2010/5/11	-6.15	2010/4/2	-6.33	2009/8/4	-6.36
2009/11/3	-5.95	2010/7/6	-6.14	2010/5/11	-6.32	2009/9/16	-6.38
2009/11/20	-6.08	2010/8/19	-6.14	2010/7/6	-6.33	2009/10/21	-6.39
2009/11/27	-6.05	2010/10/4	-6.12	2010/11/29	-6.39	2009/11/27	-6.39

2009/11/30	-6.13	2010/11/29	-6.15	2011/1/26	-6.38	2010/1/14	-6.38
2010/1/14	-6.20	2011/1/26	-6.48	2011/1/29	-6.35	2010/2/2	-6.35
2010/1/14	-6.17	2011/3/14	-6.11	2011/3/14	-6.37	2010/2/26	-6.34
2010/1/19	-6.15	2011/5/25	-6.14	2011/5/25	-6.40	2010/5/11	-6.33
2010/2/2	-6.10	2011/7/21	-6.14	2011/7/21	-6.36	2010/7/6	-6.35
2010/2/25	-5.96	2011/9/10	-6.12	2011/9/10	-6.37	2010/11/29	-6.38
2010/2/25	-6.17	2012/1/19	-6.09	2011/10/20	-6.34	2010/11/30	-6.38
2010/4/2	-6.60	2012/2/27	-6.13	2011/12/14	-6.40	2010/11/30	-6.39
2010/5/11	-6.28	2012/3/29	-6.18	2012/1/19	-6.40	2011/1/26	-6.39
2010/5/31	-6.24	2012/5/31	-6.15	2012/2/27	-6.37	2011/3/14	-6.38
2010/7/5	-6.29	2012/7/5	-6.15	2012/3/29	-6.38	2011/5/25	-6.43
2010/7/6	-6.29	2012/9/6	-6.28	2012/5/31	-6.13	2011/7/21	-6.36
2010/8/19	-6.21	2012/10/29	-6.12	2012/7/5	-6.43	2011/9/10	-6.37
2010/8/30	-6.16	2013/1/16	-6.12	2012/9/6	-6.38	2011/10/20	-6.38
2010/9/12	-6.18	2013/3/14	-6.11	2012/10/29	-6.39	2011/12/14	-6.34
2010/10/4	-6.15	2013/4/10	-6.13	2013/1/16	-6.39	2012/1/19	-6.40
2010/10/4	-6.17	2013/5/30	-6.15	2013/3/14	-6.32	2012/2/27	-6.37
2010/10/19	-6.13	2013/6/14	-6.15	2013/4/10	-6.31	2012/3/29	-6.34
2010/10/19	-6.51	2013/9/9	-6.14	2013/5/30	-6.36	2012/5/31	-6.35
2010/11/3	-6.06	2013/10/10	-6.21	2013/6/14	-6.36	2012/7/5	-6.35
2010/11/30	-6.49	2013/12/5	-6.16	2013/9/9	-6.36	2012/9/6	-6.37
2011/1/26	-6.18	2014/1/20	-6.18	2013/10/10	-6.42	2012/10/29	-6.38
2011/1/26	-6.49	2014/3/10		2013/12/5	-6.43	2013/1/16	-6.38
2011/3/14	-6.49	2014/5/20	-6.15	2014/1/20	-6.39	2013/3/14	-6.32
2011/5/25	-6.25	2014/7/1	-6.14	2014/3/10	-6.37	2013/4/10	-6.36
2011/7/21	-6.17	2014/10/9	-6.19	2014/5/20	-6.36	2013/5/30	-6.35
2011/9/10	-6.16	2014/10/29	-6.19	2014/7/1	-6.36	2013/6/14	-6.35
2012/1/19	-6.18	2015/1/27	-6.14	2014/10/10		2013/9/9	-6.37
2012/2/27	-6.25	2015/3/27	-6.14	2014/10/29	-6.40	2013/10/10	-6.38
2012/3/29	-6.17	2015/4/29	-6.03	2015/1/27	-6.42	2013/12/5	-6.42
2012/5/31	-6.36	2015/6/3	-6.04	2015/3/27	-6.42	2014/1/20	-6.42
2012/7/5	-6.10	2015/7/27	-6.02	2015/4/29	-6.33	2014/3/10	-6.36

2012/9/6	-6.06	2015/9/10	-6.29	2015/7/27	-6.29	2014/5/20	-6.33
2012/10/29	-6.09	2015/11/23	-6.30	2015/9/10	-6.16	2014/7/1	-6.36
2013/1/16	-5.94	2016/1/19	-6.08	2015/6/3	-6.27	2014/10/10	-6.39
2013/3/14	-6.25	2015/11/23	-6.07	2015/10/5	-6.35	2014/10/29	-6.39
2013/4/10	-6.28	2016/3/18	-6.00	2015/11/23	-6.30	2015/1/27	
2013/5/30	-6.45	2016/4/22	-6.02	2016/1/19	-6.19	2015/3/27	-6.36
2013/6/14	-6.43	2016/6/23	-5.99	2016/2/25	-6.19	2015/4/29	-6.27
2013/9/9	-6.22	2016/8/3	-6.00	2016/3/18	-6.30	2015/6/3	-6.27
2013/10/10	-6.20	2016/9/23	-5.98	2016/4/22	-6.15	2015/7/27	-6.31
2013/12/5	-6.25	2017/1/20	-6.02	2016/8/3	-6.32	2015/9/10	-6.06
2014/1/20	-6.57	2017/3/30	-5.97	2016/9/23	-6.33	2015/10/5	-6.36
2014/3/10	-6.76	2017/5/18	-5.99	2016/9/23	-6.28	2015/11/23	-6.07
2014/5/20	-6.46	2017/7/6	-6.00	2016/12/9	-6.28	2016/1/19	-6.31
2014/7/10	-6.44	2017/9/11	-6.00	2017/1/20	-6.27	2016/2/25	-6.34
2014/10/9	-6.27	2018/3/16	-6.05	2017/3/30	-6.35	2016/3/18	-6.27
2014/10/29	-6.19	2018/6/26	-6.07	2017/9/11	-6.24	2016/4/22	-6.31
2015/1/27	-6.49	2018/11/20	-5.98	2017/12/7	-6.00	2016/6/23	-6.29
2015/3/27	-6.46	2018/8/2	-6.05	2019/4/24	-6.27	2016/8/3	-6.32
2015/4/29	-6.31	2019/4/24	-6.08	2019/7/29	-6.20	2016/9/23	-6.32
2015/6/3	-6.25	2019/7/29	-6.06	2019/10/18	-6.30	2016/12/9	-6.33
2015/7/27	-6.19	2019/10/18	-6.00			2017/1/20	-6.33
2015/9/10	-6.30					2017/3/30	-6.25
2015/10/5	-6.13					2017/5/18	-6.32
2015/11/23	-5.91					2017/7/6	-6.28
2016/1/19	-5.96					2017/9/11	-6.29
2016/2/25	-6.28					2017/12/7	-6.31
2010/5/11						2018/3/13	-6.27
2016/3/18	-6.21					2018/6/26	-6.26
2016/4/22	-6.26					2018/11/20	-6.28
2016/6/23	-6.22					2019/8/2	-6.31
2016/8/3	-6.18					2019/7/29	-6.29
2016/9/23	-6.11					2019/10/18	-6.32



---

2017/1/20	-5.89						
2017/3/30	-6.28						
2017/5/18	-6.22						
2017/7/6	-6.21						
2017/9/11	-6.19						
2018/3/16	-6.42						
2018/6/26	-6.33						
2018/8/2	-6.27						
2018/11/20	-6.25						
2019/4/24	-6.22						
2019/7/29	-6.26						

## List of abbreviations

Abbreviation	Full name
$\delta^{18}\text{O}_p$	Precipitation $\delta^{18}\text{O}$
$\delta\text{D}_p$	Precipitation $\delta\text{D}$
$\delta^{18}\text{O}_d$	drip water $\delta^{18}\text{O}$
$\delta^{18}\text{O}_{ap}$	Annual mean precipitation $\delta^{18}\text{O}$
$\delta^{18}\text{O}_{sw}$	Seawater $\delta^{18}\text{O}$
$\delta^{18}\text{O}_w$	Annual weighted $\delta^{18}\text{O}_p$
$\delta^{18}\text{O}_c$	calcite $\delta^{18}\text{O}$
NAO	North Atlantic Oscillation
PAWE	Proximal Atlantic and West Europe
DA	Distal Atlantic
NAGR	North America and Greenland
ME	Mediterranean
NENA	Northern European and Northern Atlantic
AO	Atlantic Ocean
HYSPLIT	Hybrid Single-Particle Lagrangian Integrated Trajectory
PIMS	Percentage of initial moisture sources
LMWL	Local meteoric water line
OLSR	Ordinary least squares regression
PWLSR	Precipitation weighted least squares regression
ERT	Electric resistivity tomography
HAC	Hierarchical Agglomerative Clustering
KCZ	Karst Critical Zone
MFA	Magnetic field angle

## Bibliography

- Abouelmagd, A., Sultan, M., Milewski, A., Kehew, A.E., Sturchio, N.C., Soliman, F., Krishnamurthy, R.V., Curtim, E., 2012. Towards a better understanding of palaeoclimatic regimes that recharged the fossil aquifers in North Africa: Inferences from stable isotope and remote sensing data. *Palaeogeogr., Palaeoclim., Palaeoecol.* 329-330, 137–149.
- Aggarwal, P.K., Frohlich, K., Kulkarni, K.M., Gourcy, L.L., 2004. Stable isotope evidence for moisture sources in the Asian summer monsoon under present and past climate regimes. *Geophys. Res. Lett.* 31(8).
- Al Hagrey, S.A., Schubert-Klempnauer, T., Wachsmuth, D., Michaelsen, J., Meissner, R., 1999. Preferential flow: first results of a full-scale flow model. *Geophys. J. Int.* 138 (3), 643–654. <https://doi.org/10.1046/j.1365-246x.1999.00906.x>.
- Al Hagrey, S.A., 2007. Geophysical imaging of root-zone, trunk, and moisture heterogeneity. *J. Exp. Bot.* 58 (4), 839–854. <https://doi.org/10.1093/jxb/erl237>.
- Allen, R. G., Pereira, L. S., Raes, D., & Smith, M. 1998. Crop evapotranspiration-Guidelines for computing crop water requirements-FAO Irrigation and drainage paper 56. Fao, Rome, 300(9), D05109.
- Allen, S. T., Kirchner, J. W., & Goldsmith, G. R. 2018. Predicting spatial patterns in precipitation isotope ( $\delta^2\text{H}$  and  $\delta^{18}\text{O}$ ) seasonality using sinusoidal isoscapes. *Geophysical Research Letters*, 45, 4859– 4868. <https://doi.org/10.1029/2018GL077458>.
- Alley, R.B., Cuffey, K.M., 2001. Oxygen- and hydrogen-isotopic ratios of water in precipitation: beyond paleothermometry. *Rev. Mineral. Geochem.* 43, 527–553.
- Almalki, S.J. and Nadarajah, S., 2014. Modifications of the Weibull distribution: A review. *Reliab. Eng. Syst. Saf.*, 124, pp.32-55.
- Anagnostou, E. N., & Krajewski, W. F. 2015. Introduction to the special section on distributed and lumped hydrological models: learning from high-resolution hydrology. *Water Resources Research*, 51(9), 6997-7001.
- Aquilina, L., Ladouche, B., Dörfliker, N., 2006. Water storage and transfer in the epikarst of karstic systems during high flow periods. *J. Hydrol.* 327, 472–485.
- Araguás - Araguás, L., Froehlich, K., Rozanski, K., 2000. Deuterium and oxygen - 18 isotope composition of precipitation and atmospheric moisture. *Hydro. process*, 14(8), 1341–1355.

- Araguás - Araguás, L. J., and M. F. Diaz Teijeiro. 2005. Isotope composition of precipitation and water vapour in the Iberian Peninsula: first results of the Spanish network of isotopes in precipitation. At. Energy. Agency. Tech. Report 1453: 173-190.
- Archie, G. 1942. The electrical resistivity log as an aid in determining some reservoir characteristics. *Petroleum Transactions of the AIME*, 146, 54-62.
- Ayalon, A., M. Bar-Matthews, and E. Sass. 1998. Rainfall-recharge relationships within a karstic terrain in the Eastern Mediterranean semi-arid region, Israel:  $\delta^{18}\text{O}$  and  $\delta\text{D}$  characteristics, *J. Hydrol*, 207(1), 18-31.
- Baker, A., Mockler, N.J., Barnes, W.L., 1999. Fluorescence intensity variations of speleothem-forming groundwaters: implications for paleoclimate reconstruction. *Water Resour. Res.* 35, 407–413.
- Baker, A., Genty, D., & Fairchild, I. J. 2000. Hydrological characterisation of stalagmite dripwaters at Grotte de Villars, Dordogne, by the analysis of inorganic species and luminescent organic matter. *Hydrology and Earth system sciences*, 4(3), 439-449.
- Baker, A., Asrat, A., Fairchild, I. J., Leng, M. J., Thomas, L., Widmann, M., & Bryant, C. 2010. Decadal-scale rainfall variability in Ethiopia recorded in an annually laminated, Holocene-age, stalagmite. *The Holocene*, 20(6), 827-836.
- Baker, A., C. Bradley, S. Phipps, M. Fischer, I. J. Fairchild, L. Fuller, C. Spötl, and C. Azcurra .2012. Millennial-scale forward models and pseudoproxies of stalagmite  $\delta^{18}\text{O}$ : An example from NW Scotland, *Clim. Past*, 8, 1153–1167, doi:10.5194/cp-8-1153-2012.
- Baker, A., Bradley, C., & Phipps, S. J. 2013. Hydrological modeling of stalagmite  $\delta^{18}\text{O}$  response to glacial - interglacial transitions. *Geophysical Research Letters*, 40(12), 3207-3212.
- Baker, A., Hartmann, A., Duan, W., Hankin, S., Comas-Bru, L., Cuthbert, M.O., Treble, P.C., Banner, J., Genty, D., Baldini, L., Bartolomé, M., Moreno, A., and Pérez-Mejías, C., 2019. Global distribution and controls on cave drip water oxygen isotope composition. *Nat. Commun.*, 10, Article number: 2984.
- Baker, A. Berthelin, R., Cuthbert, M.O., Treble, P.C., Hartmann, A. and the KSS Cave Studies Team. 2020. Rainfall recharge thresholds in a subtropical climate determined using a regional cave drip water monitoring network. *J. Hydrol*, 125001.
- Baker, A., Scheller, M., Oriani, F., Mariethoz, G., Hartmann, A., Wang, Z., & Cuthbert, M. O. 2021. Quantifying temporal variability and spatial heterogeneity in rainfall recharge thresholds in a montane karst

- environment. *J. Hydrol*, 594, 125965.
- Baldini, L.M., McDermott, F., Foley, A.M., Baldini, J.U.L., 2008. Spatial variability in the European winter precipitation  $\delta^{18}\text{O}$ -NAO relationship: Implications for reconstructing NAO-mode climate variability in the Holocene. *Geophys. Res. Lett.* 35(4), L04709.
- Baldini, J. U. L., F. McDermott, L. M. Baldini, C. J. Ottley, K. L. Linge, N. Clipson, and K. E. Jarvis.2012., Identifying short-term and seasonal trends in cave dripwater trace element concentrations based on a daily-scale automatically collected dripwater dataset, *Chem. Geol.*, 330-331, 1-16.
- Barker, R., Moore, J., 1998. The application of time-lapse electrical tomography in groundwater studies. *Lead. Edge* 17 (10), 1454–1458. <https://doi.org/10.1190/1.1437878>.
- Bar-Matthews, M., Ayalon, A., Matthews, A., Sass, E., & Halicz, L. 1996. Carbon and oxygen isotope study of the active water-carbonate system in a karstic Mediterranean cave: Implications for paleoclimate research in semiarid regions. *Geochim. Cosmochim. Acta*, 60(2), 337-347.
- Besson, A., Cousin, I., Dorigny, A., Dabas, M., King, D., 2008. The temperature correction for the electrical resistivity measurements in undisturbed soil samples: analysis of the existing conversion models and proposal of a new model. *Soil Sci.* 173, 707–720.
- Binley, A., Shaw, B., Henry-Poulter, S., 1995. Flow pathways in porous media: Electrical resistance tomography and dye staining image verification. *Meas. Sci. Technol.* 7 (3), 384. <https://doi.org/10.1088/0957-0233/7/3/020>.
- Binley, A., Hubbard, S. S., Huisman, J. A., Revil, A., Robinson, D. A., Singha, K., & Slater, L. D. 2015. The emergence of hydrogeophysics for improved understanding of subsurface processes over multiple scales. *Water resources research*, 51(6), 3837-3866.
- Bourges, F., Genthon, P., Genty, D., Lorblanchet, M., Mauduit, E., d'Hulst, D. 2014. Conservation of prehistoric caves and stability of their inner climate: lessons from Chauvet and other French caves. *Sci. Total Environ.*, 493, 79-91.
- Bourges, F., Genty, D., Perrier, F., Lartiges, B., Régnier, É., François, A., et al. 2020. Hydrogeological control on carbon dioxide input into the atmosphere of the Chauvet-Pont d'Arc cave. *Sci. Total Environ.*, 716, 136844.
- Bowen, G. J., & Wilkinson, B. 2002. Spatial distribution of  $\delta^{18}\text{O}$  in meteoric precipitation. *Geology*, 30(4), 315-318.
- Bowen, G.J., 2008. Spatial analysis of the intra-annual variation of precipitation isotope ratios and its climatological corollaries. *J. Geophys. Res. Atmos.* 113.

- Bradley, C., A. Baker, C. N. Jex, and M. J. Leng. 2010., Hydrological uncertainties in the modelling of cave drip-water  $\delta^{18}\text{O}$  and the implications for stalagmite palaeoclimate reconstructions, *Quat. Sci. Rev.*, 29(17-18), 2201-2214.
- Breitenbach, S. F., Adkins, J. F., Meyer, H., Marwan, N., Kumar, K. K., Haug, G. H., 2010. Strong influence of water vapor source dynamics on stable isotopes in precipitation observed in Southern Meghalaya, NE India. *Earth Planet. Sci. Lett.* 292(1-2):0–220.
- Breitenbach, S. F., Lechleitner, F. A., Meyer, H., Diengdoh, G., Matthey, D., & Marwan, N., 2015. Cave ventilation and rainfall signals in dripwater in a monsoonal setting—a monitoring study from NE India. *Chem. Geol.*, 402, 111-124.
- Brunet, P., Clément, R., Bouvier, C., 2010. Monitoring soil water content and deficit using Electrical Resistivity Tomography (ERT)—A case study in the Cevennes area. France. *Journal of Hydrology* 380 (1), 146–153. <https://doi.org/10.1016/j.jhydrol.2009.10.032>.
- Burger, H. R., Sheehan, A. F., Jones, C. H., & Burger, H. R. 2006. Introduction to applied geophysics: Exploring the shallow subsurface (Vol. 550). New York: WW Norton.
- Cai, Z., Tian. L., Bowen, G. J., 2017. ENSO variability reflected in precipitation oxygen isotopes across the Asian Summer Monsoon region. *Earth Planet. Sci. Lett.* 475:25–33.
- Carriere, S.D., Chalikakis, K., S´en´echal, G., Danquigny, C., Emblanch, C., 2013. Combining electrical resistivity tomography and ground penetrating radar to study geological structuring of karst unsaturated zone. *J. Appl. Geophys.* 94, 31–41. <https://doi.org/10.1016/j.jappgeo.2013.03.014>.
- Cassou, C., Terray, L., Hurrell, J. W., Deser, C., 2004. North Atlantic winter climate regimes: Spatial asymmetry, stationarity with time, and oceanic forcing. *J. Clim.* 17(5), 1055–1068.
- Caterina, D., Orozco, A. F., & Nguyen, F. 2017. Long-term ERT monitoring of biogeochemical changes of an aged hydrocarbon contamination. *Journal of contaminant hydrology*, 201, 19-29.
- Celle-Jeanton H., Travi Y. and Blavoux B., 2001. Isotopic typology of the precipitation in the western Mediterranean region at three different timescales. *Geophys. Res. Lett.* 28(7), 1215–1218.
- Chailloux, D. Rapport de la radiolocalisation de la Loire Souterraine des 23 et 24 octobre 2021 par les plongeurs de l'Association Spéléologie Subaquatique du Loiret (SSL) et du Centre Normand d'Etude du Karst (CNEK). Publication interne.

- Chalikakis, K., Plagnes, V., Guerin, R., Valois, R., & Bosch, F. P. 2011., Contribution of geophysical methods to karst-system exploration: an overview. *Hydrogeology Journal*, 19(6), 1169-1180.
- Chambers, J. E., Gunn, D. A., Wilkinson, P. B., Meldrum, P. I., Haslam, E., Holyoake, S., Kirkham, M., Kuras, O., Merritt, A., and Wragg, J.: 4-D electrical resistivity tomography monitoring of soil moisture dynamics in an operational railway embankment, *Near Surf. Geophys.*, 12, 61–72, <https://doi.org/10.3997/1873-0604.2013002>, 2014.
- Chen, B., A. F. Stein, N. Castell, J. D. de la Rosa, A. M. Sanchez de la Campa, Y. Gonzalez-Castanedo., R. R. Draxler., 2012., Modeling and surface observations of arsenic dispersion from a large Cu-smelter in southwestern Europe. *Atmos. Environ.*, 49, 114–122.
- Chen, C-J., Li, T-Y. 2018. Geochemical characteristics of cave drip water respond to ENSO based on a 6-year monitoring work in Yangkou cave, Southwest China, *J. Hydrol*, 561:896–907.
- Chen, F. L., Zhang, M. J., Wang, S. J., Ma, Q., Zhu, X. F., Dong, L., 2015. Relationship between sub-cloud secondary evaporation and stable isotopes in precipitation of Lanzhou and surrounding area, *Quatern. Int.*, 380-381, 68–74.
- Clark, I., Fritz, P., 1997. *Environmental Isotopes in Hydrology*. Lewis Publishers, New York.
- Cobb, K.M., Adkins, J.F., Partin, J.W., Clark, B., 2007. Regional-scale climate influences on temporal variation of rainwater and cave dripwater oxygen isotopes in northern Borneo. *Earth Planet. Sci. Lett.* 263, 207–220
- Cole, J.E., Rind, D., Webb, R.S., Jouzel, J., Healy, R., 1999. Climatic controls on interannual variability of precipitation  $\delta^{18}\text{O}$ : Simulated influence of temperature, precipitation amount, and vapor source region. *J. Geophys. Res.*, 104, 14223–14235.
- Coscia, I., Linde, N., Greenhalgh, S., Günther, T., and Green, A.: A filtering method to correct time-lapse 3-D ERT data and improve imaging of natural aquifer dynamics, *J. Appl. Geophys.*, 80, 12–24, <https://doi.org/10.1016/j.jappgeo.2011.12.015>, 2012.
- Craig, H., 1961. Isotopic variations in meteoric waters. *Science*. 133(3465): 1702–1703.
- Craig, H., Gordon, L.I., 1965. Deuterium and oxygen 18 variations in the ocean and the marine atmosphere, *The stable isotopes in oceanographic studies and paleotemperatures*, Lab. Geol. Nucl., Pisa, Italy, 9–130.
- Crawford, J., Hughes, C. E., Lykoudis, S. 2014. Alternative least squares methods for determining the meteoric water line, demonstrated using GNIP

- data. *J. Hydrol*, 519, 2331-2340.
- Cruz, F.W., Karmann, I., Viana, O., Burns, S.J., Ferrari, J.A., Vuille, M., Sial, A.N., Moreira, M.Z., 2005. Stable isotope study of cave percolation waters insubtropical Brazil: implications for paleoclimate inferences from speleothems. *Chem. Geol.* 220, 245–262
- Cruz-San Julian, J. L. Araguas, K. Rozanski, J. Benavente, J. Cardenal, M. C. Hidalgo, S. Garcia-Lopez, J. C. Martinez-Garrido, F. Moral & M. Olias., 1992. Sources of precipitation over South-Eastern Spain and groundwater recharge. An isotopic study, *Tellus B: Chemical and Physical Meteorology*, 44:3, 226–236.
- Cuthbert, M.O., Baker, A., Jex, C.N., Graham, P.W., Treble, P., Andersen, M.S and Acworth, R.I., 2014. Drip water isotopes in semi-arid karst: implications for speleothem paleoclimatology. *Earth Planet. Sci. Lett.*, 395, 194-204
- Daniels F. and Alberty R.A., 1966. *Physical Chemistry*. John Wiley and Sons, Inc.
- Dansgaard, W., 1954. The O18-abundance in fresh water. *Geochim.Cosmochim. Acta.* 6, 241–260.
- Dansgaard, W., 1964. Stable isotopes in precipitation. *Tellus* 16, 436–468.
- Dee, S., Emile-Geay, J., Evans, M.N., Allam, A., Steig, E.J., Thompson, D.M., 2015a. PRYSM: an open-source framework for PRoxY System Modeling, with applications to oxygen-isotope systems. *J. Adv. Model. Earth Syst.* 7 (3), 1220e1247. <https://doi.org/10.1002/2015M>
- Deininger, M., J. Fohlmeister, D. Scholz, and A. Mangini. 2012. Isotope disequilibrium effects: The influence of evaporation and ventilation effects on the carbon and oxygen isotope composition of speleothems – A model approach, *Geochim. Cosmochim. Acta*, 96, 57-79.
- Deininger, M., & Scholz, D. 2019. ISOLUTION 1.0: An ISOTOpe evoLUTION model describing the stable oxygen ( $\delta^{18}\text{O}$ ) and carbon ( $\delta^{13}\text{C}$ ) isotope values of speleothems. *Int. J. Speleol.*, 48, 3. doi: <https://doi.org/10.5038/1827-806X.48.1.2219>
- Draxler, R. R., Hess, G. D., 1998. An overview of the HYSPLIT\_4 modelling system for trajectories, dispersion and deposition. *Aust. Meteorol. Mag.* 47(4), 295–308.
- Draxler, R. R., and G. D. Rolph., 2010. HYSPLIT (HYbrid Single-Particle Lagrangian Integrated Trajectory) model access via NOAA ARL READY website (<http://ready.arl.noaa.gov/HYSPLIT.php>). NOAA Air Resources Laboratory. Silver Spring, MD, 25.
- Duan, W., Ruan, J., Luo, W., Li, T., Tian, L., Zeng, G., Zhang, D., Bai, Y., Li, J.,



- Tao, T. and Zhang, P., 2016. The transfer of seasonal isotopic variability between precipitation and drip water at eight caves in the monsoon regions of China. *Geochim. Cosmochim. Acta*, 183, pp.250-266.
- Dublyansky, Y. V., Klimchouk, A. B., Tokarev, S. V., Amelichev, G. N., Langhamer, L., Spötl, C. 2018. Stable isotopic composition of atmospheric precipitation on the Crimean Peninsula and its controlling factors. *J. Hydrol*, 565, 61-73.
- Duffourg, F., Ducrocq, V., 2011. Origin of the moisture feeding the Heavy Precipitating Systems Over Southeastern France. *Nat. Hazard. Earth. Sys.* 11(4), 1163.
- Dumitru, O.A., Forray, F.L., Fornós, J.J., Ersek, V., Onac, B.P., 2017. Water isotopic variability in Mallorca: a path to understanding past changes in hydroclimate. *Hydrol. Process.* 31, 1, 104–116.
- Ellis, S.A., Cobb, K.M., Moerman, J.W., Partin, J.W., Bennett, A.L., Malang, J., Gerstner, H., Tuen, A.A., 2020. Extended cave drip water time series captures the 2015–2016 El Nino in Northern Borneo. *Geophys. Res. Lett.* 47 (5).
- Even, H., Carmi, I., Magaritz, M., Gerson, R., 1986. Timing the transport of water through the upper vadose zone in a karstic system above a cave in Israel. *Earth Surf Process Landf* 11, 181–191.
- Fairchild, I. J., G. W. Tuckwell, A. Baker, and A. F. Tooth. 2006., Modelling of dripwater hydrology and hydrogeochemistry in a weakly karstified aquifer (Bath, UK): Implications for climate change studies, *J. Hydrol*, 321(1-4), 213-231.
- Fairchild, I. J., & Baker, A. 2012., *Speleothem science: from process to past environments* (Vol. 3). John Wiley & Sons.
- Field, R.D., 2010. Observed and modeled controls on precipitation  $\delta^{18}\text{O}$  over Europe: From local temperature to the Northern Annular Mode, *J. Geophys. Res.* 115, D12101.
- Fischer, M. J., D. Matthey., 2012. Climate variability and precipitation isotope relationships in the Mediterranean region. *J. Geophys. Res. Atmos.* 117.D20.
- Ford D., Williams P. W., 1989. *Karst Geomorphology and Hydrology*. Chapman & Hall: 601 p.
- Ford, D.C. and Williams, P. 2007. *Karst Hydrogeology and Geomorphology*. John Wiley, Chichester, 562.
- Ford, D.C., Williams, P.W., 2013. *Karst Hydrogeology and Geomorphology*. John Wiley &

- Fricke H. C., O'Neil J. R., 1999. The correlation between  $18\text{O}/16\text{O}$  ratios of meteoric water and surface temperature: its use in investigating terrestrial climate change over geologic time. *Earth Planet. Sci. Lett.* 170, 181–196.
- Friedman, I., Harris, J.M., Smith, G.I., Johnson, C.A., 2002. Stable isotope composition of waters in the Great Basin, United States, 1, Air-mass trajectories, *J. Geophys. Res.* 107(D19), 4400.
- Gat, J.R., 1996. Oxygen and hydrogen isotopes in the hydrologic cycle. *Annu. Rev. Earth. Planet. Sci.* 24, 225–262.
- Gat, J. R., 2010. *Isotope Hydrology: A Study of the Water Cycle*. Imperial College Press, London.
- Gautam, P., Pant, S.R. Ando, H., 2000. Mapping of subsurface karst structure with gamma ray and electrical resistivity profiles: a case study from Pokhara valley, central Nepal. *J. Appl. Geophys.*, 45/2: 97-110. <https://doi.org/10.1002/9781118684986> Geotest user manual 2.50, Available from: <http://www.geophysik-dr-rauen.de>. Nov 2019.
- Genelle, F., Sirieix, C., Riss, J., & Naudet, V. 2012. Monitoring landfill cover by electrical resistivity tomography on an experimental site. *Engineering Geology*, 145, 18-29.
- Genty D. and Deflandre G., 1998. Drip flow variations under a stalactite of the Père Noël Cave (Belgium). Evidence of seasonal variations and air pressure constraints. *J. Hydrol*, Vol. 211, n° 1-4, pp. 208-232.
- Genty, D., Baker, A., & Vokal, B. 2001. Intra-and inter-annual growth rate of modern stalagmites. *Chemical Geology*, 176(1-4), 191-212.
- Genty, D., Blamart, D., Ouahdi, R., Gilmour, M., Baker, A., Jouzel, J., & Van-Exter, S. 2003. Precise dating of Dansgaard–Oeschger climate oscillations in western Europe from stalagmite data. *Nature*, 421(6925), 833.
- Genty, D., Blamart, D., Ghaleb, B., Plagnes, V., Causse, C., Bakalowicz, M., Zouari, K., Chkir, N., Hellstrom, J., Wainer, K., Bourges, F., 2006. Timing and dynamics of the last deglaciation from European and North African delta C-13 stalagmite profiles – comparison with Chinese and South Hemisphere stalagmites. *Quatern. Sci. Rev.* 25, 2118–2142.
- Genty, D., 2008. Palaeoclimate research in Villars Cave (Dordogne, SW-France). *Int. J. Speleol.* 37, 173–191.
- Genty, D., Labuhn, I., Hoffmann, G., Danis, P.A., Mestre, O., Bourges, F., Wainer, K., Massault, M., Van Exter, S., Régnier, E., Orengo, Ph., Falourd, S., Minster, B., 2014a. Rainfall and cave water isotopic relationships in two South-France sites. *Geochim. Cosmochim. Acta.* 131 (5), 323–343.
- Genty D., Valladas H., Beck L., Téreygeol F., Delluc B., Delluc G., Régnier E.,

- Baritaud Th., Hellstrom J., Blamart D., Gauthier C., Kaltnecker E., Moreau Ch., Dumoulin J.P., 2014b, La grotte de Villars : données chronologiques de l'occupation humaine et contexte environnemental, *Comptes Rendus PALEO*, special issue MADAPCA, pp. 153-161.
- Gibson, D. 1996. How accurate is radio-location? *Cave and Karst Science*. Vol. 23 (2), pp. 77-80.
- Goldscheider, N., 2012. A holistic approach to groundwater protection and ecosystem services in karst terrains. *AQUA mundi* Am06046, 117–124. doi:10.4409/Am-046-12- 0047
- Hartmann A., Lange J., Weiler M., Arbel Y., & Greenbaum N., 2012. A new approach to model the spatial and temporal variability of recharge to karst aquifers. *Hydrol. Earth. Syst Sci.*, 16(7), 2219–2231. 10.5194/hess-16-221.
- Hartmann, A., Barberá, J.A., Lange, J., Andreo, B., Weiler, M., 2013. Progress in the hydrologic simulation of time variant recharge areas of karst systems – Exemplified at a karst spring in Southern Spain. *Adv. Water Resour.* 54, 149–160. doi: 10.1016/j.advwatres.2013.01.010
- Hartmann, A., Gleeson, T., Rosolem, R., Pianosi, F., Wada, Y., Wagener, T., 2015. A largescale simulation model to assess karstic groundwater recharge over Europe and the Mediterranean. *Geosci. Model Dev.* 8, 1729–1746. doi:10.5194/gmd-8-1729-2015
- Hartmann, A., Baker, A., 2017. Modelling karst vadose zone hydrology and its relevance for paleoclimate reconstruction. *Earth-Sci. Rev.* 172, 178–192. <https://doi.org/10.1016/j.earscirev.2017.08.001>.
- Hayley, K., Bentley, L. R., Gharibi, M., & Nightingale, M. 2007., Low temperature dependence of electrical resistivity: Implications for near surface geophysical monitoring. *Geophysical research letters*, 34(18).
- Healy, Richard W. Estimating groundwater recharge. Cambridge University Press, 2010.
- Hendy, C. H. 1971. The isotopic geochemistry of speleothems—I. The calculation of the effects of different modes of formation on the isotopic composition of speleothems and their applicability as palaeoclimatic indicators, *Geochim. Cosmochim. Acta*, 35(8), 801-824.
- Hermans, T., Nguyen, F., Robert, T., & Revil, A. 2014. Geophysical methods for monitoring temperature changes in shallow low enthalpy geothermal systems. *Energies*, 7(8), 5083-5118.
- Hoffmann, G., Werner, M., Heimann, M., 1998. The Water isotope module of the ECHAM atmospheric general circulation model - A study on time scales from days to several years. *J. Geophys. Res.* 103, 16,871–16,896.

- Holland, H. D., Kirsipu, T. V., Huebner, J. S., & Oxburgh, U. M. 1964. On some aspects of the chemical evolution of cave waters. *The Journal of Geology*, 72(1), 36-67.
- Hu, C., Henderson, G. M., Huang, J., Chen, Z., and Johnson, K. R. 2008a. Report of a three-year monitoring programme at Heshang Cave, Central China, *Int. J. Speleol.*, 37, 143–151, doi:10.5038/1827-806X.37.3.1,
- Hu, C., Henderson, G. M., Huang, J., Xie, S., Sun, Y., & Johnson, K. R. 2008b. Quantification of Holocene Asian monsoon rainfall from spatially separated cave records. *Earth and Planetary Science Letters*, 266(3-4), 221-232.
- Hu, J., Dee, S. G., Wong, C. I., Harman, C. J., Banner, J. L., & Bunnell, K. E. 2021. Assessing proxy system models of cave dripwater  $\delta^{18}\text{O}$  variability. *Quat. Sci. Rev.*, 254, 106799.
- Hughes, C. E., Crawford, J. 2012. A new precipitation weighted method for determining the meteoric water line for hydrological applications demonstrated using Australian and global GNIP data. *J. Hydrol.* 464, 344-351.
- Hurrell, J.W., 1995. Decadal trends in the north Atlantic oscillation: regional temperatures and precipitation, *Science*, 269, 676-679.
- Hurrell, J. W., 1996. Influence of variations in extratropical wintertime teleconnections on Northern Hemisphere temperature, *Geophys. Res. Lett.*, 23, 665- 668.
- IAEA Publish chapter 4. 2000. Environmental isotopes in the hydrological cycle. 39.
- Ireson, A.M., Butler, A.P., 2013. A critical assessment of simple recharge models: application to the UK Chalk. *Hydrol. Earth Syst. Sci.* 17, 2083–2096. <http://dx.doi.org/10.5194/hess-17-2083-2013>.
- Jacob, D., Petersen, J., Eggert, B., Alias, A., Christensen, O. B., Bouwer, L. M., Braun, A., Colette, A., Déqué, M., Georgievski, G., Georgopoulou, E., Gobiet, A., Menut, L., Nikulin, G., Haensler, A., Hempelmann, N., Jones, C., Keuler, K., Kovats, S., Yiou, P. 2014. EURO-CORDEX: New high-resolution climate change projections for European impact research. *Regional Environmental Change*, 14, 563–578.
- Jean-Baptiste, P., Genty, D., Fourre, E., Regnier, E., 2019. Tritium dating of dripwater from Villars cave (SW-France). *Appl. Geochem.* 107, 152–158.
- Johnsen, S. J., Dansgaard, W., & White, J. W. C. 1989. The origin of Arctic precipitation under present and glacial conditions. *Tellus B: Chemical and Physical Meteorology*, 41(4), 452-468.
- Kaufman A., Bar-Matthews M., Ayalon A. and Carmi I. 2003. The vadose flow

- above Soreq Cave, Israel: a tritium study of the cave waters. *J. Hydrol.* 273, 155–163.
- Keller, G.V., Frischknecht, F.C., 1966. *Electrical Methods in Geophysical Prospecting*. Pergamon Press, Oxford, UK, pp. 30–33.
- Kim, J H., Yi, M. J., Park, S G., Kim, J.G., 2009. 4D inversion of DC resistivity monitoring data acquired over a dynamically changing earth model. *Journal of Applied Geophysics*, 68, 522-532.
- Kim, S. T., & O'Neil, J. R. 1997., Equilibrium and nonequilibrium oxygen isotope effects in synthetic carbonates. *Geochimica et cosmochimica acta*, 61(16), 3461-3475.
- Kiraly, L., 2003. Karstification and Groundwater Flow. *Speleogenes. Evol. Karst Aquifers* 1, 1–24.
- Kluge, T., T. Marx, D. Scholz, S. Niggemann, A. Mangini, and W. Aeschbach-Hertig .2008. A new tool for palaeoclimate reconstruction: Noble gas temperatures from fluid inclusions in speleothems, *Earth Planet. Sci. Lett.*, 269(3–4), 408-415.
- Kluge, T., Riechelmann D. F. C., Wieser M., Spotl C., Sultenfuss J., Schroder-Ritzrau A., Niggemann S. and Aeschbach-Hertig W.2010. Dating cave drip water by tritium. *J. Hydrol.* 394, 396– 406.
- Krklec, K., & Dominguez-Villar, D. 2014. Quantification of the impact of moisture source regions on the oxygen isotope composition of precipitation over Eagle Cave, central Spain. *Geochimica et cosmochimica acta*, 134, 39-54.
- Krklec, K., Domínguez-Villar, D., Lojen, S., 2018. The impact of moisture sources on the oxygen isotope composition of precipitation at a continental site in central Europe, *J. Hydrol.*, 561, 810–821.
- Kuras, O., Pritchard, J. D., Meldrum, P. I., Chambers, J. E., Wilkinson, P. B., Ogilvy, R. D., and Wealthall, G. P. 2009. Monitoring hydraulic processes with automated time-lapse electrical resistivity tomography (ALERT), *C. R. Geosci.*, 341, 868–885.
- Kurita, N. 2013. Water isotopic variability in response to meso-scale convective system over the tropical ocean. *J. Geophys. Res. Atmos.*, 118, 10 376–10 390.
- LaBrecque, D. J., Ramirez, A. L., Daily, W. D., Binley, A. M., and Schima, S. A. 1996. ERT monitoring of environmental remediation processes, *Meas. Sci. Technol.*, 7, 375,
- Lacanette, D., Malaurent, P., Caltagirone, J.P., Brunet, J., 2007. Etude des transferts de masse et de chaleur dans la grotte de Lascaux. *Karstologia* 50, 19–30.

- Lachniet, M. S. 2009. Climatic and environmental controls on speleothem oxygen-isotope values. *Quatern. Sci. Rev.*, 28(5-6), 412-432.
- Langebroek, P.M., Werner, M., Lohmann, G., 2011. Climate information imprinted in oxygen-isotopic composition of precipitation in Europe. *Earth Planet. Sci. Lett.* 311(1–2):144–154.
- Lee, J.-E., Fung, I., 2008. “Amount effect” of water isotopes and quantitative analysis of post-condensation processes. *Hydrol. Processes*, 22, 1–8, doi:10.1002/hyp.6637.
- LeGrande, A.N., Schmidt, G.A., 2006. Global gridded data set of the oxygen isotopic composition in seawater. *Geophys. Res. Lett.* 33.
- Leopold, M., Gupanis-Broadway, C., Baker, A., Hankin, S., & Treble, P. 2021. Time lapse electric resistivity tomography to portray infiltration and hydrologic flow paths from surface to cave. *Journal of Hydrology*, 593, 125810.
- Lharti, H., Sirieix, C., Riss, J., Verdet, C., Salmon, F., & Lacanette, D. 2023. Partitioning a rock mass based on electrical resistivity data: the choice of clustering method. *Geophysical Journal International*, 2023, ggad081, <https://doi.org/10.1093/gji/ggad081>
- Li, T.-Y., Shen, C.-C., Li, H.-C., Li, J.-Y., Chiang, H.-W., Song, S.-R., Yuan, D.-X., Lin, C.D.J., Gao, P., Zhou, L.-P., Wang, J.-L., Ye, M.-Y., Tang, L.-L., Xie, S.-Y., 2011. Oxygen and carbon isotopic systematics of aragonite speleothems and water in Furong Cave, Chongqing, China. *Geochim. Cosmochim. Acta.* 75(15), 4140-4156.
- Lionello, P., Malanotte-Rizzoli, P., Boscolo, R., Alpert, P., Artale, V., Li, L., Xoplaki, E. 2006. The Mediterranean climate: an overview of the main characteristics and issues. *Developments in earth and environmental sciences*, 4, 1-26.
- Long, A.J., Putnam, L.D., 2004. Linear model describing three components of flow in karst aquifers using  $^{18}\text{O}$  data. *J. Hydrol.* 296, 254–27.
- Loke, M.H., Chambers, J.E., Rucker, D. F., Kuras, O. and Wilkinson, P. B., 2013. Recent developments in the direct-current geoelectrical imaging method. *Journal of Applied Geophysics*, 95, 135-156.
- Loke, M.H., Dahlin, T., Rucker, D.F., 2014. Smoothness-constrained time-lapse inversion of data from 3D resistivity surveys. *Near Surf. Geophys.* 12 (1):5–24. <http://dx.doi.org/10.3997/1873-0604.2013025>.
- Loke, M.H., 2015. Tutorial: 2-D and 3-D electrical imaging surveys. Geotomo Software, Malaysia
- Ma, R.J., McBratney, A., Whelan, B., Minasny, B., Short, M., 2011. Comparing

- temperature correction models for soil electrical conductivity measurement. *Precis. Agric.* 12, 55–66.
- Markowska, M., Andersen, M.S., Treble, P.C., Baker, A., Tadros, C., Hankin, S., and Jex, C.N., 2015. Unsaturated zone hydrology and cave drip discharge water response: Implications for speleothem palaeoclimate record variability. *J. Hydrol.* 529, 662-675.
- Markowska, M., Cuthbert, M.O., Baker, A., Treble, P.C., Andersen, M.S., Adler, L., Griffiths, A., and Frisia, S., 2020. Modern speleothem oxygen isotope hydroclimate records in water-limited SE Australia. *Geochim. Cosmochim. Acta*, 270, 431-448.
- Martin, J. B., Kurz, M. J., & Khadka, M. B. 2016. Climate control of decadal-scale increases in apparent ages of eogenetic karst spring water. *Journal of Hydrology*, 540, 988-1001.
- Massei, N., Mahler, B. J., Bakalowicz, M., Fournier, M., & Dupont, J. P. 2007. Quantitative interpretation of specific conductance frequency distributions in karst. *Groundwater*, 45(3), 288-293.
- Mattey, D., Lowry, D., Duffet, J., Fisher, R., Hodge, E., Frisia, S., 2008. A 53 year seasonally resolved oxygen and carbon isotope record from a modern Gibraltar speleothem: reconstructed drip water and relationship to local precipitation. *Earth Planet. Sci. Lett.* 269, 80–95
- Mattey, D.P., Fairchild, I.J., Atkinson, T.C., Latin, J.-P., Ainsworth, M., Durell, R., 2010. Seasonal microclimate control of calcite fabrics, stable isotopes and trace elements in modern speleothem from St Michaels Cave, Gibraltar. In: Pedley, H.M., Rogerson, M. (Eds.), *Tufas and Speleothems: Unravelling the Microbial and Physical Controls*. The Geological Society of London, London, pp. 323-344.
- McCarthy, G. D., Haigh, I. D., Hirschi, J. J. M., Grist, J. P., Smeed, D. A. 2015. Ocean impact on decadal Atlantic climate variability revealed by sea-level observations. *Nature*, 521(7553), 508-510.
- McDermott, F., Atkinson, T. C., Fairchild, I. J., Baldini, L. M., Mattey, D. P., 2011., A first evaluation of the spatial gradients in delta (18)O recorded by European Holocene speleothems. *Global Planet. Change* 79, 275–287.
- McDonald, J. 2004. The 2002–2003 El Niño recorded in Australian cave drip waters: Implications for reconstructing rainfall histories using stalagmites, *Geophys. Res. Lett.*, 31, L22202, doi:10.1029/2004GL020859,
- Meinshausen, M., Smith, S. J., Calvin, K., Daniel, J. S., Kainuma, M. L. T., Lamarque, J. F., Matsumoto, K., Montzka, S. A., Raper, S. C. B., Riahi, K., Thomson, A., Velders, G. J. M., & van Vuuren, D. P. P. 2011. The RCP greenhouse gas concentrations and their extensions from 1765 to 2300.

- Climatic Change, 109, 213–241. <https://doi.org/10.1007/s10584-011-0156-z>
- Meyerhoff, S. B., Karaoulis, M., Fiebig, F., Maxwell, R. M., Revil, A., Martin, J. B., and Graham, W. D. 2012., Visualization of conduit-matrix conductivity differences in a karst aquifer using time-lapse electrical resistivity: ERT time-lapse of karst conductivity, *Geophys. Res. Lett.*, 39, L24401, <https://doi.org/10.1029/2012GL053933>,
- Michelangeli, P. A., Vrac, M., & Loukos, H. 2009. Probabilistic downscaling approaches: Application to wind cumulative distribution functions. *Geophysical Research Letters*, 36, L11708. <https://doi.org/10.1029/2009GL038401>
- Michelle, S. 2002. *Numerical Analysis: A Mathematical Introduction*, Chapters 4 and 6. Clarendon Press, Oxford.
- Michot, D., Benderitter, Y., Dorigny, A., Nicoullaud, B., King, D., Tabbagh, A., 2003. Spatial and temporal monitoring of soil water content with an irrigated corn crop cover using surface electrical resistivity tomography. *Water Resour. Res.* 39/5 <https://doi.org/10.1029/2002WR001581>
- Numaguti, A., 1999. Origin and recycling processes of precipitating water over the Eurasian continent: Experiments using an atmospheric general circulation model. *J. Geophys. Res. Atmos.* 104, 1957–1972.
- Opsahl, S. P., Musgrove, M., & Slattery, R. N. 2017. New insights into nitrate dynamics in a karst groundwater system gained from in situ high-frequency optical sensor measurements. *Journal of hydrology*, 546, 179-188.
- O'Reilly, C. H., Huber, M., Woollings, T., Zanna, L. 2016. The signature of low - frequency oceanic forcing in the Atlantic Multidecadal Oscillation. *Geophys. Res. Lett.*, 43(6), 2810-2818.
- Oster, Jessica L., Isabel P. Montañez, and Neil P. Kelley. 2012. Response of a modern cave system to large seasonal precipitation variability. *Geochim. Cosmochim. Acta* 91 92-108.
- Pakzad, L., Ein-Mozaffari, F., Chan, P., 2008. Using electrical resistance tomography and computational fluid dynamics modeling to study the formation of cavern in the mixing of pseudoplastic fluids possessing yield stress. *Chem. Eng. Sci.* 63 (9), 2508–2522. <https://doi.org/10.1016/j.ces.2008.02.009>.
- Palacky, G. J. 1988. Resistivity Characteristics of Geologic Targets. In *Electromagnetic Methods in Applied Geophysics* (Vol. 1, pp. 53-129).
- Pang, Z. H., Kong, Y. L., Froehlich, K., Huang, T. M., Yuan, L. J., Li, Z. Q., Wang, F. T., 2011. Processes affecting isotopes in precipitation of an arid region, *Tellus. B.*, 63, 352–359.



- Pape, J. R., Banner, J. L., Mack, L. E., Musgrove, M., Guilfoyle, A., 2010. Controls on oxygen isotope variability in precipitation and cave drip waters, central Texas, USA. *J. Hydrol*, 385(1-4), 203–215.
- Partin, J. W. Cobb, K. M., Adkins, J. F., Tuen, A. A., Clark, B. 2013. Trace metal and carbon isotopic variations in cave drip water and stalagmite geochemistry from northern Borneo. *Geochem. Geophys. Geosyst.* 14(9):3567–3585.
- Peng, H., Mayer, B., Norman, A. L., Krouse, H. R., 2005. Modelling of hydrogen and oxygen isotope compositions for local precipitation. *Tellus B.* 57(4), 273–282.
- Petit, J.R., Jouzel, J., Raynaud, D., Barkov, N.I., Barnola, J.-M., Basile, I., Bender, M., Chappellaz, J., Davis, M., Delaygue, G., Delmotte, M., Kotlyakov, V.M., Legrand, M., Lipenkov, V.Y., Lorius, C., Pepin, L., Ritz, C., Saltzman, E., Stievenard, M., 1999. Climate and atmospheric history of the past 420,000 years from the Vostok ice core, Antarctica. *Nature* 399, 429–436.
- Pfahl, S. and Sodemann, H., 2014. What controls deuterium excess in global precipitation? *Climate of the Past*, 10(2), pp.771-781.
- Pfahl, S., Wernli, H., 2008. Air parcel trajectory analysis of stable isotopes in water vapor in the eastern Mediterranean. *J. Geophys. Res.* 113: D20104.
- Proctor, C. J., Baker, A., Barnes, W. L., and Gilmour, M. A., 2000. A thousand-year speleothem proxy record of North Atlantic climate from Scotland, *Clim. Dyna.*, 16, 815–820.
- Rau, G.C., Cuthbert, M.O., Andersen, M.S., Baker, A., Rutledge, H., Markowska, M., Roshan, H., Marjo, C.E., Graham, P.W. and Acworth, R.I., 2015. Controls on cave drip water temperature and implications for speleothem-based paleoclimate reconstructions. *Quat. Sci. Rev.* 127, pp.19-36.
- Revil, A., Karaoulis, M., Johnson, T., and Kemna, A. 2012. Review: some low-frequency electrical methods for subsurface characterization and monitoring in hydrogeology, *Hydrogeol. J.*, 20, 617–658,
- Riechelmann, D. F. C., Schröder-Ritzrau, A., Scholz, D., Fohlmeister, J., Spötl, C., Richter, D. K., & Mangini, A. (2011). Monitoring Bunker Cave (NW Germany): A prerequisite to interpret geochemical proxy data of speleothems from this site. *Journal of Hydrology*, 409(3-4), 682-695.
- Risi, C., Bony, S., Vimeaux, F., 2008. Influence of convective processes on the isotopic composition ( $\delta^{18}\text{O}$  and  $\delta\text{D}$ ) of precipitation and water vapour in the tropics: 2 Physical interpretation of the amount effect. *J. Geophys. Res.* 113, D19306.

- Robert, T., Dassargues, A., Brouy`ere, S., Kaufmann, O., Hallet, V., Nguyen, F., 2011. Assessing the contribution of electrical resistivity tomography (ERT) and self-potential (SP) methods for a water well drilling program in fractured/karstified limestones. *J. Appl. Geophys.* 75 (1), 42–53. <https://doi.org/10.1016/j.jappgeo.2011.06.008>.
- Rolph, G. D., Coauthors, 2009. Description and verification of the NOAA Smoke Forecasting System: The 2007 fire season. *Wea. Forecasting*, 24, 361–378.
- Rozanski, K., Araguás - Araguás, L., Gonfiantini, R., 1993. Isotopic patterns in modern global precipitation. In: Swart, P.K., Lohmann, K.L., McKenzie, J., Savin, S. (Eds.), *Climate Change in Continental Isotopic Records*. American Geophysical Union, Washington, DC, pp. 1–37.
- Salmon, F., Lacanette, D., Lharti, H., Sirieix, C., 2023. Heat Transfer in Rock Masses: Application to the Lascaux Cave (France). *International Journal of Heat and Mass Transfer*, 207, 124029.
- Samouëlian, A., Cousin, I., Tabbagh, A., Bruand, A., and Richard, G.: Electrical resistivity survey in soil science: a review, *Soil Till. Res.*, 83, 173–193, <https://doi.org/10.1016/j.still.2004.10.004>, 2005.
- Sánchez - Murillo, R., Esquivel - Hernández, G., Corrales - Salazar, J. L., Castro - Chacón, L., Durán - Quesada, A. M., Guerrero - Hernández, M., Delgado, V., Barberena, J., Montenegro - Rayo, K., Calderón. Heyddy., Chevez, C., Peña - Paz, T., García - Santos, Saúl., Ortiz - Roque, Pedro., Alvarado - Callejas, Y., Benegas, L., Hernández - Antonio, A., Matamoros - Ortega, M., Ortega, L Terzer - Wassmuth, S Chevez, C. 2020., Tracer hydrology of the data - scarce and heterogeneous Central American Isthmus. *Hydrological Processes*. 1–16
- Saporta, G., 1990. *Probabilités et analyse des données, et Statistique*. Editions Technip, Paris (493 pp.).
- Schmidt, G.A., LeGrande, A.N., Hoffmann, G., 2007. Water isotope expressions of intrinsic and forced variability in a coupled ocean - atmosphere model, *J. Geophys. Res.* 112, D10103.
- Sharp, Z., 2007. *Principles of Stable Isotope Geochemistry*. Pearson Prentice Hall, Upper Saddle River, NJ.
- Sirieix, C., Riss, J., Rey, F., Prétou, F., Lastennet, R., 2014. Electrical resistivity tomography to characterize a karstic spring Vauclusian: Fountain Orbe (Pyrenees, France). *Hydrogeol. J.* 22 (4):911–924. <http://dx.doi.org/10.1007/s10040-013-1095-8>.
- Sjostrom, D. J., & Welker, J. M. 2009., The influence of air mass source on the seasonal isotopic composition of precipitation, eastern USA. *Journal of*

- Geochemical Exploration, 102(3), 103-112.
- Sodemann, H., Schwierz, C., Wernli, H., 2008. Interannual variability of Greenland winter precipitation sources: Lagrangian moisture diagnostic and North Atlantic Oscillation influence. *J. Geophys. Res.* 113, D03107.
- Sons
- Soil Guidelines-soil water storage capacity and available soil moisture [https://www.droughtmanagement.info/literature/BC\\_MA\\_Soil\\_Water\\_Storage\\_Capacity\\_2005.pdf](https://www.droughtmanagement.info/literature/BC_MA_Soil_Water_Storage_Capacity_2005.pdf)
- Spötl, C., I. J. Fairchild, and A. F. Tooth. 2005., Cave air control on dripwater geochemistry, Obir Caves (Austria): Implications for speleothem deposition in dynamically ventilated caves, *Geochim. Cosmochim. Acta*, 69(10), 2451-2468.
- Stein, A.F., Draxler, R.R., Rolph, G.D., Stunder, B.J.B., Cohen, M.D., Ngan, F., 2015. NOAA's HYSPLIT atmospheric transport and dispersion modeling system, *Bull. Amer. Meteor. Soc.*, 96, 2059–2077.
- Stewart, M. K. 1975. Stable isotope fractionation due to evaporation and isotopic exchange of falling waterdrops: Applications to atmospheric processes and evaporation of lakes, *J. Geophys. Res.*, 80, 1133-1146.
- Stoll, H. M., A. Mendez-Vicente, S. Gonzalez-Lemos, A. Moreno, I. Cacho, H. Cheng, and R. L. Edwards. 2015. Interpretation of orbital scale variability in mid-latitude speleothem  $\delta^{18}\text{O}$ : Significance of growth rate controlled kinetic fractionation effects. *Quat. Sci. Rev.* 127, 215-228.
- Sturm, K., Hoffmann, G., Langmann, B., Stichler, W., 2005. Simulation of  $^{18}\text{O}$  in precipitation by the regional circulation model REMOiso. *Hydrol. Process.* 19, 3425–3444.
- Tadros, Carol V., Pauline C. Treble, Andy Baker, Ian Fairchild, Stuart Hankin, Regina Roach, Monika Markowska, and Janece McDonald. 2016. ENSO–cave drip water hydrochemical relationship: a 7-year dataset from south-eastern Australia. *Hydro. Earth. Syst. Sci.*, 20, no. 11: 4625-4640.
- Tang, Y., Pang, H., Zhang, W., Li, Y., Wu, S., Hou, S., 2015. Effects of changes in moisture source and the upstream rainout on stable isotopes in summer precipitation – a case study in Nanjing, East China, *Hydrol. Earth. Syst. Sc.*, 12, 3919–3944.
- Taylor, K. E., Stouffer, R., & Meehl, G. A. 2012. An overview of CMIP5 and the experiment design. *Bulletin of the American Meteorological Society*, 93, 485–498. <https://doi.org/10.1175/BAMS-D-11-00094.1>
- Telford, W.M., Geldart, L.P. and Sheriff, R.E., 1990. *Applied Geophysics* (second edition). Cambridge University Press.

- Tooth, A. F., & Fairchild, I. J. 2003. Soil and karst aquifer hydrological controls on the geochemical evolution of speleothem-forming drip waters, Crag Cave, southwest Ireland. *J. Hydrol*, 273(1-4), 51-68.
- Treble, P. C., C. Bradley, A. Wood, A. Baker, C. N. Jex, I. J. Fairchild, M. K. Gagan, J. Cowley, and C. Azcurra. 2013. An isotopic and modelling study of flow paths and storage in Quaternary calcarenite, SW Australia: implications for speleothem paleoclimate records, *Quat. Sci. Rev*, 64, 90-103.
- Treble, P., Mah, M., Griffiths, A., Baker, A., Deininger, M., Kelly, B., Scholz, D. and Hankin, S., 2019. Separating isotopic impacts of karst and in-cave processes from climate variability using an integrated speleothem isotope-enabled forward model. 2019. *EarthArXiv*, 10.31223/osf.io/j4kn6c.
- Treble, P.C., Baker, A., Abram, N.J., Hellstrom, J.C., Crawford, J., Gagan, M.K., Borsato, A., Griffiths, A.D., Bajo, P., Markowska, M., Priestley, S.C., Hankin, S., Paterson, D., 2022. Ubiquitous karst hydrological control on speleothem oxygen isotope variability in a global study. *Communications Earth & Environment* 3 (1), 29. <https://doi.org/10.1038/s43247-022-00347-3>.
- Tremaine, D. M., & Froelich, P. N. 2013. Speleothem trace element signatures: A hydrologic geochemical study of modern cave dripwaters and farmed calcite *Geochim. Cosmochim. Acta*, 121, 522-545.
- Troch, P. A., Paniconi, C., & Dawson, C. N. 2003. A distributed hydrology-vegetation model for complex terrain. *Journal of hydrology*, 282(1-4), 101-122.
- Uemura, R., Masson-Delmotte, V., Jouzel, J., Landais, A., Motoyama, H., Stenni, B., 2012. Ranges of moisture-source temperature estimated from Antarctic ice cores stable isotope records over glacial-interglacial cycles, *Clim. Past*, 8, 1109–1125.
- Uhlemann, S.S., Sorensen, J.P.R., House, A.R., Wilkinson, P.B., Roberts, C., Goody, D.C., Binley, A.M., Chambers, J.E., 2016. Integrated time-lapse geoelectrical imaging of wetland hydrological processes. *Water Resour. Res.* 52 (3), 1607–1625. <https://doi.org/10.1002/2015WR017932>.
- Uhlemann, S., Kuras, O., Richards, L.A., Naden, E., Polya, D.A., 2017. Electrical resistivity tomography determines the spatial distribution of clay layer thickness and aquifer vulnerability, Kandal Province, Cambodia. *J. Asian Earth Sci Advance online publication*. <https://doi.org/10.1016/j.jseaes>
- Vacher, H.L., Mylroie, J.E., 2002. Eogenetic karst from the perspective of an equivalent porous medium. *Carbonates Evaporites* 17 (2), 182–196. <https://doi.org/10.1007/BF03176484>.
- Valois, R., Bermejo, L., Gu´erin, R., Hinguant, S., Pigeaud, R., Rodet, J., 2010.

- Karstic morphologies identified with geophysics around Saulges caves (Mayenne, France). *Archaeol. Prospect.* 17, 151–160. <https://doi.org/10.1002/arp.385>.
- Vanderborght, J., Kemna, A., Hardelauf, H., Vereecken, H., 2005. Potential of electrical resistivity tomography to infer aquifer transport characteristics from tracer studies: A synthetic case study. *Water Resour. Res.* 41/6 <https://doi.org/10.1029/2004WR003774>.
- Verdet, C., Sirieix, C., Marache, A., Riss, J., & Portais, J. C. 2020. Detection of undercover karst features by geophysics (ERT) Lascaux cave hill. *Geomorphology*, 360, 107177.
- Vimeux, F., Masson, V., Jouzel, J., Stievenard, M., & Petit, J. R. (1999). Glacial–interglacial changes in ocean surface conditions in the Southern Hemisphere. *Nature*, 398(6726), 410–413.
- Voltaire, A., Sanchez-Gomez, E., Salas y Méliá, D., Decharme, B., Cassou, C., Sénési, S., Valcke, S., Beau, I., Alias, A., Chevallier, M., Déqué, M., Deshayes, J., Douville, H., Fernandez, E., Madec, G., Maisonnave, E., Moine, M.-P., Planton, S., Saint-Martin, D., Chauvin, F. 2013. The CNRM-CM5 global climate model: Description and basic evaluation. *Climate Dynamics*, 40, 2091–2121. <https://doi.org/10.1007/s00382-011-1259-y>
- Vrac, M., Drobinski, P., Merlo, A., Herrmann, M., Lavaysse, C., Li, L., & Somot, S. 2012. Dynamical and statistical downscaling of the French Mediterranean climate: Uncertainty assessment. *Natural Hazards and Earth System Sciences*, 12, 2769–2784. <https://doi.org/10.5194/nhess-12-2769-2012>
- Vrac, M., Noel, T., & Vautard, R. 2016. Bias correction of precipitation through Singularity Stochastic Removal: Because occurrences matter. *Journal of Geophysical Research: Atmospheres*, 121, 5237–5258. <https://doi.org/10.1002/2015JD024511>
- Wainer K., Genty D., Blamart D., Hofmann D., Couchoud I., 2009, A new stage 3 millennial climatic variability record from a SW France speleothem, *Palaeogeogr., Palaeoclim., Palaeoecol.*, 271: 130-139.
- Wainer K., Genty D., Blamart D., Daëron M., Bar-Matthews M., Vonhof H., Dublyansky Y., Pons-Branchu E., Thomas L., van Calsteren P., Quinif Y. and Caillon N., 2011, Speleothem record of the last 180 ka in Villars cave (SW France): Investigation of a large  $\delta^{18}\text{O}$  shift between MIS6 and MIS5, *Quatern. Sci. Rev.*, 30:130-146.
- Wainer K., Genty D., Blamart D., Bar-Matthews M., Quinif Y., Plagnes V., 2013, Millennial climatic instability during penultimate glacial period recorded in a south-western France speleothem., *Palaeogeogr., Palaeoclim., Palaeoecol.*, 376:122-131.

- Wang, Y.J., Cheng, H., Edwards, R.L., An, Z.S., Wu, J.Y., Shen, C.C., Dorale, J.A., 2001. A high-resolution absolute-dated Late Pleistocene monsoon record from Hulu Cave, China. *Science*. 294, 2345–2348.
- Watlet, A., Kaufmann, O., Triantafyllou, A., Poulain, A., Chambers, J.E., Meldrum, P.I., Wilkinson, P.B., Hallet, V., Quinif, Y., Van Ruymbeke, M., Van Camp, M., 2018. Imaging groundwater infiltration dynamics in the karst vadose zone with long-term ERT monitoring. *Hydrol. Earth Syst. Sci.* 22, 1563–1592. <https://doi.org/10.5194/hess-22-1563-2018>.
- White, W. B., Karst hydrology: recent developments and open questions, *Eng. Geol.*, 65, 85–105, 2002.
- Williams, P. W.: The role of the epikarst in karst and cave hydrogeology: a review, *Int. J. Speleol.*, 37, 1–10, 2008.
- Wong, C. I., and D. O. Breecker. 2015, Advancements in the use of speleothems as climate archives, *Quatern. Sci. Rev.*, 127, 1-18.494
- Xu, S., Sirieix, C., Ferrer, C., Lacanette-Puyo, D., Riss, J., Malaurent, P., 2015. A geophysical tool for the conservation of a decorated cave. - a case study for the Lascaux cave. *Archaeol. Prospect.* <http://dx.doi.org/10.1002/arp.1513> (online in Wiley OnlineLibrary)
- Xu, S., Sirieix, C., Marache, A., Riss, J., Malaurent, Ph., 2016. 3D geostatistical modeling of Lascaux hill from ERT data. *Eng. Geol.* 213 (4):169–178. <http://dx.doi.org/10.1016/j.enggeo.2016.09.009>.
- Xu, S., Sirieix, C., Riss, J., and Malaurent, P. 2017. A clustering approach applied to time-lapse ERT interpretation – case study of Lascaux cave, *J. Appl. Geophys.*, 144, 115–124, <https://doi.org/10.1016/j.jappgeo.2017.07.006>.
- Yamanaka, T., Tsujimura, M., Oyunbaatar, D., Davaa, G., 2007. Isotopic variation of precipitation over eastern Mongolia and its implication for the atmospheric water cycle, *J. Hydrol.*, 333, 21–34.
- Yonge, C.J., Ford, D.C., Gray, J., Schwarcz, H.P., 1985. Stable isotope studies of cave seepage water. *Chem. Geol.* 58, 97–105
- Zenone, T., Morelli, G., Teobaldelli, M., Fischanger, F., Matteucci, M., Sordini, M., Armani, A., Ferr`e, C., Chiti, T., Seufert, G., 2008. Preliminary use of ground-penetrating radar and electrical resistivity tomography to study tree roots in pine forests and poplar plantations. *Funct. Plant Biol.* 35 (10), 1047–1058. <https://doi.org/10.1071/FP08062>.
- Zhang, J., Genty, D., Sirieix, C., Michel, S., Minster, B., & Régnier, E. 2020. Quantitative assessments of moisture sources and temperature governing rainfall  $\delta^{18}\text{O}$  from 20 years' monitoring records in SW-France: Importance for isotopic-based climate reconstructions. *J. Hydrol.*, 591, 125327.

- Zhang, J., Li. Ting-Yong., 2019. Seasonal and inter-annual variation of hydro-chemical characteristics and stable isotopic compositions of drip waters in Furong Cave, Southwest China based on 12 years' monitoring. *J. Hydrol.* 572:40-50.
- Zhang, J., Liang, M., Li, T., Chen, C. & Li, J. 2022. Asian-Australian monsoon evolution over the last millennium linked to ENSO in composite stalagmite  $\delta^{18}\text{O}$  records. *Quat. Sci. Rev.* 281, 107420.
- Zhang, P.Z., Cheng, H., Edwards, R.L., Chen, F.H., Wang, Y.J., Yang, X.L., Liu, J., Tan, M., Wang, X.F., Liu, J.H., An, C.L., Dai, Z.B., Zhou, J., Zhang, D.Z., Jia, J.H., Jin, L.Y., Johnson, K.R., 2008. A test of climate, sun and culture relationship from an 1810-year Chinese cave record. *Science.* 322, 940–942.
- Zhou, W., Beck, B.F., Adams, A.L., 2002. Effective electrode array in mapping karst hazards in electrical resistivity tomography. *Environ. Geol.* 42 (8), 922–928. [https:// doi.org/10.1007/s00254-002-0594-z](https://doi.org/10.1007/s00254-002-0594-z).

---

## **Caractérisation de l'infiltration dans la grotte de Villars (Dordogne) par des méthodes géophysiques et isotopiques**

**Résumé :** Cette étude, a pour but de caractériser la géométrie et la dynamique de la zone d'infiltration au-dessus d'un site karstique typique, la grotte de Villars (Dordogne, SO-France). Elle traite, d'une part, de l'origine du signal d'entrée, les précipitations, et, d'autre part, aborde les processus d'infiltration (flux d'eau, isotopes) en lien avec la géométrie des réservoirs et des zones préférentielles d'infiltration. L'analyse isotopique de l'eau de pluie couplée au modèle de rétro-trajectoires Hysplit est utilisée pour déterminer les sources des précipitations au-dessus de la grotte, tandis que le modèle KarstFor est utilisé pour modéliser les flux d'infiltration et la dynamique des réservoirs karstiques. Afin d'identifier et de caractériser la variabilité temporelle des réservoirs et des zones d'infiltration, nous avons utilisé le suivi temporel par tomographie de résistivité électrique (ERT) pour révéler une forte saisonnalité dans les zones d'infiltration à l'aide de la méthode CHA (Classification Hiérarchique Ascendante). En intégrant toutes ces méthodes, cette étude améliore considérablement notre compréhension de l'infiltration en milieu karstique avec toutes les conséquences possibles pour une meilleure compréhension des recharges souterraines, des calibrations pour les études paléoclimatiques basées sur l'étude des spéléothèmes et pour la préservation des milieux souterrains archéologiques.

**Mots clés:** Isotopes de l'eau, karst réservoirs, sources d'humidité, modèle réservoir-flux, Infiltration, tomographie de résistivité électrique , Grotte de Villars

---

## **Characterization of the infiltration in the cave of Villars (Dordogne) by geophysical and isotopic methods**

**Abstract:** This study aims to characterize the geometry and dynamics of the infiltration zone above a typical karstic site, the cave of Villars (Dordogne, SW-France). On one hand, it deals with the rainfall origin of the input signal, and, on the other hand, it addresses the infiltration processes (water fluxes, isotopes) in connection with the geometry of the reservoirs and preferential infiltration zones. Rainwater isotope analysis coupled with the Hysplit back-trajectory model is used to determine sources of rainfall above the cave, while the KarstFor model is used to model seepage fluxes and karst reservoir dynamics. In order to identify and characterize the temporal variability of reservoirs and infiltration zones, we used time-lapse electrical resistivity tomography (ERT) to reveal a strong seasonality in the infiltration zones under the help of the HAC (Hierarchical Agglomerative Clustering) method. By integrating all these methods, this study considerably improves our understanding of infiltration in karstic environments with all the possible consequences for a better understanding of underground recharges, calibrations for paleoclimatic studies based on the study of speleothems and for the preservation of archaeological underground environments.

**Keywords:** Water isotopes, karst reservoirs, moisture sources, reservoir-flow model, infiltration, electrical resistivity tomography, Villars Cave

---